Appendix E

A Primer on Absorption and Scattering Opacity

One of the two fundamental properties of light-matter interaction is *absorption*, wherein light energy disappears, and a like amount of energy is converted to heat. The other property is *scattering*, in which the path of the light ray is merely deflected by the matter. We might think that specular reflection from a polished surface is a third type, but this phenomenon can be shown to be a consequence of scattering. Thus two (and only two fates) await a photon when it suffers an encounter with matter. This is true regardless of the form the matter takes: whether in a solid (land surfaces), in condensed form (the ocean) or whether it is composed of gaseous molecules or suspended particles (atmospheres). This book concerns itself with the dual influences of absorption and scattering on radiation fields in planetary media.

Consider first the property of absorption, and imagine a medium[1] in which only absorption is important for the light field. Although it is inherently easier to understand than scattering, it is difficult to find many commonplace examples in which *only* absorption is present. Carbon soot is perhaps the best example. An object covered with soot approaches the ideal *blackbody* behavior, described in elementary thermodynamic textbooks. However, since we are interested in atmospheres and oceans in this book, let us first consider a medium consisting of finely-dispersed soot particles.

Imagine sunlight to fall on such a medium, and consider the attenuation of the light as it passes through this soot cloud. The ability of the medium to attenuate the light will depend upon three quantities: (1) the number per unit volume n of the soot particles; (2) the particle sizes, r; and (3) the distance along the light ray, s. For simplicity we assume the particles are all

---

[1] We define a 'medium' in this context as the transparent matter in which the particles are imbedded. However, in the book we often use the term in a more general sense, as for example when we refer to a liquid body as an "aqueous medium".

the same size, and the cloud has uniform spatial density. The relevant attenuation quantity depends upon the *projected cross-sectional area* of the soot cloud in the direction of the light ray, $n\pi r^2 s$. This quantity is a pure number, and is the absorption *opacity*, or *optical depth*, τ_a. (Here we have assumed that the particles act as simple geometric light obstacles, which applies for sizes much larger than the sensing wavelength.) Another way to think of τ_a is the projected shadow area, per unit area, of all the particles along a ray path. If we ignore mutual shadowing effects (which is usually permissible) a moments thought reveals that the actual distribution of particles along the light ray is unimportant, only the product ns. Thus the relevant quantity is the total *column number* per unit area $\mathcal{N}$, and $\tau = \pi r^2 \mathcal{N}$. A high opacity at a particular visible-light frequency ν means that sunlight will be absorbed high up in the atmosphere, and a small opacity means that it will penetrate deeply. If $\tau(\nu) << 1$, the atmosphere is said to be *optically-thin*, or *transparent* at that frequency, and if $\tau(\nu) >> 1$, it is said to be *opaque*.

It remains to determine the degree to which the light is transmitted, and this involves a function of τ. It is shown in Chapter 2 that for sufficiently small frequency intervals $\Delta\nu$, this function is the exponential function $\exp[-\tau(\nu)]$. This familiar relationship is known popularly as *Beer's Law*, but for our own reasons, we call it the *Extinction Law*. Since absorption and transmission are opposite sides of the coin, the absorption varies as $1 - \exp[-\tau(\nu)]$. The absorption process leads to a heating of the medium (if the absorption is molecular excitation, and then quenching, the surrounding air is heated), in contrast to the scattering process.

Atmospheres also emit their own radiation, as do all bodies whose temperatures are above absolute zero. The solar atmosphere, due to its high temperature, emits copiously in the visible spectrum, whereas the cooler atmospheres of the earth and planets emit most of their energy in the thermal infrared. The opacity also plays a key role in the ability of media to emit radiation. This is one of many examples of the principle of detailed balance which are considered in this book, and is more familiar as *Kirchoff's Law*, which says in brief, that *an efficient absorber is an efficient emitter*. To be more precise, the ability of an atmosphere to emit also depends upon its opacity per unit length, or per unit volume, and depends upon the local absorptive properties of the medium.

Scattering processes add complexity to the above situation, in redirecting and modifying the radiation field without destroying it. Even soot particles are not "mini-black holes", but scatter a small amount of light. Otherwise we would not be able to distinguish soot particle texture or color. If the particles were non-scattering, the soot cloud would be invisible, except when viewing

the light beam directly — it would behave like a neutral density filter which progressively dims the light as we move farther away from the light source.

Now consider the opposite extreme of finely-dispersed water droplets (fog), which are efficient scatterers of visible radiation. "Reflection" from a cloud of these particles causes an incident light beam to be attenuated in a very similar way to the soot cloud, according to the scattering opacity τ_s. However, the light is not destroyed (or at least only a small fraction) but only deflected from its original path. For example around a fog-enshrouded lampost we witness this process as a host of twinkling starlike points of light. In the original direction of the light, the effect is the same as absorption, that is, a dimming of the light in proportion to the number of scattering particles along the path. The opacity is calculated in exactly the same way, except that the physical process is not a heating of the medium, as in absorption[2]. In fact a measurement of the attenuation with an ideal detector of small acceptance angle in the two cases of an absorbing soot cloud and a totally-scattering water fog would be exactly the same. This assumes that they have the same opacity. Furthermore if we were to measure the radiation in directions away from the light source, the scattering fog would be a source of secondary 'emission'. The same measurement for a totally-absorbing soot cloud would register zero radiation. This secondary light source is due to scattering of the light into our line of vision, and is the reason why we can "see" the cloud itself – for that matter, it explains why we are able to view the world around us. A major complexity in a quantitative description of the scattered light is the fact that every particle "sees" not only the original light source, but also the light scattered from its neighbors. This situation gives rise to higher orders of scattering, referred to as *multiple scattering*, and this "diffusion" of the light tends to produce a more uniform spatial distribution of brightness. Multiple scattering is one of the important subjects of this book.

Consider some implications of the scattering and absorption/emission processes on the earth's atmosphere and ocean. First, because of the atmosphere's high transparency in the visible spectrum $(0.4 - 0.7\mu m)$, the earth's land and ocean surfaces are subjected to mostly direct solar heating on cloud-free days. On cloudy, overcast days the light field consists of diffuse (multiply-scattered) photons. In general, both effects provide the so-called *short-wave radiative forcing* of the climate system. At the same time, the

---

[2] Actually, the process of scattering *does* alter the velocity of the particles through a momentum exchange with the incident photons, and strictly speaking, this could cause a heating of the gas. However, these radiation pressure effects are negligible for radiation energies of concern in this book.

land and ocean radiate infrared radiation to the atmosphere, and to space (depending upon the infrared opacity as a function of wavelength). This gives rise to radiative cooling, i.e. *long-wave radiative forcing*. The combined radiative effects, when averaged over the diurnal cycle, lead to a *net radiative forcing*, which is variable over the earth's surface. Spatial and temporal variations in this forcing give rise to weather and climate, which themselves alter the radiative forcing, in a non-linear interactive system (called feedback). Long-term changes in the long-wave forcing, such as carbon dioxide increases, will alter the atmosphere and ocean in ways which we do not yet fully understand.

We have used as specific examples, absorption by soot particles and scattering by water droplets, but these same concepts apply to any finely-dispersed substance (air molecules, air bubbles in the ocean, etc.) which alters the flow of radiation.

In conclusion, absorption and scattering give rise to attenuation according to the same basic formula, $\exp(-\tau)$. If both processes are present, and this is always the case in the real world, the net opacity is found to be the *sum* of the absorption and scattering opacities, $\tau = \tau_a + \tau_s$. Absorption tends to destroy the radiation field, and heat the medium. Because of their finite temperature, the particles also radiate light into all directions, in proportion to their absorptive properties as a function of frequency. Scattering redirects an original beam of light into generally all 4π sterradians. Multiple scattering causes the radiation field to become more uniform (diffuse). These two processes give rise to shortwave and longwave radiative forcing of climate, as well as many other atmospheric phenomena. In this book, we will deal with the "up-front" radiative processes, essential to understanding climate and climate change.

Appendix F

Elementary Concepts

F.1 Coordinate Systems

Figure 3.2 shows the relationship between the *rectangular* or *Cartesian co-ordinate system* and the *spherical-polar coordinate system*. Specifically, we are interested in specifying the coordinates of the unit propagation vector $\hat{\Omega}$ in both coordinate systems. The spherical-polar system defines $\hat{\Omega}$ simply in terms of the two angles, θ and ϕ. The rectangular system defines $\hat{\Omega}$ in terms of its three projections in the (x, y, z) directions, Ω_x, Ω_y, and Ω_z. The relationships between these two sets of coordinates are

$$\Omega_x = \sin\theta\cos\phi; \qquad \Omega_y = \sin\theta\sin\phi; \qquad \Omega_z = \cos\theta \qquad \text{(F.1)}$$

where $0 \le \phi \le 2\pi$, and $0 \le \theta \le \pi$.

F.2 The Dirac Delta-function

A concept which is useful in the mathematical representation of unidirectional or *collimated light* is the *Dirac δ-function*. This 'function' has the peculiar property that it is zero for finite values of its argument, and unbounded (infinite) when the argument of the δ-function is zero, that is

$$\delta(x) = 0 \qquad (x \ne 0) \qquad \text{and} \qquad \delta(x) \to \infty \qquad (x \to 0). \qquad \text{(F.2)}$$

Furthermore, the 'area' under the function is unity, that is, it is *normalized*

$$\int_a^b dx\,\delta(x) = 1 \qquad \text{if } a \text{ and } b \text{ are of different sign.}$$
$$= 0 \qquad \text{if } a \text{ and } b \text{ are of the same sign.} \qquad \text{(F.3)}$$

It is possible to define the δ-function for a *vector* argument. If we want to represent the electric field from a concentrated 'source' of unit strength (for

example, an electron) at the point $\vec{r} = \vec{r}_0$, we write $\delta(\vec{r} - \vec{r}_0)$. In rectangular coordinates $\delta(\vec{r} - \vec{r}_0)$ can be defined as a product of one-dimensional δ-functions, that is

$$\delta(\vec{r} - \vec{r}_0) = \delta(x - x_0)\delta(y - y_0)\delta(z - z_0). \tag{F.4}$$

The integral properties analogous to those in Eqs. F.3 are

$$\int \int \int d^3\vec{r}\, \delta(\vec{r} - \vec{r}_0) = \int dx \int dy \int dz\; \delta(x - x_0)\delta(y - y_0)\delta(z - z_0) = 1 \tag{F.5}$$

when the integration domain includes $\vec{r}_0$. The integral in Eq. F.5 is zero if the integration domain does not include $\vec{r}_0$.

In spherical polar coordinates we represent a point source as

$$\delta(\vec{r} - \vec{r}_0) = \delta(\cos\theta - \cos\theta_0)\delta(\phi - \phi_0)\delta(r - r_0). \tag{F.6}$$

The volume element in spherical coordinates is $dV = dA\,dr = r^2 dr\,\sin\theta\,d\theta\,d\phi = -r^2 dr\,d(\cos\theta)\,d\phi$. dA is the element of area normal to $\vec{r}$. The normalization property is

$$\int dV\,\delta(\vec{r} - \vec{r}_0) =$$

$$\int_0^{2\pi} d\phi \int_0^{\pi} d\theta\; \sin\theta \int_0^{r_m} r^2\delta(\vec{r} - \vec{r}_0)dr = 1 \quad (r_m > r_0)$$

$$= 0 \quad (r_m < r_0). \tag{F.7}$$

r_m is the (arbitrary) radius of a spherical volume centered at the origin.

A very important property applies to the integral of the product of the δ-function with an arbitrary function, say f. For example, if $f = f(x, y)$, then

$$\int dx \int dy f(x, y)\; \delta(x - x_0)\delta(y - y_0) = f(x_0, y_0). \tag{F.8}$$

It must be kept in mind that the volume of integration must include the 'source point' (x_0, y_o) of the δ-function for Eq. F.8 to apply (otherwise the result is zero).

The one-dimensional δ-function has the units of $(\text{length})^{-1}$, while $\delta(\vec{r} - \vec{r}_0)$ has the units of $(\text{length})^{-3}$. Other mathematical forms of the δ-function in terms of the solid angle are given in the next section.

F.3 The Solid Angle

The *solid angle* ω is defined as the ratio of the area A cut out of a spherical surface (see Fig. F.1) to the square of the radius of the sphere, i.e. $\omega = A/r^2$.
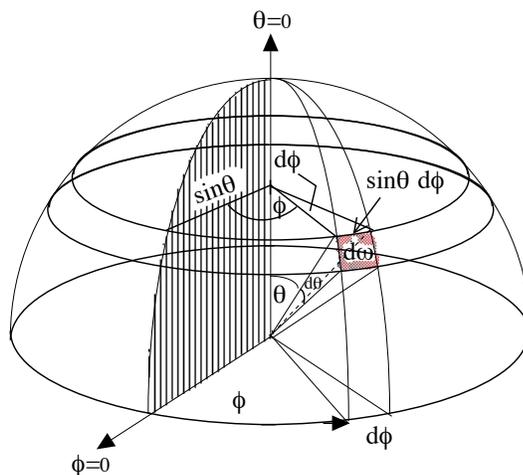
Figure F.1 Definition of the solid angle element $d\omega = \sin\theta d\theta d\phi$.

The units of ω are *steradians* [sr]. There are 2π sr in a hemisphere, and 4π sr in a full sphere. We are usually interested in a small (differential) element of solid angle, $d\omega$. As shown in Fig. F.1. $d\omega$ is expressed in spherical polar coordinates as $d\omega = dA/r^2$. Since $dA = r^2 \sin\theta d\theta d\phi$

$$d\omega = \sin\theta\ d\theta\ d\phi. \tag{F.9}$$

The integral of Eq. F.9 over the sphere, that is over 4π steradians, is

$$\int_{4\pi} d\omega \equiv \int_0^{2\pi} d\phi \int_0^{\pi} d\theta \sin\theta = 4\pi.$$

Often we consider a solar *beam* (§2.2) of light traveling in a particular direction. This direction is called the *propagation direction* and is specified by a unit vector $\hat{\Omega}_0$, which points in the direction (θ_0, ϕ_0). If we consider a general direction, described by the unit vector $\hat{\Omega}(\theta, \phi)$, a beam is a radiative energy flow which is zero for all directions except $\hat{\Omega}_0$. Thus, we can use a *two-dimensional* δ-function $\delta(\hat{\Omega} - \hat{\Omega}_0)$ to specify the direction of this energy flow. In spherical polar coordinates we have

$$\delta(\hat{\Omega} - \hat{\Omega}_0) = \delta(\cos\theta - \cos\theta_0)\delta(\phi - \phi_0) \tag{F.10}$$

where $\hat{\Omega}_0$ is specified by the angles (θ_0, ϕ_0). The normalization property of

the δ-function in Eq. F.10 is

$$\int_{4\pi} d\omega \delta(\hat{\Omega} - \hat{\Omega}_0) = 1. \tag{F.11}$$

While $\delta(\hat{\Omega} - \hat{\Omega}_0)$ is non-dimensional, it will be convenient to think of it as having the 'unit' of inverse steradians $[\mathrm{sr}^{-1}]$.

Appendix G

Derivation of the Planck Radiation Law

The derivation consists of two parts, the first being a determination of the average energy per photon state, the second finding the density of states within the *hohlraum*. We begin with a general statistical law describing the distribution of states in a system in thermodynamic equilibrium. If there are N total states, with individual discrete energies $\mathcal{E}_i$ $(i = 1, 2, \cdots, N)$, each having a degeneracy g_i, the *canonical, or Gibbs distribution* describes the probability of a particular energy state occurring for a system in contact with a heat reservoir at temperature T. It is proven in statistical mechanics treatises that

$$p(\mathcal{E}_i) \propto g_i e^{-\mathcal{E}_i/k_{\mathrm{B}}T}. \tag{G.1}$$

Since the probability summed over all states is unity, this distribution may be written as

$$p(\mathcal{E}_i) = \frac{g_i e^{-\mathcal{E}_i/k_{\mathrm{B}}T}}{\sum_{j=0}^{N} g_j e^{-\mathcal{E}_j/k_{\mathrm{B}}T}} \equiv \frac{g_i e^{-\mathcal{E}_i/k_{\mathrm{B}}T}}{Q_p(T)}. \tag{G.2}$$

Q_p is called the photon *partition function* (see §S.1.4 for more detailed examples of partition functions).

Equation G.2 describes the *Boltzmann distribution* of discrete energy states in thermodynamic equilibrium (see §4.3.4 and Eq. 4.18). It may also be transformed to yield the equilibrium distribution of molecular velocities in a gas. It is necessary to allow the range of energies to be continuous, and to convert the sums to integrals (see Eq. 4.10). Here we are interested in deriving the equilibrium distribution of photon energies, B_ν.

We next ask what is the mean energy of the quantum states having the frequency ν? If each state contains n photons of energy $h\nu$, then the energy of the nth state is $E_n = nh\nu$. The mean energy is thus the sum of E_n weighted by the probability of that energy occurring, $p(E_n) = g_n e^{-\beta E_n}/Q_p(T)$, where

$\beta \equiv (k_{\mathrm{B}}T)^{-1}$. Thus

$$\langle E(\nu)\rangle = \frac{\sum_{n=0}^{\infty} (nh\nu)\, e^{-\beta nh\nu}}{\sum_{n=0}^{\infty} e^{-\beta nh\nu}}.$$

We have factored out the common factor g_n which is the same for all states. To evaluate this expression explicitly, we note that

$$\langle E(\nu)\rangle = -\sum \frac{\partial}{\partial \beta}\left[e^{-\beta nh\nu}\right]\Big/\sum e^{-\beta nh\nu} = -\frac{d}{d\beta}\ln\left[\sum e^{-\beta nh\nu}\right]$$

where we have interchanged differentiation and summation. The sum can be evaluated as a geometric series $\sum x^n = (1-x)^{-1}$ where $x \equiv e^{-\beta h\nu}$. Thus

$$\langle E(\nu)\rangle = -\frac{d}{d\beta}\ln\frac{1}{(1-e^{-\beta h\nu})} = \frac{d}{d\beta}\ln(1-e^{-\beta h\nu}) = \frac{h\nu}{e^{h\nu/k_{\mathrm{B}}T}-1}.$$

For vanishing temperature, $\langle E(\nu)\rangle \approx h\nu \exp(-h\nu/k_{\mathrm{B}}T) \to 0$. For high temperature, $\langle E(\nu)\rangle \approx k_{\mathrm{B}}T$. The latter result tells us that the energy per photon is that predicted by the classical *Equipartition Theorem*, which states that the particle has $k_{\mathrm{B}}T/2$ of energy for every degree of freedom. A photon has *two* degrees of freedom, corresponding to the two polarization states. In quantum terminology, it has two spin directions ('up' and 'down').

We now make the correspondence of an oscillator with a standing electromagnetic wave in a cubical cavity (see Appendix K). For a given frequency ν a standing wave can have a host of discrete energies, given by $\mathcal{E}_p = (h/2\pi)c|\mathbf{k}| = h\nu$. Here $\mathbf{k}$ is the quantized wave number vector, having components $k_x = n_x(\pi/L)$, $k_y = n_y(\pi/L)$, and $k_z = n_z(\pi/L)$. L is the length of one side of the cubical cavity. We first need to know the number of standing waves $\Phi(k)dk$ having wavenumber lying between k and $k+dk$. Multiplying this number by the mean energy $\langle E(\nu)\rangle$ we obtain the expression for the energy density per unit volume. We can find $\Phi(k)$ by appealing to a simple geometrical construction, where the vector $\mathbf{k}$ is drawn in the pseudo-space of k_x, k_y, and k_z. Not all values of k_x, etc. are allowed – only those satisfying $k_x = \pi/L,\ 2\pi/L,\ 3\pi/L,\cdots$. We now visualize a volume element in this space, which is defined by incrementing each of the values of the k-components by one. Then for k large, the element is approximately a cube of side π/L whose volume is $(\pi/L)^3$. A given energy state defined by the coordinates (k_x, k_y, k_z) 'fills' the above volume element. A one-to-one correspondence exists between the volume $(\pi/L)^3$ and a specific energy state. Thus to count the total number of states out to some radial distance k in this pseudo-space, all we need to do is to evaluate the total volume and divide by $(\pi/L)^3$. There is some book-keeping we must do before we get the

correct answer. Since k is positive, we should evaluate only one quadrant of the total sphere in k-space, that is, the volume should be $4\pi k^3/3$ divided by 8. As mentioned earlier, for every specific value of $\mathbf{k}$, there are two independent states, corresponding to the two polarization states. Therefore the total number of states $N(k)$ for which the k-values are less than or equal to k is

$$N(k) = \frac{2 \times (4\pi k^3/3)}{8(\pi/L)^3} = \frac{Vk^3}{3\pi^2}$$

where $V = L^3$ is the cavity volume. The density of states (number per unit volume) is therefore

$$\Phi(k) = \frac{d}{dk}\frac{N(k)}{V} = \frac{d}{dk}\left(\frac{k^3}{3\pi^2}\right) = \frac{k^2}{\pi^2}.$$

We now return to frequency space, and find the number of states between ν and $\nu + d\nu$. Since $k = (2\pi\nu/c)$, then $k^2 = 4\pi^2\nu^2/c^2$ and $dk = 2\pi d\nu/c$. Therefore

$$\Phi(\nu)d\nu = \frac{4\nu^2}{c^2}\left(\frac{2\pi d\nu}{c}\right) = \frac{8\pi\nu^2 d\nu}{c^3}.$$

Finally, the energy density is the number of oscillators per unit volume multiplied by the average energy

$$\mathcal{U}_\nu = \frac{8\pi\nu^2\langle E(\nu)\rangle}{c^3} = \frac{8\pi\nu^2 h\nu}{c^3\left(e^{h\nu/k_{\mathrm{B}}T} - 1\right)}.$$

Since the radiation is isotropic, $\mathcal{U}_\nu = 4\pi\bar{I}_\nu/c = 4\pi I_\nu/c$ (see Eq. 2.13), we find the blackbody radiance formula

$$I_\nu^{\mathrm{BB}} = B_\nu(T) = \frac{c}{4\pi}\mathcal{U}_\nu = \frac{2h\nu^3}{c^2}\frac{1}{e^{h\nu/k_{\mathrm{B}}T} - 1}.$$

Appendix H

The Two-Level Atom

We consider the more realistic situation in which *all* the radiative and collisional processes act together. We will assume that the values of the rate processes are given, and derive equations describing the transfer of radiation through the system. Many of the properties of a complex system are embodied in the *two-level atom* concept, which envisions an atom with only two discrete energy levels. Altogether, we must consider five separate processes (see Fig. 4.7) connecting the two energy levels of the atom. We begin by considering the radiative processes.

H.1 Microscopic Radiative Transfer Equation

The radiation field is assumed to be a result of transitions from the single excited level (state 2) to the ground level (state 1) of a radiatively-significant species. The gas will be a two-component mixture consisting of the radiatively-significant species, and a radiatively inert 'buffer' gas. The latter plays the role of collisionally transforming the excited level to the ground state and vice versa. The populations in the two levels are denoted n_1 and n_2. The sum of the two populations is a constant, equal to the density of the radiatively-significant species, n. The average energy difference between the states is $E_{21} = h\nu_0$, but there is assumed to be a small spread in frequencies, due to spectral broadening. The radiative processes (see Fig. 4.7) are:

  (1) *Absorption*: $h\nu + n_1 \rightarrow n_2$
  (2) *Spontaneous emission*: $n_2 \rightarrow n_1 + h\nu$
  (3) *Stimulated emission*: $n_2 + h\nu \rightarrow n_1 + h\nu + h\nu$.

  Process (3) is one in which the emitted radiation is exactly coherent with the incident radiation, in both direction and phase. Processes (1) and (3) may be understood from classical physics, but (2) requires quantum theory

for a fundamental description. In the semi-classical theory, we assign a rate to this process which is independent of the surroundings of the atom.[1]

The rates at which the three radiative processes occur were first derived by A. Einstein in 1916.[2] The rate efficiencies are described by the *Einstein coefficients* B_{12}, A_{21}, and B_{21}. We now consider the rate equations for each individual process: Process (1) describes the rate at which absorption depletes the lower state, and is proportional to the number of atoms in the ground state n_1, to the absorption cross section $\alpha_n(\nu)$, and to the number of photons in solid angle $d\omega$, $(I_\nu/h\nu)d\omega$. Integrating over all frequencies[3] and photon directions, we find

$$(dn_2/dt)_{abs} = n_1 \int_0^\infty d\nu \int_{4\pi} d\omega \alpha_n(\nu)(I_\nu/h\nu) = 4\pi n_1 \int_0^\infty d\nu \alpha_n(\nu)(\bar{I}_\nu/h\nu).$$
$$\text{(H.1)}$$

Process (2) is the rate at which photons depopulate the upper state. Einstein asserted that its rate may be written

$$(dn_2/dt)_{spon} = -A_{21}n_2. \qquad \text{(H.2)}$$

The above equation shows that the excited states decay via this process *independently of its surroundings*. Stimulated emission, Process (3), is given by an expression similar to Eq. H.1, since the rate is also proportional to the number of photons available

$$(dn_2/dt)_{stim} = -n_2 \int_0^\infty d\nu \int_{4\pi} d\omega \alpha_n(stim;\nu)(I_\nu/h\nu)$$
$$= -4\pi n_2 \int_0^\infty d\nu \alpha_n(stim;\nu)(\bar{I}_\nu/h\nu) \qquad \text{(H.3)}$$

where $\alpha_n(stim;\nu)$ is the absorption cross section for stimulated emission.

We now write the above absorption cross sections in terms of the Einstein coefficients, $\alpha_n(\nu) \equiv h\nu B_{12}\Phi(\nu)/4\pi$, and $\alpha_n(stim;\nu) \equiv h\nu B_{21}\Phi(\nu)/4\pi$. The *line-profile function* $\Phi(\nu)$, assumed to be the same for the two processes, is normalized so that

$$\int_0^\infty d\nu \Phi(\nu) = 1. \qquad \text{(H.4)}$$

There is no *a priori* reason why the line profiles for stimulated emission and absorption should generally be the same. We made the assumption because

---

[1] Spontaneous emission may be thought of as being stimulated by fluctuations in the vacuum state of the electromagnetic field.

[2] Einstein, A. (1916). "Strahlungs-Emission und -Absorption nach der Quantentheorie". Verhandlungen der Deutschen Physikalischen Gesellschaft. 18: 318–323.

[3] Since there is only one spectral line, the limits of integration can be safely extended over the entire spectrum.

in many situations it is an excellent approximation.[4] The properties of the atom (molecule) and its surroundings determine the line shape. We assume for now that $\Phi(\nu)$ is known, and independent of position.

As we might suspect, the rates of the above three processes are related. In fact, we will show that it is sufficient to know the value of one Einstein coefficient to determine the other two. For this purpose we use the common approach of assuming a special case (that of TE), and then arguing that the result so obtained has more general validity. In TE, $I_\nu = B_\nu$, and the populations n_1 and n_2 are related through the Boltzmann equation, Eq. 4.18. We denote the ratio of the two populations in TE as n_2^*/n_1^* to distinguish it from the more general ratio n_2/n_1. Hence, from Eq. 4.18, we have

$$n_2^*/n_1^* = (g_2/g_1)\exp(-h\nu_0/k_{\mathrm{B}}T) \tag{H.5}$$

where the g_i are the statistical weights. (Note that we have used the average energy difference between the two states $E_{21} = h\nu_0$.) Assuming time-independent conditions, we have $dn_1^*/dt = -dn_2^*/dt = 0$. The radiative rates must all balance[5] so that

$$dn_1^*/dt = 0 = n_2^* A_{21} + n_2^* B_{21} \int_0^\infty d\nu\, B_\nu \Phi(\nu) - n_1^* B_{12} \int_0^\infty d\nu\, B_\nu \Phi(\nu). \tag{H.6}$$

Since the Planck function B_ν varies slowly over the line profile, we may simplify the above expression. Thus, setting $B_\nu \approx B_{\nu_0}$, and using the normalization property of $\Phi(\nu)$, Eq. 4.23, we find

$$n_2^* A_{21} + n_2^* B_{21} B_{\nu_0} = n_1^* B_{12} B_{\nu_0}.$$

Solving for B_{ν_0} we find

$$B_{\nu_0} = \frac{(A_{21}/B_{21})}{(g_1 B_{12}/g_2 B_{21})\, e^{h\nu_0/k_{\mathrm{B}}T} - 1}. \tag{H.7}$$

But we already know the functional form of the Planck function

$$B_{\nu_0} = \frac{2h\nu_0^3/c^2}{e^{h\nu_0/k_{\mathrm{B}}T} - 1}. \tag{H.8}$$

Making the correspondence of the above two equations, we obtain the following two expressions:

The Einstein Relations

---

[4] The justification for why the line profiles for absorption and emission should be the same is given by Cooper et al. (1983).

[5] It might appear that we have cheated a bit by ignoring collisional processes. In fact, when we balance the radiative processes separately from the collisional processes, we are invoking the principle of *detailed balance*.

$$A_{21} = (2h\nu_0^3/c^2)B_{21} \quad \text{(a)}; \qquad g_1 B_{12} = g_2 B_{21} \quad \text{(b)}. \tag{H.9}$$

These relationships are independent of the state of the gas, in particular of the temperature or density, and therefore must involve only the basic properties of the atom itself. We therefore assert that *the Einstein relations are quite general, and are independent of the situation assumed in their derivation.* Thus, they should apply to the more general situation of NLTE.

We now use the above relationships to write down the continuity equation for photons, which is just our familiar radiative transfer equation. We first note that dI_ν/ds is the rate at which radiative energy is lost, or gained, along a beam. Then we can write this quantity as being equal to the gains less the losses due to the three radiative processes. The result is:

The Microscopic Radiative Transfer Equation

$$\frac{dI_\nu}{ds} = -\frac{h\nu_0}{4\pi}n_1 B_{12} I_\nu \Phi(\nu) + \frac{h\nu_0}{4\pi}n_2 B_{21} I_\nu \Phi(\nu) + \frac{h\nu_0}{4\pi}n_2 A_{21}\Phi(\nu). \tag{H.10}$$

We have introduced the additional assumption that the line profile for spontaneous emission is also given by $\Phi(\nu)$. Equation H.10 may now be related to our conventional radiative transfer equation, Eq. 2.28 which we may now call the *macroscopic* radiative transfer equation

$$\frac{dI_\nu}{ds} = -k(\nu)\left(I_\nu - S_\nu\right). \tag{H.11}$$

Equating the factors multiplying I_ν in Eqs. H.10 and H.11, we find

$$k(\nu) = \frac{h\nu_0}{4\pi}\Phi(\nu)\left(n_1 B_{12} - n_2 B_{21}\right). \tag{H.12}$$

This relationship allows us to relate microscopic quantities to macroscopic quantities. Consider the above equation in the case of LTE. Replacing the quantities n_1 and n_2 by n_1^* and n_2^*, we have

$$k^*(\nu) = \frac{h\nu_0}{4\pi}\Phi(\nu)n_1^* B_{12}\left(1 - \frac{n_2^* B_{21}}{n_1^* B_{12}}\right) \tag{H.13}$$

where we denote by $k^*(\nu)$ the LTE value of the effective extinction coefficient. From the Boltzmann relation for the ratio n_2^*/n_1^* (Eq. H.5), and the Einstein relation $g_2 B_{21} = g_1 B_{12}$, we find

$$k^*(\nu) = \frac{h\nu_0}{4\pi}\Phi(\nu)n_1^* B_{12}\left(1 - e^{-h\nu_0/k_{\mathrm{B}}T}\right). \tag{H.14}$$

The above equation is the extinction coefficient in LTE, *corrected for stimulated emission*. It is clear that stimulated emission is simply *negative absorption*, since the emitted photon is coherent with, and in the same direction as the incident photon. Thus, our macroscopic equation needs a slight adjustment for the LTE situation, such that

$$\frac{dI_\nu}{ds} = -k^*(\nu)\,(I_\nu - S_\nu) \tag{H.15}$$

where $k^*(\nu)$ is given by Eq. H.14. In the more general NLTE situation we would use the Eq. H.12 for $k(\nu)$. In many atmospheric problems, the factor $e^{-h\nu_0/k_{\mathrm{B}}T} << 1$ implying that the effect of stimulated emission is negligible.

We now equate the source terms in Eqs. H.10 and H.11. Using Eq. H.12 for $k(\nu)$, we find

$$S_\nu = S_{\nu_0} = \frac{n_2 A_{21}}{n_1 B_{12} - n_2 B_{21}} = \frac{2h\nu_0^3/c^2}{(n_1 g_2/n_2 g_1) - 1} \tag{H.16}$$

where we used the Einstein relationships, Eq. H.9. An important aspect of Eq. H.16 is that the frequency-dependence of the source function has vanished, because we assumed that the line profiles for stimulated emission, spontaneous emission, and absorption are identical. This approximation is called *complete frequency redistribution*. Note that if we assume that $n_2/n_1 = n_2^*/n_1^*$, that is, make the LTE assumption, then the source function becomes the Planck function Eq. H.8, as can be seen from Eq. H.5. Therefore, Eq. H.16 is the expression for the NLTE source function. However, it is not very useful to express it in terms of another unknown, the ratio of the two populations. The equation for determining this unknown ratio comes from considering inelastic collisions.

H.2 Effects of Collisions on State Populations

So far we have considered only the effects of radiation on the excited states. We now take into account the additional effects of collisional excitation and quenching. We previously defined these rates in terms of the product of reactant concentrations and a reaction rate coefficient. For purposes of simplifying the notation, we define the collisional excitation rate per atom as $k_{\mathrm{in}}[M] \equiv C_{12}$ and the collisional quenching rate per atom as $k'_{\mathrm{in}}[M] \equiv C_{21}$. We may now write down the rate at which both collisions and radiation

populate the excited state. In a steady state we set this rate equal to zero

$$\frac{dn_1}{dt} = -n_1 C_{12} - n_1 B_{12} \int_0^\infty d\nu \Phi(\nu) \bar{I}_\nu$$
$$+ n_2 C_{21} + n_2 B_{21} \int_0^\infty d\nu \Phi(\nu) \bar{I}_\nu + n_2 A_{21} = 0. \qquad \text{(H.17)}$$

This equation is called the *statistical equilibrium equation.* It provides a second equation which, in addition to Eq. H.16, allows us to solve for *both* unknowns, n_2/n_1 and the source function. But first we will consider some relationships between the collisional rates by once again invoking the principle of detailed balance.

In deriving the Einstein relationships, we considered the state of TE, in which the radiative processes are in balance with one another, without regard to collisional processes. We use the same idea with collisions, and ignore radiative processes. Assuming TE, we set the two rates equal

$$n_2^* C_{21} = n_1^* C_{12}. \qquad \text{(H.18)}$$

Using the definitions of the coefficients, and invoking the Boltzmann distribution of excited states, Eq. 4.18, we find

$$C_{21} = C_{12} \frac{g_1}{g_2} e^{h\nu_0/k_\mathrm{B}T}. \qquad \text{(H.19)}$$

As in the case of the Einstein relationships we will argue that the above relationship is more general than the assumption used in deriving it. We cannot argue that Eq. H.19 describes an inherent atomic property, because of its dependence on the temperature. However, we observe that the collisional excitation rate (Eq. 4.9) is determined by an integration over the product of the Maxwell-Boltzmann velocity distributions of the reactants. We also recall that these distributions are maintained by elastic collisions, which are millions of times more efficient than inelastic collisions. Thus, we would expect that Eq. H.19 would be valid in non-equilibrium situations, *as long as the velocity distribution is Maxwellian.* To emphasize that there may be several different temperatures in a NLTE situation, the quantity entering the Maxwell-Boltzmann distribution is often referred to as the *kinetic* or *translational* temperature.

We now return to the statistical equilibrium equation. Solving for n_1/n_2 from Eq. H.17 we obtain

$$\frac{n_1}{n_2} = \frac{C_{21} + B_{21}J + A_{21}}{C_{12} + B_{12}J} \quad \text{where} \quad J \equiv \int_0^\infty d\nu \Phi(\nu) \bar{I}_\nu. \qquad \text{(H.20)}$$

Equation H.20 is in the form of the ratio of the net rate of excitation to

the net rate of quenching, or the 'source' divided by the 'sink' of excited states.

We consider Eqs. H.16 and H.20 to be two equations in the two unknowns, n_1/n_2 and S_ν. The quantity J depends upon the radiation field $\bar{I}_\nu$ which can be determined from the source function equation for isotropic scattering, in the usual way. Using Eq. H.19 to eliminate the collisional rate C_{12}, and Eq. H.9 to eliminate the Einstein coefficient B_{12} in Eq. H.20, we find

$$\frac{n_1}{n_2} = \frac{A_{21} + B_{21}J + C_{21}}{(g_2/g_1)C_{21}e^{-h\nu_0/k_BT} + (g_2/g_1)B_{21}J}. \tag{H.21}$$

Note carefully that T is understood to be the kinetic temperature of the gas. Thus the velocity distribution of the atoms in the gas is in LTE, while the populations of the energy states may be far from an LTE distribution. We rewrite the above equation as

$$\frac{n_1 g_2}{n_2 g_1} = \frac{A_{21} + B_{21}J + C_{21}}{B_{21}J + C_{21}e^{-h\nu_0/k_BT}}. \tag{H.22}$$

We now have the combination that appears in the denominator of Eq. H.16. Substitution of Eq. H.22 into Eq. H.16 yields

$$S_{\nu_0} = \frac{2h\nu_0^3}{c^2}\left[\frac{A_{21} + B_{21}J + C_{21}}{B_{21}J + C_{21}e^{-h\nu_0/k_BT}} - 1\right]^{-1}$$

which may be rewritten as

$$S_{\nu_0} = \frac{(2h\nu_0^3/c^2)(B_{21}J + C_{21}e^{-h\nu_0/k_BT})}{A_{21} + C_{21} - C_{21}e^{-h\nu_0/k_BT}}.$$

Using the first of the Einstein relations, Eq. H.9, we obtain

$$S_{\nu_0} = \frac{J + (2h\nu_0^3/c^2)(C_{21}/A_{21})e^{-h\nu_0/k_BT}}{1 + (C_{21}/A_{21})(1 - e^{-h\nu_0/k_BT})}.$$

Defining a new parameter, ϵ_v,

$$\epsilon_v \equiv \frac{C_{21}}{C_{21} + A_{21}(1 - e^{-h\nu_0/k_BT})^{-1}} \tag{H.23}$$

we find with some additional manipulation and using Eq. H.8

The NLTE source function

$$S_{\nu_0} = \epsilon_v B_{\nu_0} + (1 - \epsilon_v)J. \tag{H.24}$$

We have shown that the NLTE source function is the sum of two terms:

a thermal emission term, plus a term which represents the scattering contribution to the source function. $\epsilon_v B_{\nu_0}$ is interpreted as the emittance per unit volume, that is, its efficiency as a blackbody emitter as a function of frequency within the spectral line. In terms of the macroscopic absorption $(\alpha(\nu))$ and extinction $(k(\nu))$ coefficients, $\epsilon_v = \alpha(\nu)/k(\nu)$ (note that the frequency dependence cancels in the ratio). The emission coefficient is obtained from its definition $(j_\nu = S_\nu/k(\nu))$, yielding

$$j_\nu = \alpha(\nu)B_\nu(T) + \int_0^\infty d\nu\,\sigma(\nu)\bar{I}_\nu \qquad \text{(H.25)}$$

where we used the relationship $\sigma(\nu) = k(\nu) - \alpha(\nu)$. The first term in the above equation is the expression of *Kirchoff's Law* for a volume element, which states that the thermal emission is the product of the absorption coefficient and the Planck function (§5.3.1). The second term is the contribution to the volume emission from scattering within the volume (see §5.3.2).

The quantity ϵ_v is a measure of the *coupling* between the gas and the radiation field. When it is large $(\epsilon_v \to 1)$, the coupling is strong, and there is a rapid exchange between kinetic and internal energy. In this limit, $S_{\nu_0} \to B_{\nu_0}$, which is just the LTE limit. In the opposite case of weak coupling, $(\epsilon_v \to 0)$, the source function approaches the pure-scattering limit

$$S_{\nu_0} \to J = \int_0^\infty d\nu\,\Phi(\nu)\bar{I}_\nu \qquad \text{(H.26)}$$

which might be called an extreme condition of NLTE, in which the excited states are populated exclusively by radiation and collisions no longer play a role. In a planetary or stellar atmosphere, as one moves upward into lower densities and pressures, there will be a transition from LTE to NLTE as the coupling between the gas and the radiation field disappears.

Appendix I
Non-Gray Inhomogeneous Media

I.1 Transmission in Non-Gray Inhomogeneous Media

Up to now we have dealt with homogeneous paths, for which the pressure and temperature are assumed to be constant along the beam. However, unless the beam direction is horizontal, this assumption is invalid, and we must deal with the inhomogeneous nature of the medium. In general, the mean beam transmittance in a slab medium over an inhomogeneous path of a beam making an angle θ with the vertical is given by

$$\langle \mathcal{T}_{\mathrm{b}}(u,\theta) \rangle = \frac{1}{\Delta\tilde{\nu}} \int_{\Delta\tilde{\nu}} d\tilde{\nu} \left\{ \exp\left[-\int_0^u du' \mathcal{S}(u') \Phi(u',\tilde{\nu}) \sec\theta \right] \right\}. \tag{I.1}$$

To understand better the structure of Eq. I.1, let us reconsider the simple case of an isolated Lorentz line, but now let the line of sight be taken over an inhomogeneous optical path. This situation leads to an analytic result only in the special case of a well-mixed gas and a pure-Lorentzian line profile. Although it is not necessary, we will assume a vertical path ($\theta = 0$). The volume density of the absorber is given by $w^m \rho(z)$. Here w^m is its mass mixing ratio (assumed constant) and $\rho(z)$ is the total atmospheric mass density. The optical path between the heights z and z' may be transformed from the mass path variable to the geometric height variable dz'', so that $du'' = -w^m \rho(z'') dz''$. Then

$$\tau(z,z') = \int_z^{z'} dz'' w^m \rho(z'') \frac{\mathcal{S}\alpha_{\mathrm{L}}(z'')}{\pi[(\tilde{\nu} - \tilde{\nu}_0)^2 + \alpha_{\mathrm{L}}(z'')^2]}$$

$$= \left[\frac{\mathcal{S}pw^m}{2\pi\alpha_{\mathrm{L}}(z)g} \right] \ln\left[\frac{(\tilde{\nu} - \tilde{\nu}_0)^2 + \alpha_{\mathrm{L}}(z)^2}{(\tilde{\nu} - \tilde{\nu}_0)^2 + \alpha_{\mathrm{L}}(z')^2} \right] \tag{I.2}$$

where the hydrostatic equation, $dp = -\rho(z)gdz$, was used. To obtain the sec-

ond form we changed integration variables from dz'' to $d\alpha_L$, and integrated analytically. It is easily checked that the second result is dimensionless, as it must be. It is also a constant, since $\alpha_L(z)$ is proportional to $p(z)$, the total gas pressure (see Eq. 3.11).

To simplify the algebra we consider a situation in which the path is from z to $z' \to \infty$. Now the vertical mass path is simply $u = w^m p/g$ (assuming g is constant with height). Assuming $\alpha_L(z')$ approaches α_D, the Doppler width, we find for a well-mixed gas

The absorption coefficient for an inhomogeneous vertical path:

$$k_L^*(\tilde{\nu})u \equiv \frac{\mathcal{S}u}{2\pi\alpha_L} \ln\left[\frac{(\tilde{\nu} - \tilde{\nu}_0)^2 + \alpha_L(z)^2}{(\tilde{\nu} - \tilde{\nu}_0)^2 + \alpha_D^2}\right]. \tag{I.3}$$

To be more accurate, a Voigt line shape should be used in the limit $z' \to \infty$.

Equation I.3 describes the behavior of the absorption profile of a spectral line for very high resolution. With modern spectroscopic techniques, the resolving power is now sufficient to test such predictions. An example is shown in Fig. 4.5 of an individual CO_2 line profile measured for absorption of near-IR sunlight. The observed shape closely resembles the theoretical prediction, showing that the Lorentz profile (applicable to a homogeneous, horizontal path, Eq. 3.6) *does not apply* to a column-integrated inhomogeneous path.

I.1.1 The H-C-G *Scaling Approximation*

One might hope that the simple expressions derived for the homogeneous case, say for absorptance, $\langle \alpha_b(u) \rangle_{\mathrm{hom}}$ could somehow be used for the inhomogeneous case, if only we could define equivalent values for the *effective pressure*, $\langle p \rangle$, *effective temperature*, $\langle T \rangle$, and *effective path length*, $\langle u \rangle$, such that

$$\langle \alpha_b(u) \rangle_{\mathrm{inhom}} = \langle \alpha_b(\langle u \rangle, \langle p \rangle, \langle T \rangle) \rangle_{\mathrm{hom}}. \tag{I.4}$$

If we compare Eq. I.2 or Eq. I.3 for an inhomogeneous medium with that for the absorption coefficient in a homogeneous medium, Eq. 4.68, it is clear that there are significant differences in the wavenumber dependence. Hence, so-called *scaling relations* can at best be approximations, except under certain circumstances. Perhaps the most accurate such scaling relation is that due to Van de Hulst, Curtis and Godson, the H-C-G *approximation*. For a constant mixing ratio and temperature along the path, this approximation yields the following: $\langle u \rangle = u$, $\langle p \rangle = \frac{1}{2}(p+p')$, where p and p' are the pressures of the beginning and end points. It can be shown (Exercise 4.11) that this

H-C-G scaling yields accurate values of both (1) the absorption coefficient in the wings of the line ($\tilde{\nu} >> \alpha_L$) and (2) the integrated line absorption (i.e. the area under the line). The H-C-G approximation is probably the best scaling approximation available, particularly for well-mixed species. However for species, such as water vapor and ozone whose mixing ratio varies appreciably with height, this scaling can produce errors in the heating rate as large as 10%.

I.2 LBL Transmission Computation: Inhomogeneous Paths

Whereas absorption lines are pressure-broadened at low altitudes (for which a Lorentz profile is adequate), they become Doppler-broadened at high altitudes. Spectral sampling strategies allowing for efficient yet accurate integration of the Voigt profile for a given temperature and pressure (i.e. a homogeneous path) were briefly discussed in §4.7.6. The extension to non-uniform atmospheric paths with varying temperature, pressure and absorber concentration is usually done by approximating the real atmosphere by a series of homogeneous layers in which the parameters are taken to be constant in each layer, but are allowed to vary from layer to layer.

The LBLRTM (Clough et al., 2005) computer code[1] uses a sampling interval that is a suitable fraction of the average half-width of the line. Since the pressure decreases exponentially with altitude, the average half-width and therefore the sampling interval becomes smaller at higher than at lower levels in the atmosphere. The absorption coefficient for each layer may then be merged with those from neighboring layers in such a way that the absorptance for a path through two adjacent layers has the resolution of the higher layer. This merging is accomplished by interpolating the coarser-resolution results for the lower layer into the finer resolution of the higher layer. In LBLRTM (derived from FASCODE (Clough et al., 1981)) this procedure is executed in a systematic manner so that the spectral absorptance for a given atmospheric slant path is obtained with the finest spectral resolution at all atmospheric levels. The transmittance between any two boundaries may then be computed, and used to obtain the radiance along a given path (assuming LTE so that the emission is given by the Planck function) depending exclusively on wavenumber and temperature.

The need to speed up the computation by using bigger wavenumber steps in the line wings and a fine grid across the line center is recognized in most algorithms designed to perform line-by-line computations. For example, in

---

[1] LBLRTM is an accurate and efficient line-by-line radiative transfer model derived from the Fast Atmospheric Signature Code (FASCODE) (Clough et al., 1981, 1992).

another generally-available LBL code, A General Line-by-Line Atmospheric Transmittance and Radiance Code (GENLN2), described in Edwards (1992), the user-specified spectral range is first divided into a number of wide mesh intervals, which may be of constant or variable spacing. In GENLN2, the line-by-line computation proceeds in two stages: a 'wide-pass' stage followed by a 'fine-pass' computation. The 'wide-pass' stage computes absorption due to line wings of lines whose centers fall into a fixed range from the wide mesh boundaries. This step also considers absorption due to pre-computed continua accounting for the absorption of the line wings at separations greater than 25 cm^{-1} from the line center. In addition, high-resolution cross section data are used to account for absorption by molecules for which line data are lacking. The 'fine-pass' stage uses a fine spectral grid which is determined by the width of the narrowest line encountered over a particular path. For applications to the Earth's atmosphere, this approach implies that the width of the lines in the uppermost atmospheric layer of the path (where the lines are narrowest) determines the resolution. All lines within the wide mesh boundaries are included in the 'fine-pass' stage, and line wings up to 25 cm^{-1} from the line center are taken into account.

Finally, the wide-pass absorptions, interpolated to the fine spectral grid points, are added to the fine-pass absorptions at these same points to yield the monochromatic absorption coefficient. For a vertical path the optical depth is obtained as the product of the absorption coefficient and the absorber amount. For several absorbing gases the total optical depth is obtained by adding the contributions from the individual gases. Thus, the total monochromatic absorption optical depth may be written as

$$\tau_a(\tilde{\nu}) = \sum_j \tau(\tilde{\nu})_j^{\text{near lines}} + \tau(\tilde{\nu})_j^{\text{line wings}} + \tau(\tilde{\nu})_j^{\text{broadband}} \qquad \text{(I.5)}$$

where the broadband absorption includes the contribution from continua and molecular cross sections. The sum extends over all absorbing species.

Comparing the line-by-line computation in LBLRTM and GENLN2, we see that, despite differences in detailed approach, they both compute absorption at a fine spectral grid spacing, and both codes employ a variable computational grid to produce the final result: an overall absorption coefficient or optical depth (summed over absorbing species in the path) at a fine spectral resolution that may be considered monochromatic. The main difference between the two codes lies in the subsequent computation of transmittance and radiance. Whereas GENLN2 proceeds with the transmittance and radiance computation based on the fine grid spectral resolution, which is the same in every atmospheric layer, LBLRTM attempts to speed up

this part of the computation by computing transmittance with a spectral resolution that varies from layer to layer as mentioned above.

I.2.1 Inclusion of Multiple Scattering in LBL Computations

In principle, it is almost trivial to include multiple scattering in LBL computations. The reason is that LBL computations are monochromatic and therefore automatically consistent with multiple scattering algorithms. Thus, if a LBL code can be used to compute gaseous optical depths layer-by-layer throughout the medium, this information can be combined with data on scattering and absorption coefficients (Eqs. 3.9–3.10) of other scattering and absorbing species to obtain the layer-by-layer optical depth, single-scattering albedo ϖ (defined in §5.3.2, Eq. 5.44) and scattering phase function p (see §3.4). These are the data required to perform monochromatic radiative transfer computations including multiple scattering. The gaseous absorption contribution to the optical depth is given by Eq. I.5.

In view of the discussion above, it may appear surprising to learn that, in practice, the inclusion of multiple scattering in LBL codes has not been done in a satisfactory manner. In an effort to explain this situation we now briefly consider the design of the LBLRTM and GENLN2 codes discussed previously. The main problem is that these codes (and most available LBL codes) do not employ radiative transfer schemes that are well suited to perform multiple scattering computations. The radiative transfer schemes were designed to work in the thermal IR, where scattering can be safely ignored unless aerosols and clouds are present. Thus, *the radiative transfer scheme was not designed for the computation of multiple scattering effects*. As a consequence, the radiative transfer schemes used in most LBL codes integrate along the line-of-sight to obtain the radiance, assuming that the source function is known, which is the case when scattering is ignored. However, the source function due to multiple scattering depends on the radiance (see Chapters 7 and 9), which is an unknown. Hence, it is a non-trivial task to compute the multiply scattered radiation field, implying that most LBL codes must remedy this shortcoming.

The original version of FASCODE (Clough et al., 1981) treated particle scattering as equivalent to absorption *so that all scattered radiation was treated as re-emitted energy that was previously absorbed.* An approximate treatment of multiple scattering[2] was later introduced by using a two-stream approximation combined with an adding algorithm. This approach was chosen because it is consistent with the radiance/transmittance computation in FASCODE which treats one layer at a time, but which employs a spectral

---

[2] Inclusion of multiple scattering is described by Isaacs et al. (1987).

step size that may vary from layer to layer. However, this approach is inconsistent with monochromatic multiple scattering treatments which require the use of a fixed wavenumber throughout the medium.

Scattering is not considered in the GENLN2 code. However, this code can be used to compute monochromatic absorption optical depths, because it utilizes the same spectral step size in all atmospheric layers. Thus, the spectral sampling in GENLN2 is compatible with monochromatic multiple scattering algorithms. Similarly, the gaseous optical depths computed in FAS-CODE (now LBLRTM) can be interpolated to the same spectral step size in all atmospheric layers and thereby become compatible with monochromatic multiple scattering algorithms.

Thus, both FASCODE (LBLRTM) and GENLN2 can be used to compute the quantity required for LBL multiple scattering computations, namely the monochromatic (fixed wavenumber) absorption optical depth. However, the radiative transfer schemes employed in most existing LBL codes, including LBLRTM and GENLN2, are ill-suited to perform multiple scattering computations. Efforts to design and implement comprehensive and efficient LBL multiple scattering codes are are still being pursued.

Finally, we note that properly designed LBL codes that include multiple scattering in a rigorous manner would provide a testbed for 'benchmark' computations against which alternative approaches aimed at enhanced efficiency may be tested. One possible way to proceed in the pursuit of an efficient yet accurate inclusion of multiple scattering in LBL codes would be an attempt to reduce the need for multiple scattering computations by exploiting the existing redundancy in absorption coefficients across a given spectral interval over which the particle scattering and absorption coefficients do not vary appreciably. In principle, such an approach resembles the philosophy underlying the k-distribution method.

I.2.2 The Correlated-k Method

The average transmittance, Eq. I.1 may be written in k-distribution form for an inhomogenous path, in analogy to Eq. 4.95, as

$$\langle \mathcal{T}_{\rm b}(u) \rangle = \int_{k_{min}}^{k_{max}} dk f^*(k) \exp \left[- \int_0^u du' k(u') \right] \tag{I.6}$$

or, in finite-difference form

$$\langle \mathcal{T}_{\rm b}(u_{\ell_1}, u_{\ell_2}, \theta) \rangle = \sum_{j=1}^{N} f^*(k_j) \exp \left[- \sum_{\ell=\ell_1}^{\ell_2} k_\ell \Delta u_\ell \right]. \tag{I.7}$$

We have assumed a vertical path, $\theta = 0$. The k_j are the absorption coef-

ficients appropriate for the jth layer, assuming each of the layers are thin enough to be considered homogeneous. The integration extends from the center of the layer identified by u_{ℓ_1} to the center of the layer u_{ℓ_2}. The quantities f^* and g^* (introduced below) denote the distribution, and the cumulative distribution (respectively) of the absorption coefficients along the inhomogeneous path. Clearly f^* and g^* are not equal to the distributions f and g, discussed previously, since they applied to a homogeneous path.

In terms of the cumulative distribution variable $g^*(k^*) = \int_0^{k^*} dk' f^*(k')$, we can write Eq. I.7 as

$$\langle \mathcal{T}_{\mathrm{b}}(u) \rangle = \int_0^1 dg^* \exp\left[-\int_0^u du' k(g^*, u') \right].$$ (I.8)

Note carefully the difference between Eqs. I.8 and 4.98, the latter equation applying to a homogeneous path. The function $k(g^*, u')$ refers to the distribution appropriate to the particular level u'. However the distribution g^* is the cumulative distribution of k-values *for the inhomogeneous line of sight.* The finite-difference form of the above equation is

$$\langle \mathcal{T}_{\mathrm{b}}(u) \rangle = \sum_{j=1}^N \Delta g_j^* \exp\left[-\sum_{\ell=\ell_1}^{\ell_2} k_\ell(g_j^*) \Delta u_\ell \right].$$ (I.9)

The *correlated-k* (c-k) method consists of replacing Eqs. I.8 and I.9 with

$$\langle \mathcal{T}_{\mathrm{b}}(u) \rangle = \int_0^1 dg \exp\left[-\int_0^u du' k(g, u') \right]$$ (I.10)

$$\langle \mathcal{T}_{\mathrm{b}}(u) \rangle \approx \sum_{j=1}^N \Delta g_j \exp\left[-\sum_{\ell=\ell_1}^{\ell_2} k_\ell(g_j) \Delta u_\ell \right].$$ (I.11)

The replacement of the variable g^* with g implies that the single variable g maps into the distribution functions at *all* levels u'. Since g depends on wavenumber, the replacement of g^* with g assumes that there is a one-to-one correspondence, or mapping, of wave numbers from one level to another. Thus the optical depth at a specific wavenumber g is given by the integral of $k(g, u')$ over the appropriate range of u', with g fixed. Hence, the net transmittance is the weighted average over all values of g. Equations I.10 and I.11 essentially describe the integration over a *pseudo-spectral line*, as described earlier.

Example I.1: Isolated Lorentz line

It is instructive to once again consider the simplest inhomogeneous case for which we have exact analytic solutions. We may find the k-distributions for the inhomogeneous line of sight from Eq. I.3, where for simplicity we let $z' \to \infty$. Denoting k_L^* by simply k and solving for $\tilde{\nu}(k)$ we find

$$\tilde{\nu}_L(k) = \frac{\alpha_L}{\sqrt{e^{2\pi\alpha_L k/\mathcal{S}} - 1}}. \tag{I.12}$$

Note that this result depends upon the height z through the dependence of α_L on z. (More generally, it depends upon both z and z', and upon θ.) The k-distribution for the inhomogeneous path is

$$f_L^*(k) = \frac{2}{\Delta\tilde{\nu}} \frac{d\tilde{\nu}_L(k)}{dk} = \frac{(\pi\alpha_L/\mathcal{S})e^{2\pi\alpha_L k/\mathcal{S}}}{\frac{\Delta\tilde{\nu}}{2}\left(e^{2\pi\alpha_L k/\mathcal{S}} - 1\right)^{3/2}}. \tag{I.13}$$

Note also that since $k_{max} = \mathcal{S}/2\pi\alpha_L$, the denominator $\to 0$, and $f^*(k) \to \infty$ as $k \to k_{max}$. This situation presents no difficulty in practice (it occurs also for the homogeneous case, Eq. 4.104). Proceeding as in the homogeneous case, we can solve analytically for the cumulative distribution $g^*(k)$ and its inverse

$$g_L^*(k) = \frac{\alpha_L}{(\Delta\tilde{\nu}/2)\sqrt{e^{2\pi\alpha_L k/\mathcal{S}} - 1}} - 1 \tag{I.14}$$

$$k_L^*(g) = \frac{\mathcal{S}}{2\pi\alpha_L} \ln\left\{ \frac{\left[(\Delta\tilde{\nu}/2)(1+g)\right]^2 + \alpha_L^2}{\left[(\Delta\tilde{\nu}/2)(1+g)\right]^2} \right\}. \tag{I.15}$$

As in the homogeneous case, the correspondence of $\tilde{\nu}$ in the band and the variable g in the pseudo-line are one-to-one.

For an isolated line, the monotonic ordering by strength of absorption coefficients retains the relative spectral alignment of absorption lines between different levels in the atmosphere. We can carry out a 'mapping' from the variable $\tilde{\nu}$ to the variable g at one height, say z_1; we then go to a second height, and map this same variable g back into a wavenumber $\tilde{\nu}'$ at the height z_2. The wavenumber $\tilde{\nu}'$ will be found to be exactly the same wavenumber $\tilde{\nu}$, or in other words, there is a perfect *spectral correlation* at different pressure levels (see Fig. I.1). Exercise 4.12 shows how this mapping works in detail for an isolated Lorentz line. Clearly, it should work for *any* isolated line profile, so long as the line center remains fixed in wavenumber, and the broadening maintains a symmetrical line shape. It can also be shown to apply to an Elsasser band, and to a band for which the lines are randomly distributed in a spectral interval $\Delta\tilde{\nu}$. In the latter case, it is valid if the averaged absorptance corresponding to a single line can be identified.

Unfortunately, this one-to-one uniqueness does *not* work for a general molecular band, except in the weak-line and strong-line limits.[3] It is clear that for a real molecular band, a single value of k may correspond to a large number of wavenumber values $\tilde{\nu}_1$, $\tilde{\nu}_2$, etc. This value of k will map into a certain value of g (or more accurately a band of values Δg around g) at the height z_1. We then take this same value of g and find the corresponding value of k at a different height z_2, by using the relationship $k(z_2, g)$. A way

---

[3] This statement is proven by Goody et al. (1989).
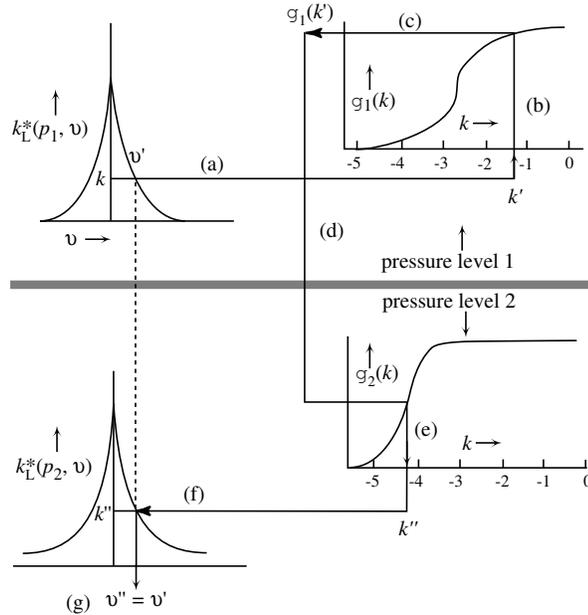
Figure I.1 Illustration of perfect wavenumber correlation at different pressure levels for an isolated line. The mapping begins at pressure p_1 and wavenumber $\tilde{\nu}$ (upper left panel). The absorption coefficient k' corresponding to this wavenumber (actually k_L^* in Eq. I.3) maps into the 'pseudo-wavenumber' variable $g_1(k')$ (upper right panel) using Eq. I.14. We now move to a different pressure level p_2 and map this value of g_1 using the inverse relationship to go from g to k (Eq. I.15), but different pressure half-width (lower right panel). This wavenumber $\tilde{\nu}''$ turns out to be the same $\tilde{\nu}'$ chosen at the initial pressure level.

of testing to see whether there is good correlation between levels would then be to replot the mapped spectrum *at the original wavenumber values* $\tilde{\nu}_1$, $\tilde{\nu}_2$, etc. If the mapped spectrum matches closely the actual spectrum calculated at z_2, then the correlation is good.

An example of this mapping is shown in Fig. I.2, which uses two contiguous atmospheric slabs separated by a large pressure difference (0.1–1.0 bars), a more extreme example than what is normally encountered in the atmosphere [taken from Fig. 11 of Lacis and Oinas (1991)]. The mapped spectrum (dashed lines) is seen to be very close to the actual spectrum (dark lines). Another way of assessing the error in the assumption of correlation is shown in Figs. I.3a and b. The left-hand panel shows the CO_2 absorption spectra for three different levels in a model atmosphere, while the right-hand panel shows a mapping from wavenumber to g such that
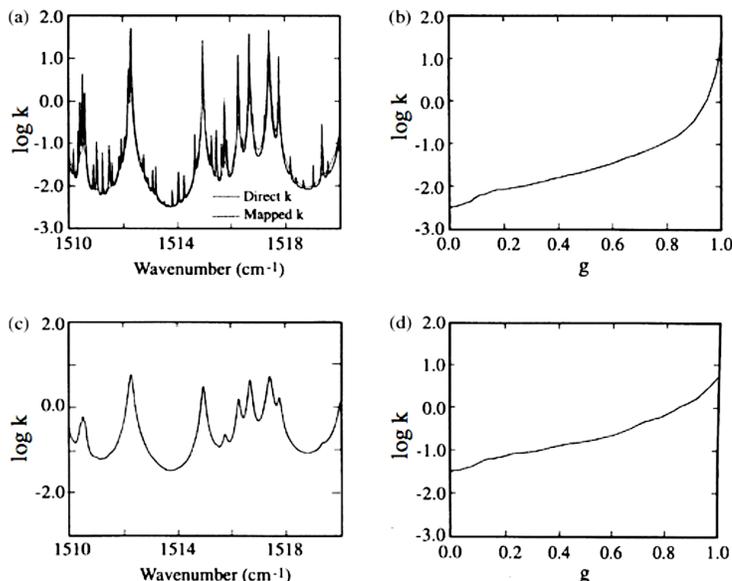
Figure I.2 Spectral correlation for the transmission across a pressure inhomogeneity of 0.1–1.0 bars (taken from Fig. 11 of Lacis and Oinas (1991)). (a) Results for the 1510–1520 cm^{-1} portion of the 6.3 μm water band at 0.1 bar and (c) 1.0 bar, respectively; (b and d) Numerical k-distributions of respective absorption spectra an (a) and (c); The dashed line in (a) is the result of mapping the absorption spectrum in (c) via the k-distributions in (d) and (b).

k increases monotonically for the bottom (high pressure) layer. The same mapping was applied to the k-spectrum of other layers in the atmosphere. The fundamental assumption of the c-k method is that a single mapping will produce a monotonically increasing k-spectrum in every layer. On the contrary, Fig. I.3 shows that a mapping which produces a monotonically increasing k-spectrum for one layer produces a k-spectrum for other layers in which neighboring k-values fluctuate by orders of magnitude (West et al., 1990). More sophisticated mapping algorithms than those described here (West et al., 1990) have been devised to minimize the errors in the c-k technique. In general, this approximation can produce irradiances and heating rate values with errors less than 1%. Although they are much more efficient (typically by factors of 1000) than LBL methods, they are most suitable for 1-D radiative-convective models. They are generally too slow for 3-D GCM models, and more drastic approximations are necessary. Overlapping absorption by bands from different constituents is easily accommodated by
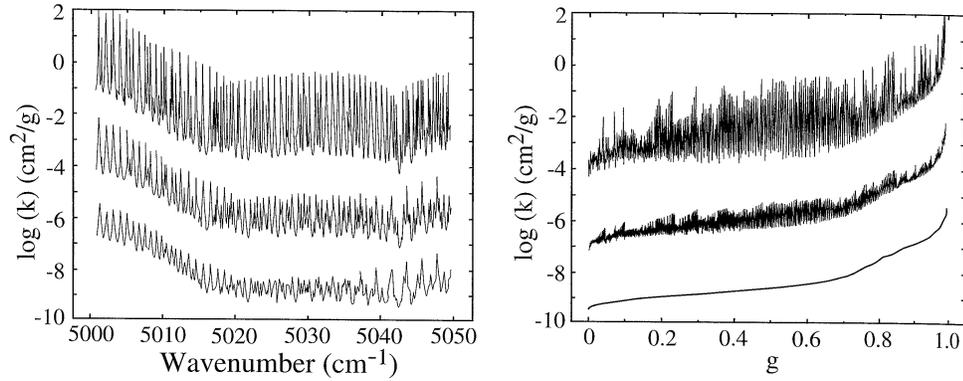
Figure I.3 LEFT PANEL: CO_2 absorption coefficient spectra computed for three different pressure-temperature values, which (from top to bottom) are respectively (0.05 bar, 200 K), (0.25 bar, 245 K) and (0.9 bar, 295 K). The coefficients for the second layer have been multiplied by 10^{-1} and the third layer by 10^{-7}. RIGHT PANEL: Spectra sorted by wavenumber such that k increases monotonically for the third layer (bottom curve). The wavenumber was mapped onto g according to the procedure described in the text. Note the non-monotonic behavior, illustrating the inadequacies of this mapping procedure in this particular example.

the correlated-k technique, and these refinements are discussed elsewhere.[4]

I.2.3 Inclusion of Multiple Scattering in the Correlated-k Method

It is straightforward to include scattering particles or Rayleigh scattering from air molecules in the c-k method, since most multiple-scattering methods assume monochromatic absorption. The assumption is made that each of the scattering coefficient, single-scattering albedo, and scattering phase function is constant over the spectral regions corresponding to the sub-intervals $k_1, k_1 + \Delta k_1$, $k_2, k_2 + \Delta k_2$, etc. The single scattering albedo for the ith spectral interval is $\varpi_i = \tau_{sc}(i)/\tau_{\text{ext}}(i)$, where $\tau_{sc}(i)$, is the total scattering optical depth (molecules plus particles), $\tau_{\text{ext}}(i) = \tau_{sc}(i) + \tau_a(i) + k_i u$ is the extinction optical depth, $\tau_a(i)$ is the particle absorption optical depth, and $k_i u$ is the molecular absorption optical depth. For example, the mean

---

[4] An excellent reference for the correlated-k method is the article by Lacis and Oinas (1991).

transmittance and mean reflectance of a non-gray, scattering atmosphere is

$$\langle \mathcal{T}_{\mathrm{b}} \rangle = \sum_{i=1}^{N} \mathcal{T}_{\mathrm{b}}(\tau_i, a_i) \Delta g_i; \quad \langle \rho \rangle = \sum_{i=1}^{N} \rho(\tau_i, a_i) \Delta g_i \qquad \text{(I.16)}$$

where Δg_i is the relative weighting of the ith k-interval. Note that the monochromatic transmittance, $\mathcal{T}_{\mathrm{b}}(\tau_i, a_i)$ and the corresponding reflectance, $\rho(\tau_i, a_i)$ can be calculated from two-stream methods, or a doubling algorithm (described in Chapters 7 and 9) for each atmospheric layer. By combining the layers using an adding algorithm the radiance and irradiance are obtained. Alternatively, the radiative transfer equation can be solved layer by layer for each spectral subinterval, and the layers combined using two-stream methods, or the DISORT algorithm. Thus, the most general problem of scattering and absorption in a vertically-inhomogeneous atmosphere can be solved accurately with such methods. Such techniques are the 'state of the art' (in terms of band models) at the present time.

Example I.2: Application of the Correlated-k Method

Suppose we wish to solve for the mean irradiance reflectance of an absorbing/scattering slab over the spectral interval $\Delta\tilde{\nu}$. Then

$$\langle \rho(2\pi) \rangle = \frac{1}{\Delta\tilde{\nu}} \int_{\Delta\tilde{\nu}} d\tilde{\nu} \rho(2\pi, \tilde{\nu}) = \int_{k_{min}}^{k_{max}} dk f(k) \rho(2\pi, k) = \int_0^1 dg \rho[2\pi, k(g)]$$

where $\rho(2\pi, k)$ is the irradiance reflectance calculated for a specific value of k. To be specific, let the slab be homogeneous and semi-infinite. (The same ideas apply to an inhomogeneous slab, except that analytic solutions will not exist.) For a specific single-scattering albedo $\varpi(k)$ the irradiance reflectance is found in Chapter 7:

$$\rho(2\pi, k) = \frac{1 - \sqrt{1 - \varpi(k)}}{1 - \sqrt{1 + \varpi(k)}} = \frac{1 - \sqrt{1 - \sigma/(\sigma + k)}}{1 + \sqrt{1 - \sigma/(\sigma + k)}} = \frac{\sqrt{\sigma + k} - \sqrt{k}}{\sqrt{\sigma + k} + \sqrt{k}}.$$

Thus

$$\langle \rho(2\pi) \rangle = \int_0^1 dg \frac{\sqrt{\sigma + k(g)} - \sqrt{k(g)}}{\sqrt{\sigma + k(g)} + \sqrt{k(g)}}. \qquad \text{(I.17)}$$

The relationship between k to g is given by the particular line, or band profile – it may be an analytic result (such as in Example 4.6), or more likely it will be derived as a table of k-values versus g-values. For a molecular band this table will be constructed from the spectroscopic parameters of the lines within the spectral interval $\Delta\tilde{\nu}$. The mean reflectance is then evaluated by numerical integration of Eq. I.17.

Appendix J

Reciprocity for the Bidirectional Reflectance

In this appendix we prove the *Principle of Reciprocity* for the bidirectional reflectance, that is

$$\rho(\nu; \theta', \phi'; \theta, \phi) = \rho(\nu; \theta, \phi; \theta', \phi'). \tag{J.1}$$

With reference to Fig. J.1, the proof first determines the exchange of radiative energy between the black elements dA_1 and dA_2 in a *hohlraum* due to reflection of energy by the surface dA_2. The theorem is proven by equating the energy exchange $dE_{\nu 123}$ from 1 to 3 via 2, and the energy exchange $dE_{\nu 321}$ from 3 to 1 via 2, and equating these two quantities (see Fig. J.1).

The energy exchange $dE_{\nu 123}$ must balance the reciprocal energy exchange $dE_{\nu 321}$ in a TE situation. Otherwise there would be a net heating/cooling of
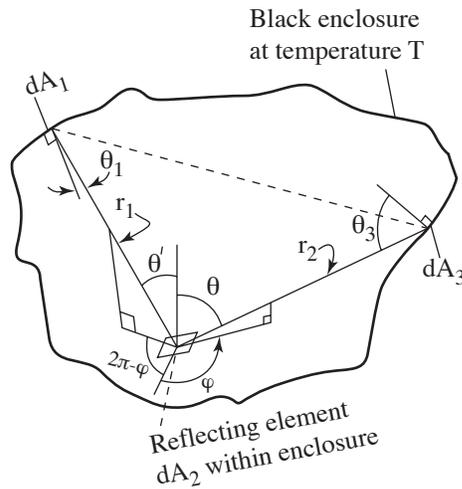
Figure J.1 Exchange of radiative energy within a *hohlraum*.

one of the areas at the expense of the other, and this violates the conditions of the *hohlraum*. Let's first consider the exchange from 1 to 3 via 2. The radiative energy reflected by dA_2 and intercepted by dA_3 is given by that 'emitted' into the solid angle subtended by dA_3, $dA_3 \cos \theta_3 / r_2^2$,

$$dE_{\nu 123} = I_{\nu r2}^+(\theta', \phi'; \theta, \phi) \cos \theta \frac{dA_3 \cos \theta_3}{r_2^2} d\nu dt. \tag{J.2}$$

The reflected radiance $I_{\nu r2}^+$ is related to the radiance $I_\nu^-(\theta', \phi')$ arriving at dA_2 through Eq. 5.15

$$I_{\nu r2}^-(\theta', \phi') = \cos \theta' \rho(\nu; \theta', \phi'; \theta, \phi) I_{\nu 1}^-(\theta', \phi') d\omega_{21} \tag{J.3}$$

where

$$d\omega_{21} = \frac{dA_1}{r_1^2} \cos \theta_1 \tag{J.4}$$

is the angle subtended by dA_1 from the point dA_2. Putting these together, we find that the rate of energy exchange per unit frequency from 1 to 3 via 2 is

$$\frac{dE_{\nu 123}}{d\nu dt} = I_{\nu 1}^-(\theta', \phi') \rho(\nu; \theta', \phi'; \theta, \phi) \cos \theta' \left[\frac{dA_1}{r_1^2} \cos \theta_1 \right] \cos \theta \left[\frac{dA_3}{r_2^2} \cos \theta_3 \right]. \tag{J.5}$$

Now consider energy exchange in the reverse direction, 3 to 1 via 2. The rate of energy per unit frequency reflected at dA_2 into the direction of dA_1 is

$$\frac{dE_{\nu 321}}{d\nu dt} = I_{\nu r2}^+(\theta, \phi; \theta', \phi') \cos \theta' dA_2 \left[\frac{dA_1}{r_1^2} \cos \theta_1 \right]. \tag{J.6}$$

But the reflected radiance at dA_2 is given by

$$I_{\nu r2}^+(\theta, \phi; \theta', \phi') = I_{\nu 3}^-(\theta, \phi)) \rho(\nu; \theta, \phi; \theta', \phi') \cos \theta d\omega_{23} \tag{J.7}$$

where $d\omega_{23} = dA_3 \cos \theta_3 / r_2^2$ is the solid angle subtended by dA_3 at the point dA_2. Putting these together, we find for the energy exchange rate

$$\frac{dE_{\nu 321}}{d\nu dt} = I_{\nu 3}^-(\theta, \phi) \rho(\nu; \theta, \phi; \theta', \phi') \cos \theta' \cos \theta \left[\frac{dA_3}{r_2^2} \cos \theta_3 \right] \left[\frac{dA_1}{r_1^2} \cos \theta_1 \right]. \tag{J.8}$$

Equating the two rates of energy exchange, we find

$$I_{\nu 1}^-(\theta', \phi') \rho(\nu; \theta', \phi'; \theta, \phi) = I_{\nu 3}^-(\theta, \phi) \rho(\nu; \theta, \phi; \theta', \phi'). \tag{J.9}$$

But in TE, the two radiances are just the Planck function, $I_{\nu 1}^- = I_{\nu 3}^- = B_\nu$. Therefore

$$\rho(\nu; \theta', \phi'; \theta, \phi) = \rho(\nu; \theta, \phi; \theta', \phi'). \tag{J.10}$$

Given the above reciprocity property for the BDRF, we now show that reciprocity also applies to the reflected irradiance. Placing the two definitions together, we have

$$\rho(\nu; -\hat{\Omega}', 2\pi) = \int_{+} d\omega \cos\theta \rho(\nu; -\hat{\Omega}', \hat{\Omega}) \tag{J.11}$$

$$\rho(\nu; 2\pi, \hat{\Omega}) = \int_{-} d\omega' \cos\theta' \rho(\nu; -\hat{\Omega}', \hat{\Omega}). \tag{J.12}$$

The first quantity, $\rho(\nu; -\hat{\Omega}', 2\pi)$ is the *directional-hemispherical reflectance*, and the second quantity, $\rho(\nu; 2\pi, \hat{\Omega})$ is the *hemispherical-directional reflectance*. If we evaluate the first of the above equations at $\hat{\Omega}' = \hat{\Omega}$, and place primes on the angular integration variables (realizing that they are dummy variables), we have

$$\rho(\nu; -\hat{\Omega}, 2\pi) = \int_{+} d\omega' \cos\theta' \rho(\nu; -\hat{\Omega}, \hat{\Omega}'). \tag{J.13}$$

Invoking reciprocity of the BDRF, $\rho(\nu; -\hat{\Omega}, \hat{\Omega}') = \rho(\nu; -\hat{\Omega}', \hat{\Omega})$, we have

$$\rho(\nu; -\hat{\Omega}, 2\pi) = \int_{+} d\omega' \cos\theta' \rho(\nu; -\hat{\Omega}', \hat{\Omega}). \tag{J.14}$$

But this is the same expression for the hemispherical-directional reflectance, Eq. J.12. Thus we find the desired reciprocity relationship

$$\rho(\nu; -\hat{\Omega}, 2\pi) = \rho(\nu; 2\pi, \hat{\Omega}). \tag{J.15}$$

Appendix K

Harmonic Electromagnetic Plane Waves

We review in this appendix some basic aspects of light. We use *light* as a shorthand for *electromagnetic radiation*, and do not necessarily imply *visible light*, which occupies only a small portion of the electromagnetic spectrum. Some simple mathematical fundamentals are provided in Appendix F, including a discussion of elementary concepts such as coordinate systems, the Dirac delta-function, and the solid angle. In this section, we restrict our attention to a review of electromagnetic plane waves, and their polarization properties. More advanced topics concerning the Stokes vector representation, partial polarization, and the Mueller matrix are described in Appendix L.

K.1 Harmonic Plane Electromagnetic Waves

Light is an electromagnetic phenomenon, along with gamma-rays, X-rays, and radio waves. It is described by solutions of the famous set of equations of J. C. Maxwell, formulated in 1865. These equations in differential form and in SI units for an isotropic, homogeneous, non-dispersive, and source-free medium, are

$$\nabla \times \mathbf{H} = \epsilon \frac{\partial \mathbf{E}}{\partial t} + \sigma \mathbf{E} \text{ (a);} \qquad \nabla \times \mathbf{E} = -\mu \frac{\partial \mathbf{H}}{\partial t} \text{ (b);}$$

$$\nabla \cdot \mathbf{H} = 0 \text{ (c);} \qquad \nabla \cdot \mathbf{E} = 0 \text{ (d).} \tag{K.1}$$

Here $\nabla \times$ and $\nabla \cdot$ denote the curl and divergence operators, respectively, $\mathbf{E}$ and $\mathbf{H}$ are the *electric* and *magnetic fields*, t is time, ϵ is the *permittivity*, σ is the *conductivity*, and μ is the *permeability*, all properties of the medium. A net charge of zero throughout the medium is assumed, and the medium

is assumed to be lossless, so that ϵ is a real-valued quantity. The basis of these equations and the medium properties are described in various texts.[1]

A solution of the coupled partial differential equations in Eqs. K.1 is sought for the case in which both **E** and **H** are harmonic functions of time, i.e. the temporal variation is of the form $\cos \omega t$ or $\Re[\exp(-i\omega t)]$, where $i = \sqrt{-1}$ is the imaginary unit and $\Re$ denotes the real part. Let us assume a non-conducting, non-magnetic, lossless *dielectric medium*, for which $\sigma = 0$, $\mu = \mu_0$, and ϵ is a real-valued quantity. Taking the curl[2] of Eqs. K.1a and K.1b, using the vector identity $\nabla \times (\nabla \times \mathbf{a}) = \nabla(\nabla \cdot \mathbf{a}) - \nabla^2 \mathbf{a}$ together with Eqs. K.1c and K.1d, and replacing $\partial^2/\partial t^2$ by $(-i\omega)^2$, we find (since ϵ is assumed to be time-independent and does not vary with position in a homogeneous medium) that both **E** and **H** satisfy the same second-order reduced wave equation or Helmholtz equation

$$\left(\nabla^2 + k^2\right)\mathbf{E} = 0; \quad \left(\nabla^2 + k^2\right)\mathbf{H} = 0; \qquad k^2 = \frac{\omega^2}{c'^2}; \quad c' = \frac{1}{\sqrt{\mu_0\epsilon}}. \quad \text{(K.2)}$$

Here c' is the speed of light in the medium, whereas $c = 1/\sqrt{\mu_0\epsilon_0} = 2.9979 \times 10^8$ $[\text{m} \cdot \text{s}^{-1}]$ is the speed of light in vacuum. It can readily be shown that *harmonic electromagnetic plane waves* of the form

$$\mathbf{E}(\mathbf{r}, t) = \Re\left\{\mathbf{E}_0 e^{i(k\hat{\Omega}\cdot\mathbf{r} - \omega t)}\right\}$$

$$\mathbf{H}(\mathbf{r}, t) = \Re\left\{\mathbf{H}_0 e^{i(k\hat{\Omega}\cdot\mathbf{r} - \omega t)}\right\} \qquad \text{(K.3)}$$

are solutions of Eq. K.2, where $\mathbf{E}_0$ and $\mathbf{H}_0$ are complex constant vectors. The unit vector $\hat{\Omega}$ points in the propagation direction of the plane wave. $k = \omega/c'$ is the *wavenumber* $[\text{cm}^{-1}]$, and ω is the *angular frequency* $[\text{rad} \cdot \text{s}^{-1}]$, related to the ordinary frequency ν, $[\text{cycles}\cdot\text{s}^{-1}]$ or $[\text{Hz}]$, by $\omega = 2\pi\nu$. These solutions are called plane waves because at any fixed time t they have the same value at each point in any plane normal to $\hat{\Omega}$, i.e. at any fixed time t, $\mathbf{E}(\mathbf{r}, t)$ and $\mathbf{H}(\mathbf{r}, t)$ are constant vectors in any plane defined by $\hat{\Omega} \cdot \mathbf{r} = \text{constant}$.

Note that we have restricted our attention to harmonic electromagnetic plane waves having a sinusoidal variation in time and space. According to Eq. K.3, each Cartesian component of **E** and **H** will be of the general form

---

[1] The *constitutive relations* $\mathbf{D} = \epsilon\mathbf{E}$ and $\mathbf{B} = \mu\mathbf{H}$, where **D** is the displacement vector and **B** is the magnetic flux vector, are included in Eqs. K.1. See Stratton, J. A., *Electromagnetic Theory*, McGraw-Hill Book CO., New York, 1941. Jackson, J. D. *Classical Electrodynamics*, New York, Wiley, 1975. A good modern text is Griffiths, D. J., *Introduction to Electrodynamics*, Prentice-Hall, 1981.

[2] For readers unfamiliar with vector analysis, see for example, Edwards (1990).

(with j denoting either x, y, or z)

$$E_j(\mathbf{r}, t) = e_j \cos(k\hat{\Omega} \cdot \mathbf{r} - \omega t + \delta_j)$$
$$H_j(\mathbf{r}, t) = h_j \cos(k\hat{\Omega} \cdot \mathbf{r} - \omega t + \phi_j) \qquad (K.4)$$

where e_j and h_j are arbitrary real coefficients, and δ_j and ϕ_j are arbitrary phase angles.

The harmonic electromagnetic plane waves in Eqs. K.3 are solutions of Helmholtz equation (Eq. K.2) for arbitrary values of $\mathbf{E}_0$ and $\mathbf{H}_0$, but must also satisfy Maxwell's equations. Substituting Eqs. K.3 in Eqs. K.1a and K.1b (with $\sigma = 0$), we find that

$$\sqrt{\mu}\,\hat{\Omega} \times \mathbf{H}_0 = \sqrt{\epsilon}\,\mathbf{E}_0; \qquad \sqrt{\epsilon}\,\hat{\Omega} \times \mathbf{E}_0 = \sqrt{\mu}\mathbf{H}_0 \qquad (K.5)$$

from which it follows that $\mathbf{E}_0 \cdot \mathbf{H}_0 = 0$, $\mathbf{E}_0 \cdot \hat{\Omega} = \mathbf{H}_0 \cdot \hat{\Omega} = 0$, so that both $\mathbf{E}_0$ and $\mathbf{H}_0$ are orthogonal to each other and to the propagation direction $\hat{\Omega}$. In other words, $\mathbf{E}_0$, $\mathbf{H}_0$, and $\hat{\Omega}$ form a right-handed triad, and both $\mathbf{E}_0$ and $\mathbf{H}_0$ are *transverse* to the the propagation direction $\hat{\Omega}$.

If we choose the coordinate system such that $\hat{\Omega}$ is along the positive z-axis, we can write

$$\mathbf{E} = \mathbf{E}_\| + \mathbf{E}_\perp; \quad \mathbf{E}_\| = E_\| \hat{e}_\|; \quad \mathbf{E}_\perp = E_\perp \hat{e}_\perp \qquad (K.6)$$

$$\mathbf{H} = \mathbf{H}_\| + \mathbf{H}_\perp; \quad \mathbf{H}_\| = \sqrt{\frac{\epsilon}{\mu}}\hat{e}_z \times \mathbf{E}_\| = H_\| \hat{e}_\perp; \quad \mathbf{H}_\perp = \sqrt{\frac{\epsilon}{\mu}}\hat{e}_z \times \mathbf{E}_\perp = H_\perp \hat{e}_\|.$$
$$(K.7)$$

where $H_\| = -\sqrt{\frac{\epsilon}{\mu}}E_\|$, and $H_\perp = \sqrt{\frac{\epsilon}{\mu}}E_\perp$. Here each of the components $E_\|$, $E_\perp$, $H_\|$, and $H_\perp$ satisfies the Helmholtz equation, and $\hat{e}_\perp$, $\hat{e}_\|$, and $\hat{e}_z$ are unit vectors forming a right-handed triad

$$\hat{e}_\perp \cdot \hat{e}_\| = \hat{e}_\perp \cdot \hat{e}_z = \hat{e}_\| \cdot \hat{e}_z = 0, \qquad \hat{e}_\perp \times \hat{e}_\| = \hat{e}_z. \qquad (K.8)$$

$E_\|$ and $E_\perp$ are electric field components that are parallel and perpendicular to any plane containing the z-axis.[3]

From Eqs. K.3 and K.6–K.7, it follows that

$$E_\| = \Re\{\mathcal{E}_\|\}; \qquad E_\perp = \Re\{\mathcal{E}_\perp\}. \qquad (K.9)$$

where the complex amplitudes $\mathcal{E}_\|$ and $\mathcal{E}_\perp$ are given by

$$\mathcal{E}_\| = a_\| \exp[i(kz - \omega t + \delta_\|)] \qquad (K.10)$$
$$\mathcal{E}_\perp = a_\perp \exp[i(kz - \omega t + \delta_\perp)]. \qquad (K.11)$$

---

[3] The plane spanned by the interface normal and $\hat{e}_\|$ is the plane of incidence in the case of reflection and refraction at a plane interface.

Here $a_\parallel$ and $a_\perp$ are real-valued electric field *amplitudes* and $\delta_\parallel$ and $\delta_\perp$ are real-valued *phase angles*. Similar forms can be derived for the magnetic components.

If we define the wavenumber in vacuum, $k_0 \equiv \omega/c \equiv 2\pi/\lambda_0$, where λ_0 is the *vacuum wavelength*, we can express Eqs. K.9–K.11 in a more compact form

$$E_{\parallel,\perp} = \Re\left\{ a_{\parallel,\perp} \exp\left\{ i\left[(k_0 m z - \omega t) + \delta_{\parallel,\perp} \right] \right\} \right\} \qquad \text{(K.12)}$$

where, in general, m is the *complex refractive index* of the medium: $m = m_\mathrm{r} + i m_\mathrm{i}$. In a lossless medium (assumed above) $m_\mathrm{i} = 0$, so that $m = m_r \equiv c/c' = \lambda_0/\lambda = k/k_0 = \sqrt{\epsilon_0/\epsilon}$, the real part of the refractive index, the ratio of the propagation speed *in vacuum* to that in the medium.[4] These solutions apply to an ideal *harmonic* or *monochromatic* (single frequency) plane wave of infinite transvese spatial extent ($-\infty < x, y < +\infty$) traveling in the positive z-direction. The value of m_r varies slightly with frequency in natural media: in air it is very close to unity – for example, $m_\mathrm{r}(\lambda = 1\ \mu\mathrm{m}) = 1.0 + 2.892 \times 10^{-4}$. In pure water, $m_\mathrm{r}(\lambda = 486\ \mathrm{nm}) = 1.3371$.

The solution for a conducting (lossy) medium ($\sigma \neq 0$) is worked out in Exercise K.2. In this case, the wave is *damped* or *attenuated* along the propagation direction. The solution can be expressed mathematically in the same form as Eqs. K.12, except that the appearance of a 'damping factor' $\exp(-k_0 m_\mathrm{i} z)$ (see Eq. K.25), where m_i is the imaginary part of the complex refractive index $m = m_\mathrm{r} + i m_\mathrm{i}$, shows that the presence of a finite conductivity is associated with *absorption* along the propagation direction.

K.1.1 Energy Transfer

Light waves transmit energy. It is this feature that makes it possible to detect light away from sources, and it explains how the sun warms the earth and ultimately sustains life. The rate at which energy is transported by light is expressed by the *Poynting vector* **S**. This quantity is related to the electric and magnetic field vectors, **E** and **H** through $\mathbf{S} = \mathbf{E} \times \mathbf{H}$. This expression gives both the magnitude and direction of instantaneous energy flow. In other words, $\mathbf{E} \times \mathbf{H}$ is the *radiative power* per unit area carried along the propagation direction.

---

[4] There are actually *two* light speeds to consider: the *phase speed*, $v_p = c' = \omega/k$, and the *group speed*, $v_g = \partial\omega/\partial k$. Since $k = m(\omega)\omega/c$, and $m(\omega)$ is generally a function of frequency, ω (that is to say, the medium is *dispersive*) then $v_p \neq v_g$. However in a *non-dispersive medium*, $v_p = v_g$.

For time-harmonic plane-wave solutions it follows from Eqs. K.6–K.9 that

$$\mathbf{S} = \mathbf{E} \times \mathbf{H} = \sqrt{\frac{\epsilon}{\mu}} \, [\mathbf{E}_\parallel \hat{\mathbf{e}}_\parallel + \mathbf{E}_\perp \hat{\mathbf{e}}_\perp] \times [\mathbf{E}_\parallel \hat{\mathbf{e}}_{\mathbf{z}} \times \hat{\mathbf{e}}_\parallel + \mathbf{E}_\perp \hat{\mathbf{e}}_{\mathbf{z}} \times \hat{\mathbf{e}}_\perp]$$

$$= \sqrt{\frac{\epsilon}{\mu}} \, [E_\parallel E_\parallel + E_\perp E_\perp] \hat{e}_z = \sqrt{\frac{\epsilon}{\mu}} \, [\Re(\mathcal{E}_\parallel)\Re(\mathcal{E}_\parallel) + \Re(\mathcal{E}_\perp)\Re(\mathcal{E}_\perp)]\hat{\Omega}. \quad (\text{K.13})$$

Here $\hat{\Omega}$ is a unit vector in the propagation direction of the wave. We are seldom interested in the instantaneous value of $\mathbf{S}$. Of greater interest is the *time-averaged value*

$$\langle \mathbf{S} \rangle = \frac{1}{\langle t \rangle} \int_0^{\langle t \rangle} dt\, \mathbf{S}(t) \quad (\text{K.14})$$

where $\langle t \rangle$ is the averaging time. For a periodic function, $\langle t \rangle$ is an integral number of *wave periods*, where one period is $1/\nu$. It is shown in Exercise K.2 that the time average of the product of two time-harmonic functions of the same periodicity is

$$\langle \Re\{a(t)\} \cdot \Re\{b(t)\} \rangle = \frac{1}{2}\Re\{ab^*\} = \frac{1}{2}\Re\{a^*b\} \quad (\text{K.15})$$

where $a(t)$ and $b(t)$ both are of the form in Eqs. K.10 and K.11. The asterisk denotes complex conjugation. Using this result in Eq. K.13, we find that the flow in the general direction $\hat{\Omega}$ is

$$\langle \mathbf{S} \rangle = \frac{m_{\text{r}}}{2\mu c} \left\{ \frac{\epsilon}{2} [\mathcal{E}_\parallel \cdot \mathcal{E}_\parallel^* + \mathcal{E}_\perp \cdot \mathcal{E}_\perp^*] \right\} \hat{\Omega} \quad (\text{K.16})$$

where we have used $c' = 1/\sqrt{\mu_0 \epsilon}$ and $m_{\text{r}} = c/c' = \sqrt{\epsilon/\epsilon_0}$. The quantity in the curly brackets is the energy density $\mathcal{U} = \mathcal{U}_{\text{e}} + \mathcal{U}_{\text{m}}$ of the harmonic plane electromagnetic wave, consisting of the sum of electric field ($\mathcal{U}_{\text{e}}$) and magnetic field ($\mathcal{U}_{\text{m}}$) energy densities. Equation K.16 shows that the energy density of a harmonic plane electromagnetic wave propagates with velocity $c' = c/m_{\text{r}}$ in the $\hat{\Omega}$-direction.

Also, Eq. K.16 shows that a plane electromagnetic wave may be considered to have two components

$$I_\parallel = (m_{\text{r}}/2\mu c)|\mathcal{E}_\parallel|^2 \qquad \text{and} \qquad I_\perp = (m_{\text{r}}/2\mu c)|\mathcal{E}_\perp|^2. \quad (\text{K.17})$$

$I_\parallel$ and $I_\perp$ are called the *intensity components*.[5] Equation K.16 tells us that the average radiative power is $I_\parallel + I_\perp$. The fact that light waves have these two independent components accounts for the phenomenon of *polarization*

---

[5] This definition of intensity is is close to our definition of irradiance (Chapter 2).

Figure K.1 A simple wave packet. (a) The wave $a\cos(\overline{k}z-\overline{\omega}t)$. (b) The wave $2a\cos\left[\frac{1}{2}(z\delta k - t\delta\omega)\right]$. (c) The wave packet $2a\cos\left[\frac{1}{2}(z\delta k - t\delta\omega)\right]\cos(\overline{k}z - \overline{\omega}t)$. The ordinate represents one of the two independent variables (t or z) while the other is kept constant.

associated with the *transverse* character of electromagnetic waves. It distinguishes light waves from *scalar waves*, such as sound waves in liquids or gases, which are *longitudinal* waves having only a single energy-carrying component.

K.1.2 Addition of Plane Waves

The harmonic or monochromatic plane wave solutions are *elementary* solutions to Maxwell's equations. Clearly, they are idealizations. Any real wave is a linear superposition of monochromatic plane waves of different frequencies, directions, and phases. If all waves in a group have almost the same frequency, we have a *wave packet*. Consider a wave packet consisting of only two waves, both propagating along the z-axis, and having slightly different frequencies and wave numbers. Let the waves have the same amplitude $a_\parallel$, and consider only one polarization component, say $E_\parallel$. The total electric field is the coherent sum of the individual waves, i.e.

$$E_\parallel(z,t) = \Re\left\{a_\parallel e^{i(kz-\omega t+\delta_1)} + a_\parallel e^{i[(k+\delta k)z-(\omega+\delta\omega)t+\delta_2]}\right\} \tag{K.18}$$

where $\delta\omega$ and δk are the (small) differences in frequencies and wave numbers, and δ_1 and δ_2 are the respective phase angles. We may combine the two terms by using the well-known relationship between the cosine-function and the complex exponentials. The result is

$$E_\parallel(z,t) = 2a_\parallel \cos[(1/2)(z\delta k - t\delta\omega + \delta')]\Re\left\{e^{i(\overline{k}z-\overline{\omega}t+\overline{\delta})}\right\} \tag{K.19}$$

where $\overline{\omega} = \omega + \frac{1}{2}\delta\omega$, $\overline{k} = k + \frac{1}{2}\delta k$, and $\overline{\delta} = (\delta_1 + \delta_2)/2$. These are the mean angular frequency, the mean wavenumber, and the mean phase angle, respectively. δ' is the phase angle difference $\delta_1 - \delta_2$. The resultant wave is a plane wave of angular frequency $\overline{\omega}$ and wavelength $2\pi/\overline{k}$ propagating in the z-direction. However, the amplitude of the wave is not constant, but varies with time and position, between the values of $2a_\parallel$ and zero (see Fig. K.1).

This is a mathematical description of the phenomenon of *beats*. The two waves change from being totally in phase (where *constructive interference* occurs) to being totally out of phase (where *destructive interference* occurs).

If we set the two frequencies or wave numbers equal, we have two monochromatic plane waves with differing phases, i.e.

$$E_{\parallel}(z,t) = 2a_{\parallel} \cos\left[(1/2)(\delta_1 - \delta_2)\right] \Re\left\{e^{i(kz - \omega t + \bar{\delta})}\right\}. \qquad (K.20)$$

When the phases are equal, $\delta_1 = \delta_2$, the amplitude in Eq. K.20 has its maximum value, $2a_{\parallel}$. Again we have constructive interference for in-phase waves. For $\delta_1 - \delta_2 = \pm n\pi$ $(n = 1, 2, \cdots)$, we obtain a zero amplitude for out-of-phase waves, and the destructive interference is complete.

K.1.3 Standing Waves

We now consider the superposition of two plane waves travelling in *opposite* directions. This situation will lead us to the concept of a *standing wave*, a topic of importance to the subject of blackbody radiation. We imagine two oppositely-directed waves of the same frequency, phase and amplitude (the latter we set equal to unity). Again, consider only one component (say the parallel component) of the electric field. The total **E**-field component is

$$E_{\parallel}(z,t) = \Re\left\{e^{i(kz - \omega t - \pi/2)} + e^{i(-kz - \omega t - \pi/2)}\right\} \qquad (K.21)$$

where we have chosen the phase $\delta = -\pi/2$ for convenience. Using the relationship $\cos kX = (1/2)[\exp(ikX) + \exp(-ikX)]$, we write Eq. K.21 as

$$E_{\parallel}(z,t) = 2\cos(kz + \pi/2)\Re\left\{e^{-i\omega t}\right\} = 2\sin(kz)\cos(\omega t).$$

The result is a wave that neither moves forward or backward. It vanishes at values of z for which $\sin(kz) = 0$, that is, where $kz = n\pi$ $(n = 0, 1, \cdots)$. In between these *nodes*, the disturbance vibrates harmonically with time. The maxima are located at the *anti-nodes*, at $kz = n\pi/2$ $(n = 1, 3, \cdots)$.

For a standing wave located in a finite cavity, the electric field must vanish at the boundaries, say at $z = 0$ and at $z = L$. The nodes will of course correspond with the boundaries, so that $k = n\pi/L$ $(n = 0, 1, \cdots)$. For example, the two lowest-order *wave-modes* are given by

$$E^{(1)}(z,t) = 2\cos(\pi z/L)\cos(\omega t); \qquad E^{(2)}(z,t) = 2\cos(2\pi z/L)\cos(\omega t).$$

The $n = 1$ wave-mode is fixed at the two ends; the $n = 2$ wave-mode is fixed at both ends and in addition is fixed at the center, $z = L/2$. Higher-order wave-modes $E^{(n)}$ have $n + 1$ nodes, etc.

In a three-dimensional cavity (taken to be cubic of sides L for convenience), there are three independent components (actually six, taking into

account the perpendicular component). Each has its own wave number, so that

$$k_x = n_x\pi/L; \quad k_y = n_y\pi/L; \quad k_z = n_z\pi/L \qquad (n_x, n_y, n_z = 0, 1, \cdots).$$

In vector notation, we write $\mathbf{k} = \pi\mathbf{n}/L$ where $\mathbf{n}$ is a unit vector in a three-dimensional pseudo-space with Cartesian components n_x, n_y, and n_z.

The above results are applicable to the study of blackbody radiation and is used in the derivation of the *Planck distribution* in Appendix G. A radiation field may be thought of as a system of standing waves in a large cavity, or *hohlraum*. The cavity 'walls' are unimportant except for establishing the boundary conditions. In the quantum theory each standing wave may be associated with a *photon*, a particle of light having a quantized energy and momentum given by

$$\text{photon energy} = \mathcal{E}_p = h\nu = \frac{hc}{\lambda} = \frac{h}{2\pi}\omega = \frac{h}{2\pi}c|\vec{k}|$$

$$\text{photon momentum} = \mathcal{P}_p = \frac{h\nu}{c} = \frac{h}{\lambda} = \frac{h}{2\pi}|\vec{k}|.$$

where h is Planck's constant $= 6.63 \times 10^{-34}$ [J · s].

In this appendix we found that the linear superposition of electromagnetic fields leads to the phenomena of beating, interference, and standing waves. These are all results of *coherent addition* of light waves, and is to be contrasted with the very different situation of *incoherent addition*, which we are mainly concerned with in this book.

K.1.4 Polarization

We now consider the way in which the electric field vector of a harmonic plane wave varies in space and time. Defining the variable part of the phase factor of Eqs. K.9–K.11 as $\phi = kz - \omega t$, we may write the electric field components as

$$E_\parallel = a_\parallel \cos(\phi + \delta_\parallel); \qquad\qquad E_\perp = a_\perp \cos(\phi + \delta_\perp). \qquad (\text{K.22})$$

We can determine how $\mathbf{E}$ varies in space by eliminating ϕ. It is easily shown that

$$\left(\frac{E_\parallel}{a_\parallel}\right)^2 + \left(\frac{E_\perp}{a_\perp}\right)^2 - 2\frac{E_\parallel E_\perp}{a_\parallel a_\perp}\cos\delta = \sin^2\delta \qquad (\text{K.23})$$

where $\delta \equiv \delta_\parallel - \delta_\perp$. This is the equation of an ellipse, which is inscribed into a rectangle whose sides are parallel to the coordinate axes, and whose lengths are $2a_\parallel$ and $2a_\perp$ (see Fig. K.2).

Figure K.2 Elliptically polarized wave. The vibrational ellipse for the electric vector. The ellipse is inscribed into a rectangle whose sides are parallel to the co-ordinate axes whose lengths are $2a_\parallel$ and $2a_\perp$. The ellipse touches the sides at the points $(\pm a_\parallel, \pm a_\perp \cos \delta)$ and $(\pm a_\parallel \cos \delta, \pm a_\perp)$.

At a given point in space, the tip of the electric field vector will therefore trace out an ellipse – the wave is said to be *elliptically polarized*. The properties of the ellipse are determined by three quantities: either $a_\parallel, a_\perp$, and $\delta = \delta_\parallel - \delta_\perp$; or by the major and minor axes, a and b, and the angle ψ. The latter is the angle the major axis makes with the horizontal (parallel axis) as shown in Fig. K.2. It may be shown that these quantities are related to the first set by

$$a^2 + b^2 = a_\parallel^2 + a_\perp^2; \qquad \pm ab = a_\parallel a_\perp \sin \delta;$$

$$\tan 2\psi = (\tan 2\alpha) \cos \delta; \qquad \tan \alpha = \frac{a_\parallel}{a_\perp}. \tag{K.24}$$

K.1.5 Polarization: linear and circular

The special cases of linear and circular polarization occur when the ellipse in Eq. K.23 degenerates into either a straight line or a circle. When the phase difference of the two components is an integral multiple of π, that is when $\delta = \delta_\parallel - \delta_\perp = m\pi$ for $(m = 0, \pm 1, \pm 2, \cdots)$, Eq. K.23 yields

$$\frac{E_\perp}{E_\parallel} = (-1)^m \frac{a_\perp}{a_\parallel}.$$

In this case, **E** is *linearly polarized*. The two components bear a constant ratio to one another. Considering the time-dependent factor ϕ (see Eq. K.22), we see that the **E**-vector oscillates in magnitude (with angular frequency ω) along a straight line, from the value $-a_\parallel$ to $+a_\parallel$. When the components have equal magnitude, $a_\parallel = a_\perp = a$, and in addition the phase angles are in quadrature, that is $\delta = \delta_\parallel - \delta_\perp = m\pi/2$ where $m = (\pm 1, \pm 3, \pm 5, \cdots)$, Eq. K.23 reduces to the equation for a circle, i.e.

$$E_\parallel^2 + E_\perp^2 = a^2.$$

Additional information on the *Stokes-vector* representation of light, and other advanced topics, is given in Appendix L and in other texts.[6] In the

---

[6] Plane waves, polarization, and the Stokes parameters are discussed in the following
   references: Chapter 1 of Born and Wolf (1980), Coulson (1988), and Kliger et al. (1990).

natural environment light is *partially-polarized* or in some limiting situations, *unpolarized*. Simply stated, the latter means that there is no preference between the parallel- and perpendicular-directions, and no permanent phase relationships exist between these two components. Sunlight, diffuse visible light emanating from an optically-thick cloud cover, and thermal IR emission are important examples of (nearly) unpolarized light. Rayleigh scattering from a clear sky is a counter-example, as the degree of linear polarization of scattered light can be quite high. Despite its importance in some applications, we will ignore polarization on the grounds that we are mainly concerned with the energy flow, rather than the accurate radiance distribution. This approach is called the *scalar approximation*. Even though caution is advised, it often provides reasonably accurate results even for the directional distribution of radiation. In addition there are ways to estimate the polarization by making first-order corrections to scalar solutions (for example, see §7.2).

Exercises

K.1 Consider a harmonic plane electromagnetic wave propagating in the z-direction through an isotropic, homogeneous medium with conductivity σ and permittivity ϵ. For this geometry Maxwell's equations simplify to

$$\frac{\partial^2 E_\parallel}{\partial z^2} = \mu\epsilon \frac{\partial^2 E_\parallel}{\partial t^2} + \mu\sigma \frac{\partial E_\parallel}{\partial t}$$

$$\frac{\partial^2 E_\perp}{\partial z^2} = \mu\epsilon \frac{\partial^2 E_\perp}{\partial t^2} + \mu\sigma \frac{\partial E_\perp}{\partial t}.$$

(a) Show that the electric field strength diminishes along the beam according to the exponential *Extinction Law* (§2.7), that is, the above set of equations has a solution of the form

$$E_\parallel = a_\parallel \exp\{i[(\omega t - k_0 m_{\mathrm{r}} z)] - k_0 m_{\mathrm{i}} z\} \tag{K.25}$$

where

$$k_0 = \frac{2\pi}{\lambda_0} = \frac{\omega}{c} = \omega\sqrt{\mu_0 \epsilon_0}$$

and m_{r} and m_{i} are the real and imaginary parts of the complex refractive index.

A practical non-mathematical approach is found in Shurcliff, W. A. and S. S. Ballard, *Polarized Light*, Van Nostrand, Princeton, 1964; An influential journal review article is Hansen and Travis (1974).

(b) Find the expressions for the two quantities, m_r and m_i, and for the speed of light in the medium in terms of the electric and magnetic properties of the medium. Show that the absorption coefficient $\alpha = k_0 m_i$ is given by

$$\alpha = \omega \sqrt{\frac{\epsilon\mu}{2} \left[-1 + \sqrt{1 + \left(\frac{\sigma}{\omega\epsilon}\right)^2} \right]}.$$

K.2 (a) Show that the real part of the time-average of the product of two complex quantities, A^* and B^* (having the same periodicity) is given by

$$\langle \Re(A) \cdot \Re(B) \rangle = \frac{1}{2} \Re(AB^*). \qquad (K.26)$$

(b) Solve for the H-components of the plane wave traveling in a dielectric medium. From these expressions, show that the Poynting vector is given by Eq. K.16.

Appendix L

Representations of Polarized Light

L.1 Stokes Parameters

In addition to the frequency, three independent quantities are needed to completely specify a time-harmonic electromagnetic plane wave. Since the quantities used in Appendix K are combinations of amplitudes and angles, which have different units, it is more convenient to use quantities having the same dimensions. In 1852 G. G. Stokes introduced his four parameters

$$I = a_\parallel^2 + a_\perp^2; \qquad Q = a_\parallel^2 - a_\perp^2; \qquad U = 2a_\parallel a_\perp \cos \delta; \qquad V = 2a_\parallel a_\perp \sin \delta.$$
(L.1)

Only three of these are independent, since $I^2 = Q^2 + U^2 + V^2$. We already found that I is the energy carried by the wave. The other parameters are related to the angle ψ $(0 \leq \psi < \pi)$ specifying the orientation of the ellipse (Fig. K.2) and the *ellipticity* angle, $\chi(-\pi/4 \leq \chi \leq \pi/4)$, which is given by $\tan \chi = \pm b/a$. The relationships are as follows (Born and Wolf, 1980):

$$Q = I \cos 2\chi \cos 2\psi; \qquad U = I \cos 2\chi \sin 2\psi; \qquad V = I \sin 2\chi. \qquad \text{(L.2)}$$

L.2 The Poincaré Sphere

Equations L.2 provide a simple geometrical representation of all the different states of polarization: Q, U and V may be regarded as the Cartesian coordinates of a point P on a sphere of radius I, such that 2χ and 2ψ are the spherical coordinates of this point (Fig. K.2). Every possible state of polarization of a plane wave is represented by a point on this *Poincaré Sphere*, developed by H. Poincaré in 1892. A point in the upper hemisphere (χ positive) represents *right-handed polarization*, that is, when the observer views the wave 'head-on', $\vec{E}$ rotates in a *clockwise* direction. *Left-handed* polarization corresponds to a point in the lower hemisphere (χ negative); when the observer views $\vec{E}$ 'head on,' it rotates in a *counter-clockwise* direction.
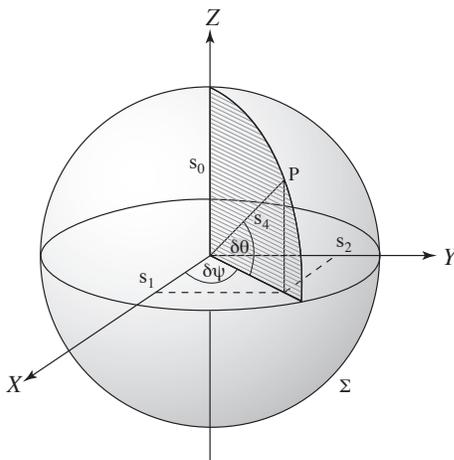
Figure L.1 Poincaré's representation of the state of polarization of a monochromatic wave. (The Poincaré sphere).

Linear polarization occurs when the phase difference δ is zero, or an integral multiple of π. From Eq. L.1, V is zero, and from Eq. L.2, the z-component of the point P on the Poincaré sphere is zero. Linear polarization is represented by points in the equatorial plane. For circular polarization, $a_\parallel = a_\perp$, and $\delta = \pi/2$ or $\delta = -\pi/2$, according to whether the polarization is right- or left-handed. Thus right-handed circular polarization corresponds to the north pole ($Q = U = 0, V = I$), and left-handed circular polarization corresponds to the south pole ($Q = U = 0, V = -I$). *Elliptical polarization* corresponds to a general point on the sphere, other than those in the equatorial plane or at the poles.

The Poincaré Sphere is useful in giving a simple geometrical visualization of the Stokes parameters. It applies only to a light wave which is *perfectly polarized,* an idealization which seldom occurs in nature. We now consider the general situation in which correlation between the two electric field components is not perfect.

L.3 Partial Polarization and the Incoherency of Natural Light

So far we have assumed that light is a plane wave with constant amplitude and phase difference between the two components. However, a more realistic view is that light is a mixture of plane waves, whose $\vec{E}$-field oscillates over a staggering number of cycles in one second. For example for visible light of $\lambda = 500$ nm, a wave oscillates at 6×10^{14} cycles in one second. Even a

detector with a very short integration time (say, 10^{-4} s) will time-average over many oscillations. The effective Stokes parameters measured by a detector is therefore not the instantaneous values (given by Eq. L.2), but the time-averaged values

$$I = \left\langle a_\parallel^2 \right\rangle + \left\langle a_\perp^2 \right\rangle ; \ Q = \left\langle a_\parallel^2 \right\rangle - \left\langle a_\perp^2 \right\rangle ; \ U = \left\langle 2a_\parallel a_\perp \cos\delta \right\rangle ; \ V = \left\langle 2a_\parallel a_\perp \sin\delta \right\rangle .$$
(L.3)

Generally, a light wave consists of a mixture of waves from different sources, which are statistically uncorrelated over the averaging time of a detector. Suppose we pass the light from such a 'natural' source, e. g. a hot filament, through a filter which passes only a narrow band of frequencies. Even though the frequencies of all the waves are practically equal, the phase angles will differ from one wave to the other. We may visualize the E-components at a point in space as being harmonic in time over immeasurably short time intervals (of the order of $10^{-8} - 10^{-9}$ s), but 'switching' randomly from one phase angle to another over longer time intervals. If this switching occurs in completely random ways, there will be as many positive phase differences as negative phase differences, or in other words, the time averages of the products $2a_\parallel a_\perp \cos\delta$ and $2a_\parallel a_\perp \sin\delta$ will be zero. Similarly, we can visualize the amplitudes being harmonic, and of specific amplitudes over short time intervals, but in a mixture of uncorrelated waves, the average values of the two polarization components will be the same, that is, $\langle a_\parallel^2 \rangle = \langle a_\perp^2 \rangle$. *Thus, for an uncorrelated mixture of plane waves, Q, U, and V all vanish.* This situation is known as *unpolarized* light. Examples of unpolarized light are direct sunlight, diffuse skylight from an overcast sky, and infrared thermal radiation. However, most scattered light in natural media is partially polarized. It is clear that if some correlation exists between amplitudes or phases, Q, U, and V may be finite, but smaller in value than in the case of a mixture of *coherent* waves. Thus, we see that the difference between coherent and *incoherent* light is the *degree of correlation* between the two E-field components. In this case, the relationship $I^2 = Q^2 + U^2 + V^2$ (valid for fully polarized light) becomes an *inequality*, $I^2 \geq Q^2 + U^2 + V^2$. This property gives us a quantitative measure of the *degree of polarization*, defined as

$$P = \frac{\sqrt{Q^2 + U^2 + V^2}}{I}.$$
(L.4)

What is the physical significance of the Stokes parameters? We can relate I, Q, U, and V to a set of ideal measurements, involving a linear polarizer (such as a polaroid filter), and a retardation plate (such as a thin calcite crystal). The polaroid removes the $\vec{E}$-field component of light that passes

through in a direction perpendicular to its axis of polarization, and transmits the other component with 100% transmission[1]. The retardation plate will affect the relative phases of the two components, i. e. it will introduce a relative phase shift, δ. Suppose we have a radiation detector which measures the radiative energy which has passed through a polarizer-retarder combination. It may be shown[2] that the radiance of transmitted light is given by

$$I(\psi, \delta) = (1/2) \left[I' + Q' \cos 2\psi + (U' \cos \delta + V' \sin \delta) \sin 2\psi \right] \qquad (L.5)$$

where primed quantities represent the Stokes parameters of the incident light, $\delta = \delta_\parallel - \delta_\perp$ is the retardation of the $\perp$-component, relative to the $\parallel$-component, and ψ is the angle of the polarizer axis with the horizontal ($\parallel$) axis. It is clear from Eq. L.5 that we can use a number of measurements of the incoming beam (varying ψ) to solve for the Stokes parameters of the incident light. If we first consider only a linear polarizer in the beam, so that there is no retardation ($\delta = 0$), and make measurements at $\psi = 0°$, $45°$, $90°$, and $135°$, the first three Stokes parameters may be obtained from these four measurements of $I(\psi, \delta)$:

$$I' = I(0°, 0) + I(90°, 0) \qquad \text{(a)}$$
$$Q' = I(0°, 0) - I(90°, 0) \qquad \text{(b)}$$
$$U' = I(45°, 0) - I(135°, 0) \quad \text{(c)}. \qquad (L.6)$$

It is clear from Eq. L.6 that the fourth component V' cannot be measured with a linear polarizer alone: a retarder is needed. Suppose we use a polarizer/quarter-wave plate combination. For $\delta = \pi/2$, we get

$$V' = I(45°, \pi/2) - I(135°, \pi/2). \qquad (L.7)$$

The physical significance of the Stokes parameters can now be stated in terms of *preferences* as follows: (1) Q gives preference to the $\parallel$-component over the $\perp$-component; (2) U gives preference to the component making an angle of $45°$ over that making an angle of $135°$; and V gives preference to the $45°$ component over the $135°$ component when passed through a polarizer-retarder combination. If unpolarized light were subjected to these measurements, the intensities $I(\psi, \delta)$ would be independent of ψ and δ, so that $Q' = U' = V' = 0$.

---

[1] Ideally, a polaroid filter would have no effect on that component parallel to the polarization axis, but in all real polaroids, some absorption will take place along this axis also.

[2] The equivalent form of Eq. L.5 in Chandrasekhar (1960), Eq. 163 (p. 129) has been shown by Hansen and Travis (1974) to have an error in sign. This error arises in the inconsistency between Chandrasekhar's definition of phase difference in his Eq. 154 (p. 28) with the definition of phase difference employed for the Stokes parameters.

If we were to add two polarized light beams together, what is the polarization of the mixture? We found earlier that if we add together two coherent plane waves of the same frequency and amplitude, we obtained an intensity that varies between zero and twice the amplitude of an individual wave. This occurred because of mutual interference, which depended upon the phase angle difference between the two waves. However, if we add together two partially-polarized waves with *no* (time-average) correlation between the phases, *the net result is that the Stokes parameters of the mixture is the sum of the individual Stokes parameters*. This is the most important property of the Stokes parameters. In this book we consider such light mixtures, or in other words, we consider *incoherent light fields*.

Despite our emphasis on incoherent light in this book, it is important to remember that coherent processes are also at work in the natural environment; otherwise we would be deprived of a host of beautiful phenomena, such as rainbows, iridescence, haloes, mirages, etc..[3] This co-existence of coherent and incoherent light is explained by the notion of *partial coherence*, and the spatial scales over which the various phenomena occur. As discussed in §3.2, a natural radiation field is coherent over an inner scale, called the *coherence length, d* (usually $d \approx \lambda$). Thus, light transmitted through a dielectric particle will undergo coherent interaction with its mutual parts, provided the circumference of the particle is of the order of λ. On the other hand, if the particle is much larger than λ, the various beams will behave as if they are refracted and transmitted independently.[4] In this case, the laws of geometrical optics provide a good description of the overall interaction.

L.4 The Stokes Vector Representation of Polarized Light

The *Stokes vector* $\vec{I}$ is a four-vector having the four Stokes parameters as its components,

$$\vec{I} = [I \; Q \; U \; V]^{T}. \tag{L.8}$$

where the superscript ^{T} denotes the transpose. In view of the linearity property of light fields, the Stokes vector of a mixture of two incoherent light

---

[3] For a lucid description of coherent processes in nature, this classic text should be consulted: Minnaert (1954). A later edition of this book was published in 1995 by Springer, with color photos by Pekka Parviainen (Minnaert, 1995).

[4] This description assumes that the particle is optically homogeneous. If the particle is inhomogeneous, scattering from irregularities causes the internal radiation field to be multiply-scattered, and mutual interference complicates the description. See §3.2 for more discussion.

fields whose Stokes vectors are $\vec{I_1}$ and $\vec{I_2}$ is simply $\vec{I} = \vec{I_1} + \vec{I_2}$, or

$$\vec{I} = [I_1 \; Q_1 \; U_1 \; V_1]^T + [I_2 \; Q_2 \; U_2 \; V_2]^T = [I_1 + I_2 \; Q_1 + Q_2 \; U_1 + U_2 \; V_1 + V_2 \;]^T.$$
(L.9)

The additivity principle also tells us that an unpolarized radiation field can be represented as the sum of two *linearly-polarized* fields which have equal E-field components and have their polarization directions normal to one another. Thus, two linearly-polarized incoherent light fields of equal intensity $(I/2)$ add together to give an unpolarized field:

$$\vec{I} = (I/2)[1 \; 1 \; 0 \; 0 \;]^T + (I/2)[1 \; -1 \; 0 \; 0 \;]^T = I[1 \; 0 \; 0 \; 0 \;]^T.$$
(L.10)

Note that the first vector in Eq. L.10 has its polarization direction in the $\parallel$-direction, so that from Eq. L.6, the component in the 90°-direction is zero. The second vector has a zero component in the 0°-direction, so that Q is the negative of that of the first vector.

It is also easy to see that an arbitrarily-polarized light field may be represented by the sum of an unpolarized (u) and a perfectly-polarized (p) light field

$$\vec{I} = \vec{I_u} + \vec{I_p} = [I - \sqrt{U^2 + Q^2 + V^2} \; 0 \; 0 \; 0 \;]^T + [\sqrt{U^2 + Q^2 + V^2} \; Q \; U \; V \;]^T.$$
(L.11)

In view of the additivity of Stokes parameters it is easy to see why it is possible to represent any arbitrarily-polarized, incoherent radiation field as the linear sum of an unpolarized part I_u and a 100% polarized part, I_p, $I = I_u + I_p$. The degree of polarization is then written $P = I_p/I$, which gives us a more intuitive interpretation of P than provided by Eq. L.4.

For perfectly-polarized light $(\vec{I_u} = 0)$, $\vec{I}$ is a vector whose tip lies on the Poincaré sphere. We may visualize partially-polarized light as a vector $\vec{I_p}$, to which is added a 'smeared-out' component of radius $\vec{I_u}$. Over the averaging time period $\langle t \rangle$, the tip of the vector $\vec{I_u}$ traces out with equal probability all 4π steradians of the Poincaré sphere.

L.5 The Mueller Matrix

The action of any optical device on an incoherent light beam can be thought of as producing a Stokes vector which is a linear combination of the Stokes components of the light. Formally, we can represent the effect of an optical

device in terms of a *Mueller matrix* operation on $\vec{I}$, or in mathematical terms

$$\vec{I} = [\,I\;Q\;U\;V\,]^T = \mathbf{M}\vec{I'} = \begin{bmatrix} M_{11} & M_{12} & M_{13} & M_{14} \\ M_{21} & M_{22} & M_{23} & M_{24} \\ M_{31} & M_{32} & M_{33} & M_{34} \\ M_{41} & M_{42} & M_{43} & M_{44} \end{bmatrix} [\,I'\;Q'\;U'\;V'\,]^T.$$

(L.12)

The input radiation field components are denoted by primes, and the output radiation field components are unprimed. The components M_{ij} may be derived for various types of polarization analyzers, including polaroid filters (or in general *dichroic linear polarizers*) and retarding plates (see Coulson (1988), pp. 577–584). We are often concerned with the action of scattering particles on the state of polarization of an incident radiation field. This action can also be represented as a linear matrix operator, called the *scattering matrix*, $\mathbf{S}$, whose elements depend upon the angle Θ between the incident and scattered wave (the scattering angle), i.e., $S_{ij} = S_{ij}(\Theta)$. In addition S_{ij} depends upon the light-interaction properties of the particles. For the simplest type of scattering, i.e. *Rayleigh scattering*, the scattering matrix is given by

$$\mathbf{S}_{\text{Ray}}(\Theta) = \frac{3\sigma}{4\pi} \begin{bmatrix} 1 + \cos^2\Theta & \cos^2\Theta - 1 & 0 & 0 \\ \cos^2\Theta - 1 & 1 + \cos^2\Theta & 0 & 0 \\ 0 & 0 & 2\cos\Theta & 0 \\ 0 & 0 & 0 & 2\cos\Theta \end{bmatrix}$$

(L.13)

where σ is the scattering coefficient, defined in Chapter 2.

The radiation field in atmospheres and oceans can be highly polarized. For example, for clear skies or pure oceans where Rayleigh scattering dominates the radiative transfer, Eq. L.13 shows that for scattering angles near $\Theta = \pi/2$, there is 100% linear polarization for $\Theta = \pi/2$. However, in reality there are slight deviations from this idealized Rayleigh scattering so that the light is about 96% polarized for $\Theta = \pi/2$. (The presence of aerosols reduces this number to no more than 80% in actual cloud-free situations.) Reflection from water or ice surfaces can also lead to high linear polarizations. However, the elliptic component V is always very small, and it is seldom necessary to specify all four Stokes parameters. In fact, since I conveys the information on the energy carried by the field, it is often permissible to ignore the Q and U components as well. This assumption is the principal approximation made in this book. We note, however, that although I 'carries the energy', it is sometimes necessary to solve the full *vector* equation (for the Stokes' parameters) to calculate it properly. The *scalar* equation is in many cases

adequate as can be confirmed by comparison between *vector* and *scalar* solutions.

Exercises

L.1 (a) Find the Stokes vector for Rayleigh-scattered light from a small volume element dV having a concentration of n molecules. Use the equation $\vec{I} = ndV\mathbf{S}_{\mathrm{Ray}}\vec{I'}$, where $\mathbf{S}_{\mathrm{Ray}}$ is given by Eq. L.13. Assume that the solar radiation is unpolarized and given by

$$\vec{I'} = [F^{\mathrm{s}}\delta(\cos\theta_0 - \cos\theta)\delta(\phi_0 - \phi),\ 0\ 0\ 0\ ]^T \qquad (\text{L.14})$$

where F^{s} is the solar irradiance $[\mathrm{W}\cdot\mathrm{m}^{-2}]$ and (θ_0, ϕ_0) is the direction of the incoming solar beam.

(b) Describe the state of polarization for Rayleigh-scattered light evaluated at the scattering angles $\Theta = \pi/2$ and $\Theta = 0$.

L.2 2. Devise a number of 'thought experiments' to find the elements of the Mueller matrix for the following optical instruments:

(a) an ideal linear polarizer, e.g. a polaroid filter, with its axis along the horizontal ($\parallel$) axis.

(b) the same as (a) but with its axis along the perpendicular ($\perp$) axis.

Appendix M

Spherical Shell Geometry

For solar zenith angles greater than about $80°$ and twilight situations, we have to take the curvature of the Earth into account and solve the radiative transfer equation appropriate for a spherical shell atmosphere (the treatment of spherical geometry is described in Sobolev (1975)). The geometry is illustrated in Fig. M.1. In plane geometry the slant path is the same for all layers of equal geometrical thickness, whereas in spherical geometry the slant path changes from layer to layer.

In spherical shell geometry, the derivative of the radiance consists of three terms in addition to the one term occurring for slab geometry. These ad-
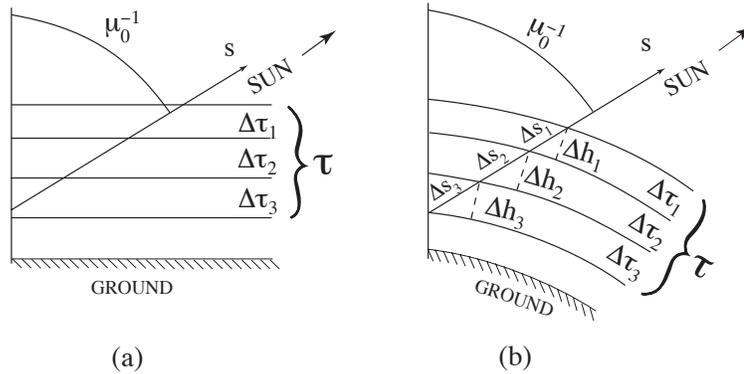
Figure M.1 Illustration of plane versus spherical geometry. (a) In plane geometry the slant path is the same for all layers of equal geometrical thickness. (b) In spherical geometry the slant path changes from layer to layer.

ditional terms express the change in the radiance associated with changes in polar angle, azimuthal angle, and solar zenith angle. Hence, for a spherical shell medium illuminated by a direct (collimated) beam of radiation, the appropriate radiative transfer equation for the diffuse radiance may be expressed as

$$\hat{\Omega} \cdot \nabla I(r, u, \phi, \mu_0) = -k(r)[I(r, u, \phi, \mu_0) - S(r, u, \phi, \mu_0)]. \qquad (M.1)$$

Here r is the distance from the center of the planet and k is the extinction coefficient, while u and ϕ are the cosine of the polar angle and the azimuthal angle, respectively. The symbol $\hat{\Omega} \cdot \nabla$ denotes the derivative operator or the 'streaming term' appropriate for this geometry. To arrive at this term we must use spherical geometry. If we map the radiance from a set of global spherical coordinates to a local set with reference to the local zenith direction, then as explained in Appendix N, the streaming term becomes[1]

$$\hat{\Omega} \cdot \nabla \equiv u \frac{\partial}{\partial r} + \frac{1 - u^2}{r} \frac{\partial}{\partial u}$$
$$+ \frac{1}{r} f(u, \mu_0) \left[\cos(\phi - \phi_0) \frac{\partial}{\partial \mu_0} + \frac{\mu_0}{1 - \mu_0^2} \sin(\phi - \phi_0) \frac{\partial}{\partial(\phi - \phi_0)} \right]$$
$$(M.2)$$

where the factor f is given by

$$f(u, \mu_0) \equiv \sqrt{1 - u^2} \sqrt{1 - \mu_0^2}. \qquad (M.3)$$

For a slab geometry, only the first term contributes. The curvature gives rise to additional terms. Thus, for spherically symmetric geometry, the second term must be added, while the third and fourth terms are required for a spherical shell medium illuminated by direct (collimated) beam radiation. The source function in Eq. M.1 is

$$S(r, u, \phi, \mu_0) \equiv \frac{\varpi(r)}{4\pi} \int_0^{2\pi} d\phi' \int_{-1}^1 du' p(r, u', \phi'; u, \phi) I(r, u', \phi', \mu_0)$$
$$+ \frac{\varpi(r)}{4\pi} p(r, -\mu_0, \phi_0; u, \phi) F^s e^{-\tau Ch(r, \mu_0)}. \qquad (M.4)$$

The first term in Eq. M.4 is due to multiple scattering and the second term is due to first-order scattering. We have used the diffuse/direct splitting so that Eq. M.1 describes the diffuse radiation field only. We note that for isotropic

---

[1] The derivation of the 'streaming' term given in Appendix N is taken from: A. Kylling: *Radiation Transport in Cloudy and Aerosol Loaded Atmospheres*, Ph.D. Thesis, University of Alaska, Fairbanks, USA, 1992, and the discussion of the azimuthally-averaged equation from: Dahlback and Stamnes (1991).

scattering, the primary scattering 'driving term' becomes isotropic, which implies that the radiance becomes azimuth independent. The argument in the exponential, $Ch(r, \mu_0)$, is the *air-mass factor* or the *Chapman function*: the quantity by which the vertical optical depth must be multiplied to obtain the slant optical depth. For a slab geometry, $Ch(r, \mu_0) = 1/\mu_0 = \sec\theta_0$. Hence $\exp[-\tau Ch(r, \mu_0)]$ yields the attenuation of the incident solar irradiance F^{s} (normal to the beam) along the solar beam path.

We find that Eq. M.4 may be written as follows

$$
S(r, u, \phi, \mu_0) =
$$
$$
\frac{\varpi(r)}{4\pi} \int_0^{2\pi} d\phi' \int_{-1}^1 du' \left[\sum_{m=0}^{2N-1} (2 - \delta_{0m}) p^m(\tau, u', u) \cos m(\phi - \phi') \right] I(r, u', \phi')
$$
$$
+ \left[\sum_{m=0}^{2N-1} X_0^m(\tau, u) \cos m(\phi - \phi_0) \right] e^{-\tau Ch(r, \mu_0)} \tag{M.5}
$$

where $p^m(\tau, u', u)$ and $X_0^m(\tau, u)$ are defined by Eqs. 6.31 and 6.34.

M.1 "Isolation" of Azimuth Dependence

The extra derivative terms in Eq. M.2 makes the spherical geometry case more difficult to treat than the corresponding slab problem. In general, we could expand the radiance in a Fourier series containing both *sine* and *cosine* terms to account for the appearance of both types of terms in the derivative operator. However, if the effects of sphericity are small, it is useful to treat the second, third, and fourth derivative terms in Eq. M.2 (which are due to the spherical geometry) as a perturbation. Thus, if we ignore these terms, we are left with a plane parallel problem to solve and the derivative terms can be included in an iterative manner by utilizing the plane parallel solutions. Then, since the first term in Eq. M.5 is essentially a Fourier cosine series, and the diffuse radiance described by Eq. M.1 is driven by the second term in Eq. M.5, which contains only *cosine* terms, we may expand the radiance as previously expressed by Eq. 6.32 ignoring *sine* terms. The reason is that we have assumed that the third and fourth terms in Eq. M.2, which contain *sine* terms, can be treated as a perturbation and hence can be evaluated in an iterative manner from the plane parallel solutions.

With these assumptions, Eq. M.1 becomes

$$\sum_{m=0}^{2N-1} \left\{ u \frac{\partial I^m(r,u,\mu_0)}{\partial r} + \frac{1-\mu_0^2}{r} \frac{\partial I^m}{\partial u} \right.$$
$$\left. + k(r) \left[I^m(r,u,\mu_0) - S^m(r,u,\mu_0) \right] \right\} \cos m(\phi_0 - \phi) = J(r,u,\phi,\mu_0).$$

(M.6)

Here

$$S^m(r,u,\mu_0) \equiv \frac{\varpi(r)}{2} \int_{-1}^{1} p^m(r,u',u) I^m(r,u') du' + X_0^m(r,u) e^{-\tau Ch(r,\mu_0)}$$

(M.7)

and

$$J(r,u,\phi,\mu_0) \equiv \frac{1}{r} f(u,\mu_0) \left\{ \cos(\phi_0 - \phi) \sum_{m=0}^{2N-1} \cos m(\phi_0 - \phi) \frac{\partial I^m(r,u,\mu_0)}{\partial \mu_0} \right.$$
$$\left. + \frac{\mu_0}{1-\mu_0^2} \sin(\phi - \phi_0) \sum_{m=0}^{2N-1} m \sin m(\phi - \phi_0) I^m(r,u,\mu_0) \right\}.$$

(M.8)

In the following example, we describe how the equations may be solved in a simplified geometry.

Example: Zenith Sky and Mean Radiance – Iterative Approach

If we are interested in only the zenith sky radiance (which is azimuthally independent), then only the $m = 0$ term in Eq. 6.32 contributes. For $m = 0$, the second term in Eq. 6.32 is identically zero. Upon averaging over azimuth the first term becomes proportional to $\partial I^1(r,u,\mu_0)/\partial \mu_0$ and may also be discarded if our interest lies solely in the zenith sky radiance. Thus, the zenith sky radiance is obtained by setting $J(r,u,\mu_0) = 0$ in Eq. M.6 and solving it for $m = 0$ only. Similarly, for isotropic scattering there is no azimuth dependence and the complete solution is again arrived at by setting $J(r,u,\mu_0) = 0$ in Eq. M.6 and solving the equation for $m = 0$ only.

If our interest is in photolysis and heating rates, only the mean radiance is needed. We therefore average Eq. M.6 over azimuth to obtain:

$$u \frac{\partial I^0(r,u,\mu_0)}{\partial r} + \frac{1-\mu_0^2}{r} \frac{\partial I^0}{\partial u} + \frac{1}{r} \left[J_1(r,u,\mu_0|I^1) + J_2(r,u,\mu_0|I^1) \right] = -k(r) \left[I^0(r,u,\mu_0) - S^0(r,u,\mu_0) \right]$$

where $S^0(r,u,\mu_0)$ is obtained by setting $m = 0$ in Eq. M.7 and

$$J_1(r,u,\mu_0|I^1) = \frac{1}{2} f(u,\mu_0) \frac{\partial I^1(r,u,\mu_0)}{\partial \mu_0}$$

$$J_2(r,u,\mu_0|I^1) = \frac{1}{2} f(u,\mu_0) \frac{\mu_0}{1-\mu_0^2} I^1(r,u,\mu_0).$$

We note that J_1 and J_2 depend functionally on the first azimuth-dependent Fourier component of the radiance, I^1, as indicated. Dividing by $-k(r)$, and introducing $d\tau = -k(r)dr$, we obtain

$$u\frac{\partial I(\tau, u)}{\partial \tau} = I(\tau, u) - \frac{\varpi(r)}{2}\int_{-1}^{1} du' p(r, u', u)I(r, u') - S^*(\tau, u)$$

where

$$S^*(\tau, u) \equiv X_0(\tau(r), u)e^{-\tau Ch[\tau, \mu_0]} + \frac{1 - u^2}{kr}\frac{\partial I}{\partial u} + \frac{1}{kr}(J_1 + J_2). \qquad \text{(M.9)}$$

To simplify the notation, we have dropped the $m = 0$ superscript. If we ignore the three last terms in the expression for $S^*(\tau, u)$, we are left with an equation which is identical to that obtained for plane geometry except that the primary scattering term is evaluated in spherical geometry using the correct path length. We shall refer to this approach, in which the primary scattering driving term is included correctly but the multiple scattering is done in plane geometry, as the 'pseudo-spherical' approximation. Having obtained a 'pseudo-spherical' solution, we may proceed to evaluate the terms we neglected and then solve the equation again including those terms. Repetition of this procedure provides an iteration scheme that is expected to converge if the perturbation terms (i.e., the three last terms on the right side of Eq. M.9) are small compared with the driving term. Suffice it to say here that this approach has been found to be quite useful for obtaining both the mean radiance and the zenith sky radiance in twilight situations.

In a stratified planetary atmosphere, spherical effects (i.e., the angle derivatives), become important around sunrise and sunset. Thus, the first term in Eq. M.9 is the dominant one and the other terms may be treated as perturbations. It has been shown (by using a perturbation technique to account for the spherical effects) that in a stratified atmosphere, mean radiances may be calculated with sufficient accuracy for zenith angles less than 90° by including only the first term in Eq. M.9, when spherical geometry is used to compute the direct beam attenuation. Then, we may ignore all angle derivatives and simply write the streaming term as

$$\hat{\Omega} \cdot \nabla \cong u\frac{\partial}{\partial \tau}. \qquad \text{(M.10)}$$

While this 'pseudo-spherical' approach works adequately for the computation of radiances in the zenith– and nadir-viewing directions, and mean radiances (for zenith angles less than 90°), it may not work for computation of radiances in directions off-zenith (or off-nadir) unless it can be shown that the angle derivative terms are indeed small.

Exercises

M.1 The optical depth in a curved atmosphere is required to compute the attenuation of solar irradiance. For an overhead sun, the vertical optical depth between altitude z_0 and the sun is

$$\tau(z_0, \nu) = \int_{z_0}^{\infty} dz k(z, \nu)$$

where $k(z, \nu)$ is the extinction coefficient at frequency ν, and dz is measured along the vertical. For a non-vertical path dz must be replaced by the actual length along the ray path. In slab geometry the actual path length along a ray is simply dz/μ_0 where μ_0 is the cosine of the solar zenith angle. In spherical geometry the situation is somewhat more complex. Then dz must be replaced by the actual ray path through a curved atmosphere.

(a) For solar zenith angles $\theta_0 < 90°$, use geometrical considerations to derive the following expression for the optical depth between level z_0 and the Sun in a spherical atmosphere

$$\tau(z_0, \nu, \mu_0) = \int_{z_0}^{\infty} dz \frac{k(z, \nu)}{\sqrt{1 - \left(\frac{R+z_0}{R+z}\right)^2 \left(1 - \mu_0^2\right)}} \qquad (\theta_0 < 90°)$$

where R is the radius of the planet and z_0 the distance above the Earth's surface.

(b) Similarly for $\theta_0 > 90°$ show that the following expression applies

$$\tau(z_0, \nu, \mu_0) = 2 \int_{z_s}^{\infty} dz k(z, \nu) \left[1 - \left(\frac{R + z_s}{R + z}\right)^2\right]^{-\frac{1}{2}}$$

$$- \int_{z_0}^{\infty} dz k(z, \nu) \left[1 - \left(\frac{R + z_0}{R + z}\right)^2 \left(1 - \mu_0^2\right)\right]^{-\frac{1}{2}}$$

where z_s is a screening height below which the atmosphere is essentially opaque to radiation of frequency ν.

For practical computations we may divide the spherical atmosphere into a number of concentric shells. Let Δh_j denote the (vertical) thickness of the shell lying between r_j ($r_j = R + z_j$) and r_{j+1} ($r_{j+1} = r_j - \Delta h_j$) where z_j is the vertical distance from the surface of the planet to location r_j. (Note that r_1 is at the top of the atmosphere and r_{L+1} is at the bottom of the deepest layer (shell) considered if the atmosphere is divided into L concentric shells.)

(c) Show that approximate expressions for the optical depth that may be used in practical computations are given by

$$\tau(\tau, \nu, \mu_0) = \sum_{j=1}^{p} \Delta \tau_j^v \left(\frac{\Delta S_j}{\Delta h_j}\right) \qquad \theta_0 < 90°$$

$$\tau(\tau, \nu, \mu_0) = \sum_{j=1}^{p} \Delta\tau_j \left(\frac{\Delta S_j}{\Delta h_j}\right) + 2 \sum_{j=p+1}^{L-1} \Delta\tau_j \left(\frac{\Delta S_j}{\Delta h_j}\right) + \Delta\tau_L \left(\frac{\Delta S_L}{\Delta h_L}\right) \qquad (\theta_0 > 90°).$$

Here L is the layer in the atmosphere below which attenuation is complete, τ_j is the vertical optical depth of shell j, and

$$\Delta S_j = \sqrt{r_j^2 - r_p^2(1 - \mu_0^2)} - \sqrt{r_{j+1}^2 - r_p^2(1 - \mu_0^2)}$$

where r_j and r_{j+1} are the distances from the center of the planet to the upper and lower boundary, respectively of layer j, and r_p is the distance from the center to the point at which the optical depth is evaluated.

M.2 (a) Show that the Chapman function may be written

$$Ch(X, \theta) \equiv \frac{\mathcal{N}(z, \theta)}{n(z)H} = \int_0^\infty dY \exp[-\sqrt{X^2 + 2XY \cos\theta + Y^2} + X].$$

Here $X = R_\oplus/H$, $Y = z/H$, and $\mathcal{N}(z, \theta)$ is the slant column number for a spherically-symmetric exponential atmosphere. (b) Defining $\ln V = -\sqrt{X^2 + 2XY \cos\theta + Y^2} + X$, show that

$$Ch(X, \theta) = \int_0^1 \frac{dV(1 - \ln V/X)}{\sqrt{(1 + \sin\theta - \frac{\ln V}{X})(1 - \sin\theta - \frac{\ln V}{X})}}.$$

(c) Using the relationship

$$\int_0^1 \frac{dV}{\sqrt{\xi^2 - \ln V}} = 2e^{\xi^2} \int_\xi^\infty ds\, e^{-s^2}$$

show that, on neglecting terms of order X^{-1},

$$Ch(X, \theta) = \sqrt{2X} e^{X \cos^2\theta/2} [1 - erf(\sqrt{X/2}\cos\theta)]$$

where erf is the error function.

(c) Show that, to order X^{-2}, that

$$Ch(X, \theta) = \frac{2\xi e^{\xi^2}}{\cos\theta} [1 - erf(\xi)]$$

where $\xi = \sqrt{X/2}\cot\theta$.

(e) Show that $Ch(X \to \infty, \theta) \to \sec\theta$ for both forms (c) and (d).

Appendix N

The Streaming term in Spherical Geometry

Since the Earth's atmosphere has the form of a spherical shell, the radiative transfer equation must be cast in a form applicable to spherical geometry. The components of the streaming term $(\hat{\Omega} \cdot \nabla)$ in spherical geometry are

$$\hat{\Omega} = \cos \Phi \sin \Theta \; \mathbf{e}_x + \sin \Phi \sin \Theta \; \mathbf{e}_y + \cos \Theta \; \mathbf{e}_z \qquad \text{(N.1)}$$

$$\nabla = \mathbf{e}_r \; \frac{\partial}{\partial r} + \mathbf{e}_{\Theta_0} \; \frac{1}{r} \frac{\partial}{\partial \Theta_0} + \mathbf{e}_{\Phi_0} \; \frac{1}{r \sin \Theta_0} \frac{\partial}{\partial \Phi_0}$$

where

$$\mathbf{e}_r = \sin \Theta_0 \cos \Phi_0 \; \mathbf{e}_x + \sin \Theta_0 \sin \Phi_0 \; \mathbf{e}_y + \cos \Theta_0 \; \mathbf{e}_z \qquad \text{(N.2)}$$

$$\mathbf{e}_{\Theta} = \cos \Theta_0 \cos \Phi_0 \; \mathbf{e}_x + \cos \Theta_0 \sin \Phi_0 \; \mathbf{e}_y - \sin \Theta_0 \; \mathbf{e}_z \qquad \text{(N.3)}$$

$$\mathbf{e}_{\Phi} = - \sin \Phi_0 \; \mathbf{e}_x + \cos \Phi_0 \; \mathbf{e}_y$$

and the angles are defined in Fig. N.1.
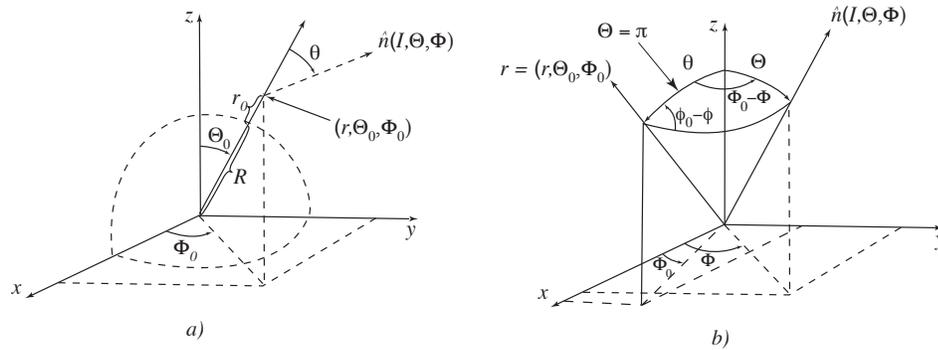
Figure N.1 The geometric setting. Note that in panel *b)* the directional vector $\hat{n}$ has been parallel shifted to have its starting point at the surface of the Earth.

Taking the dot product of $\hat{\Omega}$ and ∇ gives

$$
\hat{\Omega} \cdot \nabla = [\cos\Theta \cos\Theta_0 + \sin\Theta \sin\Theta_0 \cos(\Phi_0 - \Phi)]\frac{\partial}{\partial r}
$$
$$
-\frac{1}{r}[\cos\Theta \sin\Theta_0 - \sin\Theta \cos\Theta_0 \cos(\Phi_0 - \Phi)]\frac{\partial}{\partial\Theta_0}
$$
$$
-\frac{1}{r}\frac{\sin\Theta}{\sin\Theta_0}\sin(\Phi_0 - \Phi)\frac{\partial}{\partial\Phi_0}. \tag{N.4}
$$

For practical reasons it is preferable to refer the system of spherical coordinates to the local zenith direction. Thus we want to map the radiance from the set of global coordinates $(r, \Theta_0, \Phi_0, \Theta, \Phi)$ to the local set $(r, \mu_0, \phi_0, \mu, \phi)$, i.e.[1]

$$
I(r, \Theta_0, \Phi_0, \Theta, \Phi) \quad\Rightarrow\quad I(r, \mu_0, \phi_0, \mu, \phi) \tag{N.5}
$$

where

$$
\mu \equiv \cos\theta \equiv \mathbf{e}_r \cdot \hat{\Omega} = \cos\Theta \cos\Theta_0 + \sin\Theta \sin\Theta_0 \cos(\Phi_0 - \Phi) \tag{N.6}
$$
$$
\mu_0 \equiv \cos\theta_0 \tag{N.7}
$$

and the local polar (θ_0, θ) and azimuthal angles (ϕ_0, ϕ) are defined in Fig. N.1. In view of Eq. N.6 we may rewrite N.4 as

$$
\hat{\Omega} \cdot \nabla = \mu\frac{\partial}{\partial r} + \frac{1}{r}\frac{\partial\mu}{\partial\Theta_0}\frac{\partial}{\partial\Theta_0} + \frac{1}{r}\frac{1}{\sin^2\Theta_0}\frac{\partial\mu}{\partial\Phi_0}\frac{\partial}{\partial\Phi_0}. \tag{N.8}
$$

Since μ is a function of both Θ_0 and Φ_0

$$
\frac{\partial}{\partial\Theta_0} = \frac{\partial}{\partial\theta_0} + \frac{\partial\mu}{\partial\Theta_0}\frac{\partial}{\partial\mu} \tag{N.9}
$$
$$
\frac{\partial}{\partial\Phi_0} = \frac{\partial\phi_0}{\partial\Phi_0}\frac{\partial}{\partial\phi_0} + \frac{\partial\mu}{\partial\Phi_0}\frac{\partial}{\partial\mu}
$$

and Eq. N.8 becomes

$$
\hat{\Omega} \cdot \nabla = \mu\frac{\partial}{\partial r} + \frac{1}{r}\left[\left(\frac{\partial\mu}{\partial\Theta_0}\right)^2 + \frac{1}{\sin^2\theta_0}\left(\frac{\partial\mu}{\partial\Phi_0}\right)^2\right]\frac{\partial}{\partial\mu} + \frac{1}{r}\frac{\partial\mu}{\partial\Theta_0}\frac{\partial}{\partial\theta_0}
$$
$$
+ \frac{1}{r}\frac{1}{\sin^2\theta_0}\frac{\partial\mu}{\partial\Phi_0}\frac{\partial\phi_0}{\partial\Phi_0}\frac{\partial}{\partial\phi_0}. \tag{N.10}
$$

Using Eq. N.6 and some relationships from spherical trigonometry

$$
\left[\left(\frac{\partial\mu}{\partial\Theta_0}\right)^2 + \frac{1}{\sin^2\theta_0}\left(\frac{\partial\mu}{\partial\Phi_0}\right)^2\right] = 1 - \mu^2 \tag{N.11}
$$

---

[1] The global coordinates r, Θ_0 and Φ_0 denote a point in $\mathbf{R^3}$, whereas Θ and Φ are the coordinates of a point on the unit sphere $\mathbf{S^2} = \{x, y : x^2 + y^2 = 1\}$, and similar for the local coordinates. Hence both $I(r, \Theta_0, \Phi_0, \Theta, \Phi)$ and $I(r, \mu_0, \phi_0, \mu, \phi)$ are real–valued functions defined on $\mathbf{R^3} \times \mathbf{S^2}$.

$$\frac{\partial \mu}{\partial \Theta_0} = -\cos\Theta \sin\Theta_0 + \sin\Theta \cos\Theta_0 \cos(\Phi_0 - \Phi) = -\sqrt{1 - \mu^2} \cos(\phi_0 - \phi)$$

$$\text{(N.12)}$$

$$\frac{\partial \mu}{\partial \Phi_0} = -\sin\Theta \sin\Theta_0 \sin(\Phi_0 - \Phi) = -\sqrt{1 - \mu^2} \sin\theta_0 \sin(\phi_0 - \phi) \qquad \text{(N.13)}$$

$$\frac{\partial \phi_0}{\partial \Phi_0} = \frac{\partial(\phi_0 - \phi)}{\partial(\Phi_0 - \Phi)} = \cos\theta_0 \sin(\phi_0 - \phi) \qquad \text{(N.14)}$$

we may finally write the streaming term in spherical geometry referenced to the local zenith direction as

$$\mu\frac{\partial}{\partial r} + \frac{1 - \mu^2}{r}\frac{\partial}{\partial \mu} + \frac{\sqrt{1 - \mu^2}\sqrt{1 - \mu_0{}^2}}{r}\left[\cos(\phi - \phi_0)\frac{\partial}{\partial \mu_0} + \right.$$

$$\left. \frac{\mu_0}{1 - \mu_0^2}\sin(\phi - \phi_0)\frac{\partial}{\partial(\phi - \phi_0)}\right]. \qquad \text{(N.15)}$$

We note that in a plane parallel geometry only the first term in Eq. N.15 is included. For a spherically symmetric atmosphere the second term must be added. The full expression is, as stated above, valid for an inhomogeneous spherical shell, i.e. a planetary atmosphere.

N.1   The streaming term pertinent to calculation of mean radiances

Quite generally the radiance may be expanded in a Fourier series

$$I(r, \mu_0, \phi_0, \mu, \phi) = \sum_{m=0}^{\infty} \{I_m^c(r, \mu_0, \mu) \cos m(\phi - \phi_0)$$

$$+ I_m^s(r, \mu_0, \mu) \sin m(\phi - \phi_0)\}. \qquad \text{(N.16)}$$

Combining Eq. N.15 and Eq. N.16 we find

$$\left\{\mu\frac{\partial}{\partial r} + \frac{1 - \mu^2}{r}\frac{\partial}{\partial \mu} + \frac{\sqrt{1 - \mu^2}\sqrt{1 - \mu_0{}^2}}{r}\cos(\phi - \phi_0)\frac{\partial}{\partial \mu_0}\right\} I(r, \mu_0, \phi_0, \mu, \phi)$$

$$+ \frac{\sqrt{1 - \mu^2}\sqrt{1 - \mu_0{}^2}}{r}\frac{\mu_0}{1 - \mu_0^2}\sin(\phi - \phi_0)$$

$$\cdot \sum_{m=0}^{\infty} \{-m\, I_m^c(r, \mu_0, \mu) \sin m(\phi - \phi_0) + m\, I_m^s(r, \mu_0, \mu) \cos m(\phi - \phi_0)\}.$$

$$\text{(N.17)}$$

If our interest lies in the mean radiance

$$\overline{I}(r, \theta, \phi) = \frac{1}{4\pi} \int_0^{2\pi} d\phi_0 \int_0^{\pi} \sin\theta d\theta_0 \ I(r, \theta_0, \phi_0, \phi, \theta)$$

$$= \frac{1}{4\pi} \int_0^{2\pi} d\phi_0 \int_{-1}^{1} d\mu_0 \ I(r, \mu_0, \phi_0, \phi, \mu) \tag{N.18}$$

we average Eq. N.18 over azimuth to get

$$\mu \frac{\partial I_0^c(r, \mu_0, \mu)}{\partial r} + \frac{1 - \mu^2}{r} \frac{\partial I_0^c(r, \mu_0, \mu)}{\partial \mu} + \frac{1}{2} \frac{\sqrt{1 - \mu^2}\sqrt{1 - \mu_0^2}}{r} \frac{\partial I_1^c(r, \mu_0, \mu)}{\partial \mu_0}$$

$$+ \frac{1}{2} \frac{\sqrt{1 - \mu^2}\sqrt{1 - \mu_0^2}}{r} \frac{\mu_0}{1 - \mu_0^2} I_1^c(r, \mu_0, \mu). \tag{N.19}$$

Note that only the cosine terms 'survived' the averaging over azimuth.

Appendix O
Isolation of the Azimuth-Dependence

The purpose of this Appendix is to provide a derivation of the azimuthal components of the radiance field. We start with the half-range equations for the diffuse radiance which we write in full-range form for the present purpose

$$
u\frac{dI(\tau, u, \phi)}{d\tau} =
$$
$$
I(\tau, u, \phi) - \frac{\varpi}{4\pi} \int_0^{2\pi} d\phi' \int_{-1}^1 \left\{ du' p(u', \phi'; u, \phi) I(\tau, u', \phi') \right.
$$
$$
\left. - \frac{\varpi F^{\mathrm{s}}}{4\pi} p(-\mu_0, \phi_0; u, \phi) e^{-\tau/\mu_0} \right\}.
$$
$$
(O.1)
$$

Since, as noted in Chapter 6 the expansion of the phase function in Legendre polynomials is essentially a Fourier cosine series, i.e.

$$
p(u', \phi'; u, \phi) = \sum_{m=0}^{2N-1} (2-\delta_{0m}) \left\{ \sum_{l=m}^{2N-1} (2l+1)\chi_l^m \Lambda_l^m(u)\Lambda_l^m(u') \right\} \cos[m(\phi-\phi')],
$$
$$
(O.2)
$$

we expand the radiance likewise

$$
I(\tau, u, \phi) = \sum_{m=0}^{2N-1} I^m(\tau, u) \cos[m(\phi_0 - \phi)].
$$
$$
(O.3)
$$

Substitution of eqns. O.2 and O.3 into the integral term of eqn. O.1 yields

$$\frac{\varpi}{4\pi} \int_0^{2\pi} d\phi' \int_{-1}^1 du' p(u', \phi'; u, \phi) I(\tau, u', \phi') =$$

$$\frac{\varpi}{4\pi} \int_0^{2\pi} d\phi' \int_{-1}^1 du' \left\{ \sum_{m=0}^{2N-1} (2 - \delta_{0m}) \right.$$

$$\left. \cdot \sum_{l=m}^{2N-1} (2l + 1) \chi_l^m \Lambda_l^m(u) \Lambda_l^m(u') \cos[m(\phi - \phi')] \right\}$$

$$\cdot \left\{ \sum_{r=0}^{2N-1} I^r(\tau, u') \cos[r(\phi_0 - \phi')] \right\}. \tag{O.4}$$

Focussing on the integration over azimuth we find that for arbitrary m-values only the $r = m$ term contributes. Thus, we obtain $2\pi I^0(\tau, u')$ for $m = 0$, $2\pi I^1(\tau, u') cos(\phi_0 - \phi)$ for $m = 1$, and in general contributes.

$$\sum_{m=0}^{2N-1} \int_0^{2\pi} d\phi'(2 - \delta_{0m}) \sum_{r=0}^{2N-1} I^r(\tau, u') \cos[m(\phi - \phi')] \cos[r(\phi_0 - \phi')] =$$

$$2\pi \sum_{m=0}^{2N-1} I^m(\tau, u') \cos[m(\phi_0 - \phi)]. \tag{O.5}$$

Therefore Eq. O.4 reduces to

$$\frac{\varpi}{4\pi} \int_0^{2\pi} d\phi' \int_{-1}^1 du' p(u', \phi'; u, \phi) I(\tau, u', \phi') =$$

$$\sum_{m=0}^{2N-1} \left\{ \frac{\varpi}{2} \int_{-1}^1 du' p^m(u', u) I^m(\tau, u') \right\} \cos[m(\phi_0 - \phi)] \tag{O.6}$$

where

$$p^m(u', u) = \sum_{l=m}^{2N-1} (2l + 1) \chi_l \Lambda_l^m(u) \Lambda_l^m(u'). \tag{O.7}$$

It is now clear that substitution of Eq. O.2 and O.3 into Eq. O.1 yields the desired result given in Chapter 6, i.e. Eqs. 6.33–6.34.

O.1 Treatment of the Lower Boundary Condition

Since we are dealing with reflection it is natural to use half-range quantities here. The diffuse reflectance at the lower boundary, $\tau = \tau^*$, is written as

(see §6.7.4)

$$I^+(\tau^*, \mu, \phi) = \epsilon(\mu)B(T_s) + \frac{\mu_0 F^s}{\pi}\rho_d(-\mu_0, \phi_0; \mu, \phi)e^{-\tau^*/\mu_0}$$

$$+ \frac{1}{\pi}\int_0^{2\pi} d\phi' \int_{-1}^1 d\mu'\mu'\rho_d(-\mu', \phi'; \mu, \phi)I^-(\tau^*, \mu', \phi')$$

$$(O.8)$$

where ρ_d is the bidirectional reflectance and ϵ is the emittance. First we note that only the $m = 0$ component of the radiance contributes to irradiances, since

$$F^{\pm} = \int_0^{2\pi} d\phi \int_0^1 d\mu\mu I^{\pm}(\tau, \mu, \phi)$$

$$= \int_0^{2\pi} d\phi \int_0^1 d\mu\mu \sum_{m=0}^{2N-1} I^{m\pm}(\tau, \mu)\cos[m(\phi - \phi_0)]$$

$$= 2\pi \int_0^1 d\mu\mu I^{0\pm}(\tau, \mu). \qquad (O.9)$$

Next we note that Kirchhoff's law states

$$\epsilon(\mu) + \frac{1}{\pi}\int_0^{2\pi} d\phi' \int_0^1 d\mu'\mu'\rho_d(-\mu', \phi'; \mu, \phi) = 1 \qquad (O.10)$$

suggesting that we should use Eq. O.10 to compute the emittance from the reflectance for consistency. Below we shall start by looking at the simple case of a Lambert reflector before we consider the more general case.

O.2 Lambertian Surface

A Lambert reflector is defined such that the reflected radiation is isotropic regardless of the directional dependence of the incident radiation. This implies that the bidirectional reflectance is independent of direction, i. e., $\rho_d(-\mu', \phi'; \mu, \phi) = \rho_L = $ constant. Now, integrating the left side of Eq. O.8, we find that the reflected irradiance becomes

$$F^+(\tau^*) = \int_0^{2\pi} d\phi \int_0^1 d\mu\mu I^+(\tau^*, \mu, \phi) = \pi I^{0+}(\tau^*) \qquad (O.11)$$

since the reflected radiation is isotropic. Integration of the first term on the right side yields $\pi\epsilon B(T_s)$, where we have used Kirchhoff's law yielding $\epsilon(\mu) + \rho_L = 1$, which implies $\epsilon = $ constant (independent of μ) in this special

case. The second term yields $\rho_L \mu_0 F^s e^{-\tau^*/\mu_0}$, and the third term becomes

$$\int_0^{2\pi} d\phi \int_0^1 \mu d\mu \left[\frac{\rho_L}{\pi} \int_0^{2\pi} d\phi' \int_0^1 d\mu' \mu' I^-(\tau^*, \mu', \phi') \right] =$$
$$2\pi \rho_L \int_0^1 d\mu' \mu' I^{0-}(\tau^*, \mu') \qquad (O.12)$$

where $I^{0-}(\tau^*, \mu') = \frac{1}{2\pi} \int_0^{2\pi} I^-(\tau^*, \mu', \phi) d\phi$ is the azimuthally-averaged downward radiance (or the $m = 0$ azimuthal component since we have expressed the radiance in a Fourier cosine series). Thus, for a Lambert reflector we have the following simple boundary condition relating the radiance reflected by the surface to the downward radiance there

$$I^{0+}(\tau^*) = \epsilon B(T_s) + \frac{\mu_0}{\pi} F^s \rho_L e^{-\tau^*/\mu_0} + 2\rho_L \int_0^1 d\mu' \mu' I^{0-}(\tau^*, \mu'). \qquad (O.13)$$

O.3 Non-Lambertian Surface

We shall assume that the bidirectional reflectance is azimuthally-symmetric so that we may expand it in a Fourier cosine series as

$$\rho_d(-\mu', \phi'; \mu, \phi) = \sum_{m=0}^{2N-1} \rho_d^m(-\mu', \mu) \cos[m(\phi' - \phi)]. \qquad (O.14)$$

In this more general case we find that the third term on the right side of Eq. O.8 becomes

$$\frac{1}{\pi} \int_0^{2\pi} d\phi' \int_{-1}^1 d\mu' \mu' \rho_d(-\mu', \phi'; \mu, \phi) I^-(\tau^*, \mu', \phi') =$$
$$\frac{1}{\pi} \int_0^{2\pi} d\phi' \int_{-1}^1 d\mu' \mu' \left\{ \sum_{m=0}^{2N-1} \rho_d^m(-\mu', \mu) \cos[m(\phi' - \phi)] \right.$$
$$\left. \cdot \sum_{r=0}^{2N-1} I^{r-}(\tau^*, \mu') \cos[r(\phi_0 - \phi')] \right\}. \qquad (O.15)$$

Since

$$\sum_{m=0}^{2N-1} \int_0^{2\pi} d\phi' \sum_{r=0}^{2N-1} I^{r-}(\tau^*, \mu') \cos[m(\phi' - \phi)] \cos[r(\phi_0 - \phi')] =$$
$$\pi(1 + \delta_{0m}) \sum_{m=0}^{2N-1} I^{m-}(\tau^*, \mu') \cos[m(\phi_0 - \phi)] \qquad (O.16)$$

we find

$$\frac{1}{\pi} \int_0^{2\pi} d\phi' \int_{-1}^1 d\mu' \mu' \rho_{\mathrm{d}}(-\mu', \phi'; \mu, \phi) I^-(\tau^*, \mu', \phi') =$$

$$\sum_{m=0}^{2N-1} \left\{ 2 \int_0^1 d\mu' \mu' \rho_{\mathrm{d}}^m(-\mu', \mu) I^{m-}(\tau^*, \mu') \right\} \cos[m(\phi_0 - \phi)].$$

$$(\mathrm{O}.17)$$

Finally, substitution of Eqs. O.3 and O.17 into Eq. O.8 yields

$$\sum_{m=0}^{2N-1} \left\{ I^{m+}(\tau^*, \mu) - \epsilon(\mu) B(T_{\mathrm{s}}) \delta_{0m} - \frac{1}{\pi} F^{\mathrm{s}} \rho_{\mathrm{d}}^m(-\mu_0, \mu) e^{-\tau^*/\mu_0} - \right.$$

$$\left. (1 + \delta_{0m}) \int_0^1 d\mu' \mu' \rho_{\mathrm{d}}^m(-\mu', \mu) I^{m-}(\tau^*, \mu') \right\} \cos[m(\phi_0 - \phi)] = 0. \ (\mathrm{O}.18)$$

Thus, we see that each Fourier component of the radiance must satisfy the boundary condition

$$I^{m+}(\tau^*, \mu) = \epsilon(\mu) B(T_{\mathrm{s}}) \delta_{0m} + \frac{1}{\pi} F^{\mathrm{s}} \rho_{\mathrm{d}}^m(-\mu_0, \mu) e^{-\tau^*/\mu_0}$$

$$+ (1 + \delta_{0m}) \int_0^1 d\mu' \mu' \rho_{\mathrm{d}}^m(-\mu', \mu) I^{m-}(\tau^*, \mu'). \quad (\mathrm{O}.19)$$

We note that for $m = 0$ and $\rho_{\mathrm{d}} = \text{constant} = \rho_{\mathrm{L}}$ we retain the azimuthally-independent case pertinent for a Lambertian surface considered above as we should.

Appendix P

Scaling Transformation for Anisotropic Scattering

We will show that the transfer equation is invariant under certain scale changes of the optical depth and the phase function. The so-called δ-M method, discussed in Chapter 6, turns out to be one such invariant scaling transformation.

We start with the general radiative transfer equation (Eq. 5.45) for the total radiance which in slab geometry may be written

$$u\frac{dI(\tau,\hat{\Omega})}{d\tau} = I(\tau,\hat{\Omega}) - \frac{\varpi}{4\pi}\int_{4\pi} d\omega' \, p(\hat{\Omega}',\hat{\Omega})I(\tau,\hat{\Omega}') \qquad (\text{P.1})$$

where we have ignored the thermal emission term. If we define a kernel

$$G(\hat{\Omega}',\hat{\Omega}) \equiv \frac{1}{4\pi}[-\varpi p(\cos\Theta) + 4\pi\delta(\hat{\Omega}' - \hat{\Omega})] \qquad (\text{P.2})$$

then we may rewrite Eq. P.1 as

$$u\frac{dI(\tau,\hat{\Omega})}{d\tau} = \int_{4\pi} G(\hat{\Omega}',\hat{\Omega})I(\tau,\hat{\Omega}')d\omega'. \qquad (\text{P.3})$$

Now, by introducing a new optical depth, $\hat{\tau}$, and a new kernel, $\hat{G}$, through

$$\tau = \beta\hat{\tau} \qquad (\text{P.4})$$
$$G = \beta^{-1}\hat{G} \qquad (\text{P.5})$$

we find that Eq. P.3 becomes

$$u\frac{dI(\hat{\tau},\hat{\Omega})}{d\hat{\tau}} = \int_{4\pi} \hat{G}(\hat{\Omega}',\hat{\Omega})I(\hat{\tau},\hat{\Omega}')d\omega' \qquad (\text{P.6})$$

In view of the definition of G (Eq. P.2) we may rewrite Eq. P.6 as

$$u\frac{dI(\hat{\tau},\hat{\Omega})}{d\hat{\tau}} = I(\hat{\tau},\hat{\Omega}) - \frac{\hat{\varpi}}{4\pi}\int_{4\pi} \hat{p}(\hat{\Omega}',\hat{\Omega})I(\tau,\hat{\Omega}')d\omega' \qquad (\text{P.7})$$

where

$$\hat{G}(\hat{\Omega}', \hat{\Omega}) = \frac{1}{4\pi}[-\hat{\varpi}\hat{p}(\cos\Theta) + 4\pi\delta(\hat{\Omega}' - \hat{\Omega})] = \beta G(\hat{\Omega}', \hat{\Omega})$$

$$= \frac{1}{4\pi}[-\beta a p(\cos\Theta) + 4\pi\beta\delta(\hat{\Omega}' - \hat{\Omega})] \qquad (P.8)$$

which implies

$$\hat{\varpi}\hat{p}(\cos\Theta) = [\beta\varpi p(\cos\Theta) + 4\pi(1 - \beta)\delta(\hat{\Omega}' - \hat{\Omega})]. \qquad (P.9)$$

If we now require the scaled phase function to be normalized to unity as usual, then integration of Eq. P.9 over 4π steradians yields

$$\hat{\varpi} = \varpi\beta + (1 - \beta) \qquad (P.10)$$

or

$$1 - \hat{\varpi} = \beta(1 - \varpi). \qquad (P.11)$$

This last equation implies that if $\varpi = 1$, then $\hat{\varpi} = 1$, *i. e.* conservative scattering remains conservative under the scaling transformation.

Since expansion of the scattering phase function in Legendre polynomials has been shown to be an extremely useful way of "isolating" the azimuth dependence in slab geometry, we proceed by expanding both scattering phase functions in this manner

$$p(\cos\Theta) = \sum_{n=0}^{\infty}(2n + 1)\chi_n P_n(\cos\Theta) \qquad (P.12)$$

$$\hat{p}(\cos\Theta) = \sum_{n=0}^{\infty}(2n + 1)\hat{\chi}_n P_n(\cos\Theta) \qquad (P.13)$$

where $P_n(\cos\Theta)$ is the Legendre polynomial, and the expansion coefficients are defined by Eq. 6.22. The δ-function may also be expanded in Legendre polynomials, i.e.

$$4\pi\delta(\hat{\Omega}' - \hat{\Omega}) = 4\pi\delta(\mu' - \mu)\delta(\phi' - \phi) = 2\delta(1 - \cos\Theta) = \sum_{n=0}^{\infty}(2n + 1)P_n(\cos\Theta).$$
$$(P.14)$$

We note that the expansion coefficients in this case are all unity. Substitution of Eqs. P.12 and P.14 into Eq. P.6 yields

$$\sum_{n=0}^{\infty}[\hat{a}\hat{\chi}_n - \beta a\chi_n - (1 - \beta)](2n + 1)P_n(\cos\Theta) = 0 \qquad (P.15)$$

which implies

$$\hat{a}\hat{\chi}_n = \beta a \chi_n + (1 - \beta) \tag{P.16}$$

or

$$1 - \hat{\varpi}\hat{\chi}_n = \beta(1 - \varpi\chi_n) \tag{P.17}$$

or

$$\hat{\tau}\hat{\varpi}(1 - \hat{\chi}_n) = \tau\varpi(1 - \chi_n) \tag{P.18}$$

where we have used Eqs. P.3 and P.9 in the last step. Since $\chi_0 = 1$ Eqs. P.16 and P.10 imply $\hat{\varpi}\hat{\chi}_0 = \beta\varpi + 1 - \beta = \hat{\varpi}$ or $\hat{\chi}_0 = 1$. This shows that the expanded *scaled* phase function is correctly normalized as implied by Eq. P.10.

Finally, by defining $h_n = (2n+1)(1 - \varpi\chi_n)$ and using Eq. P.17, we obtain

$$\hat{h}_n = (2n + 1)(1 - \hat{\varpi}\hat{\chi}_n) = \beta h_n = (\tau/\hat{\tau})h_n \tag{P.19}$$

or

$$\hat{\tau}\hat{h}_n = \tau h_n. \tag{P.20}$$

The radiative transfer equation is invariant under scale changes of the optical depth and phase function which leave invariant the parameter

$$\eta_n \equiv h_n\tau = (2n + 1)(1 - \varpi\chi_n)\tau. \tag{P.21}$$

It is clear that $\beta = 1 - \varpi f$ in the δ-M method.

Appendix Q

Reciprocity, Duality, and Effects of Surface Reflection

The purpose of this Appendix is to provide some details that were omitted in §6.8 regarding the relationship between the reflection and transmission for *unidirectional* (parallel beam or 'solar') and *uniform* (isotropic over the downward hemisphere) illumination of an inhomogeneous slab. The reflectance and transmittance for unidirectional illumination of a slab will be shown to be equivalent to the angular distribution of the azimuthally-averaged reflected and transmitted radiances, respectively, pertaining to uniform illumination of the slab with unit incident radiance. For an *inhomogeneous* slab the transmittance for unidirectional illumination from one side (e.g. the *top*) is equivalent to the angular distribution of the radiance pertaining to illumination from the other side (the *bottom*) of the slab. We will then derive an analytic expression for the radiance reflected from a Lambert surface underlying an inhomogeneeous slab, which in turn is required to derive simple analytic expressions for the reflectance and transmittance of an inhomogeneous slab overlying a partially reflecting surface in terms of the solution pertaining to the same slab overlying a *black* surface.

Q.1 Principle of Reciprocity

If the angular scattering depends only on the scattering angle, i.e. the angle between the direction of incidence and the direction in which the photon is scattered, then the phase function may be written

$$p(\Theta) = p(\cos\Theta) = p[uu' + (1-u^2)^{\frac{1}{2}}(1-u'^2)^{\frac{1}{2}}\cos(\phi-\phi')] \qquad (Q.1)$$

where we have used Eq. 3.22. We see that the phase function satisfies the following relations

$$p(\mu,\phi;\mu',\phi') = p(\mu',\phi';\mu,\phi) \qquad (Q.2)$$

$$p(-\mu, \phi; -\mu', \phi') = p(\mu', \phi'; \mu, \phi) \tag{Q.3}$$

$$p(\mu, \phi; -\mu', \phi') = p(-\mu', \phi'; \mu, \phi) = p(\mu', \phi'; -\mu, \phi). \tag{Q.4}$$

The above relations are usually referred to as Helmholtz' reciprocity principle. They are a consequence of time reversal invariance and they apply to a single scattering event.

Q.2   Homogeneous Slab

For a slab of finite thickness multiple scattering cannot, in general, be neglected. Therefore we do not expect reciprocity to be directly applicable. What is important here is, however, that the above reciprocity relations imply the following reciprocity rules for the reflectance and transmittance of a homogeneous slab of arbitrary (but finite) thickness τ^*

$$\rho(\tau^*; \mu, \phi; \mu_0, \phi_0) = \rho(\tau^*; \mu_0, \phi_0; \mu, \phi) \tag{Q.5}$$

$$\mathcal{T}(\tau^*; \mu, \phi; \mu_0, \phi_0) = \mathcal{T}(\tau^*; \mu_0, \phi_0; \mu, \phi). \tag{Q.6}$$

The radiation reflected and transmitted by the slab may be expressed as

$$I^+(0, \mu, \mu_0, \phi) = \mu_0 F^{\mathrm{s}} \rho(\tau^*; \mu, \phi; \mu_0, \phi_0) \tag{Q.7}$$

$$I^-(\tau^*, \mu, \mu_0, \phi) = \mu_0 F^{\mathrm{s}} \mathcal{T}(\tau^*; \mu, \phi; \mu_0, \phi_0) \tag{Q.8}$$

where $\mu_0 F^{\mathrm{s}}$ is the (vertical) irradiance of the incident 'solar' radiation. Averaging over azimuth, we obtain

$$I^+(0, \mu, \mu_0) = \mu_0 F^{\mathrm{s}} \rho(\tau^*; \mu; \mu_0) \tag{Q.9}$$

$$I^-(\tau^*, \mu, \mu_0) = \mu_0 F^{\mathrm{s}} \mathcal{T}(\tau^*; \mu; \mu_0) \tag{Q.10}$$

where

$$\rho(\tau^*; \mu, \mu_0) = \frac{1}{2\pi} \int_0^{2\pi} d\phi \rho(\tau^*; \mu, \phi; \mu_0, \phi_0) \tag{Q.11}$$

$$\mathcal{T}(\tau^*; \mu, \mu_0) = \frac{1}{2\pi} \int_0^{2\pi} d\phi \mathcal{T}(\tau^*; \mu, \phi; \mu_0, \phi_0). \tag{Q.12}$$

Q.3 Collimated incidence:

The reflectance and transmittance for collimated beam ('solar') incidence is obtained by integration

$$\rho_{\mathrm{b}}(\tau^*, \mu_0) = \frac{2\pi}{\mu_0 F^{\mathrm{s}}} \int_0^1 d\mu \mu I^+(0, \mu, \mu_0) \mu d\mu = 2\pi \int_0^1 d\mu \mu \rho(\tau^*, \mu, \mu_0) \quad \text{(Q.13)}$$

$$\mathcal{T}_{\mathrm{b}}(\tau^*, \mu_0) = \frac{2\pi}{\mu_0 F^{\mathrm{s}}} \int_0^1 d\mu \mu I^-(\tau^*, \mu, \mu_0) = 2\pi \int_0^1 d\mu \mu \mathcal{T}(\tau^*, \mu, \mu_0). \quad \text{(Q.14)}$$

Another integration yields the spherical albedo and transmittance

$$\bar{\rho}_{\mathrm{b}}(\tau^*) = 2 \int_0^1 d\mu_0 \mu_0 \rho(\tau^*, \mu_0) = 4\pi \int_0^1 d\mu \mu \int_0^1 d\mu_0 \rho(\tau^*, \mu, \mu_0) \quad \text{(Q.15)}$$

$$\bar{\mathcal{T}}_{\mathrm{b}}(\tau^*) = 2 \int_0^1 d\mu_0 \mu_0 \rho(\tau^*, \mu_0) = 4\pi \int_0^1 d\mu \mu \int_0^1 d\mu_0 \mathcal{T}(\tau^*, \mu, \mu_0). \quad \text{(Q.16)}$$

The subscript 'b' is used to remind us that the illumination is collimated.

Q.4   Uniform incidence

The emergent angular distribution of the reflected and transmitted radiances for *uniform* illumination with unit incident radiance, and hence irradiance $F_{\mathrm{uni}}(\tau = 0) = \pi$, are

$$I^+_{\mathrm{uni}}(0, \mu) = 2\pi \int_0^1 d\mu_0 I^+(0, \mu, \mu_0) = 2\pi \int_0^1 d\mu_0 \mu_0 \rho(\tau^*, \mu, \mu_0) \quad \text{(Q.17)}$$

$$I^-_{\mathrm{uni}}(\tau^*, \mu) = 2\pi \int_0^1 d\mu_0 I^-(\tau^*, \mu, \mu_0) = 2\pi \int_0^1 d\mu_0 \mu_0 \mathcal{T}(\tau^*, \mu, \mu_0). \quad \text{(Q.18)}$$

The plane albedo and transmittance are given by

$$\frac{F^+_{\mathrm{uni}}(0)}{\pi} = 2 \int_0^1 d\mu \mu I^+(0, \mu) = 4\pi \int_0^1 d\mu \mu \int_0^1 d\mu_0 \rho(\tau^*, \mu, \mu_0) \quad \text{(Q.19)}$$

$$\frac{F^-_{\mathrm{uni}}(\tau^*)}{\pi} = 2 \int_0^1 d\mu \mu I^-(\tau^*, \mu) = 4\pi \int_0^1 d\mu \mu \int_0^1 d\mu_0 \mathcal{T}(\tau^*, \mu, \mu_0). \quad \text{(Q.20)}$$

The subscript 'uni' is used to remind us that the illumination is uniform.

Q.5 Duality:

Since $\rho(\tau^*; \mu, \mu_0) = \rho(\tau^*; \mu_0, \mu)$ and $\mathcal{T}(\tau^*; \mu, \mu_0) = \mathcal{T}(\tau^*; \mu_0, \mu)$, the duality relations given in §6.8 follow by comparing the above expressions for collimated and uniform incidence.

Q.6 Inhomogeneous Slab

The expressions given above pertaining to a homogeneous slab will now be generalized to apply to a vertically inhomogeneous slab. We must distinguish between illumination from the top and the bottom. Thus, considering first illumination from the *top* we find that the same expressions as before (given by Eqs. Q.13–Q.16 and Eqs. Q.17–Q.20 above) apply for unidirectional and uniform illumination, respectively. However, for *unidirectional* and *uniform* illumination from the *bottom* we obtain the following expressions

$$\tilde{\rho}_{\mathrm{b}}(\tau^*, \mu_0) = 2\pi \int_0^1 d\mu\mu\tilde{\rho}(\tau^*, \mu, \mu_0);$$

$$\tilde{I}^-_{\mathrm{uni}}(\tau^*, \mu) = 2\pi \int_0^1 d\mu_0\mu_0\tilde{\rho}(\tau^*, \mu, \mu_0), \tag{Q.21}$$

$$\tilde{\mathcal{T}}_{\mathrm{b}}(\tau^*, \mu_0) = 2\pi \int_0^1 d\mu\mu\tilde{\mathcal{T}}(\tau^*, \mu, \mu_0);$$

$$\tilde{I}^+_{\mathrm{uni}}(0, \mu) = 2\pi \int_0^1 d\mu_0\mu_0\tilde{\mathcal{T}}(\tau^*, \mu, \mu_0), \tag{Q.22}$$

$$\tilde{\tilde{\rho}}_{\mathrm{b}}(\tau^*) = 4\pi \int_0^1 d\mu\mu \int_0^1 d\mu_0\tilde{\rho}(\tau^*, \mu, \mu_0);$$

$$\frac{\tilde{F}^-_{\mathrm{uni}}(\tau^*)}{\pi} = 4\pi \int_0^1 d\mu\mu \int_0^1 d\mu_0\tilde{\rho}(\tau^*, \mu, \mu_0) \tag{Q.23}$$

$$\tilde{\tilde{\mathcal{T}}}_{b}(\tau^*) = 4\pi \int_0^1 d\mu\mu \int_0^1 d\mu_0\tilde{\mathcal{T}}(\tau^*, \mu, \mu_0);$$

$$\frac{\tilde{F}^+_{\mathrm{uni}}(0)}{\pi} = 4\pi \int_0^1 d\mu\mu \int_0^1 d\mu_0\tilde{\mathcal{T}}(\tau^*, \mu, \mu_0). \tag{Q.24}$$

Q.7 Reciprocity and Duality:

As noted in §6.8 for an inhomogeneous slab the reflectance and transmittance satisfy the following reciprocity relations

$$
\begin{aligned}
\rho(\tau^*, \mu, \mu_0) &= \rho(\tau^*, \mu_0, \mu); \\
\tilde{\rho}(\tau^*, \mu, \mu_0) &= \tilde{\rho}(\tau^*, \mu_0, \mu); \\
\mathcal{T}(\tau^*, \mu, \mu_0) &= \tilde{\mathcal{T}}(\tau^*, \mu_0, \mu).
\end{aligned}
\tag{Q.25}
$$

A crucial difference between the homogeneous and the *in*homogeneous slab is the reciprocity relating the transmittance due to illumination from one side to the illumination from the other side. Of course, for a homogeneous slab it makes no difference to which side we apply the illumination.

By comparing the expressions pertinent for collimated and uniform incidence and using these reciprocity relations we find that it is now a simple matter to generalize the duality relations for a homogeneous slab to obtain the expressions valid for an inhomogeneous slab provided in §6.8.

Q.8 Derivation of the Reflected radiance Component I_r

In §6.9 we derived simple analytic expressions for the radiation reflected and transmitted by a slab overlying a partially reflecting (Lambert) surface in terms of the reflected radiance reflected at the lower boundary, I_r. In fact, the quantity

$$
\frac{I_\mathrm{r}}{\mu_0 F^\mathrm{s}} = \frac{\rho_\mathrm{L} \mathcal{T}(\mu_0; 2\pi)}{\pi(1 - \tilde{\bar{\rho}} \rho_\mathrm{L})} = \frac{\rho_\mathrm{L} \mathcal{T}(-\hat{\Omega}_0, -2\pi)}{\pi[1 - \tilde{\bar{\rho}} \rho_\mathrm{L}]}
$$

appears in Eqs. 6.75 and 6.76 for the bidirectional reflectance and transmittance of a slab overlying a Lambertian surface. Below we derive an expression for I_r in terms of the reflectance and transmittance pertinent to an inhomogeneous slab overlying a black (i.e *non-reflecting* surface).

In general, the radiance reflected at the lower boundary, $I^+(\tau^*, \mu, \phi)$, is related to the incident radiance, $I^-(\tau^*, \mu, \phi)$, through

$$
I^+(\tau^*, \mu, \phi) = \int_0^{2\pi} d\phi' \int_0^1 d\mu' \mu' \rho(-\mu', \phi'; \mu, \phi) I^-(\tau^*; \mu', \phi')
\tag{Q.26}
$$

or by averaging over azimuth

$$
I^+(\tau^*, \mu) = 2\pi \int_0^1 d\mu' \mu' \rho(-\mu', \mu) I^-(\tau^*, \mu') \equiv I_\mathrm{r}
\tag{Q.27}
$$

where $\rho(-\mu', \phi'; \mu, \phi)$ is the bidirectional reflectance of the surface, and

$\rho(-\mu', \mu)$ its azimuthal mean. Here I_r is a constant because we are dealing with a Lambert surface for which $\rho(-\mu', \mu) = \rho_L = $ constant.

Next we consider the total reflected radiance $I_{tot}^+(0; \mu, \phi)$, which consists of three separate components: (a) the contribution from the atmosphere assuming a non-reflecting or black lower boundary ($\rho = 0$); (b) the diffusely-transmitted component arising from I_r (see Eq. 5.34); and (c) the directly-transmitted component arising from I_r. In mathematical terms, we write

$$I_{tot}^+(0; \mu, \phi) = I^+(0; \mu, \phi; \rho = 0) + \int_0^{2\pi} d\phi' \int_0^1 d\mu' \mu' \tilde{\mathcal{T}}_d(\mu', \phi'; \mu, \phi) I_r + I_r e^{-\tau^*/\mu} \tag{Q.28}$$

since we have assumed that the reflected radiance is azimuth-independent and given by Eq. Q.27. Removing I_r from the integral (it is independent of angle), we combine terms (b) and (c), to obtain the total transmittance

$$I_r \left[e^{-\tau^*/\mu} + \int_0^{2\pi} d\phi' \int_0^1 d\mu' \mu' \tilde{\mathcal{T}}_d(\mu'; \mu) \right]. \tag{Q.29}$$

The second term is recognized as the diffuse part of the *hemispherical-directional transmittance* $\tilde{\mathcal{T}}_d(2\pi; \mu)$ pertaining to radiation incident from below. We note the absence of azimuthal dependence. Reciprocity applies also to the *diffuse transmittance*

$$\tilde{\mathcal{T}}_d(2\pi; \mu) = \tilde{\mathcal{T}}_d(\mu; 2\pi). \tag{Q.30}$$

In words, the *hemispherical-directional transmittance* is also the *directional-hemispherical transmittance*. Therefore

$$I_{tot}^+(0; \mu, \phi) = I^+(0; \mu, \phi; \rho = 0) + I_r \tilde{\mathcal{T}}(\mu; 2\pi) \tag{Q.31}$$

where $\tilde{\mathcal{T}}(\mu; 2\pi) = e^{-\tau^*/\mu} + \tilde{\mathcal{T}}_d(\mu; 2\pi)$, or the total transmittance is the sum of the beam and diffuse transmittances. We note that the remaining ϕ-dependence of the total radiance is due to the first term, and is traceable to a ϕ-dependence of the collimated beam illumination. The extra term in the above equation (arising from the boundary) is azimuthally independent by assumption (Lambert reflector).

The first term may be expressed in terms of the incident radiation field (assumed to be a collimated solar beam) and the atmospheric reflectance as $\mu_0 F^s \rho(-\mu_0, \phi_0; \mu, \phi)$. Therefore

$$I_{tot}^+(0; \mu, \phi) = \mu_0 F^s \rho(-\mu_0, \phi_0; \mu, \phi) + I_r \tilde{\mathcal{T}}(\mu; 2\pi). \tag{Q.32}$$

Proceeding in a similar manner we find that the transmitted radiance can be expressed as

$$I_{tot}^-(\tau^*; \mu, \phi) = \mu_0 F^s \mathcal{T}(-\mu_0, \phi_0; \mu, \phi) + I_r \tilde{\rho}(\mu; 2\pi). \tag{Q.33}$$

Here the first term is the diffusely transmitted radiance, while the second term stems from radiation reflected first from the surface and then from the atmosphere above.

It remains to determine I_r. Setting the reflected irradiance πI_r equal to a constant, ρ_L, times the downward irradiance at τ^*, we have

$$\pi I_r = \rho_L \left[\mu_0 F^s e^{-\tau^*/\mu_0} + \mu_0 F^s \mathcal{T}_d(\mu_0; 2\pi) + \pi I_r \tilde{\tilde{\rho}} \right]. \qquad (Q.34)$$

The first term on the left side is the directly-transmitted beam irradiance, the second term is the diffusely-transmitted component for a completely black surface, and the third term is the (downward) reflected component due to the upward reflection from the Lambert surface followed by downward reflection by the atmosphere. We recognize $\tilde{\tilde{\rho}}$ as the *spherical albedo* pertaining to illumination from below. Solving the above for I_r we obtain

$$I_r = \frac{\mu_0 F^s \rho_L \left[e^{-\tau^*/\mu_0} + \mathcal{T}_d(\mu_0; 2\pi) \right]}{\pi(1 - \tilde{\tilde{\rho}}\rho_L)} = \frac{\mu_0 F^s \rho_L \mathcal{T}(\mu_0; 2\pi)}{\pi(1 - \tilde{\tilde{\rho}}\rho_L)} \qquad (Q.35)$$

where we have once again combined the sum of the direct and diffuse transmittances into a total transmittance.

Appendix R

Probabilistic Aspects of Radiative Transfer

In this section we consider an alternate formulation of the radiative transfer process. This approach will focus on properties of the scattering medium, which are independent of the distribution of sources of radiation, either external or internal. The *point-direction gain* and the *escape probability* are the basic quantities of interest. These quantities incorporate all the basic scattering properties of the medium, through the single-scattering albedo and the phase function, plus the knowledge of the total optical depth. Through the point-direction gain, and its angular moments it is possible to solve problems differing in their sources of radiation. In the days before computers, this approach provided a considerable advantage, since in principle, these fundamental quantities could be calculated once and for all, and presented in tables for general use. This approach is no longer necessary, since computers make it a relatively simple matter to alter the boundary conditions or internal sources of radiation in the program code. However, these probabilistic concepts are still of great pedagogical interest. We will therefore discuss only the essential elements of the method.

We begin with a 'thought-experiment' which will illustrate the concept. We assume a slab geometry, and an isotropic scattering law. The medium may be inhomogeneous, so that the single-scattering albedo depends upon the optical depth. Consider an interior point at the optical depth τ' within the medium. Within the thin layer between τ' and $\tau' + d\tau'$, is contained an isotropic source of radiation, given by $Q(\tau')$, whose detailed specification will not concern us. Q will generally consist of the sum of a thermal source, $(1 - \varpi)B$ plus an imbedded source of first-order scattered photons, S^*. (We will continue to suppress the frequency subscript.) The emergent photons will execute a variety of scattering trajectories, depending upon the specific emission direction, and upon the random nature of the angular scattering process.
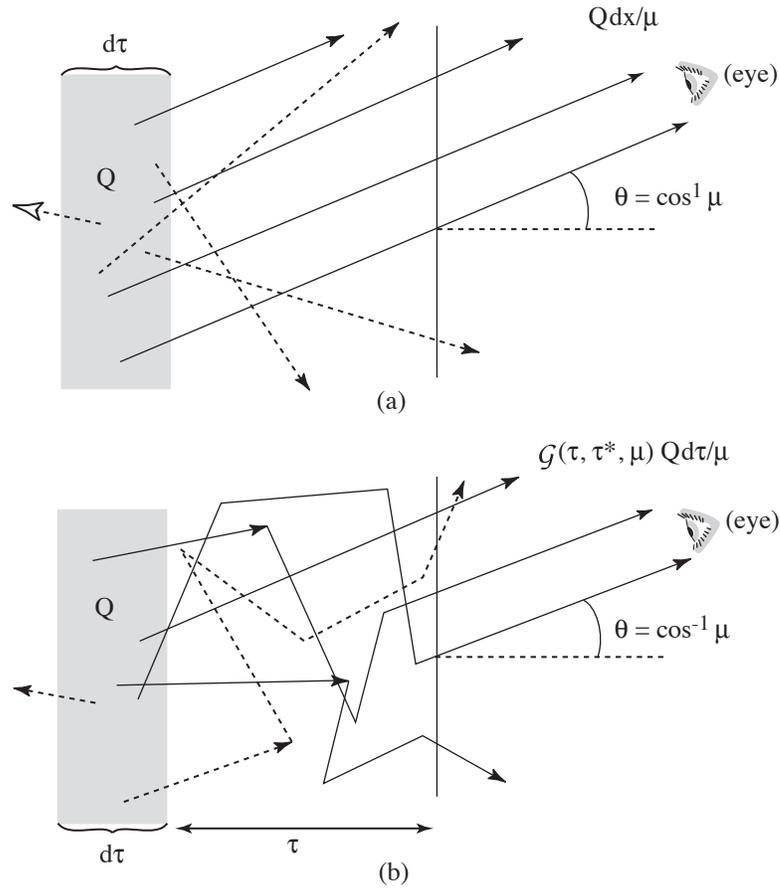
Figure R.1 Illustration of the Point direction Gain concept. (a) Without an interacting medium, the radiance emitted by the region within the thin layer of thickness $d\tau$, in direction $\cos^{-1}\mu$, is given by $Q\frac{d\tau}{\mu}$. (b) When the thin layer is imbedded in an absorbing/scattering medium, the radiance emitted in the same direction is $\mathcal{G}Q\frac{d\tau}{\mu}$, where $\mathcal{G}$ is the point-direction gain.

We are interested in those photons which eventually reach the surface ($\tau = 0$), and which leave the medium in the direction given by μ. (There is no dependence on the azimuthal angle ϕ, because of the assumption of an isotropic source, and an isotropic phase function.) The differential contribution to the emergent radiance due to this thin layer may be written

$$dI^+(0,\mu) \equiv \mathcal{G}(\tau',\mu;\varpi,\tau^*)Q(\tau')\frac{d\tau'}{\mu}$$

where $\mathcal{G}$ is the (dimensionless) *point-direction gain*. To understand the mean-

ing of this quantity, consider the contribution to the emergent radiance from the same source *in the absence of a medium.* This is just

$$dI^+(0, \mu) = Q(\tau') \frac{d\tau'}{\mu} \qquad (\mathcal{G} = 1).$$

The presence of the term $d\tau'/\mu$ is explained by the fact that the column of emitting material is in the direction μ. The change in the radiation field, $\mathcal{G}$, is a result of the intervening medium. We may now write down an expression for the emergent radiance from the entire medium, which is just a linear sum over all layers (an integral in the limit of very small layer thicknesses):

$$I^+(0, \mu) = \int_0^{\tau^*} \frac{d\tau'}{\mu} \mathcal{G}(\tau', \mu; \varpi, \tau^*) Q(\tau'). \tag{R.1}$$

The radiance emerging from the bottom of the medium (assuming no reflection from the boundary) is given by

$$I^-(\tau^*, \mu) = \int_0^{\tau^*} \frac{d\tau'}{\mu} \tilde{\mathcal{G}}(\tau^* - \tau', \mu; \varpi, \tau^*) Q(\tau'). \tag{R.2}$$

For an inhomogeneous medium, the point-direction gain is different for downward emitted radiation than for upward radiation, hence the different symbol, $\tilde{\mathcal{G}}$. For a homogeneous medium, $\tilde{\mathcal{G}} = \mathcal{G}$.

The above experiment is called *direct*, in that we seek the external radiation field derived from a certain internal source. We now consider the *inverse* experiment, that is, we are given an external radiation field, $I^-(0, \mu)$ and we seek to determine the internal source function. We assume that no thermal sources of radiation are present, and we *postulate* that the source function arising from this incident radiation field is given by

$$S(\tau) = \frac{\varpi}{4\pi} \int_0^{2\pi} d\phi \int_0^1 d\mu \mathcal{G}(\tau, \mu; \varpi, \tau^*) I^-(0, \mu, \phi).$$

In the particular case of an incident collimated beam

$$I^-(0, \mu, \phi) = F^s \delta(\mu - \mu_0) \delta(\phi - \phi_0)$$

the source function is

$$S_3(\tau) = \frac{\varpi}{4\pi} F^s \mathcal{G}(\tau, \mu_0; \varpi, \tau^*) \tag{R.3}$$

where the subscript 3 refers to *Prototype Problem 3* (i.e. collimated incidence). Since S_3 satisfies the Milne-Schwarzschild equation (Eq. 6.80)

$$S_3(\tau) = \frac{\varpi}{4\pi} F^s e^{-\tau/\mu_0} + \frac{\varpi}{2} \int_0^{\tau^*} d\tau' E_1(|\tau - \tau'|) S_3(\tau')$$

then $\mathcal{G}$ satisfies the following equation

$$\mathcal{G}(\tau, \mu_0; \varpi, \tau^*) = e^{-\tau/\mu_0} + \frac{\varpi}{2} \int_0^{\tau^*} d\tau' E_1(|\tau - \tau'|)\mathcal{G}(\tau', \mu_0; \varpi, \tau^*). \quad \text{(R.4)}$$

We now return to the direct experiment, and assume that the internal source is just $Q = S^* = [\varpi/4\pi]F^s e^{-\tau/\mu_0}$, that is, it is provided by an external collimated beam with irradiance F^s. From Eq. R.1, the emergent radiance from this source is

$$I^+(0, \mu) = F^s \int_0^{\tau^*} \frac{d\tau'}{\mu} \frac{\varpi}{4\pi} \mathcal{G}(\tau', \mu; \varpi, \tau^*) e^{-\tau'/\mu_0}.$$

We set the angle $\mu = \mu_0$, so that

$$I^+(0, \mu_0) = F^s \int_0^{\tau^*} \frac{d\tau'}{\mu_0} \frac{\varpi}{4\pi} \mathcal{G}(\tau', \mu_0; \varpi, \tau^*) e^{-\tau'/\mu_0}$$

and use the relationship between radiance and the source function (where we set $S(\tau') = S_3(\tau')$)

$$I^+(0, \mu_0) = \int_0^{\tau^*} \frac{d\tau'}{\mu_0} e^{-\tau'/\mu_0} S_3(\tau').$$

The above two equations for $I^+(0, \mu_0)$ are valid for all μ_0 and τ^*, if and only if

$$S_3(\tau) = \frac{\varpi}{4\pi} F^s \mathcal{G}(\tau, \mu_0; \varpi, \tau^*) \qquad \text{(R.5)}$$

which is the same result as in the inverse experiment, Eq. R.3. It is another illustration of the *Principle of Duality*, discussed in §6.8.

Other relationships connecting $\mathcal{G}$ and its angular moments may be established with the classical functions of radiative transfer theory. It suffices to mention only one set of relationships to the X-, Y-, and H- functions, described by V. A. Ambartsumyan and S. Chandrasekhar. These functions have played a key role in the development of the classical theory of radiative transfer.[1] It may be shown that these functions are equal to the point direction gain evaluated at the upper and lower bounds of the medium (assumed homogeneous):

$$X(\mu; \varpi, \tau^*) \equiv \mathcal{G}(0, \mu; \varpi, \tau^*); \quad Y(\mu; \varpi, \tau^*) \equiv \mathcal{G}(\tau^*, \mu; \varpi, \tau^*) \qquad \text{(R.6)}$$

$$H(\mu; \varpi) \equiv \mathcal{G}(0, \mu; \varpi, \tau^* \to \infty). \qquad \text{(R.7)}$$

It should be apparent that knowledge of $\mathcal{G}$ allows one to solve entire classes

---

[1] See Chandrasekhar (1960). For a readable exposition of classical methods of the Russian school, see Sobolev (1963).

of radiative transfer problems. This is the case for the source function for an arbitrary incident radiance on either or both faces, and also for the emergent radiances for any arbitrary disposition of internal sources.

R.1 The Escape Probability

As discussed earlier, the quantity $(\varpi/4\pi)\mathcal{G}$ has a dual interpretation. In the inverse problem, it is the source function for the problem of an isotropically-scattering slab of optical depth τ^* illuminated by a collimated beam of radiation of irradiance unity (see Eq. R.5). For the direct problem, we can interpret it in terms of a *directional escape probability*. The formal relationship is

$$\mathcal{P}(\tau, \mu; \varpi, \tau^*) \equiv \frac{\varpi}{4\pi}\mathcal{G}(\tau, \mu; \varpi, \tau^*). \tag{R.8}$$

The quantity $\mathcal{P}d\omega$ is interpreted as the joint probability of two successive events: (1) first, $\varpi/4\pi$ is the probability per unit solid angle that a photon, having suffered an extinction event at τ, will emerge as a scattered photon; and (2) $\mathcal{G}d\omega$ is the probability that a photon will emerge from the upper surface of the medium in the direction μ within the solid angle $d\omega$. If we then integrate the product of these two probabilities over all emergent angles in the upper hemisphere, we obtain the *hemispherical escape probability*

$$\mathcal{P}(\tau; \varpi, \tau^*) \equiv \int_0^{2\pi} d\phi \int_0^1 d\mu \mathcal{P}(\tau, \mu; \varpi, \tau^*) = \frac{\varpi}{2} \int_0^1 d\mu \mathcal{G}(\tau, \mu; \varpi, \tau^*). \tag{R.9}$$

Here $\mathcal{P}(\tau; \varpi, \tau^*)$ is the probability of a photon emerging from the medium in *any* (upward) direction, and it is seen to be proportional to the zeroth-order moment of the point-direction gain. The escape probability for a homogeneous medium is proportional to the source function for *Prototype Problem 1* (uniform incidence). Suppose the medium is optically thin, so that $\mathcal{G} \approx e^{-\tau/\mu}$, from Eq. R.4. Then $\mathcal{P} \to P$ where

$$P(\tau; \varpi, \tau^*) \equiv \frac{\varpi}{2} \int_0^1 d\mu e^{-\tau/\mu} = \frac{\varpi}{2} E_2(\tau) = S_1(\tau) \tag{R.10}$$

where $S_1(\tau)$ is the source function for *Prototype Problem 1*. The above quantity, the *single-flight escape probability*, is given a special symbol because of its importance. It describes the probability of direct escape of all photons emerging at that point either from thermal emission or from a scattering. It is clear that those photons which have been scattered one or more times are counted in the general escape probability $\mathcal{P}$. Note that the single-flight escape probability out the *bottom* of the medium is $P(\tau^* - \tau)$.

Appendix S

Details and Derivations

S.1 Chapter 4 - Details and Derivations

S.1.1 §4.5 – Absorption in Molecular Lines and Bands

We are concerned with molecular absorption by solar near-IR (1 to 3 μm) and thermal IR radiation which occupies the spectrum from about 3 to 100 μm. We shall refer to this entire range, 1 to 100 μm ($100 - 10,000$ cm^{-1}), generically as the IR spectral range. The molecular excited states of interest are those of vibration ($500 - 10,000$ cm^{-1}) and rotation ($1 - 500$ cm^{-1}). This range of energies contrasts with that of the higher-lying electronic states ($10,000 - 100,000$ cm^{-1}) which interact primarily with visible and ultraviolet radiation. To a first approximation the internal excitation energy is the sum of these three types of energies, electronic (E_e), vibrational (E_v), and rotational (E_r). We shall also be concerned with the kinetic energy of the molecules, since it plays an important indirect role in determining the populations of the various absorbing states.

Mastery of the subject of IR spectroscopy demands a thorough familiarity with quantum mechanics, a subject which is beyond the scope of this book. Our approach is to consider only a few of the simpler ideas underlying the physics of vibrational and rotational spectra. Fortunately an understanding of the radiative transfer process itself does not require detailed spectroscopic knowledge. This situation has been made possible in recent years by the availability of accurate compilations of line strengths and frequencies for all the major terrestrial molecular species. We will follow this empirical approach, as opposed to the more traditional and perhaps more intellectually-satisfying spectroscopic approach.

We first consider some elementary physics of the absorption process. It is important to note that the major molecular species (O_2, N_2) of the Earth's atmosphere have essentially no importance for IR absorption. This lack of

IR absorption is due to the symmetrical structure of homonuclear, diatomic molecules, as will be explained shortly. Four of the most important IR-absorbing molecular species are the minor constituent polyatomic molecules, water vapor (H_2O), carbon dioxide (CO_2), ozone (O_3), and methane (CH_4). Although dozens of other species have a small overall effect on the radiative energy budget, and together with their isotopic variants are important in remote sensing, we will discuss only these four representative species.

The absorption of light gives rise to excited states, which may be due to a combination of electronic, vibrational, and rotational motions (we will ignore the small effects associated with nuclear spin). We will begin with a consideration of molecular vibration, ignoring for the time being electronic or rotational energy. Separating the three is a useful abstraction, because the total internal energy of a molecule is given approximately by the sum of the three kinds of energy. Before discussing specifics, we will attempt to provide a visualization of the physics of the absorption process, in the same spirit as our earlier discussion of the Lorentz atom with regard to the scattering process (§3.2). The constituent atoms are held together in a semi-rigid structure by attractive forces provided by the electron 'cloud' which is more-or-less shared by all the atoms. The bonding forces can be either electrostatic (ionic bonding) or quantum-mechanical (exchange or covalent bonding). The nature of these forces does not concern us here. We need only consider their behaviour as 'springs' binding the various positively-charged nuclei together. The simplest example is a diatomic molecule which acts in many ways like a classical oscillator. Upon being "struck", either by a collision with another molecule or by absorption of a photon of the proper frequency, the constituent atoms are set into internal motion, alternately stretching and compressing the molecule. In addition, the bonds may 'bend' so that the angles between the various axes may also oscillate. Classically, the energy of oscillation of a molecule can vary continuously, but in reality, the number of energy states is a discrete set, due to the quantum nature of energy states.

According to classical-mechanical analyses, the internal motion of a semi-rigid system, no matter how complicated, can be decomposed into a sum of elementary motions, the so-called *normal modes*. A diatomic molecule, modelled by a simple harmonic oscillator, has only one normal mode of oscillation, along the internuclear axis. However, with increasing complexity of the molecule, more normal modes are possible. The general rule is that if a molecule has N atoms, the number of independent modes (or degrees of freedom) is $3N-6$ for a non-linear molecule ($N > 2$), and $3N-5$ for a linear molecule. Figure S.1 illustrates some of the normal modes of N_2, O_2, CO_2,
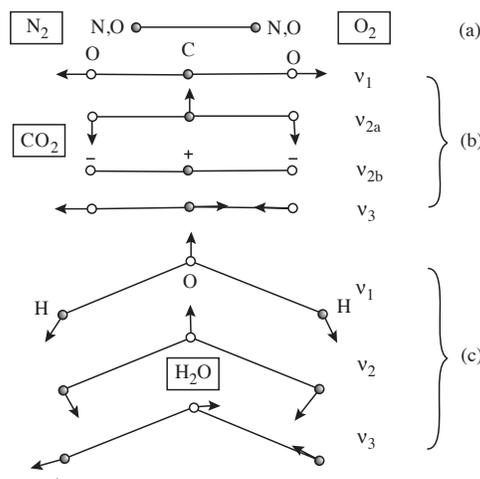
Figure S.1 Normal modes of vibration of N_2, O_2, CO_2, and H_2O. (a) N_2 and O_2 are diatomic, homonuclear molecules with only one mode of vibration. (b) CO_2 is a linear, triatomic molecule. Its ν_1 stretching mode is symmetric and therefore optically inactive. ν_{2a} and ν_{2b} are two separate modes but with the same energy, and are said to be *degenerate*. The two modes differ only by a 90° rotation about the internuclear axis. ν_3 is the asymmetrical bending mode. (c) Both H_2O and O_3 (not shown) have three normal modes, all of which are optically active.

and H_2O. If the motions are of small amplitude, the quantum mechanical result for the total vibrational energy is

$$E_v = \sum_k h\nu_k(v_k + 1/2) \qquad (v_k = 0, 1, 2 \cdots) \qquad (S.1)$$

where the subscript v stands for 'vibration'. The sum is over all modes denoted by the index k, $h\nu_k$ is the *vibrational constant* for that mode, ν_k is the mode frequency, and v_k is an integer, the *vibrational quantum number*. The value of $h\nu_k$ will depend upon the molecule, as well as the particular electronic energy state, and is usually in the range $300 - 3000$ cm^{-1} (corresponding to values of $h\nu_k$ in the range 0.037- 0.37 eV). The constant $1/2$ in Eq. S.1 is a quantum-mechanical feature associated with the 'zero-point energy'. The lowest vibrational energy levels are somewhat higher than thermal energy[1] $\sim k_B T \sim 210$ cm^{-1} for $T = 300$ K. For a classical simple harmonic oscillator, elementary analysis shows that $h\nu_k$ depends upon the square-root of the 'spring constant' k_e divided by the reduced mass. It is usually written

---

[1] A temperature of $T = 300$ K corresponds to a thermal energy of $k_B T$. Thus, $h\nu = k_B T$ corresponds to a wavenumber of $\tilde{\nu} = (k_B T)/(hc) =$
$(1.3806 \times 10^{-23}$ J K$^{-1} \times 300$ K$)/(6.626 \times 10^{-34}$J s $\times 2.998 \times 10^{10}$ cm s$^{-1}) = 208.5$ cm^{-1}.
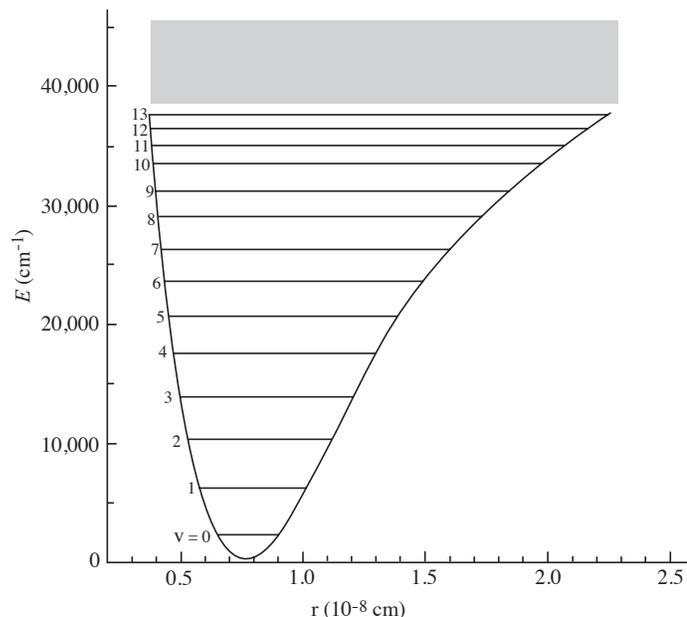
Figure S.2 Potential curve of the H_2 ground state with vibrational levels (Herzberg, 1950). The continuous term spectrum, above $v_k = 14$, is indicated by vertical hatching.

in terms of a *vibrational constant* (ω_e in cm^{-1}) as $h\nu_k = hc\omega_e$. The intermolecular force for a diatomic molecule is given by the spatial derivative of the potential energy function $V(r)$, which for small-amplitude oscillations, is given by $-k_e(r - r_e)$. Here r_e is the equilibrium nuclear separation. Figure S.2 shows the function $V(r)$ for the H_2 molecule, along with the array of vibrational energy states (Herzberg, 1950). Departures from strictly harmonic oscillations are described by higher order terms.

In addition to being excited by molecular collisions, molecular vibrations may also be induced by absorption of radiation provided the radiative energy is in resonance with a normal mode. Classically we can think of this interaction as the temporary creation of an induced electric dipole moment by the incident electromagnetic field. Such an interaction occurs *if the new configuration results in an electron distribution whose first moment* ('center of gravity') *is displaced from its original position.* In their ground, or lowest energy states, the dipole moment of symmetrical molecules, such as N_2, O_2, CO_2, and CH_4 is zero. However, there are asymmetrical stretching or bending modes of vibration (for example the ν_2 state of CO_2) which result in an electric dipole. Radiative transitions between these states and the ground

state are allowed because there is a *change* in the dipole moment. Note that the homonuclear molecules N_2 and O_2 are symmetrical in both their ground and (single) excited state, and therefore have no vibrational spectra, that is, they are radiatively inactive.

In quantum theory, absorption takes place if there is a finite dipole *matrix element*[2] between the initial and excited states. Sometimes this matrix element is zero for certain combinations, and the transition is *forbidden*, at least for dipole transitions. Higher-order moments, such as *electric quadrupole* and *magnetic dipole* moments may exist but their associated absorptions are much weaker than electric dipole transitions. So-called *selection rules* follow from considerations of whether a transition is 'dipole-allowed' or 'dipole-forbidden'. The wave number of a vibrational transition is given by $hc\tilde{\nu} = E_v(v') - E_v(v'')$ with the selection rule $\Delta v = v' - v'' = \pm 1$, the so-called *fundamental* rule. Because of deviations from strict harmonic oscillator behavior of a real molecule, higher order transitions (*overtone bands*) can occur where $\Delta v = \pm 2, \pm 3$, etc.

Up to now we have ignored rotation, but rotational energy always accompanies vibrational energy. Rotation imposes a 'fine structure' on the vibrational transitions, giving rise to a far richer absorption spectrum than Eq. S.1 would imply.

S.1.2 Molecular Rotation: the Rigid Rotator

Molecular rotation is easy to understand in principle. For simplicity we assume that the molecule is a *rigid rotator*, that is, the internuclear separation is fixed, regardless of the rotation. A diatomic molecule will be characterized by one moment of inertia, I, expressed classically as $M_1 r_1^2 + M_2 r_2^2$ where M_j and r_j are the nuclear masses and distances along the principal axis from the center of gravity of the nuclei. The two radii are given by

$$r_1 = \frac{M_2}{M_1 + M_2} r \qquad \text{and} \qquad r_2 = \frac{M_1}{M_1 + M_2} r$$

where $r = r_1 + r_2$ is the internuclear separation. The classical expression for the energy of rotation is $E_r = I\omega^2/2 = \mathcal{L}^2/2I$, where ω is the angular velocity of rotation about the principal axis, I is the corresponding moment of inertia, and $\mathcal{L}$ is the angular momentum. The usual quantum-mechanical

---

[2] The electric dipole matrix element is the convolution of the ground- and excited-state quantum mechanical wave functions with the electric dipole moment ex, where e is the electron charge and x is the displacement of the charge from the equilibrium position.

'prescription' is to replace the classical angular momentum with the quantized quantity $(h/2\pi)$ times an integer where h is Planck's constant. Since we are dealing with the square of the angular momentum, the quantum-mechanical equivalent is $\mathcal{L}^2 \rightarrow (h/2\pi)^2 J(J+1)$ where J is a positive integer, called the *rotational quantum number*. Thus, the rotational energy of a rigid-rotator is given by

$$E_{\mathrm{r}}(J) = \frac{1}{2I}\left(\frac{h}{2\pi}\right)^2 J(J+1) = hcB_v J(J+1) \qquad (J = 0, 1, \cdots) \qquad \text{(S.2)}$$

where $B_v \equiv h/(8\pi^2 cI)$ is the *rotational constant* corresponding to a particular electronic and vibrational state, which explains the subscript v on B_v.

How does rotation affect absorption and emission? Again, we invoke the principle that a change in electric dipole moment must be involved. For a radiative interaction it is necessary to have a permanent electric dipole moment. Since the dipole moment is a vector quantity, a change of its direction would constitute a change in the dipole moment. This interaction leads to pure rotational transitions, whose energies occur in the far-IR and microwave portion of the spectrum. The wavenumber of the emitted or absorbed photon is $\Delta E_{\mathrm{r}}/hc$, so that Eq. S.2 gives:

$$\tilde{\nu} = B_v J'(J'+1) - B_v J''(J''+1) \qquad \text{(S.3)}$$

where the selection rule is $\Delta J = J' - J'' = \pm 1$, that is, J may change or 'jump' by only one unit. The pure rotational spectrum of a rigid rotator can be seen to be a sequence of equidistant lines. Linear molecules, such as N_2, O_2, or CO_2, are symmetrical in their ground states. They have no permanent dipole moment and thus no pure rotational spectrum. Finally, it should be mentioned that pure rotational transitions prevail in the microwave spectrum. For example H_2O exhibits intense microwave absorption at 22 and 183 GHz (1 GigaHertz $= 1 \times 10^9$ Hz). Although the ground state of O_2 possesses no electric dipole moment, it does have an unusually large magnetic dipole. Thus weak ('forbidden') magnetic dipole transitions occur in the microwave spectrum, which are important for atmospheric absorption because of the very high abundance of O_2.

S.1.3 Molecular Vibration and Rotation: the Vibrating Rotator

Recognizing that vibration and rotation can occur simultaneously, we now consider the *vibrating rotator*. If there were no interaction between rotation and vibration, the energy would be simply the sum $E_{\mathrm{v}} + E_{\mathrm{r}}$. However, if the

centrifugal force and the Coriolis force associated with the rotating frame are considered, the situation becomes more complicated. The energy levels can be written as so-called *term values*

$$\frac{E(v,J)}{hc} = \omega_e(v+1/2) - \omega_e x_e(v+1/2)^2 + B_v J(J+1) - D_v J^2(J+1)^2. \quad \text{(S.4)}$$

ω_e and $\omega_e x_e$ are vibrational constants, expressed in wavenumber units. The quadratic terms are the 'interaction' terms for an *anharmonic oscillator*. Note the presence of two rotational constants, B_v and D_v, whose subscript v indicates their dependence on the vibrational mode. The term involving $\omega_e x_e$ is an anharmonic correction, which takes into account departures from simple harmonic oscillator motion.

The total molecular energy includes the electronic energy E_e. With this addition, the values of the rotational constants may also depend upon the particular electronic energy state. The wave number of a spectral line in a *vibration-rotation band* within a given electronic state is given by the difference of the *term values* of the two states defined by (v', J') and (v'', J'')

$$\tilde{\nu} = \tilde{\nu}_k + B_{v'} J'(J'+1) - B_{v''} J''(J''+1) \qquad [\text{cm}^{-1}] \qquad \text{(S.5)}$$

and where $\tilde{\nu}_k$ is the basic wavenumber of the pure vibrational transition without taking into account any rotation (that is when J' and J'' are set equal to zero). With $\Delta J = J' - J'' = +1$ and $\Delta J = J' - J'' = -1$, we obtain the wave numbers of the *R-branch* and *P-branch*, respectively

$$\tilde{\nu}_R = \tilde{\nu}_k + 2B_{v'} + (3B_{v'} - B_{v''})J'' + (B_{v'} - B_{v''})J''^2 \quad (J = 0, 1, \cdots) \quad \text{(S.6)}$$
$$\tilde{\nu}_P = \tilde{\nu}_k \qquad - (B_{v'} + B_{v''})J'' + (B_{v'} - B_{v''})J''^2 \quad (J = 1, 2, \cdots). \quad \text{(S.7)}$$

Figure S.3 shows the various transitions in a vibration-rotation band, illustrating the separation into two branches.

This description of a diatomic molecule is still approximate. Each electron (having a small mass compared to that of the nucleus) has a small moment of inertia about the internuclear axis. Nevertheless the total angular momentum of the electrons is comparable to that of the nucleus (which we denote by the vector $\mathbf{N}$), because of their fast orbital motions. Only the *component* of the total angular momentum $\boldsymbol{\Lambda}$ of the electrons along the internuclear axis contributes (the other components average to zero) because the electric field points along this axis. The associated quantum number Λ is a positive number. The total angular momentum $\mathbf{J}$ of the molecule is the vector sum of the nuclear angular momentum $\mathbf{N}$ (which points perpendicular to the internuclear axis) and the component of the total angular momentum $\boldsymbol{\Lambda}$ of the electrons (which points along the internuclear axis). The magnitude
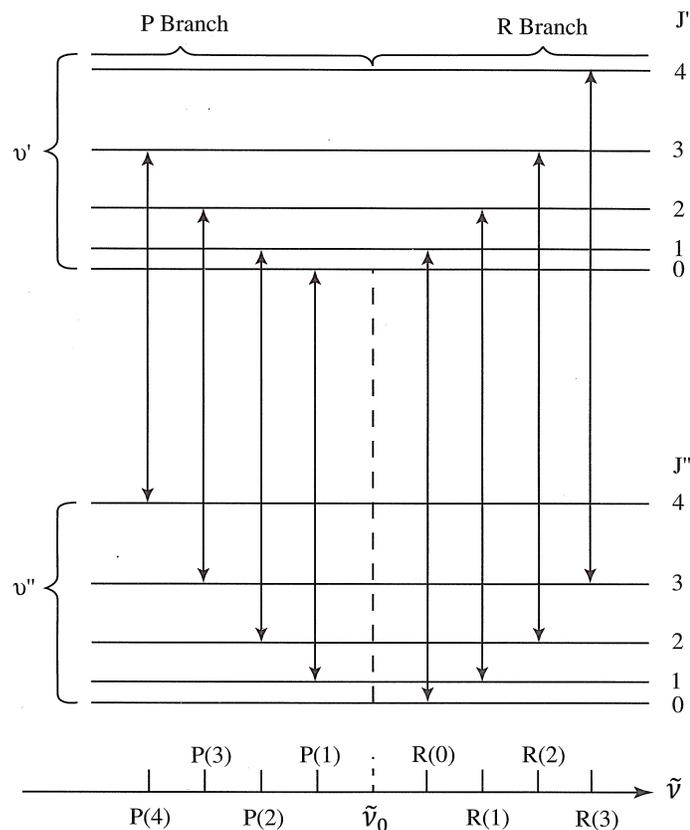
Figure S.3 Energy levels of the vibrating rotator [adapted from Fig. 11.5 of Rybicki and Lightman (1979)]. v'' and J'' are the vibrational and rotational quantum numbers of the lower state. v' and J' refer to the upper (excited) state. The vertical lines indicate allowed transitions ($\Delta J = \pm 1$). $R(j)$ ($j = 1, 2, 3, 4$) denotes the R-branch ($\Delta J = +1$) ending in the $J' = j$ state. In the lower part of the diagram, idealized absorption is shown versus wavenumber. $P(j)$ ($j = 0, 1, 2, 3$) denotes the P-branch ($\Delta J = -1$) ending in the $J'' = j$ state. The vertical dashed line indicates the band head at $\tilde{\nu} = \tilde{\nu}_0$, which is missing in homonuclear diatomic molecules, because the transition from $v' = 0$ to $v'' = 0$ is forbidden.

of the total angular momentum $\mathbf{J}$ is constant, and quantized according to $|\mathbf{J}| = \sqrt{J(J+1)}h/2\pi$ where h is Planck's constant. The quantum number J ($\geq \Lambda$) is given by $J = \Lambda, \Lambda + 1, \cdots$. For $\Lambda \neq 0$, there is a precession of $\mathbf{N}$ and $\boldsymbol{\Lambda}$ about the (constant) vector $\mathbf{J}$. Thus a more accurate picture of the diatomic molecule is a *symmetric top* nutating about the direction of the total angular momentum. The energy levels that result are thus the sum of

the nuclear rotational energy and the nutational energy

$$E_r/hc = B_v J(J+1) + (A_v - B_v)\Lambda^2 \text{ where } B_v = \frac{h}{8\pi^2 c I_B} \text{ and } A_v = \frac{h}{8\pi^2 c I_A}.$$

The primary moment of inertia is I_B, and I_A is the much smaller moment about the internuclear axis. Hence, A_v is generally much larger than B_v. Λ is usually a small (integral) value. Thus for a given electronic state, the levels of the symmetric top are the same as those of the simple rotator, except that there is a shift of magnitude $(A_v - B_v)\Lambda^2$, and levels with $J < \Lambda$ are absent.

Ignoring electronic transitions, the selection rules are rather simple, since Λ does not change during the transition. Then for $\Lambda = 0$, $\Delta J = \pm 1$, and for $\Lambda \neq 0$, $\Delta J = 0, \pm 1$. In the first case, since the constant term $(A - B)\Lambda^2$ disappears when the two term values are subtracted, we obtain exactly the same branches as discussed for the simple rotator. In the second case there is a constant shift, but otherwise the term values are the same. However more importantly, a new branch arises, the so-called *Q-branch* with $\Delta J = 0$. The wave numbers of the lines in this branch are

$$\tilde{\nu}_Q = \tilde{\nu}_k + (B_{v''} - B_{v'})\Lambda^2 + (B_{v'} - B_{v''})J + (B_{v'} - B_{v''})J^2. \qquad \text{(S.8)}$$

The only case of atmospheric interest for which a diatomic molecule has a Q-branch in its IR spectrum is that of nitric oxide (NO), which has a non-zero value of Λ in its ground state. Its fundamental band at 5.3 μm is important for the energy budget of Earth's lower thermosphere.

Q-branches are more common in polyatomic molecular spectra, for example in the pure bending mode of the ν_2 mode of CO_2. The $\Delta v = 1$ transitions "pile up" at very nearly the same frequency, accounting for the very strong Q-branch in the 15 μm band ($667 - 668$ cm^{-1}, see Fig. 4.4).

More complex molecules are categorized in terms of the relationships of the various moments of inertia. For the most complicated molecule, all three moments of inertia are different and also unequal to zero. This configuration is called an *asymmetric top*, and is represented by the important molecules, H_2O and O_3. If all three moments are equal, we have the *spherical top*, represented by CH_4. If two of the three moments of inertia are equal, we have a *symmetric top*, already mentioned in the case of a diatomic molecule. It is represented by the molecule $CFCl_3$. Finally, we have the case where one of the moments of inertia is effectively zero, in which case we have a *linear* molecule, examples of which are CO_2, N_2O, CO, and NO. Equation S.2 applies to the rotational energy for both the spherical top ($A_v = B_v$) and the linear molecule ($\Lambda = 0$). However, a more detailed analysis shows that linear

molecules and spherical tops do not have the same rotational structure, as levels of equal J will 'split' in different ways. This 'splitting' occurs as the theory is made more precise to consider all the various couplings between electronic, vibrational, and rotational energies. Electron and nuclear *spin* are important for setting additional selection rules, and in perturbing single energy levels into multiple levels. A *fine structure* results from the interaction of the magnetic dipole of the spinning electron with the electric field of the other electrons. A *Hyperfine structure* results from a similar interaction of the nuclear spin.

S.1.4 Line Strengths

The rather formidable task of spectroscopy is to analyze the line frequencies of an absorption or emission spectrum in terms of the various quantum numbers, rotational and vibrational constants, etc. We will henceforth take a less formidable empirical approach and assume that we are given the complete set of *spectroscopic constants* (ω_e, $\omega_e x_e$, B, D, etc.) necessary to determine the frequency (or wavenumber) of all transitions within a specified frequency range. In addition to the spectroscopic constants, modern compilations of the *absorption line strengths* are also readily available. Knowledge of line strengths is necessary for determining the overall opacity of the atmosphere as a function of frequency. The strengths depend not only upon the nature of the individual transition, but also upon the equilibrium number of ground-state molecules. Thus it is necessary to return to the consideration of the Boltzmann distribution of energy states.

We will first consider a vibration-rotation band produced by a simple harmonic-oscillator rigid-rotator. We will assume LTE conditions, so that the distribution of excited states is given by Boltzmann's formula (Eq. 4.18). First consider molecular rotation only, in which the energy levels are denoted by the quantum number J and are given by Eq. S.2. Since the quantum theory tells us that the statistical weight g_J (§4.3.4) of a rotational level J is $2J + 1$, the ratio of state populations with different J-values becomes

$$\frac{n(J)}{n(J')} = \frac{2J + 1}{2J' + 1} \exp\left\{ -\frac{hcB}{k_{\mathrm{B}}T} \left[J(J + 1) - J'(J' + 1) \right] \right\}. \qquad \text{(S.9)}$$

A more convenient ratio is that of an excited state population to the total number of states n within a given electronic and vibrational state

$$\frac{n(J)}{n} = \frac{(2J + 1)}{Q_{\mathrm{r}}} \exp\left[-\frac{hcB_v}{k_{\mathrm{B}}T} J(J + 1) \right] \qquad \text{(S.10)}$$

where Q_r is the *rotational partition function*

$$Q_r = \sum_{J'} (2J' + 1) \exp\left[-\frac{hcB_v J'(J' + 1)}{k_B T}\right]. \tag{S.11}$$

For sufficiently large T or small B_v, the spacing is very small compared with the total extent of the rotational energy. In this limiting case we may replace the sum with an integral, which is easily evaluated

$$Q_r \approx \int_0^\infty dJ(2J + 1) \exp\left[-hcB_v J(J + 1)/k_B T\right] = \frac{k_B T}{hcB_v}.$$

The distribution of rotational energies with rotational quantum number J is shown in Fig. S.4 for a number of molecules of atmospheric interest. This distribution is very important for the absorption coefficient, since the number of molecules in the ground (vibrational and electronic) state determine the rate of excitation. Since $B_v = h/8\pi^2 cI$ is inversely proportional to the moment of inertia I, and therefore to the molecular mass, it follows that light molecules, such as H_2, will have more widely separated rotational energy levels (see Fig. S.4) than heavier molecules. Consequently, because the average separation between states is relatively high in H_2, there are relatively few rotational states populated by collisions.

The LTE absorption cross section $\alpha_{in}^*(\nu)$ for an individual vibration-rotation line (denoted by subscript i, whereas subscript n is used to denote cross section as explained in Chapter 2) can be written as the product of a numerical factor and a frequency-dependent line profile

$$\alpha_{in}^*(\nu) = \mathcal{S}_i \Phi_i(\nu). \tag{S.12}$$

Here $\mathcal{S}_i$ is the *line strength* or *line radiance* of the ith line $(v'', J'') \to (v', J')$ given by (double-primes denote the lower state, and single-primes denote the excited state)

$$\mathcal{S}_i = \int d\nu \alpha_{in}^*(\nu) \qquad [\text{m}^2 \cdot \text{s}^{-1}] \tag{S.13}$$

where the frequency integration is over the width of a single line. The absorption coefficient is given by $\alpha_i(\nu) = \alpha_{in}(\nu)n$, where n is the total density of radiatively-active molecules (the sum over all ground and excited states). In tropospheric radiation problems, it is permissible to assume LTE, so that Eq. 4.33 applies. In the present context, absorption and extinction are synonymous. In Eq. 4.33, the initial (absorbing) state in the generalization to a multi-level molecule is $n_1^* \to n(v'', J'')$. Also we let $B_{12} \to B_i$. Thus, equating
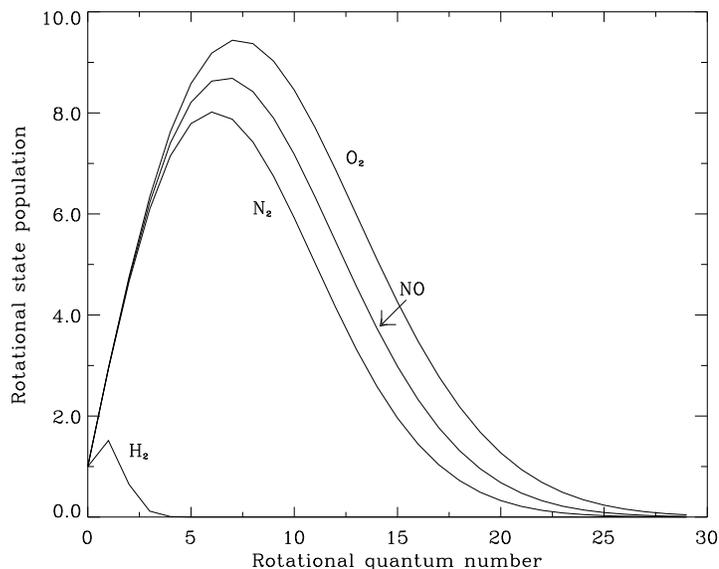
Figure S.4 Distribution of rotational energy levels with rotational quantum number J for the molecules O_2, H_2, N_2, and NO assuming $T = 250$ K.

Eqs. 4.33 and S.12, we find the following expression for the LTE absorption coefficient:

$$k^*(\nu) \to \alpha^*(\nu) = \frac{h\nu_i}{4\pi}\Phi_i(\nu)n(v'', J'')B_i\big(1 - e^{-h\nu_i/k_B T}\big) \equiv \mathcal{S}_i n\Phi_i(\nu) \quad \text{(S.14)}$$

where ν_i denotes the central frequency of the line, and $h\nu_i = E(v', J') - E(v'', J'')$ is the difference in energies of the two states connecting the transition i. The notation $\Phi_i(\nu)$ reminds us that the line profile may depend upon the particular transition, i, and differ from line to line, and band to band. This variation is usually small and slowly-varying with frequency over lines within the same band. Solving Eq. S.14 for the line strength, we find

$$\mathcal{S}_i = \frac{h\nu_i}{4\pi}B_i\frac{n(v'', J'')}{n}\big(1 - e^{-h\nu_i/k_B T}\big). \quad \text{(S.15)}$$

Substitution from Eq. S.10 for the population ratio of a rotational state yields

$$\mathcal{S}_i = \frac{h\nu_i(2J'' + 1)}{4\pi Q_i}B_i \exp\big[-hcB_v J''(J'' + 1)/k_B T\big]\big(1 - e^{-h\nu_i/k_B T}\big). \quad \text{(S.16)}$$

We should note here that differences may occur between the expressions

above and those found in the literature. First, our definition of the absorption coefficient in terms of the total density of molecules, as opposed to the number of molecules in the specific ground state, accounts for the factor $n(v'', J'')/n$ in Eq. S.15. Second, the assumption of LTE allowed us to express stimulated emission as negative absorption. Not all authors include the associated factor, $(1 - e^{-h\nu_i/k_{\rm B}T})$, which is often near unity. Third, we have defined the Einstein coefficients in terms of the mean radiance $\bar{I}_\nu$, instead of the energy density $\mathcal{U}_\nu$, which is often used in the astrophysical literature, and accounts for a factor of $4\pi/c$ between definitions involving $\bar{I}_\nu$ and $\mathcal{U}_\nu$.

In Eq. S.16 we see the explicit dependence of the line strength on temperature through the Boltzmann distribution of initial-state populations. So far we have assumed that transitions connect only a ground state with an excited state. In fact, absorption can originate from a higher vibrational state, which occurs for so-called *hot-bands*. Including the possibility of initial vibrational excitation, we have

$$\mathcal{S}_i = \mathcal{S}_{\rm io} \frac{Q_{\rm v}(T_o)Q_{\rm r}(T_o)}{Q_{\rm v}(T)Q_{\rm r}(T)} \frac{e^{-E_i''/k_{\rm B}T}}{e^{-E_i''/k_{\rm B}T_o}} \frac{(1 - e^{-E_i/k_{\rm B}T})}{(1 - e^{-E_i/k_{\rm B}T_o})}. \tag{S.17}$$

The vibrational partition function, $Q_{\rm v}$, is defined analogously to $Q_{\rm r}$ (see Eq. S.11). E_i'' denotes the initial state energy. $\mathcal{S}_{\rm oi}$ is simply the line strength obtained from Eq. S.16 evaluated at the reference temperature T_o. Fortunately, the result in Eq. S.17 may be applied to any polyatomic molecule for which we know the various partition functions, line strengths, and central line frequencies. For standard tabulations, the temperature dependence of all the various terms are subsumed into the following semi-empirical expression

$$\mathcal{S}_i = \mathcal{S}_{\rm io} \left(\frac{T_o}{T}\right)^m \exp\left[-\frac{E_i''}{k_{\rm B}}\left(\frac{1}{T} - \frac{1}{T_o}\right)\right]. \tag{S.18}$$

Here m is a dimensionless quantity of order unity which serves as a fitting parameter.

The strength of a line can be determined in two basic ways: (1) from quantum theoretical calculations, and (2) from laboratory measurements. The first method requires rather accurate knowledge of the wave functions, a very difficult problem for polyatomic molecules. In practice, laboratory results which rely upon the *Extinction Law* are used. The HITRAN spectroscopic data base contains information about several hundred thousands of lines.[3] Specifically, it includes spectroscopic data for seven major atmospheric absorbers, O_2, H_2O, CO_2, O_3, N_2O, CO, and CH_4. Included in the

---

[3] An early version of the HITRAN data base is described by Rothman et al. (1983). The HITRAN data base is being updated continuously as more and better spectroscopic data become available. The latest published version is described by Rothman et al. (2013).

listing for each line are: ν_i, $\mathcal{S}_{\mathrm{io}}$, width of the line at standard sea-level pressure and reference temperature, and energy E_i'' of the lower state. A data base such as HITRAN is extremely useful to atmospheric radiative transfer practitioners, because it provides a well-accepted standard against which theory can be compared with data, and with other theories.

S.2 Chapter 5 - Details and Derivations

S.2.1 §5.4.3 – Derivations

We first obtain a formal solution of Eq. 5.55 by choosing the integrating factor $e^{\tau/\mu}$ to obtain

$$\frac{d}{d\tau}\left(I_\nu^- e^{\tau/\mu}\right) = \left(\frac{dI_\nu^-}{d\tau} + \frac{1}{\mu}I_\nu^-\right)e^{\tau/\mu} = \frac{B_\nu(\tau)}{\mu}e^{\tau/\mu}. \qquad (S.19)$$

In accordance with the physical picture in Fig. 5.10 of downward beams which start at the 'top' and interact with the medium in the slab on their way downwards, we integrate Eq. S.19 along the vertical from the 'top' ($\tau = 0$) to the 'bottom' ($\tau = \tau^*$) of the medium to obtain

$$\int_0^{\tau^*} d\tau' \frac{d}{d\tau'}\left(I_\nu^- \, e^{\tau'/\mu}\right) = I_\nu^-(\tau^*,\mu,\phi)e^{\tau^*/\mu} - I_\nu^-(0,\mu,\phi) = \int_0^{\tau^*} \frac{d\tau'}{\mu}e^{\tau'/\mu}B_\nu(\tau').$$

Solving for $I_\nu^-(\tau^*,\mu,\phi)$, we find

$$I_\nu^-(\tau^*,\mu,\phi) = I_\nu^-(0,\mu,\phi)e^{-\tau^*/\mu} + \int_0^{\tau^*} \frac{d\tau'}{\mu}B_\nu(\tau')\,e^{-(\tau^*-\tau')/\mu} \qquad (S.20)$$

for the downward radiance emerging from the bottom of the slab. For an interior point, $\tau < \tau^*$, we integrate from 0 to τ. The solution is easily found by replacing τ^* by τ in Eq. S.20, that is

$$I_\nu^-(\tau,\mu,\phi) = I_\nu^-(0,\mu,\phi)e^{-\tau/\mu} + \int_0^{\tau} \frac{d\tau'}{\mu}B_\nu(\tau')\,e^{-(\tau-\tau')/\mu}. \qquad (S.21)$$

We now turn to the solution for the upper-half range radiance. The integrating factor for Eq. 5.54 is $e^{-\tau/\mu}$, which yields

$$\frac{d}{d\tau}\left(I_\nu^+ e^{-\tau/\mu}\right) = \left(\frac{dI_\nu^+}{d\tau} - \frac{1}{\mu}I_\nu^+\right)e^{-\tau/\mu} = -\frac{B_\nu(\tau)}{\mu}e^{-\tau/\mu}.$$

In this case the physical picture in Fig. 5.10 involves upward beams which start at the bottom of the slab and interact with the medium on their way upwards. Therefore, we integrate from the 'bottom' to the 'top' of the

$$\int_{\tau^*}^0 d\tau' \frac{d}{d\tau'}\left(I_\nu^+ e^{-\tau'/\mu}\right) = I_\nu^+(0,\mu,\phi) - I_\nu^+(\tau^*,\mu,\phi)e^{-\tau^*/\mu}$$

$$= -\int_{\tau^*}^0 \frac{d\tau'}{\mu}e^{-\tau'/\mu}B_\nu(\tau') = \int_0^{\tau^*} \frac{d\tau'}{\mu}e^{-\tau'/\mu}B_\nu(\tau').$$

Solving for $I_\nu^+(0,\mu,\phi)$, we find

$$I_\nu^+(0,\mu,\phi) = I_\nu^+(\tau^*,\mu,\phi)e^{-\tau^*/\mu} + \int_0^{\tau^*} \frac{d\tau'}{\mu}e^{-\tau'/\mu}B_\nu(\tau').$$

To find the radiance at an interior point τ, we integrate from τ^* to τ, to obtain

$$I_\nu^+(\tau,\mu,\phi) = I_\nu^+(\tau^*,\mu,\phi)e^{-(\tau^*-\tau)/\mu} + \int_\tau^{\tau^*} \frac{d\tau'}{\mu}\,e^{-(\tau'-\tau)/\mu}\,B_\nu(\tau'). \quad \text{(S.22)}$$

S.2.2 Example 5.6 – Derivations

Here we illustrate the use of the formal solution of the radiative transfer equation (Eqs. 5.67, 5.68 and 5.70) in deriving the reflectance of an idealized flat surface of a solid material illuminated by a collimated beam. The solid material is modeled as a homogeneous, semi-infinite ($\tau^* \to \infty$) slab medium. Even though the medium is optically infinite, because of the dense packing of the scatterers, the penetration of photons is actually quite shallow. The surface is located at an optical depth $\tau = 0$. The particles of the medium are assumed to be independent scatterers of single-scattering albedo ϖ. The particles scatter according to a phase function p. The absorption is assumed to dominate the scattering (ϖ is small), so that only the singly-scattered photons leave the surface.

Under these assumptions, the reflected radiance is a simplified form of Eq. 5.68

$$I^+(0,\mu,\phi) = \int_0^\infty \frac{d\tau'}{\mu}S(\tau',\mu,\phi)e^{-\tau'/\mu} \quad\quad\quad \text{(S.23)}$$

where the source function S is obtained from Eq. 5.70. To evaluate S and thus I^+, we note that we need to determine the two unknown half-range radiances, I^+ and I^- throughout the medium. This circularity is always present in the scattering theory, and to solve this problem is one of the main goals of this book. However in this simple example, we have simplified the problem in order to specify the radiation field explicitly. The single-scattering assumption permits us to replace the radiances on the right-hand side of Eq. 5.70 with the incident radiation field. In this case I^- is

the solar radiance, evaluated within the medium from the extinction law, $I^-(\tau, \mu', \phi') = F^s \delta(\mu' - \mu_0)\delta(\phi' - \phi_0)e^{-\tau/\mu'}$. The term involving I^+ within the medium can be neglected, since it represents higher-order scattering. Inserting this result into Eq. 5.70, and ignoring thermal emission, we find

$$S(\tau, \mu, \phi) = \frac{\varpi}{4\pi} \int_0^{2\pi} d\phi' \int_0^1 d\mu' p(-\mu', \phi'; \mu, \phi) F^s \delta(\mu' - \mu_0)\delta(\phi' - \phi_0)e^{-\tau/\mu'}$$

(S.24)

Inserting this result into Eq. S.23 we find

$$I^+(0, \mu, \phi) = \frac{\varpi}{4\pi} p(-\mu_0, \phi_0; \mu, \phi) F^s \int_0^\infty \frac{d\tau'}{\mu} e^{-\tau'/\mu_0} e^{-\tau'/\mu}$$

$$= \frac{\varpi}{4\pi(1 + \mu/\mu_0)} p(-\mu_0, \phi_0; \mu, \phi) F^s.$$

(S.25)

The reflectance (BRDF) is given by

$$\rho(-\mu_0, \phi_0; \mu, \phi) = \frac{I^+(0, \mu, \phi)}{\mu_0 F^s} = \frac{\varpi}{4\pi} \frac{p(-\mu_0, \phi_0; \mu, \phi)}{(\mu + \mu_0)}.$$

(S.26)

S.3 Chapter 6 - Details and Derivations

S.3.1 Derivations of Eqs. 6.3 and 6.4

We can write Eq. 5.45 in terms of the half-range radiances in a slab geometry as

$$-\mu \frac{dI_\nu^-(\tau, \hat{\Omega})}{d\tau} = I_\nu^-(\tau, \hat{\Omega}) - (1 - \varpi)B_\nu - \frac{\varpi}{4\pi} \int_+ d\omega' p(+\hat{\Omega}', -\hat{\Omega}) I_\nu^+(\tau, \hat{\Omega}')$$

$$- \frac{\varpi}{4\pi} \int_- d\omega' p(-\hat{\Omega}', -\hat{\Omega}) I_\nu^-(\tau, \hat{\Omega}')$$

(S.27)

$$\mu \frac{dI_\nu^+(\tau, \hat{\Omega})}{d\tau} = I_\nu^+(\tau, \hat{\Omega}) - (1 - \varpi)B_\nu - \frac{\varpi}{4\pi} \int_+ d\omega' p(+\hat{\Omega}', +\hat{\Omega}) I_\nu^+(\tau, \hat{\Omega}')$$

$$- \frac{\varpi}{4\pi} \int_- d\omega' p(-\hat{\Omega}', +\hat{\Omega}) I_\nu^-(\tau, \hat{\Omega}').$$

(S.28)

The notation $I_\nu^-(\tau, \mu, \phi) \equiv I_\nu^-(\tau, \hat{\Omega}) \equiv I_\nu(\tau, -\hat{\Omega})$ and $p(-\hat{\Omega}', +\hat{\Omega})$ (for example) indicates that a photon is moving downward before the scattering $(-\hat{\Omega}')$, and upward $(+\hat{\Omega})$ after the scattering. We now substitute for the total radiance, the sum of the direct and diffuse components (Eqs. 6.1 and

6.2) into Eq. S.27 to obtain

$$
-\mu \frac{dI^-_{\nu\mathrm{d}}(\tau,\hat{\Omega})}{d\tau} - \mu \frac{dI^-_{\nu\mathrm{s}}(\tau,\hat{\Omega})}{d\tau} =
$$

$$
I^-_{\nu\mathrm{d}}(\tau,\hat{\Omega}) + I^-_{\nu\mathrm{s}}(\tau,\hat{\Omega}) - (1-\varpi)B_\nu - \frac{\varpi}{4\pi}\int_- d\omega' p(-\hat{\Omega}',-\hat{\Omega})I^-_{\nu\mathrm{s}}(\tau,\hat{\Omega}')
$$

$$
- \frac{\varpi}{4\pi}\int_+ d\omega' p(+\hat{\Omega}',-\hat{\Omega})I^+_{\nu\mathrm{d}}(\tau,\hat{\Omega}') - \frac{\varpi}{4\pi}\int_- d\omega' p(-\hat{\Omega}',-\hat{\Omega})I^-_{\nu\mathrm{d}}(\tau,\hat{\Omega}').
$$

$$(\text{S.29})$$

The two non-integral terms involving the direct component cancel, because $-\mu dI^-_{\nu\mathrm{s}}/d\tau = I^-_{\nu\mathrm{s}}$. If we substitute for $I^-_{\nu\mathrm{s}}$ from Eq. 6.1 in the first integral term, we obtain

$$
-\mu \frac{dI^-_{\nu\mathrm{d}}(\tau,\hat{\Omega})}{d\tau} = I^-_{\nu\mathrm{d}}(\tau,\hat{\Omega}) - (1-\varpi)B_\nu - S^*_\nu(\tau,-\hat{\Omega})
$$

$$
- \frac{\varpi}{4\pi}\int_+ d\omega' p(\hat{\Omega}',-\hat{\Omega})I^+_{\nu\mathrm{d}}(\tau,\hat{\Omega}') - \frac{\varpi}{4\pi}\int_- d\omega' p(-\hat{\Omega}',-\hat{\Omega})I^-_{\nu\mathrm{d}}(\tau,\hat{\Omega}')
$$

$$(\text{S.30})$$

where

$$
S^*_\nu(\tau,-\hat{\Omega}) = \frac{\varpi}{4\pi}\int_- d\omega' p(-\hat{\Omega}',-\hat{\Omega})F^s_\nu e^{-\tau/\mu_0}\delta(\hat{\Omega}'-\hat{\Omega}_0)
$$

$$
= \frac{\varpi}{4\pi}p(-\hat{\Omega}_0,-\hat{\Omega})F^s_\nu e^{-\tau/\mu_0}. \tag{S.31}
$$

We repeat this procedure for the upward component to obtain

$$
\mu \frac{dI^+_{\nu\mathrm{d}}(\tau,\hat{\Omega})}{d\tau} = I^+_{\nu\mathrm{d}}(\tau,\hat{\Omega}) - (1-\varpi)B_\nu - S^*_\nu(\tau,+\hat{\Omega})
$$

$$
- \frac{\varpi}{4\pi}\int_+ d\omega' p(+\hat{\Omega}',+\hat{\Omega})I^+_{\nu\mathrm{d}}(\tau,\hat{\Omega}') - \frac{\varpi}{4\pi}\int_- d\omega' p(-\hat{\Omega}',+\hat{\Omega})I^-_{\nu\mathrm{d}}(\tau,\hat{\Omega}')
$$

$$(\text{S.32})$$

where

$$
S^*_\nu(\tau,+\hat{\Omega}) = \frac{\varpi}{4\pi}\int_- d\omega' p(-\hat{\Omega}',+\hat{\Omega})F^s_\nu e^{-\tau/\mu_0}\delta(\hat{\Omega}'-\hat{\Omega}_0)
$$

$$
= \frac{\varpi}{4\pi}p(-\hat{\Omega}_0,+\hat{\Omega})F^s_\nu e^{-\tau/\mu_0}. \tag{S.33}
$$

S.3.2 Isotropic Scattering in Slab Geometry

It is sometimes permissible to assume that the scattering is isotropic, so that $p = 1$. The source term is therefore also isotropic: $S^{*\pm}(\tau, \hat{\Omega}) = S^*(\tau)$, and the radiative transfer equations for the half-range diffuse radiances (Eqs. S.30 and S.32) are greatly simplified because the integrals are independent of the azimuthal angle ϕ. Assuming a black lower boundary, we find

$$\mu \frac{dI_\mathrm{d}^+(\tau, \mu)}{d\tau} = I_\mathrm{d}^+(\tau, \mu) - (1-\varpi)B - S^*(\tau) - \frac{\varpi}{2} \int_0^1 d\mu' I_\mathrm{d}^+(\tau, \mu') - \frac{\varpi}{2} \int_0^1 d\mu' I_\mathrm{d}^-(\tau, \mu')$$
$$(S.34)$$

$$-\mu \frac{dI_\mathrm{d}^-(\tau, \mu)}{d\tau} = I_\mathrm{d}^-(\tau, \mu) - (1-\varpi)B - S^*(\tau) - \frac{\varpi}{2} \int_0^1 d\mu' I_\mathrm{d}^+(\tau, \mu') - \frac{\varpi}{2} \int_0^1 d\mu' I_\mathrm{d}^-(\tau, \mu')$$
$$(S.35)$$

where $S^*(\tau) = \frac{\varpi}{4\pi} F^s e^{-\tau/\mu_0}$.

Because S^* is isotropic in this case, the radiances are independent of the angle ϕ, which is an enormous simplification over the anisotropic scattering case. A great deal of the early work in the field was performed on this type of problem, because of its analytic simplicity rather than its resemblance to real problems. Nevertheless, there are a few practical problems for which the isotropic approximation is useful, such as in the integral equation approach (§6.10), in the prototype problems (§6.7), as well as in the discussion of the radiative equilibrium problem (Chapter 8).

From Eq. 6.12 the source function is:

$$S(\tau) = (1 - \varpi)B + S^* + \frac{\varpi}{2} \int_0^1 d\mu \left[I_\mathrm{d}^+(\tau, \mu) + I_\mathrm{d}^-(\tau, \mu) \right]. \qquad (S.36)$$

Given the source function $S(\tau)$, the diffuse radiances follow from Eqs. 5.67 and 5.68

$$I_\mathrm{d}^-(\tau, \mu) = \int_0^\tau \frac{d\tau'}{\mu} S(\tau') e^{-(\tau-\tau')/\mu} \qquad (S.37)$$

$$I_\mathrm{d}^+(\tau, \mu) = \int_\tau^{\tau^*} \frac{d\tau'}{\mu} S(\tau') e^{-(\tau'-\tau)/\mu}. \qquad (S.38)$$

S.3.3 The conservative limit for Prototype Problem 2: The Milne Problem

The classical *Milne Problem* can be thought of as the limit of the imbedded-source problem, in which there is no absorption so that $\varpi \to 1$. Then the

source term is zero, and one is left with the simple radiative transfer equation

$$u\frac{dI(\tau, u)}{d\tau} = I(\tau, u) - \frac{1}{2}\int_{-1}^{+1} du' I(\tau, u').$$

Note that we consider the full-range radiance $(-1 \leq u \leq +1)$ because no particular simplifications follow from using half-range radiances, and because it is the traditional form of the Milne problem. The medium is usually taken to be semi-infinite, and a source of radiation is assumed to be placed at an infinite distance below the upper boundary at $\tau = 0$. The radiation therefore trickles upward and escapes without any losses into the half-space above the upper boundary. As we shall see in Chapter 7 the upward irradiance is the same in all directions, since there is neither absorption nor scattering in the medium.

S.4 Chapter 7 - Details and Derivations

S.4.1 §7.2.2 – Derivations

It is not obvious that the *Neumann series expansion* given by Eq. 7.13 in §7.2.2 converges, that is, whether it is the desired solution to Eq. 7.11. A proof that it is indeed absolutely convergent is obtained by evaluating a second series expansion in closed form, and whose terms are upper bounds to those in the above series expansion.

The proof of convergence also provides us with an approximate solution which offers more insight into the general nature of the multiple-scattering series. We assume the conditions of *Prototype Problem 2*, in which the only source of radiation is thermal emission, and for which the 'imbedded source' is constant with τ. For simplicity we assume that this source is independent of optical depth, $S^{(1)} = (1 - \varpi)B = \text{constant}$. Consider the second-order contribution to the source function

$$S^{(2)}(\tau) \equiv \Lambda^{(1)}(\tau, \tau_1)S^{(1)}(\tau_1) = \frac{\varpi}{2}S^{(1)}\int_0^{\tau^*} d\tau_1 E_1(|\tau - \tau_1|)$$

$$= \frac{\varpi}{2}S^{(1)}\left[\int_0^{\tau} d\tau_1 E_1(\tau - \tau_1) + \int_{\tau}^{\tau^*} d\tau_1 E_1(\tau_1 - \tau)\right]. \quad \text{(S.39)}$$

Using the property $dE_2(t)/dt = -E_1(t)$, and noting that $E_2(0) = 1$, we find

$$S^{(2)}(\tau) = \frac{\varpi}{2} S^{(1)} \left[\int_0^\tau d\tau_1 \frac{dE_2(\tau - \tau_1)}{d\tau_1} + \int_\tau^{\tau^*} d\tau_1 (-) \frac{dE_2(\tau_1 - \tau)}{d\tau_1} \right]$$
$$= \varpi S^{(1)} \left[1 - 1/2 E_2(\tau) - 1/2 E_2(\tau^* - \tau) \right]$$
$$\equiv \varpi S^{(1)} \left[1 - P(\tau) - P(\tau^* - \tau) \right]. \tag{S.40}$$

$P(\tau) \equiv \frac{1}{2} E_2(\tau)$ and $P(\tau^* - \tau) \equiv \frac{1}{2} E_2(\tau^* - \tau)$ are the hemispherical *single-flight escape probabilities* for a photon released at the optical depth τ (see Eq. R.10). $P(\tau)$ describes the probability of escape without further scattering through the top ($\tau = 0$), and $P(\tau^* - \tau)$ through the bottom ($\tau = \tau^*$) of the slab, respectively. As usual, we are assuming a black lower boundary, so that a photon is lost when it reaches either boundary.

Since $1 - P(\tau) - P(\tau^* - \tau)$ is the probability of photon capture upon emission at τ, the interpretation of Eq. S.40 is clear. The source function of second-order scattered photons is the product of two factors: ($\varpi S^{(1)} =$ probability of a photon being scattered following an extinction event) $\times$ (the probability that a photon is 'captured'). It defines the contribution from photons which are emitted from a unit volume[4] which suffer *one extinction* and survive the extinction as a scattering event.

We are interested in an upper bound to the source function, which occurs where the escape probability is a *minimum*, that is, at the mid-point in the slab, $\tau = \tau^*/2$. Replacing the equality Eq. S.40 with the inequality, we have

$$S^{(2)}(\tau) < \varpi S^{(1)} \left[1 - 2P(\tau^*/2) \right].$$

Continuing the procedure, we find that the third-order term is

$$S^{(3)}(\tau) = \left(\frac{\varpi}{2} \right)^2 \int_0^{\tau^*} d\tau_1 E_1(|\tau - \tau_1|) \int_0^{\tau^*} d\tau_2 E_1(|\tau_1 - \tau_2|). \tag{S.41}$$

An upper limit follows from evaluating both the integrals at $\tau^*/2$

$$S^{(3)}(\tau) < S^{(1)} \left(\frac{\varpi}{2} \right)^2 \int_0^{\tau^*} d\tau_1 E_1(|\tau_1 - \tau^*/2|) \int_0^{\tau^*} d\tau_2 E_1(|\tau_2 - \tau^*/2|)$$
$$= S^{(1)} (\varpi)^2 \left[1 - 2P(\tau^*/2) \right]^2.$$

Repeating this process for every order of scattering, we find the general upper bound

$$S^{(n)}(\tau) < S^{(1)} (\varpi)^{n-1} \left[1 - 2P(\tau^*/2) \right]^{n-1}.$$

---

[4] A unit volume in 'tau-space' is not the same as in geometrical space. Imagine a small cylindrical volume whose length is $d\tau$ and whose cross-sectional area dA has units m^2. Then the volume will be $dAd\tau$, whose units are m^2, in contrast to the geometrical volume $dzdA$, which has units of m^3.

The total source function thus obeys the following inequality

$$S(\tau) = \sum_{n=1}^{\infty} S^{(n)} < S^{(1)} \sum_{n=0}^{\infty} x^n \quad \text{where} \quad x \equiv \varpi[1 - 2P(\tau^*/2)].$$

The above sum is easily evaluated by recognizing that the geometric series expansion of $(1 - x)^{-1}$ is $1 + x + x^2 + \cdots$. Thus, since $S^{(1)} = (1 - \varpi)B$, we obtain:

$$S(\tau) < \frac{(1 - \varpi)B}{1 - \varpi[1 - 2P(\tau^*/2)]}. \tag{S.42}$$

Since $0 < P(\tau) < 1$, and $0 < \varpi \le 1$, this result is finite. Note that in the limit of an optically-thick, conservatively-scattering medium where the escape probability goes to zero, $S \to (1 - \varpi)B/(1 - \varpi) = B$, as it should. *Thus, we have shown that the Neumann series converges for any first-order scattering source that is finite everywhere in the medium.* Equation S.42 is also interesting in its own right, since it provides in some circumstances a useful estimate for the actual source function. If we use the more general first-order source function (Eq. 7.6) we can replace the upper limit with the approximation

$$S(\tau, \mu, \phi) \approx \frac{(1 - \varpi)B + \frac{\varpi F^s}{4\pi} p(-\mu_0, \phi_0; \mu, \phi) e^{-\tau/\mu_0}}{1 - \varpi[1 - 2P(\tau^*/2)]}. \tag{S.43}$$

In astrophysics, the above equation is called the *Sobolev approximation*, and in infrared atmospheric physics it goes by the name of the *cooling-to-space approximation* (§8.2.6).

Now let $\tau^* << 1$. We note that $1 - 2P(\tau^*/2) = 1 - E_2(\tau^*/2) \approx 1 - e^{-\tau^*/2\bar{\mu}} \approx \tau^*$ (assuming $\bar{\mu} = 1/2$). The multiple-scattering series becomes

$$S(\tau, \mu, \phi) \approx [(1 - \varpi)B + \frac{\varpi F^s}{4\pi} p(-\mu_0, \phi_0; \mu, \phi) e^{-\tau/\mu_0}][1 + \varpi\tau^* + (\varpi\tau^*)^2 + \cdots].$$

S.4.2 Exponential-Kernal Approximation

An alternate method of solving radiative transfer problems is to begin with the Milne-Schwarzschild integral-equation for the source function. The source function yields the diffuse radiance through an integration, which may then be added to the direct (solar) radiance. We illustrate this approach by again solving *Prototype Problem 1*, and comparing to the previous results. Equation 6.80 is written for isotropic scattering for a general internal (thermal)

source S^{int} and a boundary contribution S^*

$$S(\tau) = S^{\text{int}}(\tau) + S^*(\tau) + \frac{\varpi}{2}\int_0^{\tau^*} d\tau' E_1(|\tau' - \tau|)S(\tau'). \tag{S.44}$$

The boundary contribution may be written in terms of a general distribution of radiance $I^-(0, \mu, \phi)$ falling on the top of the medium. From Eq. 5.64

$$S^*(\tau) = \frac{\varpi}{4\pi}\int_{4\pi} d\omega' I^-(0, \mu', \phi')e^{-\tau/\mu} \tag{S.45}$$

and for hemispherically-isotropic radiation of radiance $\mathcal{I}$

$$S^*(\tau) = \frac{\varpi}{2}\mathcal{I}\int_0^1 d\mu' e^{-\tau/\mu'} = \frac{\varpi}{2}\mathcal{I}E_2(\tau) \tag{S.46}$$

where E_2 is the exponential integral of order 2.

The *exponential-kernal approximation* consists of the following replacement

$$E_1(|\tau' - \tau|) = \int_0^1 \frac{d\mu'}{\mu'}e^{-|\tau'-\tau|/\mu'} \approx \frac{1}{\bar{\mu}}e^{-|\tau'-\tau|/\bar{\mu}} \tag{S.47}$$

where $\bar{\mu}$ has its usual meaning. This approximation may be thought of as a one-point quadrature evaluation of the integral, or as a replacement of the angular integral with the integrand evaluated at the mean angle of the inclination of the rays. Note that E_2 in the expression for S^* becomes $\sim e^{-\tau/\bar{\mu}}$. The nth exponential integral is approximated by

$$E_n(\tau) \approx e^{-\tau/\bar{\mu}}\bar{\mu}^{n-2}. \tag{S.48}$$

Substituting these results into Eq. S.44 with $S^{\text{int}}(\tau) = 0$, we find

$$S(\tau) = \frac{\varpi}{2}\mathcal{I}e^{-\tau/\bar{\mu}} + \frac{\varpi}{2}\int_0^{\tau^*} \frac{d\tau'}{\bar{\mu}}e^{-|\tau'-\tau|/\bar{\mu}}S(\tau'). \tag{S.49}$$

This equation can be shown to have a solution consisting of positive and negative exponentials. Substituting the trial solution $S(\tau) = Ae^{\Gamma\tau} + Ce^{-\Gamma\tau}$ into Eq. S.49, where Γ is given by Eq. 7.32, and carrying out the integrations, we obtain

$$Ae^{\Gamma\tau} + Ce^{-\Gamma\tau} = \frac{\varpi}{2}\mathcal{I}e^{-\tau/\bar{\mu}} + \frac{\varpi}{2}\int_0^\tau \frac{d\tau'}{\bar{\mu}}e^{-(\tau-\tau')/\bar{\mu}}[Ae^{\Gamma\tau'} + Ce^{-\Gamma\tau'}]$$

$$+ \int_\tau^{\tau^*} \frac{d\tau'}{\bar{\mu}}e^{-(\tau'-\tau)/\bar{\mu}}[Ae^{\Gamma\tau'} + Ce^{-\Gamma\tau'}] = Ae^{\Gamma\tau} + Ce^{-\Gamma\tau}$$

$$+ e^{-\tau/\bar{\mu}}\left[\frac{\varpi}{2}\left(1 - \frac{A}{(1-\Gamma\bar{\mu})} - \frac{C}{(1+\Gamma\bar{\mu})}\right)\right] - \frac{\varpi}{2}\left[\frac{Ae^{-\Gamma\tau^*}}{(1+\Gamma\bar{\mu})} + \frac{Ce^{\Gamma\tau^*}}{(1-\Gamma\bar{\mu})}\right].$$

After cancellation of equal terms on the left and right, we obtain an equation in which the left side is zero. In order for this equation to be correct *for all values of* τ, it is necessary that the coefficients of the two linearly-independent terms (one of which is proportional to $e^{-\tau/\bar{\mu}}$ and the other being just a constant) be separately equal to zero, that is

$$1 - \frac{A}{(1 - \Gamma\bar{\mu})} - \frac{C}{(1 + \Gamma\bar{\mu})} = 0; \qquad \frac{Ae^{-\Gamma\tau^*}}{(1 + \Gamma\bar{\mu})} + \frac{Ce^{\Gamma\tau^*}}{(1 - \Gamma\bar{\mu})} = 0.$$

These equations are easily solved to yield

$$A = \frac{-\mathcal{I}(1 - \Gamma\bar{\mu})e^{\Gamma\tau^*}}{\mathcal{D}}; \qquad C = \frac{-\rho_\infty\mathcal{I}(1 - \Gamma\bar{\mu})e^{-\Gamma\tau^*}}{\mathcal{D}}$$

where we have used the definition of ρ_∞, Eq. 7.35, and $\mathcal{D}$, Eq. 7.40. Noting that $1 - \Gamma\bar{\mu} = (\varpi/2)(1 + \rho_\infty)$, we find the same solution for $S(\tau)$ as obtained earlier, Eq. 7.41. Given the source function, the diffuse radiance is given by

$$I_{\mathrm{d}}^+(\tau) \approx I^+(\tau, \bar{\mu}) = \int_\tau^{\tau^*} \frac{d\tau'}{\bar{\mu}} S(\tau')e^{-(\tau'-\tau)/\bar{\mu}} \qquad (\text{S.50})$$

$$I_{\mathrm{d}}^-(\tau) \approx I^-(\tau, \bar{\mu}) = \int_0^\tau \frac{d\tau'}{\bar{\mu}} S(\tau')e^{-(\tau-\tau')/\bar{\mu}}. \qquad (\text{S.51})$$

The total radiance is the sum of the diffuse and direct ('solar') terms, $I_{\mathrm{d}} + I_{\mathrm{s}}$, where the direct term is

$$I_{\mathrm{s}}(\tau) = \frac{\varpi}{2}\mathcal{I}E_2(\tau) \approx \frac{\varpi}{2}\mathcal{I}e^{-\tau/\bar{\mu}}.$$

Carrying out the integrations, one finds that the total radiances $I^\pm(\tau)$ agree with the earlier results, Eqs. 7.36–7.37. If $\mu \neq \bar{\mu}$, the radiance $I(\tau, \mu)$ agrees with the results, Eqs. 7.56–7.57.

We have shown that, at least for *Prototype Problem 1*, the exponential-kernal methods yields the same solution as the traditional two-stream differential-equation approach. It should be obvious that the two methods are equivalent, since they both rely upon the same approximation replacing the angular variation of the radiance with a constant value.

S.4.3 Angular Distribution of Emergent Radiances for Isotropic Scattering

The angular distribution of the radiance for *Prototype Problem 3* can be obtained in the same fashion as in *Prototype Problem 1*. The procedure is straightforward, but the algebra is rather daunting. However, a 'short-cut' is possible, provided we are interested only in the emergent radiances. We may

use the closed-form results for the emergent radiances expressed in terms of X- and Y-functions by S. Chandrasekhar as follows[5]

$$I^+(0,\mu;\tau^*) = \frac{\varpi F^{\mathrm{s}}\mu_0}{4\pi(\mu + \mu_0)}\left[X(\mu)X(\mu_0) - Y(\mu)Y(\mu_0)\right] \qquad \text{(S.52)}$$

$$I^-(\tau^*,\mu;\tau^*) = \frac{\varpi F^{\mathrm{s}}\mu_0}{4\pi(\mu - \mu_0)}\left[Y(\mu)X(\mu_0) - X(\mu)Y(\mu_0)\right]. \qquad \text{(S.53)}$$

For a semi-infinite medium, Chandrasekhar's result is written (see Exercise 7.5)

$$I^+(0,\mu;\tau^* \to \infty) = \frac{\varpi F^{\mathrm{s}}\mu_0}{4\pi(\mu + \mu_0)}H(\mu)H(\mu_0) \approx \frac{\varpi F^{\mathrm{s}}\mu_0}{4\pi(\mu + \mu_0)}$$
$$\times \left[\frac{(\bar{\mu} + \mu)}{(\bar{\mu} + \mu\sqrt{1 - \varpi})}\right]\left[\frac{(\bar{\mu} + \mu_0)}{(\bar{\mu} + \mu_0\sqrt{1 - \varpi})}\right]. \quad \text{(S.54)}$$

S.4.4 Derivations (§7.5.1)

Assuming collimated incidence, $S^*(\tau, u) = (\varpi F^{\mathrm{s}}/4\pi)p(-\mu_0, u)e^{-\tau/\mu_0}$, we approximate the angular dependence of the radiance as a constant plus a term linear in u, $I(\tau, u) \approx [I_0(\tau) + uI_1(\tau)]$, which upon substitution into Eq. 7.90 yields

$$u\frac{d(I_0 + uI_1)}{d\tau} = (I_0 + uI_1) - \frac{\varpi}{2}\int_{-1}^{1}du'p(u', u)(I_0 + u'I_1) - \frac{\varpi F^{\mathrm{s}}}{4\pi}p(-\mu_0, u)e^{-\tau/\mu_0}.$$
$$\text{(S.55)}$$

We expand the scattering phase function in Legendre polynomials as usual, and find that the azimuthally-averaged scattering phase function is (see Eq. 6.27)

$$p(u', u) = \sum_{\ell=0}^{2N-1}(2\ell + 1)\chi_\ell P_\ell(u)P_\ell(u')$$

where the moments of the scattering phase function are given by (see Eq. 6.29)

$$\chi_\ell = \frac{1}{2P_\ell(u)}\int_{-1}^{+1}du'p(u', u)P_\ell(u').$$

In the two-stream approximation, we normally retain only two terms: (1) the zeroth moment which is unity because of the normalization of the scattering

---

[5] See Chandrasekhar (1960), page 209, Eqs. 3, 4, and 5.

phase function ($\chi_0 = 1$); and (2) the first moment which we refer to as the *asymmetry factor*, χ_1 or more commonly denoted by g. Then

$$\frac{\varpi}{2} \int_{-1}^{1} du' p(u', u)(I_0 + u' I_1) = \varpi(I_0 + 3gu\langle u \rangle_2 I_1)$$

where the $\langle \, \rangle$ symbol denotes an angular average over the sphere

$$\langle u \rangle_2 \equiv \frac{1}{2} \int_{-1}^{1} du\, u^2.$$

Note that the symbol $\langle u \rangle_2$ is used instead of the numerical value $1/3$ to facilitate comparison with the two-stream approximation. Since $p(-\mu_0, u) = 1 - 3gu\mu_0$, Eq. S.55 becomes

$$u\frac{d(I_0 + uI_1)}{d\tau} = I_0 + uI_1 - \varpi(I_0 + 3gu\langle u \rangle_2 I_1) - \frac{\varpi F^{\mathrm{s}}}{4\pi}(1 - 3gu\mu_0)e^{-\tau/\mu_0}. \quad \text{(S.56)}$$

To proceed, we first integrate Eq. S.56 over u (from -1 to 1), which yields the first equation below. We then multiply Eq. S.56 by u, and integrate again, to obtain the second equation below. Thus, we are left with the following pair of coupled equations for the moments of radiance, I_0 and I_1

$$\frac{dI_1}{d\tau} = \frac{1}{\langle u \rangle_2}(1 - \varpi)I_0 - \frac{\varpi F^{\mathrm{s}}}{4\pi\langle u \rangle_2}e^{-\tau/\mu_0} \qquad \text{(S.57)}$$

$$\frac{dI_0}{d\tau} = (1 - 3g\varpi\langle u \rangle_2)I_1 + \frac{3\varpi F^{\mathrm{s}}}{4\pi}g\mu_0 e^{-\tau/\mu_0}. \qquad \text{(S.58)}$$

To derive the two-stream equations, we start by writing Eq. 7.90 in terms of the half-range radiances

$$\mu\frac{dI_{\mathrm{d}}^{+}(\tau, \mu)}{d\tau} = I_{\mathrm{d}}^{+}(\tau, \mu) - \frac{\varpi}{2}\int_{0}^{1} d\mu' p(-\mu', \mu)I_{\mathrm{d}}^{-}(\tau, \mu')$$

$$- \frac{\varpi}{2}\int_{0}^{1} d\mu' p(\mu', \mu)I_{\mathrm{d}}^{+}(\tau, \mu') - \frac{\varpi F^{\mathrm{s}}}{4\pi}p(-\mu_0, \mu)e^{-\tau/\mu_0}$$

$$\equiv I_{\mathrm{d}}^{+}(\tau, \mu) - S^{+}(\tau, \mu) \qquad \text{(S.59)}$$

$$-\mu\frac{dI_{\mathrm{d}}^{-}(\tau, \mu)}{d\tau} = I_{\mathrm{d}}^{-}(\tau, \mu) - \frac{\varpi}{2}\int_{0}^{1} d\mu' p(-\mu', -\mu)I_{\mathrm{d}}^{-}(\tau, \mu')$$

$$- \frac{\varpi}{2}\int_{0}^{1} d\mu' p(\mu', -\mu)I_{\mathrm{d}}^{+}(\tau, \mu') - \frac{\varpi F^{\mathrm{s}}}{4\pi}p(-\mu_0, -\mu)e^{-\tau/\mu_0}.$$

$$\equiv I_{\mathrm{d}}^{-}(\tau, \mu) - S^{-}(\tau, \mu) \qquad \text{(S.60)}$$

We proceed by integrating both equations over the hemisphere by applying the operator $\int_{0}^{1} d\mu$. If the $I^{\pm}(\tau, \mu)$ are replaced by their averages over each

hemisphere, $I^{\pm}(\tau)$, and the explicit appearance of μ is replaced by some average value $\bar{\mu}$, this procedure leads to the following pair of coupled equations for $I^{\pm}$ (dropping the 'd' subscript)

$$\bar{\mu}\frac{dI^+}{d\tau} = I^+ - \varpi(1-b)I^+ - \varpi b I^- - S^{*+} \tag{S.61}$$

$$-\bar{\mu}\frac{dI^-}{d\tau} = I^- - \varpi(1-b)I^- - \varpi b I^+ - S^{*-} \tag{S.62}$$

where

$$S^{*+} \equiv \frac{\varpi F^{\mathrm{s}}}{2\pi}b(\mu_0)e^{-\tau/\mu_0} \equiv X^+(\tau)e^{-\tau/\mu_0}$$

$$S^{*-} \equiv \frac{\varpi F^{\mathrm{s}}}{2\pi}[1-b(\mu_0)]e^{-\tau/\mu_0} \equiv X^-(\tau)e^{-\tau/\mu_0}. \tag{S.63}$$

S.4.5 Accuracy of the Two-Stream Method – Details (§7.6)

Table S.1 *Two-stream results compared to accurate results for the diffuse upward and downward irradiances at the top and bottom of a homogeneous layer.[a]*

Case	μ_0	τ^*	ϖ	g	F$^+(0)$ Exact	Twostr	Error (%)	F$^-(\tau^*)$ Exact	Twostr	Error (%)
1	1.000	1.00	1.0000	0.7940	0.173	0.174	0.65	1.813	1.812	-0.07
2	1.000	1.00	0.9000	0.7940	0.124	0.133	7.03	1.516	1.522	0.38
3	0.500	1.00	0.9000	0.7940	0.226	0.221	-2.14	0.803	0.864	7.59
4	1.000	64.00	1.0000	0.8480	2.662	2.683	0.81	0.480	0.454	-5.50
5	1.000	64.00	0.9000	0.8480	0.376	0.376	-0.05	0.000	0.000	0.00

Note: [a]The lower surface was assumed to be black.

In Tables S.1–S.3 we show results for beam illumination of a homogeneous slab (*Prototype Problem 3*). Table S.1 shows upward irradiance at the top and downward irradiance at the bottom of a slab of optical depth $\tau^* = 1$ and 64. The error varies from being negligible to as large as 7%. Table S.2 shows the net irradiance and the irradiance divergence at several levels in an optically thick slab ($\tau^* = 64$). For a conservative slab ($\varpi = 1.0$) the errors are small (4-5%) for the net irradiance and negligible for the irradiance divergence. For a moderately absorbing slab ($\varpi = 0.9$) the error is of similar magnitude for the net irradiance and irradiance divergence; it is relatively

Table S.2 *Two-stream results compared to accurate results for the net irradiance, $F = F^+ - F^-$, and the irradiance divergence,*
$$F_{layer,i+1} - F_{layer,i}.^a$$

| Case | 1 | $\mu_0 = 1.000$ | $\varpi = 1.0000$ | $\tau^* = 64.00$ | $g = 0.8480$ |

τ	Net irradiance		Error	Divergence		Error
	Exact	Twostr	(%)	Exact	Twostr	(%)
.000	0.48000	0.45804	-4.6	0.00000	0.00026	0.0
3.200	0.48000	0.45778	-4.6	0.00000	0.00035	0.0
6.400	0.48000	0.45743	-4.7	0.00000	0.00070	0.0
12.800	0.48000	0.45674	-4.8	0.00000	0.00180	0.0
32.000	0.48000	0.45493	-5.2	0.00000	0.00092	0.0
48.000	0.48000	0.45401	-5.4	0.00000	0.00039	0.0
64.000	0.48000	0.45362	-5.5	0.00000	0.00000	0.0

| Case | 2 | $\mu_0 = 1.000$ | $\varpi = 0.9000$ | $\tau^* = 64.00$ | $g = 0.8480$ |

τ	Net irradiance		Error	Divergence		Error
	Exact	Twostr	(%)	Exact	Twostr	(%)
.000	2.77600	2.76577	-0.4	1.16100	1.16050	0.0
3.200	1.60500	1.60526	0.0	0.77500	0.78321	1.1
6.400	0.83000	0.82205	-1.0	0.63400	0.63931	0.8
12.800	0.19600	0.18274	-6.8	0.19400	0.18143	-6.5
32.000	0.00220	0.00131	-40.2	0.00210	0.00130	-38.3
48.000	0.00010	0.00002	-81.0	0.00010	0.00002	-81.3
64.000	0.00000	0.00000	0.0	0.00000	0.00000	0.0

Note: [a]The lower surface was assume to be black.

small closer to the top of the medium ($\tau < 12$), but becomes as large as 80% deep within the medium. Results for the mean radiance at the top and bottom of a Rayleigh scattering slab are shown in Table S.3. The slab overlies a Lambert reflector with albedo-values $\rho_L = 0$ (non-reflecting), $\rho_L = 0.25$, and $\rho_L = 0.80$. The error varies depending on the angle of illumination (μ_0), the optical depth of the slab (τ^*), and surface reflectance (ρ_L), but it is typically small (several %) except for a few cases where it is 10% or larger.

Tables S.4 and S.5 show results for an imbedded (thermal) source (*Prototype Problem 2*). Table S.4 displays emerging irradiances (top and bottom) and the irradiance divergence. The temperature was assumed to vary linearly with optical depth across the slab from 270 K at the top to 280 K at the bottom. The lower boundary ('surface') temperature was taken to be zero K for the non-scattering case $\varpi = 0$, and 300 K for the non-absorbing

Table S.3 *Two-stream results compared to accurate results for the mean radiance for conservative Rayleigh scattering ($\varpi = 1$, $g = 0$).*

μ_0	τ	$\rho_{\mathrm{L}} = 0.00$		Error	$\rho_{\mathrm{L}} = 0.25$		Error	$\rho_{\mathrm{L}} = 0.80$		Error
		Exact	Twostr	(%)	Exact	Twostr	(%)	Exact	Twostr	(%)
					$4\pi\overline{I(0)}/F^s$					
0.10	0.02	1.045	1.016	-2.8	1.089	1.061	-2.6	1.187	1.161	-2.2
0.10	0.25	1.170	1.085	-7.3	1.189	1.107	-6.9	1.239	1.165	-6.0
0.10	1.00	1.212	1.119	-7.7	1.220	1.128	-7.5	1.247	1.166	-6.5
0.40	0.02	1.047	1.017	-2.9	1.235	1.210	-2.1	1.653	1.640	-0.8
0.40	0.25	1.284	1.164	-9.3	1.402	1.296	-7.5	1.707	1.645	-3.7
0.40	1.00	1.534	1.374	-10.4	1.584	1.431	-9.7	1.778	1.650	-7.2
0.92	0.02	1.040	1.017	-2.2	1.477	1.467	-0.7	2.453	2.471	0.7
0.92	0.25	1.279	1.191	-6.9	1.597	1.542	-3.4	2.404	2.466	2.6
0.92	1.00	1.691	1.572	-7.1	1.851	1.754	-5.2	2.398	2.457	2.5
					$4\pi\overline{I(\tau)}/F^s$					
0.10	0.02	0.864	0.834	-3.4	0.912	0.881	-3.4	1.018	0.985	-3.3
0.10	0.25	0.192	0.156	-18.6	0.224	0.188	-16.1	0.307	0.271	-11.6
0.10	1.00	0.057	0.054	-4.4	0.082	0.081	-1.1	0.168	0.183	9.2
0.40	0.02	0.998	0.968	-3.0	1.203	1.168	-2.9	1.661	1.613	-2.9
0.40	0.25	0.787	0.693	-11.9	0.988	0.883	-10.6	1.502	1.382	-8.0
0.40	1.00	0.385	0.344	-10.6	0.540	0.500	-7.4	1.071	1.099	2.6
0.92	0.02	1.018	0.996	-2.2	1.495	1.461	-2.3	2.561	2.500	-2.4
0.92	0.25	1.028	0.950	-7.6	1.560	1.453	-6.9	2.928	2.776	-5.2
0.92	1.00	0.881	0.822	-6.7	1.384	1.320	-4.6	3.109	3.241	4.2

case ($\varpi = 1.0$). The total integrated Planck function ($\sigma_{\mathrm{B}} T^4/\pi$) was used to 'drive' the radiation field. The cases with no absorption ($\varpi = 0$) are 'extreme' because the two-stream approximation is known to have problems in this limit. These cases may therefore be considered as less favorable situations. We note that the error is never larger than about 11% for emerging irradiances, while the error is negligible for the irradiance divergence. In the conservative case the two-stream approximation yields slightly non-zero values for the irradiance divergence.

In Table S.5 two-stream results are compared with accurate multi-stream results for slabs of optical depths $\tau^* = 0.1$, 1.0, 10.0, 100.0, single-scattering albedo $\varpi = 0.1$ and 0.95, and asymmetry factors $g = 0.05$ and 0.75. The internal source was taken to be (isotropic) thermal radiation. The surface temperature was taken to be zero K, the top temperature to be 200 K, and the bottom temperature to be 300 K. Again, the temperature was assumed to vary linearly with optical depth in the slab, and the Planck function was

Table S.4 *Upward and downward irradiances and the irradiance divergence for a single layer in the limits $\varpi = 0$ and $\varpi = 1$ for isotropic scattering.*[a]

τ^*	ϖ	$F^+(0)$ Exact	$F^+(0)$ Twostr	Error (%)	$F^-(\tau^*)$ Exact	$F^-(\tau^*)$ Twostr	Error (%)
1.0	0.0	248.2	274.2	10.5	259.1	286.9	10.8
1000.0	0.0	301.4	301.4	0.0	348.5	348.5	0.0
10.0	1.0	53.623	41.791	-22.1	405.674	417.553	2.9

τ^*	ϖ	$dF(0)/d\tau$ Exact	$dF(0)/d\tau$ Twostr	Error (%)	$dF(\tau^*)/d\tau$ Exact	$dF(\tau^*)/d\tau$ Twostr	Error (%)
1.0	0.0	-669.4	-657.0	-1.8	-823.4	-820.2	-0.4
1000.0	0.0	-602.6	-602.6	0.0	-697.1	-697.1	0.0
10.0	1.0	0.000	-0.013	0.0	0.000	0.004	0.0

Note: [a]The temperature at the top of the layer is 270 K and 280 K at the bottom. It is assumed to vary linearly with optical depth across the layer. The surface temperature is 0 K for the $\varpi = 0$ cases and 300 K for the $\varpi = 1$ case. The Planck function was integrated over the interval 0.0–10,000.0 cm^{-1}. Exact results are from 16–stream calculations by the DISORT algorithm (described in Chapter 9).

Table S.5 *Two-stream results compared to accurate results for thermal radiation for different optical depths, single-scattering albedos, and asymmetry factors.*

τ^*	ϖ	g	$F^+(0)$ Exact	$F^+(0)$ Twostr	Error (%)	$F(0)-F(\tau^*)$ Exact	$F(0)-F(\tau^*)$ Twostr	Error (%)
0.10	0.10	0.05	19.271	20.919	8.55	-39.839	-42.721	7.23
0.10	0.95	0.75	1.264	1.282	1.40	-2.575	-2.581	0.23
1.00	0.10	0.05	80.164	87.250	8.84	-195.348	-214.882	10.00
1.00	0.95	0.75	11.317	11.615	2.64	-24.135	-24.577	1.83
10.00	0.10	0.05	63.725	61.501	-3.49	-265.788	-265.497	-0.11
10.00	0.95	0.75	53.001	48.385	-8.71	-136.632	-130.601	-4.41
100.00	0.10	0.05	56.541	55.965	-1.02	-270.983	-269.922	-0.39
100.00	0.95	0.75	39.423	34.325	-12.93	-172.113	-153.005	-11.10

integrated between wavenumbers 300 cm^{-1} and 800 cm^{-1} which includes the main portion of the thermal radiation. The maximum error in the two-stream results is about 12%.

S.5 Chapter 9 - Details and Derivations

The relationship between full-range and half-range Gaussian quadrature points and weights are displayed in Table S.5.

N	j	$2N+1-j$	u_j	w'_j	μ_j	w_j	μ_{2N+1-j}	w_{2N+1-j}
1	1	2	0.57735	1.00000	0.21132	0.50000	0.78868	0.50000
2	1	4	0.33998	0.65215	0.06943	0.17393	0.93057	0.17393
	2	3	0.86114	0.34785	0.33001	0.32607	0.66999	0.32607
3	1	6	0.23862	0.46791	0.03377	0.08566	0.96623	0.08566
	2	5	0.66121	0.36076	0.16940	0.18038	0.83060	0.18038
	3	4	0.93247	0.17132	0.38069	0.23396	0.61931	0.23396
4	1	8	0.18343	0.36268	0.01986	0.05061	0.98014	0.05061
	2	7	0.52553	0.31371	0.10167	0.11119	0.89833	0.11119
	3	6	0.79667	0.22238	0.23723	0.15685	0.76277	0.15685
	4	5	0.96029	0.10123	0.40828	0.18134	0.59172	0.18134
5	1	10	0.14887	0.29552	0.01305	0.03334	0.98695	0.03334
	2	9	0.43340	0.26927	0.06747	0.07473	0.93253	0.07473
	3	8	0.67941	0.21909	0.16030	0.10954	0.83970	0.10954
	4	7	0.86506	0.14945	0.28330	0.13463	0.71670	0.13463
	5	6	0.97391	0.06667	0.42556	0.14776	0.57444	0.14776
6	1	12	0.12523	0.24915	0.00922	0.02359	0.99078	0.02359
	2	11	0.36783	0.23349	0.04794	0.05347	0.95206	0.05347
	3	10	0.58732	0.20317	0.11505	0.08004	0.88495	0.08004
	4	9	0.76990	0.16008	0.20634	0.10158	0.79366	0.10158
	5	8	0.90412	0.10694	0.31608	0.11675	0.68392	0.11675
	6	7	0.98156	0.04718	0.43738	0.12457	0.56262	0.12457

S.5.1 Quadrature Formulas (§9.2.1)

The solution of the isotropic-scattering problem involves the following integral over angle

$$\int_{-1}^{1} du\, I(\tau, u) = \int_{0}^{1} d\mu\, I^{+}(\tau, \mu) + \int_{0}^{1} d\mu\, I^{-}(\tau, \mu).$$

In the two-stream approximation we replaced the integration over u with the simple formula

$$\int_{-1}^{1} du\, I \approx I^{+}(\tau) + I^{-}(\tau).$$

The accuracy can be improved by including more points in a *numerical-integration or quadrature formula*

$$\int_{-1}^{1} du\, I(\tau, u) \approx \sum_{j=1}^{m} w'_j I(\tau, u_j).$$

w'_j is a *quadrature weight* and u_j is a *discrete ordinate*. The simplest example is the *trapezoidal rule*

$$\int_{-1}^{1} du\, I \approx \Delta u(\frac{1}{2}I_1 + I_2 + I_3 + \cdots + I_{m-1} + \frac{1}{2}I_m)$$

and the more accurate Simpson's rule is

$$\int_{-1}^{1} du I \approx \frac{\Delta u}{3}(I_1 + 4I_2 + 2I_3 + 4I_4 + \cdots + I_m)$$

where Δu is the (equal) spacing between the adjacent points u_j, and the I_j denotes $I(\tau, u_j)$.

If we evaluate $I(\tau, u)$ at m points, we can replace I with its *approximating polynomial* $\phi(u)$, which is a polynomial of degree $(m - 1)$. Consider the following form for $\phi(u)$, for $m = 3$:

$$\phi(u) = I(u_1)\frac{(u - u_2)(u - u_3)}{(u_1 - u_2)(u_1 - u_3)} + I(u_2)\frac{(u - u_1)(u - u_3)}{(u_2 - u_1)(u_2 - u_3)}$$
$$+ I(u_3)\frac{(u - u_1)(u - u_2)}{(u_3 - u_1)(u_3 - u_2)}.$$

Here $\phi(u)$ is a second-degree polynomial which, when evaluated at the points u_1, u_2, and u_3 yields $I(u_1)$, $I(u_2)$, and $I(u_3)$, respectively. This expression for $\phi(u)$ is an example of *Lagrange's interpolation formula*, which can be abbreviated by use of the notation $\prod$ to indicate *products* of terms. For example, we may define

$$F(u) \equiv \prod_{j=1}^{m}(u - u_j) = (u - u_1)(u - u_2)\cdots(u - u_m).$$

Then, since the polynomial $(u-u_1)(u-u_2)\cdots(u-u_{j-1})(u-u_{j+1})\cdots(u-u_m)$ becomes $F(u)/(u - u_j) = \prod_{k \neq j}^{m}(u - u_k)$, we can write the polynomial $\phi(u)$ in a shorthand form

$$\phi(u) = \sum_{j=1}^{m} I(u_j)\frac{F(u)}{(u - u_j)F'(u_j)}$$

where $F'(u_j)$ is defined as $dF/du\rfloor_{u=u_j}$. We see that $F'(u)$ is a sum of m polynomials of degree $(m - 1)$, which, when evaluated at $u = u_j$, all vanish except for the polynomial $(u-u_1)(u-u_2)\cdots(u-u_{j-1})(u-u_{j+1})\cdots(u-u_m)$.

Hence, the quadrature formula arising from the assumption that the radiance is a polynomial of degree $(m - 1)$ is

$$\int_{-1}^{1} du \, I(u) = \sum_{j=1}^{m} w'_j I(u_j); \qquad w'_j = \frac{1}{F'(u_j)} \int_{-1}^{1} \frac{du \, F(u)}{(u - u_j)}.$$

The quadrature points u_j are, so far, arbitrary.

It can be shown that the error incurred by using the Lagrange interpolation formula is proportional to the mth derivative of the function $[I(u)]$ being approximated (see e.g. Burden and Faires (1985), p. 153). Thus, if $I(\tau, u)$ happens to be a polynomial of degree $(m - 1)$ or smaller, then the m-point quadrature formula is exact (see Exercise 9.1).

As already mentioned, the error in the Lagrange interpolation polynomial of degree $(m - 1)$ is proportional to the mth derivative of the function being approximated. The resulting quadrature schemes (usually referred to as the *Newton-Cotes formulas*) rely on using even spacing between the points at which the function is evaluated. But it is possible to obtain higher accuracy by choosing the quadrature or sampling points in an optimal manner. Gauss showed that if $F(u)$ is an mth-degree *Legendre polynomial $P_m(u)$*, and the quadrature points u_j are the roots of that polynomial, we get an accuracy of a polynomial of degree $(2m - 1)$. As seen earlier (see §6.2.4, Eq. 6.24), these polynomials are orthogonal and they are also orthogonal to every power of u less than m, that is:

$$\int_{-1}^{1} du \, P_m(u) u^\ell = 0 \qquad (\ell = 0, 1, 2, \cdots, m - 1).$$

Note that if u_j is a root of an even-degree Legendre polynomial, then $-u_j$ is also a root. Also, all m roots are real.

S.5.2 The Double-Gauss Method

We will proceed using a variant of the standard discrete-ordinate method, which will in general turn out to be the most accurate solution for a given order of approximation. It is customary to choose the *even-degree* Legendre polynomials as the approximating polynomial. This choice is made because the roots of the even-degree polynomials appear in *pairs*: if we use a negative index to label quadrature points in the downward hemisphere and a positive index for quadrature points in the upper hemisphere, then $u_{-i} = -u_{+i}$. The quadrature weights are the same in each hemisphere, i.e. $w'_i = w'_{-i}$. The 'full-range' approach is not optimal because it assumes that $I(\tau, u)$ is a smoothly-varying function of u $(-1 \leq u \leq +1)$ with no "rapid variation"

for all values of τ. We noted earlier that, in the absence of any information about the integrand, the Legendre polynomial yields optimum accuracy. However, we note that, at least for small τ, the radiance changes rather rapidly as u passes through zero, that is, as the line of sight passes through the horizontal. In fact at $\tau = 0$, this change is quite abrupt. Since there is no incoming diffuse radiation, $I(\tau, u)$ (for u slightly negative) is zero; and for slightly positive u-values it will generally have a finite value. It will clearly be difficult to 'fit' such a discontinuous distribution with a small number of terms involving polynomials that span continuously the full range between $u = -1$ and $u = 1$. Since the region near $\tau = 0$ is the most troublesome in terms of getting accurate solutions, we should pay the most attention to this region.

To remedy this situation, the *'Double-Gauss' method* was devised.[6] In this method, the hemispheres are treated separately. Instead of approximating $\frac{1}{2} \int_{-1}^{1} du I(u)$ by the sum $\frac{1}{2} \sum_{i=-N}^{+N} w_i' I(u_i)$ where w_i' and u_i are the weights and roots of the even-degree Legendre polynomial P_{2N}, we break the angular integration into two hemispheres, and approximate each integral separately

$$\int_{-1}^{1} du \ I = \int_{0}^{1} d\mu \ I^{+} + \int_{0}^{1} d\mu \ I^{-} \approx \sum_{j=1}^{M} w_j I^{+}(\mu_j) + \sum_{j=1}^{M} w_j I^{-}(\mu_j)$$

where the w_j and μ_j are the weights and roots of the approximating polynomial for the half-range. Note that we have used the *same* set of weights and roots for both hemispheres, which is not necessary, but obviously convenient. Now within each hemisphere, if we are to obtain the highest accuracy, we must again use Gaussian-Legendre quadrature. However, our new interval is $(0 \leq \mu \leq 1)$ instead of $(-1 \leq u \leq 1)$. This change is easily accomodated by defining the variable $u = 2\mu - 1$, so that the orthogonal polynomial is $P_M(2\mu - 1)$. The new quadrature weight is given by

$$w_j = \frac{1}{P_M'(2\mu_j - 1)} \int_{0}^{1} d\mu \frac{P_M(2\mu - 1)}{(\mu - \mu_j)} \tag{S.64}$$

and the μ_j are the roots of the half-range polynomials. It is easy to find the weights for $M = 1$ ($N = 2M = 2$) from the above formula (see Example 9.1 below).

Algorithms to compute the roots and weights are usually based on the full range. It is therefore useful to relate the half-range quadrature points μ_j and weights w_j to the corresponding points u_j and weights w_j' for the full

---

[6] Sykes (1951) is generally given the credit for this suggestion. Actually, this method was first proposed by J. Yvon, according to Kourganoff (1952), p. 101.

range. Since the linear transformation $t = (2x - x_1 - x_2)/(x_2 - x_1)$ will map any interval $[x_1, x_2]$ into $[-1, 1]$ provided $x_2 > x_1$, Gaussian quadrature can be used to approximate

$$\int_{x_1}^{x_2} dx I(x) = \int_{-1}^{1} dt I \left[\frac{(x_2 - x_1)t + x_2 + x_1}{2} \right] \frac{(x_2 - x_1)}{2}.$$

Choosing $x_1 = 0$, $x_2 = 1$, $x = \mu$ and $t = u$, we find

$$\int_0^1 d\mu I(\mu) = \frac{1}{2} \int_{-1}^{1} du I[(u+1)/2]$$

and by applying Gaussian quadrature to each integral, we find on setting $M = 2N$ for the half-range

$$\int_0^1 d\mu I(\mu) = \sum_{j=1}^{2N} w_j I(\mu_j) = \frac{1}{2} \int_{-1}^{1} du I[(u+1)/2] = \frac{1}{2} \sum_{\substack{j=-N \\ j \neq 0}}^{N} w_j' I[(u_j + 1)/2].$$

(S.65)

Thus, for even-degree Legendre polynomials the half-range points μ_j and weights w_j are related to the corresponding full-range points u_j and weights w_j' by

$$\mu_j = \frac{u_j + 1}{2}; \qquad w_j = \frac{1}{2} w_j'. \tag{S.66}$$

S.5.3 Four-stream approximation ($N = 2$)

In this case we obtain four coupled differential equations from Eqs. 9.7 and 9.8 as follows (again by assuming that we have chosen a quadrature satisfying

$\mu_{-i} = -\mu_i,\ w_{-i} = w_i)$

$$\mu_1 \frac{dI^+(\tau, \mu_1)}{d\tau} = I^+(\tau, \mu_1) - Q'^+(\tau, \mu_1)$$
$$-w_2 \frac{\varpi}{2} p(-\mu_2, \mu_1) I^-(\tau, \mu_2) - w_1 \frac{\varpi}{2} p(-\mu_1, \mu_1) I^-(\tau, \mu_1)$$
$$-w_1 \frac{\varpi}{2} p(\mu_1, \mu_1) I^+(\tau, \mu_1) - w_2 \frac{\varpi}{2} p(\mu_2, \mu_1) I^+(\tau, \mu_2)$$

$$\mu_2 \frac{dI^+(\tau, \mu_2)}{d\tau} = I^+(\tau, \mu_2) - Q'^+(\tau, \mu_2)$$
$$-w_2 \frac{\varpi}{2} p(-\mu_2, \mu_2) I^-(\tau, \mu_2) - w_1 \frac{\varpi}{2} p(-\mu_1, \mu_2) I^-(\tau, \mu_1)$$
$$-w_1 \frac{\varpi}{2} p(\mu_1, \mu_2) I^+(\tau, \mu_1) - w_2 \frac{\varpi}{2} p(\mu_2, \mu_2) I^+(\tau, \mu_2)$$

$$-\mu_1 \frac{dI^-(\tau, \mu_1)}{d\tau} = I^-(\tau, \mu_1) - Q'^-(\tau, \mu_1)$$
$$-w_2 \frac{\varpi}{2} p(-\mu_2, -\mu_1) I^-(\tau, \mu_2) - w_1 \frac{\varpi}{2} p(-\mu_1, -\mu_1) I^-(\tau, \mu_1)$$
$$-w_1 \frac{\varpi}{2} p(\mu_1, -\mu_1) I^+(\tau, \mu_1) - w_2 \frac{\varpi}{2} p(\mu_2, -\mu_1) I^+(\tau, \mu_2)$$

$$-\mu_2 \frac{dI^-(\tau, \mu_2)}{d\tau} = I^-(\tau, \mu_2) - Q'^-(\tau, \mu_2)$$
$$-w_2 \frac{\varpi}{2} p(-\mu_2, -\mu_2) I^-(\tau, \mu_2) - w_1 \frac{\varpi}{2} p(-\mu_1, -\mu_2) I^-(\tau, \mu_1)$$
$$-w_1 \frac{\varpi}{2} p(\mu_1, -\mu_2) I^+(\tau, \mu_1) - w_2 \frac{\varpi}{2} p(\mu_2, -\mu_2) I^+(\tau, \mu_2).$$

We may rewrite these equations in matrix form as follows

$$\frac{d}{d\tau} \begin{bmatrix} I^+(\tau, \mu_1) \\ I^+(\tau, \mu_2) \\ I^-(\tau, \mu_1) \\ I^-(\tau, \mu_2) \end{bmatrix} = \begin{bmatrix} -\alpha_{11} & -\alpha_{12} & -\beta_{11} & -\beta_{12} \\ -\alpha_{21} & -\alpha_{22} & -\beta_{21} & -\beta_{22} \\ \beta_{11} & \beta_{12} & \alpha_{11} & \alpha_{12} \\ \beta_{21} & \beta_{22} & \alpha_{21} & \alpha_{22} \end{bmatrix} \begin{bmatrix} I^+(\tau, \mu_1) \\ I^+(\tau, \mu_2) \\ I^-(\tau, \mu_1) \\ I^-(\tau, \mu_2) \end{bmatrix}$$
$$- \begin{bmatrix} Q^+(\tau, \mu_1) \\ Q^+(\tau, \mu_2) \\ Q^-(\tau, \mu_1) \\ Q^-(\tau, \mu_2) \end{bmatrix} \tag{S.67}$$

where

$$Q^{\pm}(\tau,\mu_i) = \pm\mu_i^{-1}Q'^{\pm}(\tau,\mu_i), \qquad i = 1,2$$

$$\alpha_{11} = \mu_1^{-1}[w_1\frac{\varpi}{2}p(\mu_1,\mu_1) - 1] = \mu_1^{-1}[w_1\frac{\varpi}{2}p(-\mu_1,-\mu_1) - 1]$$

$$\alpha_{12} = \mu_1^{-1}w_2\frac{\varpi}{2}p(\mu_1,\mu_2) = \mu_1^{-1}w_2\frac{\varpi}{2}p(-\mu_1,-\mu_2)$$

$$\alpha_{21} = \mu_2^{-1}w_1\frac{\varpi}{2}p(\mu_2,\mu_1) = \mu_2^{-1}w_1\frac{\varpi}{2}p(-\mu_2,-\mu_1)$$

$$\alpha_{22} = \mu_2^{-1}[w_2\frac{\varpi}{2}p(\mu_2,\mu_2) - 1] = \mu_2^{-1}[w_2\frac{\varpi}{2}p(-\mu_2,-\mu_2) - 1]$$

$$\beta_{11} = \mu_1^{-1}w_1\frac{\varpi}{2}p(\mu_1,-\mu_1) = \mu_1^{-1}w_1\frac{\varpi}{2}p(-\mu_1,\mu_1)$$

$$\beta_{12} = \mu_1^{-1}w_2\frac{\varpi}{2}p(\mu_1,-\mu_2) = \mu_1^{-1}w_2\frac{\varpi}{2}p(-\mu_1,\mu_2)$$

$$\beta_{21} = \mu_2^{-1}w_1\frac{\varpi}{2}p(\mu_2,-\mu_1) = \mu_2^{-1}w_1\frac{\varpi}{2}p(-\mu_2,\mu_1)$$

$$\beta_{22} = \mu_2^{-1}w_2\frac{\varpi}{2}p(\mu_2,-\mu_2) = \mu_2^{-1}w_2\frac{\varpi}{2}p(-\mu_2,\mu_2).$$

We introduce the two-element row vectors

$$\mathbf{I}^{\pm} = \left\{I^{\pm}(\tau,\mu_i)\right\}, \qquad \mathbf{Q}^{\pm} = \{Q^{\pm}(\tau,\mu_i)\}, \qquad i = 1,2$$

where $\{I^{\pm}(\tau,\mu_i)\}$ or $\{Q^{\pm}(\tau,\mu_i)\}$ stands for the two-element row vector with $\mu_i = 1$ and $\mu_i = 2$. Then we may write Eq. S.67 in a more compact form as

$$\frac{d}{d\tau}\begin{bmatrix}\mathbf{I}^+\\\mathbf{I}^-\end{bmatrix} = \begin{bmatrix}-\tilde{\alpha} & -\tilde{\beta}\\\tilde{\beta} & \tilde{\alpha}\end{bmatrix}\begin{bmatrix}\mathbf{I}^+\\\mathbf{I}^-\end{bmatrix} - \begin{bmatrix}\mathbf{Q}^+\\\mathbf{Q}^-\end{bmatrix} \qquad (S.68)$$

where the elements of the 2×2 matrices $\tilde{\alpha}$ and $\tilde{\beta}$ are given by the four elements in the lower right and left corner, respectively, of the 4×4 matrix in Eq. S.67.

S.6 The merit of the interpolation scheme

Equations 9.43 and 9.44 provide a convenient means of computing the radiances for arbitrary angles, at any desired optical depth. However, the merit of these expressions depends crucially on the ability to compute efficiently the eigenvectors $\tilde{g}_j(\pm\mu)$ and the particular solution vector $\tilde{Z}_0(\pm\mu)$. Since the eigenvectors $g_j(\mu)$ are known at the quadrature points ($\mu = \mu_i, i = \pm 1, \ldots, \pm N$), this information can be used as a basis for interpolation using any standard interpolation scheme. To illustrate the problems one might encounter in interpolation using standard techniques we show in Fig. S.5 the eigenvector corresponding to the smallest eigenvalue for a scattering
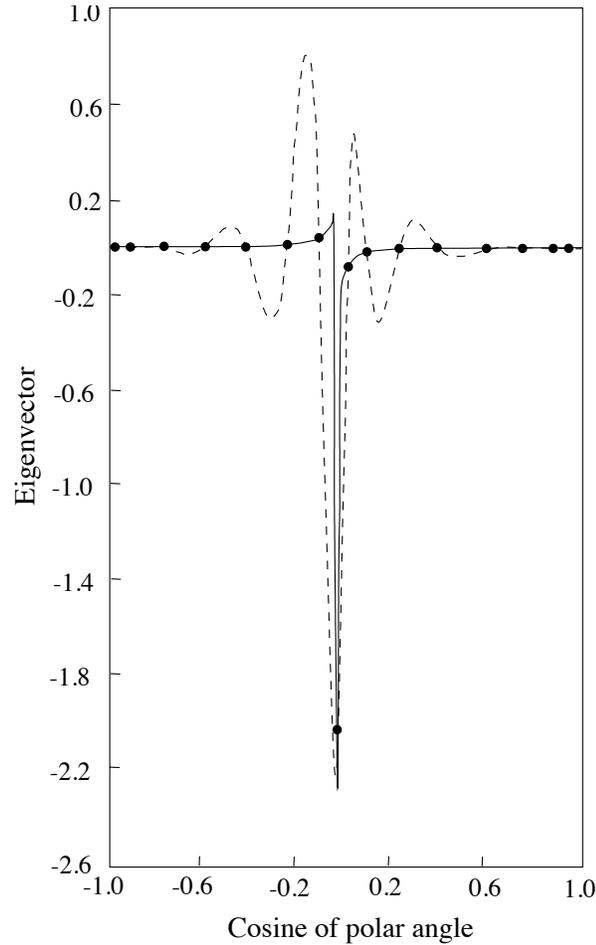
Figure S.5 Interpolated eigenvector. The solid line pertains to the use of the analytic formula in Eq. 9.41, the dashed line is a cubic spline interpolation, and the filled circles refer to values at the quadrature points. Note that the spline fails to produce accurate results, whereas the analytic formula gives adequate results.

phase function typical of atmospheric aerosols with single-scattering albedo $\varpi = 0.9$. This example illustrates the typical behavior of some of the eigenvectors. A 16-stream computation ($N = 8$) was used in this example. The values at the quadrature points to be interpolated are indicated by the dots. We see a pronounced dip close to $\mu = 0$, which obviously is difficult to fit with a polynomial expression. A cubic spline interpolation also performs poorly on both sides of the dip as illustrated, whereas the analytic expression (Eq. 9.41) yields quite adequate results.

To illustrate the consequence of using different interpolation schemes we computed diffuse radiances for a slab of optical thickness $\tau^* = 1.0$. The slab was illuminated by a collimated beam with $F^s = 1.0$ at an angle of incidence with $\mu_0 = 0.5$. The results are based on Eqs. 9.43 and 9.44. Figure S.6 shows the azimuthally-averaged diffuse radiance at optical depth $\tau = 0.05$. The solid line results from using the analytic expressions (Eqs. 9.41 and 9.42) to compute the eigenvectors and the particular solution vector. The results obtained by using cubic spline interpolation of the eigenvectors are shown by the dashed line. We notice that the cubic spline interpolation leads to erroneous results for $-0.6 < u < -0.1$.

This example illustrates that an interpolation scheme which interpolates the eigenvectors, is perhaps best suited as a general purpose interpolation scheme since it can provide radiances at any desired angle and depth. As we have seen, the analytic expressions (Eqs. 9.41 and 9.42) yield adequate results.

S.7 Removal of Numerical Ill-Conditioning

By "ill-conditioning" we mean that when Eqs. 9.50 and 9.51 are written in matrix form the resulting matrix cannot be successfully inverted by existing computers that work with "finite-digit" arithmetic. As we shall see below, if τ^* is sufficiently large, some of the elements of the matrix become huge while others become tiny, and this situation leads to ill-conditioning.

Attempts to solve Eqs. 9.50 and 9.51 as they stand reveal that they are notoriously ill-conditioned. In fact, this problem explains why the discrete-ordinate method has not been used very frequently by researchers in the past. We shall now show that this ill-conditioning can be completely eliminated, which makes the method very useful for solving practical problems. The root of the ill-conditioning problem lies in the occurrence of exponentials with positive arguments in Eqs. 9.50 and 9.51 (recall that $k_j > 0$ by convention) which must be removed. This removal is achieved by the scaling transformation

$$C_{+j} = C'_{+j}e^{k_j\tau_\mathrm{t}} \qquad \text{and} \qquad C_{-j} = C'_{-j}e^{-k_j\tau_\mathrm{b}}. \tag{S.69}$$

where we have written τ_t and τ_b for the optical depths at the top and the bottom of the layer, respectively. This was done deliberately in anticipation of generalizing this scaling scheme to apply to a multi-layered medium. In the present one-layer case we have, of course, $\tau_\mathrm{t} = 0$ and $\tau_\mathrm{b} = \tau^*$.

Inserting Eqs. S.69 into Eqs. 9.50 and 9.51 and solving for the C'_j instead of the C_j, we find that all the exponential terms in the coefficient
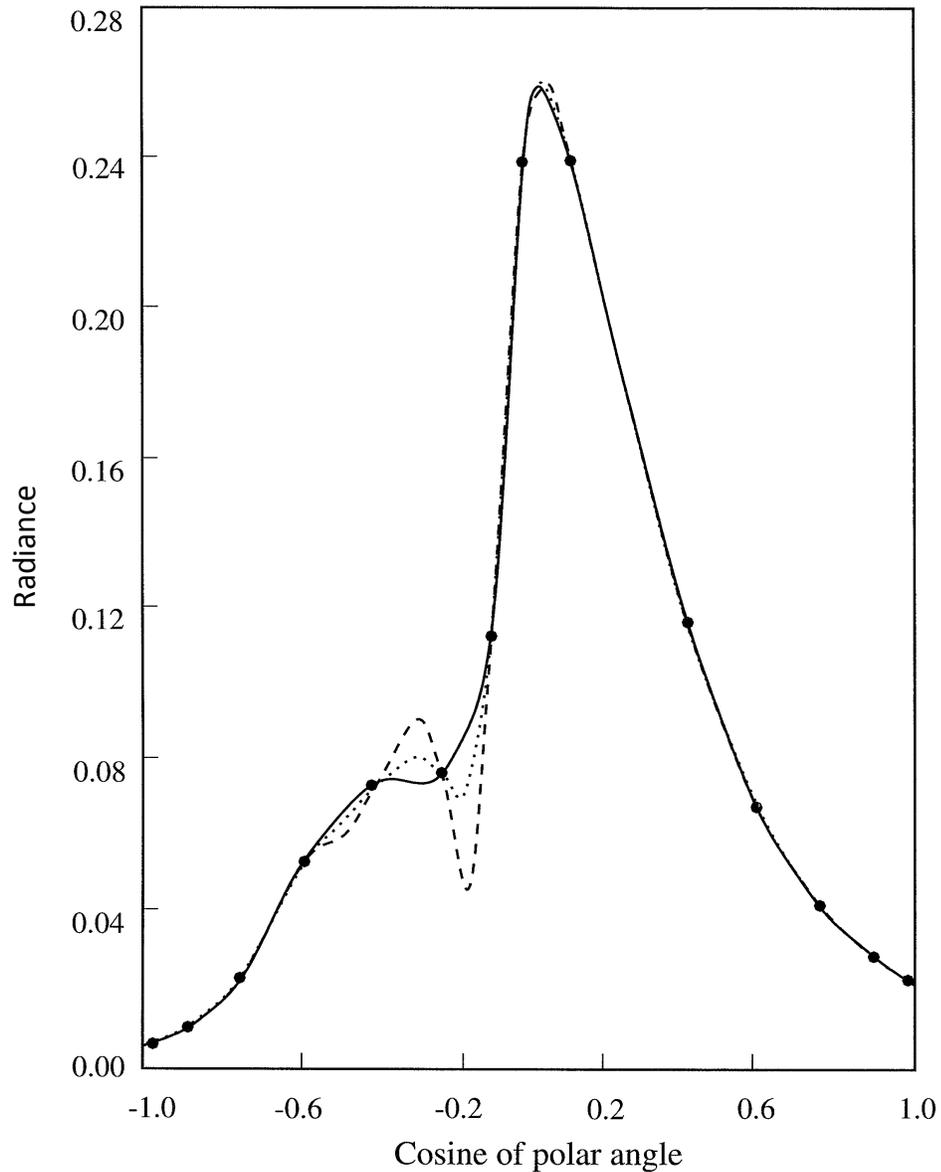
Figure S.6 Azimuthally-averaged radiance at $\tau = 0.05$ for oblique incidence ($\mu_0 = 0.5$) of collimated light of unit irradiance on a slab of total optical depth $\tau^* = 1$. The slab consists of particles that scatter radiation according to an isotropic scattering phase function (aerosol particles, see Fig. 6.3) with single-scattering albedo $\varpi = 0.9$. The solid line is obtained from the analytic expressions (Eqs. 9.43 and 9.44 using Eqs. 9.41 and 9.42), the dashed line from cubic spline interpolation of the eigenvectors, and the dotted line from cubic spline interpolation of the radiances at the quadrature points. The filled circles denote the values of the radiances at the quadrature points.

matrix have negative arguments ($k_j > 0, \tau_{\mathrm{b}} > \tau_{\mathrm{t}}$). Consequently, numerical ill-conditioning is avoided implying that the system of algebraic equations determining the C'_j will be unconditionally stable for arbitrary layer thickness.

As stated above, the merit of the scaling transformation is to remove all positive arguments of the exponentials occurring in the matrix elements of the coefficient matrix. To demonstrate how this scheme works we shall use the two-stream case as an example.

S.7.1 Removal of Ill-Conditioning – Two-Stream Case ($N = 1$)

In this simple case, Eqs. 9.50 and 9.51 reduce to

$$C_1 g_1(-\mu_1)e^{-k\tau_{\mathrm{t}}} + C_{-1}g_{-1}(-\mu_1)e^{k\tau_{\mathrm{t}}} = C_1 g_1^- e^{-k\tau_{\mathrm{t}}} + C_{-1}g_{-1}^- e^{k\tau_{\mathrm{t}}} = (RHS)_{\mathrm{t}}$$

$$r_1 C_1 g_1(+\mu_1)e^{-k\tau_{\mathrm{b}}} + r_{-1}C_{-1}g_{-1}(+\mu_1)e^{k\tau_{\mathrm{b}}} = r_1 C_1 g_1^+ e^{-k\tau_{\mathrm{b}}} + r_{-1}C_{-1}g_{-1}^+ e^{k\tau_{\mathrm{b}}} = (RHS)_{\mathrm{b}}$$

where we have used Eqs. 9.24 and 9.25. The left hand side may be written in matrix form as

$$\begin{bmatrix} g_1^- e^{-k\tau_{\mathrm{t}}} & g_{-1}^- e^{k\tau_{\mathrm{t}}} \\ r_1 g_1^+ e^{-k\tau_{\mathrm{b}}} & r_{-1}g_{-1}^+ e^{k\tau_{\mathrm{b}}} \end{bmatrix} \begin{bmatrix} C_1 \\ C_{-1} \end{bmatrix}.$$

This matrix is ill-conditioned because one element becomes very large while another one becomes very small as $k\tau_{\mathrm{b}}$ (the product of the eigenvalue and the optical depth) becomes large. In practice this limits solutions to problems for which $k\tau_{\mathrm{b}} < 3$ or 4. As we go beyond the two-stream case the problem becomes more severe because some of the eigenvalues become large. We recall that for isotropic scattering the eigenvalues are flanked by the values $1/\mu_1$, $1/\mu_2$ etc., showing that the larger N is, the larger the biggest eigenvalue. This is the case also for anisotropic scattering. Hence, it is clear that for the method to be of any practical value this problem must be overcome.

Using the scaling transformation we find that the matrix above becomes

$$\begin{bmatrix} g_1^- & g_{-1}^- e^{-k(\tau_{\mathrm{b}}-\tau_{\mathrm{t}})} \\ r_1 g_1^+ e^{-k(\tau_{\mathrm{b}}-\tau_{\mathrm{t}})} & r_{-1}g_{-1}^+ \end{bmatrix} \begin{bmatrix} C'_1 \\ C'_{-1} \end{bmatrix}.$$

In the limit of large values of $k(\tau_{\mathrm{b}} - \tau_{\mathrm{t}})$ this matrix becomes

$$\begin{bmatrix} g_1^- & 0 \\ 0 & r_{-1}g_{-1}^+ \end{bmatrix}$$

which shows that the ill-conditioning problem has been eliminated.

S.8 Numerical Implementation of the Discrete Ordinate Method

The solution of the radiative transfer equation described in previous sections has been implemented numerically into a code written in FORTRAN. This code applies to vertically inhomogeneous, non-isothermal, plane-parallel media and it includes all the physical processes discussed previously, namely thermal emission, scattering, absorption, bidirectional reflection and thermal emission at the lower boundary. The medium may be forced at the top boundary by direct (collimated) or diffuse illumination and by internal and boundary sources as well.[7]

As discussed in §6.6 for strongly forward-peaked scattering, it is difficult to obtain accurate solutions to the radiative transfer equation. The δ-M method, which replaces the forward-scattering peak of the scattering phase function by a δ-function (see §6.6), is useful and improves the accuracy significantly, especially for irradiances and the mean radiance. The radiance computation is also generally improved by using δ-M but further improvements are desirable and essential if one desires to use low-order discrete ordinate approximations (say $N < 10$) to reduce the computational burden. Special algorithms have been invented to correct the radiance computation for strongly forward-peaked scattering. The development of such algorithms starts with the notion that the single scattering solution can be computed exactly and used to improve the accuracy. Such an algorithm, described in §9.9, is implemented in the DISORT code and used in conjunction with the δ-M method to provide acceptable accuracy for as little as 10 streams. Without these algorithms similar accuracy will typically require a quintupling of the number of streams which implies that they provide computational savings of the order of $5^3 = 125$ since the most time-consuming computation in DISORT is the solution of the algebraic eigenvalue problem and the inversion of the matrix required to obtain the constants of integration in which the computation time varies as the cube of half the number of streams (i.e. N^3).

In §6.9 we derived simple expressions for the irradiance reflectance and transmittance for media without internal sources and showed that an analytic correction allows us to find the solutions pertaining to reflecting (Lambert) surfaces. These expressions which are implemented in DISORT, offer substantial computational advantages when only integrated quantities such as irradiance reflectance and transmittance are required.

---

[7] A description of the code called DISORT is provided in a NASA report by Stamnes et al. (2000), and in Lin et al. (2015), and Laszlo et al. (2016).
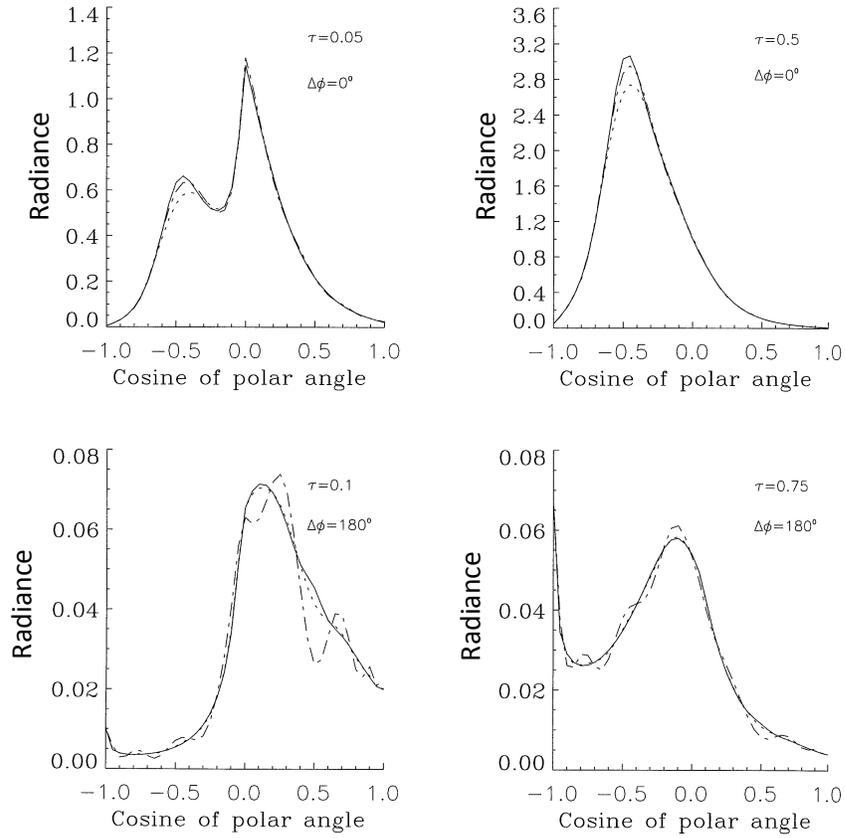
Figure S.7 Comparison of accurate (48-stream) and approximate 16-stream diffuse radiances computed with and without δ-M scaling at several optical depths within an aerosol layer of total optical depth $\tau^* = \tau_L = 1$ for $\Delta\phi = 0$ and 180°, $\varpi = 0.9$, and $\mu_0 = 0.5$. The solid curve is for 48 streams, the dashed and dotted-dashed curves are for 16 streams with and without δ-M scaling, respectively. Note that the ordinate scale is not the same in the various diagrams.
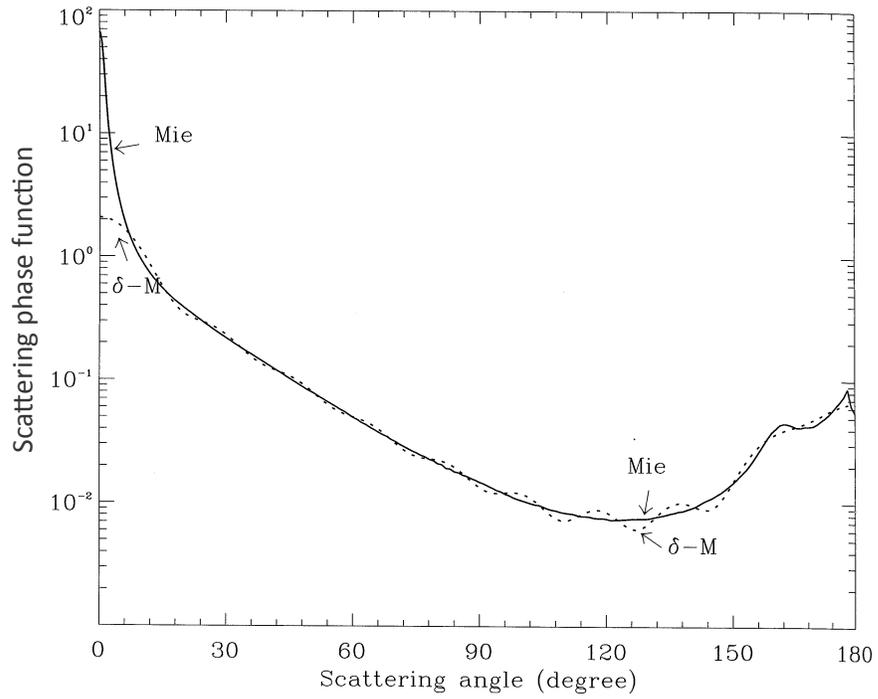
Figure S.8 Scattering phase function computed by Mie theory and the δ-M representation for $N = 10$.
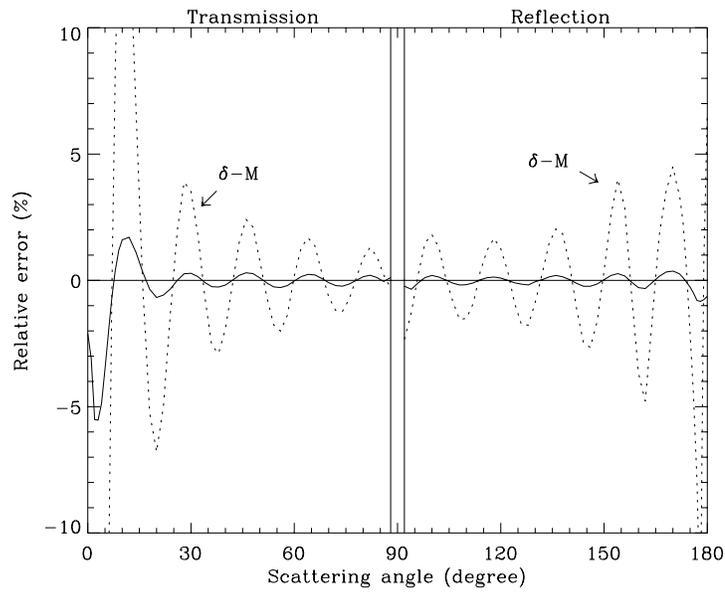
Figure S.9 Relative error of the reflected and transmitted radiances computed by strict application of δ-M and by applying a correction to the δ-M method (solid line) which is simply the difference between the singly-scattered radiance computed from the exact scattering phase function and from the δ-M scaled scattering phase function. This example pertains to vertical (collimated) illumination of a homogeneous slab of total optical depth 0.8 consisting of particles with scattering properties defined in Fig. S.8.
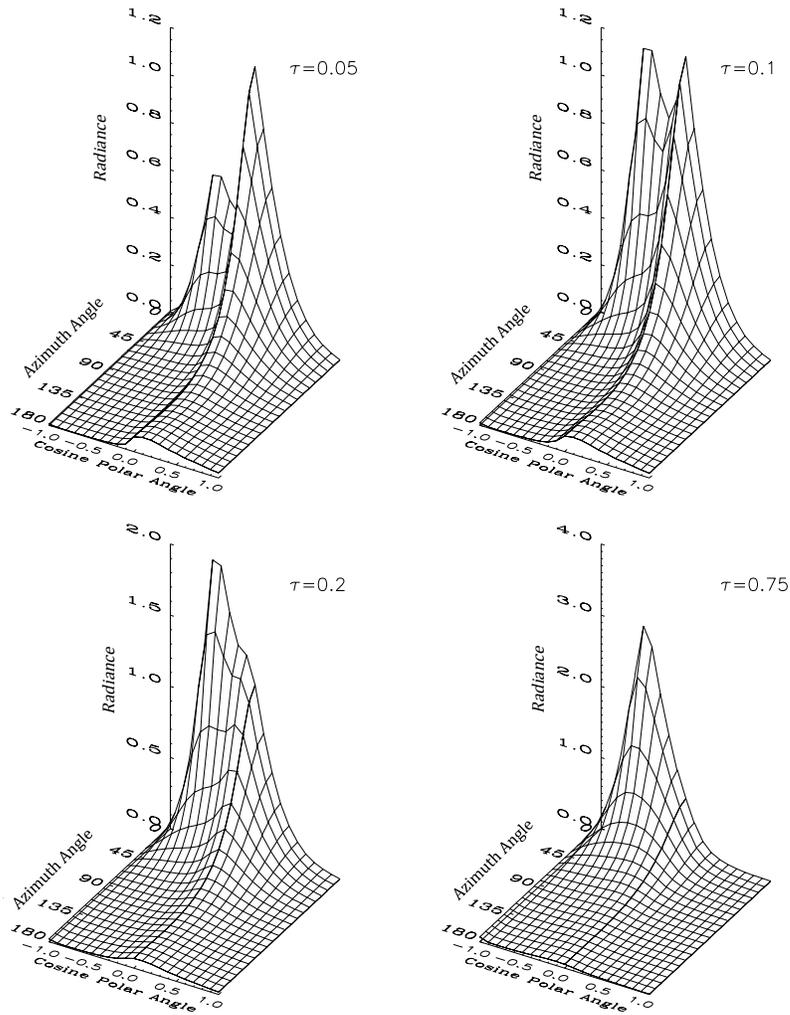
Figure S.10 Three-dimensional display of diffuse radiance versus polar and azimuth angles for several optical depths within a layer consisting of aerosol particles of total optical depth $\tau^* = 1$, single-scattering albedo $\varpi = 0.9$, and cosine of solar zenith angle $\mu_0 = 0.5$.
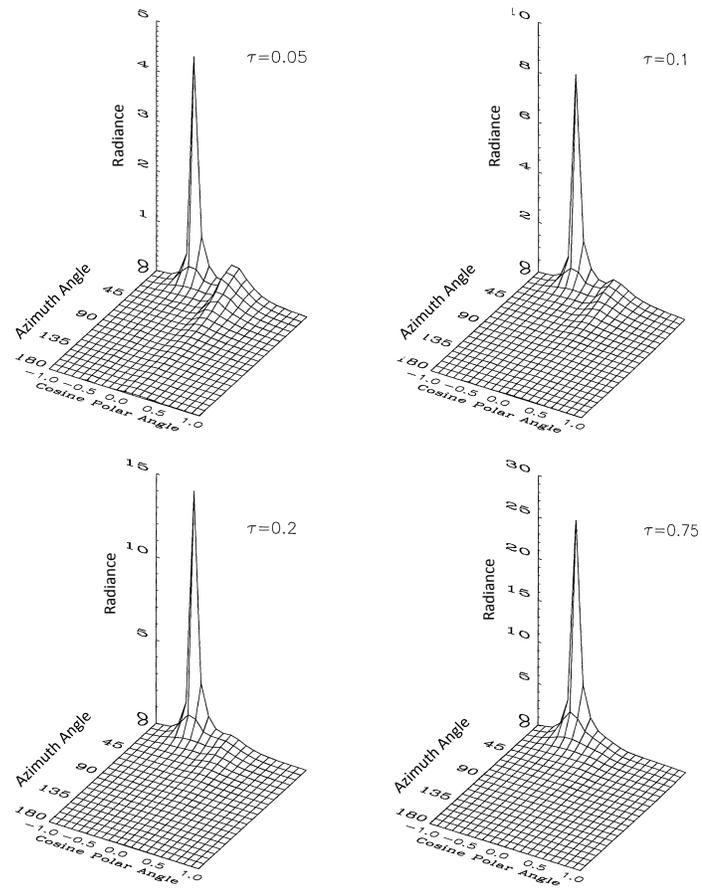
Figure S.11 Three-dimensional display of diffuse radiance versus polar and azimuth angles for several optical depths within a layer consisting of oceanic particles (hydrosols) of optical depth $\tau^* = 1$, single-scattering albedo $\varpi = 0.9$, and cosine of solar zenith angle $\mu_0 = 0.5$.
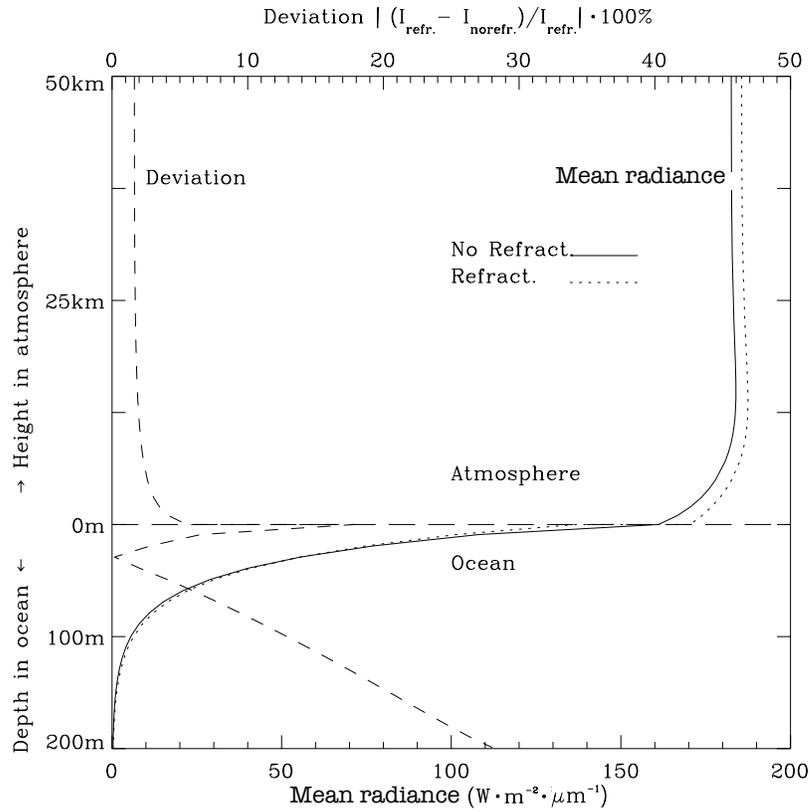
Figure S.12 Distribution of the total mean radiance (total scalar irradiance/4π in ocean optics terminology) with height in the atmosphere and depth in the ocean. The result of neglecting the refraction occurring at the atmosphere-ocean interface is also shown. The computation was done for a solar zenith angle of $30°$ and a wavelength of 500 nm.
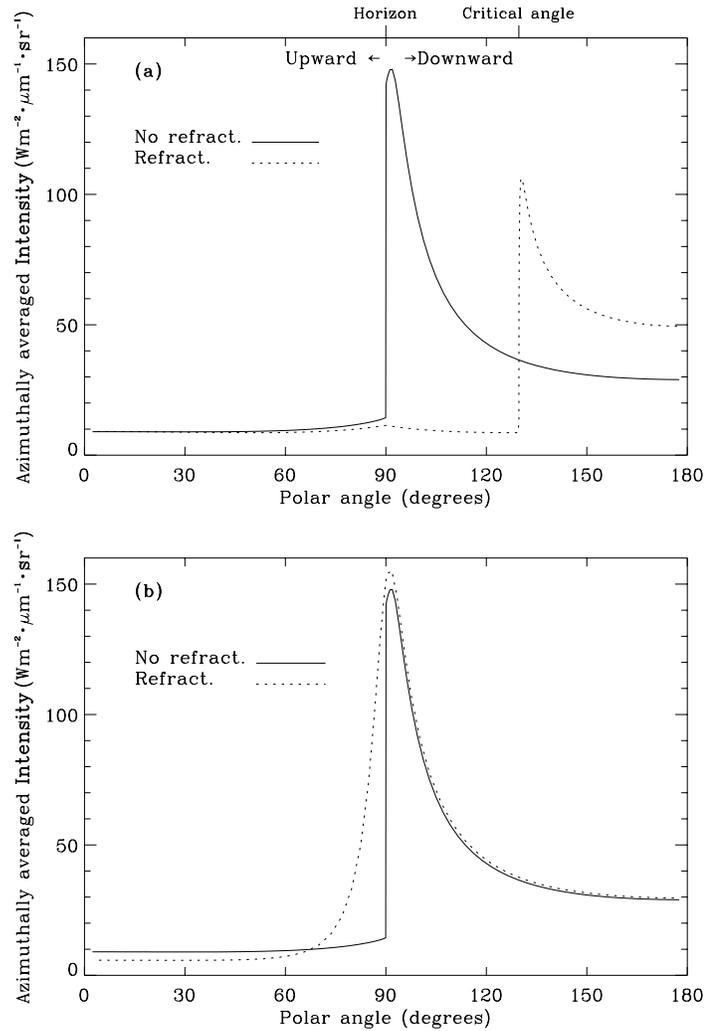
Figure S.13 Distributions of the azimuthally-averaged radiance including refraction in the ocean ($m_{\mathrm{ocn,r}} = 1.33$), and ignoring it ($m_{\mathrm{ocn,r}} = 1.0$). The computation was done for a solar zenith angle of $30°$ and a wavelength of 500 nm. (a) Just below the ocean surface; (b) just above the ocean surface.

Appendix T

Inherent Optical Properties

T.1 Atmosphere

As discussed in Chapter 1, the stratified vertical structure of the bulk properties of an atmosphere is a consequence of hydrostatic balance. For an atmosphere in a state of rest, the pressure $p(z)$ must support the weight of the fluid above it. By equating pressure forces and gravitational forces and invoking the ideal gas law, one finds that the bulk gas properties at any height is determined by the barometric law (Eq. 1.5).

T.1.1 Aerosol IOPs

It is customary to assume a log-normal distribution of aerosol sizes as proposed by Davies (1974). Based on AERONET[1] data, Ahmad et al. (2010) adopted a bi-modal log-normal volume size distribution (assuming spherical particles of radius r):

$$v(r) = \frac{dV(r)}{dr} = \frac{1}{r}\frac{dV(\ln r)}{d\ln r} = \sum_{i=1}^{2} \frac{V_i}{\sqrt{2\pi}\sigma_i}\frac{1}{r}\exp\left[-\left(\frac{\ln r - \ln r_{vi}}{\sqrt{2}\sigma_i}\right)^2\right].$$

$$(\text{T.1})$$

The subscript i represents the mode, V_i is the total volume of particles with mode i, r_{vi} is the mode radius, also called the volume geometric mean radius, and σ_i is the geometric standard deviation. Since the numerator in

---

[1] AERONET (Holben et al., 1998, 2001) is a federated instrument network and data archive managed by the National Aeronautics and Space Administration (NASA) Goddard Space Flight Center (GSFC) in partnership with the Laboratoire d'Optique Atmosphérique (LOA) of the Université des Sciences et Technologies de Lille (France).

the exponential of Eq. T.1 $\ln(r/r_{vi})$ is dimensionless, so is σ_i, and because

$$\int_0^\infty \frac{dr}{\sqrt{2\pi}\sigma} \frac{1}{r} \exp\left[- \left(\frac{\ln r - \ln r_v}{\sqrt{2}\sigma} \right)^2 \right] = 1$$

integration over all sizes for both modes, yields:

$$\int_0^\infty dr\, v(r) = V_1 + V_2 = V.$$

In terms of the number density, Eq. T.1 becomes

$$n(r) = \frac{dN(r)}{dr} = \frac{1}{r}\frac{dN(r)}{d\ln r} = \sum_{i=1}^2 \frac{N_i}{\sqrt{2\pi}\sigma_i} \frac{1}{r} \exp\left[- \left(\frac{\ln r - \ln r_{ni}}{\sqrt{2}\sigma_i} \right)^2 \right] \quad \text{(T.2)}$$

where the number of particles N_i and the mean geometric (or mode) radius r_{ni} are related to V_i and r_{vi} as follows

$$\ln r_{ni} = \ln r_{vi} - 3\sigma_i^2 \quad \text{(T.3)}$$

$$N_i = \frac{V_i}{\frac{4}{3}\pi r_{ni}^3} \exp(-4.5\sigma_i^2). \quad \text{(T.4)}$$

Integration of Eq. T.2 over all sizes for both modes, yields:

$$\int_0^\infty dr\, n(r) = N_1 + N_2 = N.$$

If we use the subscript $i = f$ to denote the fine mode, and the subscript $i = c$ to denote the coarse mode, we have $V = V_f + V_c$, and the volume fraction of fine mode particles becomes $f_v = V_f/V$.

Relationship between effective radius and mode radius

The particle size distribution may also be characterized by an effective radius

$$r_{\text{eff}} = \frac{\int_{r_{min}}^{r_{max}} dr\, r^3\, n(r)}{\int_{r_{min}}^{r_{max}} dr\, r^2\, n(r)} \quad \text{(T.5)}$$

and an effective variance

$$v_{\text{eff}} = \frac{\int_{r_{min}}^{r_{max}} dr\, r^2\, (r - r_{\text{eff}})^2\, n(r)}{r_{\text{eff}}^2 \int_{r_{min}}^{r_{max}} r^2\, dr\, n(r)} \quad \text{(T.6)}$$

where r_{eff}^2 is included in the denominator to make v_{eff} dimensionless (Hansen and Travis, 1974). The effective radius r_{eff} can be used to describe the IOPs in an approximate manner as will be discussed below for cloud as well as

snow/ice materials. For a single mode, the lognormal size distribution is given by (see Eq. T.2)

$$n(r) = \frac{dN(r)}{dr} = \frac{N}{\sqrt{2\pi}\sigma} \frac{1}{r} \exp\left[-\left(\frac{\ln r - \ln r_n}{\sqrt{2}\sigma} \right)^2 \right] \tag{T.7}$$

where r_n is the mode radius, $n(r)$ is the number density $[\text{m}^{-3}{\cdot}\text{m}^{-1}]$, and $N = \int_0^\infty dr\, n(r) \; [\text{m}^{-3}]$ is the total number of particles per unit volume. Using Eq. T.7, one can show that Eq. T.5 leads to (see Stamnes and Stamnes (2015) for details)

$$r_{\text{eff}} = r_n \exp[2.5\sigma^2] \tag{T.8}$$

and

$$v_{\text{eff}} = \exp\left[\sigma^2\right] - 1. \tag{T.9}$$

IOPs of a polydispersion – Integrating over the size distribution

For a polydispersion of spherical particles (denoted by the subscript p) we may compute the absorption and scattering coefficients and the scattering phase function by integrating over the size distribution $n(r)$ $[\text{m}^{-3}{\cdot}\text{m}^{-1}]$

$$\alpha_p(\lambda) = \int_{r_{min}}^{r_{max}} dr\, (\pi r^2) Q_\alpha(r) n(r) \tag{T.10}$$

$$\sigma_p(\lambda) = \int_{r_{min}}^{r_{max}} dr\, (\pi r^2) Q_\sigma(r) n(r) \tag{T.11}$$

$$p_p(\lambda, \Theta) = \frac{\int_{r_{min}}^{r_{max}} dr\, p_p(\lambda, \Theta, r) n(r)}{\int_{r_{min}}^{r_{max}} dr\, n(r)}. \tag{T.12}$$

The absorption or scattering "efficiency" $Q_\alpha(r)$ or $Q_\sigma(r)$ is defined as the ratio between the absorption or scattering cross section and the geometrical cross section πr^2. A Mie code (Du, 2004) is used to compute the IOPs of aerosol particles ($Q_\alpha(r), Q_\sigma(r)$, and $p_p(\lambda, \Theta, r)$ in Eqs. T.10–T.12), and a numerical quadrature is employed to integrate over the log-normal size distributions to obtain $\alpha_p(\lambda), \sigma_p(\lambda)$, and $p_p(\lambda, \Theta)$. Based on the bi-modal log-normal volume size distribution of the aerosols (Eq. T.1) the user specifies the fine mode volume fraction $f_v = V_f/V$, the volume mode radii r_{vf} and r_{vc} as well as the corresponding standard deviations σ_f and σ_c in addition to the refractive index of the particles relative to air.

In analogy to the liquid water content defined in Eq. T.15 below, we may introduce the aerosol mass content (AMC) for each mode defined as

$$\text{AMC} = \rho_a \int_{r_{min}}^{r_{max}} dr \, (\frac{4\pi r^3}{3}) n(r) \equiv \rho_a \, f_V \qquad [\text{kg} \cdot \text{m}^{-3}] \qquad (\text{T.13})$$

where ρ_a is the bulk aerosol density [kg·m^{-3}], and where we have defined the aerosol **volume fraction** (not to be confused with the fine mode volume fraction, f_v) as

$$f_V \equiv \int_{r_{min}}^{r_{max}} dr \, (\frac{4\pi r^3}{3}) n(r) = \text{AMC}/\rho_a \qquad (\text{dimensionless}). \qquad (\text{T.14})$$

T.1.2 Cloud IOPs

It is customary to introduce the liquid water content (LWC) defined as

$$\text{LWC} \equiv \rho_w \int_{r_{min}}^{r_{max}} dr \, (\frac{4\pi r^3}{3}) n(r) \equiv \rho_w \, f_V \qquad [\text{kg} \cdot \text{m}^{-3}] \qquad (\text{T.15})$$

where ρ_w is the liquid water mass density [kg·m^{-3}] and f_V stands for the dimensionless liquid (cloud) particle volume fraction defined in Eq. T.14, i.e. $f_V = \text{LWC}/\rho_w$. In Eq. T.5 for the effective radius r_{eff} the numerator is proportional to the concentration or LWC, while the denominator is related to the scattering coefficient (see Eq. T.11, omitting the subscript p) $\sigma = \int_0^\infty dr(\pi r^2) Q_\sigma(r) \, n(r)$ [m^{-1}]. If the size of the droplet is large compared to the wavelength λ, then $Q_\sigma(r) \to 2$. Therefore, in the visible spectral range where $2\pi r/\lambda >> 1$, we find

$$\sigma \approx \frac{3}{2} \frac{1}{\rho_w} \frac{\text{LWC}}{r_{\text{eff}}} = \frac{3}{2} \frac{f_V}{r_{\text{eff}}} \qquad [\text{m}^{-1}]. \qquad (\text{T.16})$$

Ice Cloud IOPs

Nonspherical ice crystal size distributions are usually expressed in terms of the maximum dimension (or length) L. Assuming that light scattering is proportional to the cross-sectional area of nonspherical particles, we may define an *effective size* (analogous to the effective radius for spherical droplets, Eq. T.5) as follows[2]

$$D_e \equiv \int_{L_{min}}^{L_{max}} dL \, D^2 \cdot L \cdot n(L) \Big/ \int_{L_{min}}^{L_{max}} dL \, D \cdot L \cdot n(L). \qquad (\text{T.17})$$

---

[2] The material below is taken from Fu and Liou (1993). A discussion of ice crystal optical properties is provided by Liou and Takano (1994), Kahnert (2003), and Wendisch and Yang (2012). A special issue of *Journal of Quantitative Spectroscopy & Radiative Transfer (volume 55, number 5, May, 1996)* was devoted to scattering by nonspherical particles.

Here $D(L)$ denotes the width, $n(L)$ is the distribution, and L_{max} and L_{min} are the maximum and minimum lengths of the ice crystals. Thus, the effective width (or size) is defined solely in terms of the ice crystal size distribution. The numerator is related to the ice water content (IWC) given by

$$\text{IWC} = \frac{3\sqrt{3}}{8}\rho_i \int_{L_{min}}^{L_{max}} dL \; D^2 \cdot L \cdot n(L) \tag{T.18}$$

where the volume of an hexagonal ice crystal, $3\sqrt{3}D^2L/8$, is used and ρ_i is the bulk density of ice. The extinction coefficient is defined by

$$k \equiv \int_{L_{min}}^{L_{max}} dL \; k(D,L)n(L). \tag{T.19}$$

$k(D,L)$ is the extinction cross section for a single crystal. In the geometric optics limit, the extinction cross section is twice the effective cross-sectional area and may be expressed as

$$k(D,L) = \frac{3}{2}D\left[\frac{\sqrt{3}}{4}D + L\right]. \tag{T.20}$$

This expression for $k(D,L)$ is based on the assumption that the ice crystals are hexagonal and randomly oriented in space. In this case it can be shown that k/IWC is linearly related to $1/D_e$, *i.e.*

$$k \approx \text{IWC}(a + b/D_e) \tag{T.21}$$

where a and b are constants. By further assuming that the absorption is small, one may express the absorption cross section, as the product of the imaginary part of the refractive index, m_i, and the particle volume

$$\alpha_n(\lambda) = \frac{3\sqrt{3}\pi m_i(\lambda)}{2\lambda}D^2L. \tag{T.22}$$

The extinction and absorption cross sections defined above, combined with the notion that D and L are related, allow us to express the single-scattering co-albedo approximately in terms of best-fit constants c and d as

$$1 - \varpi_c \approx c + d \cdot D_e. \tag{T.23}$$

For cases in which the geometric optics assumption (underlying Eq. T.21), and the assumption of small absorption (underlying Eq. T.23) are not valid,

higher-order expansions may be used to represent the single-scattering properties of ice crystals more accurately

$$k_c = \text{IWC} \sum_{n=0}^{N} a_n/D_e^n; \qquad 1 - \varpi_c = \sum_{n=0}^{N} b_n/D_e^n \qquad (\text{T.24})$$

where a_n and b_n are coefficients to be determined by fitting accurate values to the above expressions, and N is the total number of terms required to achieve a desired accuracy. Note that Eqs. T.24 reduce to Eqs. T.21 and T.23 for $N = 1$. Finally, the moments of the scattering phase function may be determined in a similar fashion. For example, the first moment (i.e. the asymmetry factor, g_c) may be expressed in terms of coefficients, c_n, as follows

$$g_c = \sum_{n=0}^{N} c_n/D_e^n. \qquad (\text{T.25})$$

To determine the unknown coefficients one may use ray-tracing techniques developed for hexagonally-shaped particles if $D_e > 30$. For smaller D_e values solutions developed for spheroidally-shaped particles may be adopted in the absence of solutions valid for hexagonally-shaped crystals. Since the smaller sizes are usually associated with IR wavelengths where ice is highly absorbing, the detailed shape may not be critical in scattering and absorption computations.

In spite of a considerable effort by several groups worldwide to compute the optical properties of nonspherical particles the situation is less than satisfactory in that exact and approximate solutions seem to be generally lacking for nonspherical particles with size parameters between 20 and 30, in particular for shapes deviating substantially from that of the sphere (Liou and Takano, 1994). For size parameters larger than 30, raytracing based on geometrical optics may be used, while a variety of approaches have been tried for size parameters comparable to the wavelength of light. Because these approaches are generally based on theories valid for relatively small departures from the spherical shape they suffer from numerical ill-conditioning[3] when they are applied to particles with (i) large real and/or imaginary refractive index, (ii) large size compared with the wavelength of the incident light, and (iii) extreme shapes that deviate substantially from that of a sphere.

---

[3] This ill-conditioning is quite similar to that described in Chapter 9 in connection with the scaling transformation needed to make sure the matrix to be inverted to obtain the constants of integration in the discrete-ordinate method did not have some very large and some very small elements (see §9.7).

T.1.3 Snow and Ice IOPs

As discussed in Chapter 10, assuming that snow grains and sea ice inclusions consist of spherical particles, we may obtain their IOPs from Mie computations, which require the refractive index and the size distribution of the particles as input. Then, the IOPs, i.e. the absorption and scattering coefficients and the scattering phase function, $\alpha_p(\lambda), \sigma_p(\lambda)$, and $p_p(\lambda, \Theta)$, can be obtained from Eqs. T.10–T.12. Two options are available (i) direct Mie calculations based on available information about the particle refractive index and size assuming a log-normal size distribution; (ii) a fast, yet accurate parameterization based on Mie calculations.

Direct Mie calculations

For this option the snow grains and ice inclusions (air bubbles and brine pockets) are assumed to consist of homogeneous spheres with a single-mode log-normal volume size distribution (see Eq. T.1), and we use the refractive index data base for ice compiled by Warren and Brandt (2008). The user specifies the effective radius r_{eff} and the width of the distribution σ, from which the geometrical mean radius r_n is computed using Eq. T.8. r_n and σ constitute the only input required for using a Mie code to compute absorption and scattering coefficients as well the scattering phase function.

Parameterization based on Mie calculations

For a specific value of r, we can compute $Q_\alpha(r)$, $Q_\sigma(r)$, and $p_p(\lambda, \Theta, r)$ using Mie theory, but evaluation of Eqs. T.10–T.12 requires knowledge of the particle size distribution $n(r)$, which is usually unknown. We may simplify Eqs. T.10–T.12 by making the following assumptions (Stamnes et al., 2011) (i) the particle size distribution is characterized by an effective radius given by Eq. T.5, which obviates the need for an integration over r; (ii) the particles are weakly absorbing, so that

$$Q_\alpha(r) \equiv Q_\alpha \approx \frac{16\pi\, r_{\text{eff}}\, m_{i,p}}{3\lambda} \frac{1}{m_{\text{rel}}} [m_{\text{rel}}^3 - (m_{\text{rel}}^2 - 1)^{3/2}] \qquad (\text{T.26})$$

where $m_{\text{i,p}}$ is the imaginary part of the refractive index of the particle, λ is the wavelength in vacuum, and $m_{\text{rel}} = m_{\text{r,p}}/m_{\text{r,med}}$ is the ratio of the real part of the refractive index of the particle $(m_{\text{r,p}})$ to that of the surrounding medium $(m_{\text{r,med}})$; (iii) the particles are large compared to the wavelength $(2\pi r/\lambda \gg 1)$ implying

$$Q_\sigma(r) \equiv Q_\sigma = 2. \qquad (\text{T.27})$$

The scattering phase function may be represented by the Henyey-Greenstein function, which depends only on the asymmetry factor $g \equiv \langle \cos \Theta \rangle = \frac{1}{2} \int_{-1}^{1} p(\Theta) \cos \Theta \, d(\cos \Theta)$. With these assumptions, Eqs. T.10–T.12 become:

$$\alpha_p(\lambda) = \alpha(\lambda) \frac{1}{m_{\text{rel}}} \left[1 - (m_{\text{rel}}^2 - 1)^{3/2} \right] f_V \tag{T.28}$$

$$\sigma_p(\lambda) = \frac{3}{2} \frac{f_V}{r_{\text{eff}}} \tag{T.29}$$

$$p_p(\lambda, \Theta) = \frac{1 - g^2}{(1 + g^2 - 2g \cos \Theta)^{3/2}}. \tag{T.30}$$

Here $\alpha(\lambda) = 4\pi m_{i,p}/\lambda$ is the absorption coefficient of the material of which the particle is composed, and $f_V \equiv \frac{4\pi}{3} \int n(r) r^3 dr \approx \frac{4}{3} \pi r_{\text{eff}}^3 n_e$, where $n_e =$ number of particles per unit volume with radius r_{eff}. Note that Eq. T.29 is identical to Eq. T.16. Thus, it is clear that f_V represents the volume fraction of the particles as defined in Eq. T.14.

For wavelengths $\lambda \leq 1.2$ μm, the absorption and scattering efficiency for snow grains as well as brine inclusions and air bubbles in sea ice may be parameterized by Eqs. T.26 and T.27, and we may use the Henyey-Greenstein scattering phase function (Eq. T.30). To extend the validity to near infrared wavelengths, we may use modified parameterizations, based in part on fits to Mie calculations. For the absorption efficiency the modified parameterizations work well for all wavelengths shorter than 4 μm, while for the scattering efficiency and g they work well for wavelengths shorter than about 2.8 μm, but deviate significantly from Mie calculations for longer wavelengths. Thus, for wavelengths longer than 2.8 μm it may be preferable to use results from Mie theory [for details see Stamnes et al. (2011)].

Impurities, air bubbles, brine pockets, and snow

If the volume fraction of impurities, assumed to be distributed homogeneously within a snow grain, or in an ice sheet (fresh water ice or sea ice), or a brine pocket, is not too large, which is the case for typical situations occurring in nature, scattering by impurities can be ignored, so that their effects can be included by simply adding the imaginary part $m_{\text{i,imp}}$ of the refractive index for impurities to $m_{\text{i,p}}$ in Eq. T.26. The corresponding absorption coefficient is $\alpha_{\text{imp}} = 4\pi m_{\text{i,imp}}/\lambda$. For snow, the number of snow grain particles per unit volume is $N = (\frac{4}{3}\pi r_{\text{eff}}^3)^{-1} \frac{\rho_s}{\rho_i}$. Here r_{eff} is the effective particle radius, while ρ_s and ρ_i are the mass densities of snow and pure ice, respectively. The optical thickness and the single-scattering albedo of an ice layer can be calculated from the refractive indices of pure ice (Warren and Brandt, 2008) and impurities $m_{\text{i,imp}}$. Sea ice is assumed to consist of pure

ice with embedded brine pockets, air bubbles, and impurities. To include the effects of the embedded components, we first calculate the absorption coefficient α for sea ice (assuming non-absorbing air bubbles, $Q_{\alpha,\text{bu}} = 0$)

$$\alpha = \pi r_{\text{br}}^2 N_{\text{br}} Q_{\alpha,\text{br}} + \left[1 - \frac{4}{3}\pi r_{\text{br}}^3 N_{\text{br}} - \frac{4}{3}\pi r_{\text{bu}}^3 N_{\text{bu}} \right] \frac{4\pi(m_{\text{i,p}} + f_{\text{imp}} m_{\text{i,imp}})}{\lambda}$$

(T.31)

where f_{imp} is the volume fraction of impurities, N_{br} and N_{bu} are the number concentrations of brine pockets and air bubbles, respectively, r_{br} and r_{bu} are the corresponding effective radii, and $Q_{\alpha,\text{br}}$ is the absorption efficiency for brine pockets. The two terms on the right side of Eq. T.31 represent the absorption coefficients of brine pockets and surrounding ice (including impurities), respectively. In Eq. T.31, we have used the general relation $\alpha = 4\pi\, m_{\text{i,p}}/\lambda$, where λ is the wavelength in vacuum, and the expression inside the square brackets is the volume fraction of the ice surrounding all brine pockets and bubbles.

For brine pockets, which are in the liquid phase, the refractive index of sea water applies. The volume fraction V_{imp} of impurities typically lies in the range between 1×10^{-7} and 1×10^{-5}. The scattering coefficient σ of sea ice is given by

$$\sigma = \sigma_{\text{br}} + \sigma_{\text{bu}}; \quad \sigma_{\text{br}} = \pi r_{\text{br}}^2 N_{\text{br}} Q_{\sigma,\text{br}}; \quad \sigma_{\text{bu}} = \pi r_{\text{bu}}^2 N_{\text{bu}} Q_{\sigma,\text{bu}}$$

(T.32)

where σ_{br} and σ_{bu} are the scattering coefficients for brine pockets and air bubbles, respectively, and $Q_{\sigma,\text{br}}$ and $Q_{\sigma,\text{bu}}$ are the corresponding scattering efficiencies. Here we have ignored the scattering coefficient for pure sea ice because it is very small compared to either σ_{br} or σ_{bu}. The optical thickness τ, the single-scattering albedo ϖ, and the asymmetry factor g for a layer of sea ice of thickness h now become

$$\tau = (\alpha + \sigma)h; \qquad \varpi = \frac{\sigma}{\alpha + \sigma}; \qquad g = \frac{\sigma_{br} g_{\text{br}} + \sigma_{\text{bu}} g_{\text{bu}}}{\sigma_{\text{br}} + \sigma_{\text{bu}}}.$$

(T.33)

Salinity, density, and temperature may vary within the sea ice. Conditions representative for multiyear ice in the central Arctic in mid-May and September are: ice thickness 3 m, salinity 0.3%, density 0.9 mg $\cdot$ m^{-3} and surface temperature -10 °C. There is strong absorption in the IR portion of the solar spectrum and relatively weak absorption in the visible region. Salinity is unimportant for the optical properties of sea water but plays a significant role for sea ice, because of brine pocket development associated with brine rejection when sea ice melts. Therefore, the albedo of first-year ice is only about half the value of multi-year ice due to air bubble and brine pocket formation leading to increased scattering in the uppermost layer of
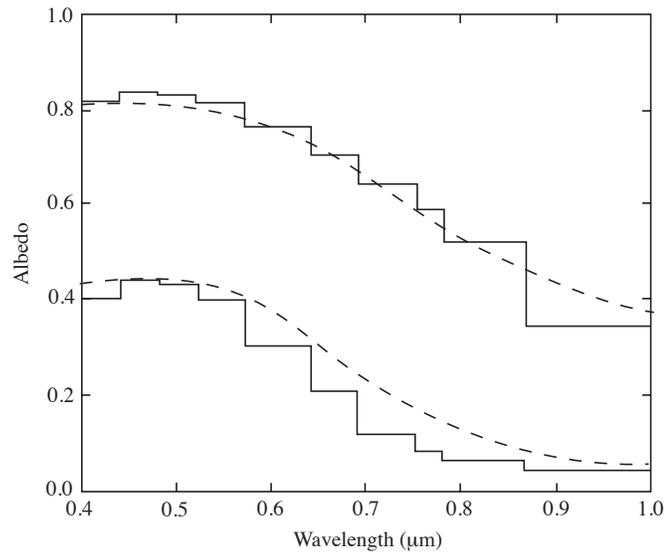
Figure T.1 Measured (broken lines) and computed (solid lines) albedo of first-year sea ice (lower set of curves) and multi-year sea ice (upper set of curves). The salinity and density were taken to be constant within the ice, and the temperature was assumed to vary linearly with depth from the surface value to a bottom temperature fixed at $-2\,°$C. Adapted from Jin et al. (1994).

multi-year ice. An illustration is provided in Fig. T.1 which shows a comparison between measured (Grenfell and Maykut, 1977), and computed (Jin et al., 1994) results. No attempt was made to 'tune' the model to get better agreement.

T.1.4 Water IOPs – Bio-optical models

In open ocean water, it is customary to assume that the IOPs of dissolved and particulate matter can be parameterized in terms of the chlorophyll concentration. In turbid waters, the IOPs will depend on the presence of several types of particulate matter including *inorganic (mineral) particles* and *organic (algae) particles*, in addition to pure water. The IOPs produced in this manner are said to result from a bio-optical model. For illustration purposes, we describe one such *bio-optical model* below (Ruddick et al., 2013), hereafter referred to as the CCRR (Coast Color Round Robin) *bio-optical model*.

Absorption and scattering by pure water

For *pure water*, we use the absorption coefficient $\alpha_w(\lambda)$ based on the data published by Pope and Fry (1997) for wavelengths between 400 and 700 nm, and by Kou et al. (1993) for wavelengths between 720 and 900 nm. Pure water scattering coefficients $\sigma_w(\lambda)$ are based on data published by Morel (1974).

Absorption and scattering by water impurities

The CCRR bio-optical model has three input parameters that are allowed to vary: (i) the *chlorophyll concentration* (CHL), (ii) the concentration of mineral particles (MIN), and (iii) the absorption coefficient $\alpha_{\mathrm{CDOM}}(443)$ due to colored dissolved organic matter (CDOM). It should be noted that the "mineral particle" component can include also non-algae particles whose absorption does not covary with that of the *algae particles* (Ruddick et al., 2013).

The absorption coefficient for *mineral particles* at 443 nm is given by[4]

$$\alpha_{\mathrm{MIN}}(443) = 0.031 \times \mathrm{MIN}$$

and its spectral variation is described by (Babin et al., 2003b)

$$\alpha_{\mathrm{MIN}}(\lambda) = \alpha_{\mathrm{MIN}}(443) \exp[-0.0123(\lambda - 443)]. \qquad \text{(T.34)}$$

The scattering coefficient at 555 nm is given by (Babin et al., 2003a)

$$\sigma_{\mathrm{MIN}}(555) = 0.51 \times \mathrm{MIN}$$

and the spectral variation of the attenuation coefficient is:

$$k_{\mathrm{MIN}}(\lambda) = k_{\mathrm{MIN}}(555) \times (\lambda_0/\lambda)^c, \quad c = 0.3749, \quad \lambda_0 = 555 \text{ nm} \qquad \text{(T.35)}$$

where λ is given in nm, and

$$\begin{aligned} k_{\mathrm{MIN}}(555) &= \alpha_{\mathrm{MIN}}(555) + \sigma_{\mathrm{MIN}}(555) \\ &= [0.031 \times \exp(-0.0123(555 - 443)) + 0.51] \times \mathrm{MIN} = 0.52 \times \mathrm{MIN}. \end{aligned}$$

The spectral variation of the scattering coefficient for mineral particles follows from

$$\sigma_{\mathrm{MIN}}(\lambda) = k_{\mathrm{MIN}}(\lambda) - \alpha_{\mathrm{MIN}}(\lambda). \qquad \text{(T.36)}$$

---

[4] Note on units: $\alpha_{\mathrm{MIN}}(\lambda)/\mathrm{MIN}$ has units $[\mathrm{m^2 \cdot g^{-1}}]$, so that if MIN has units of $[\mathrm{g \cdot m^{-3}}]$, then the units of $\alpha_{\mathrm{MIN}}(\lambda)$ will be $[\mathrm{m^{-1}}]$.

The absorption coefficient for *pigmented particles* (*algae particles* or phytoplankton) can be written

$$\alpha_{\text{pig}}(\lambda) = A_{\phi}(\lambda) \times [\text{CHL}]^{E_{\phi}(\lambda)} \qquad [\text{m}^{-1}] \qquad (\text{T.37})$$

where $A_{\phi}(\lambda)$ and $E_{\phi}(\lambda)$ are given by Bricaud et al. (1998). The chlorophyll concentration CHL [mg·m^{-1}] represents pigmented particles (algae particles or phytoplankton).

The attenuation coefficient for pigmented particles at 660 nm is given by (Loisel and Morel, 1998)

$$k_{\text{pig}}(660) = k_0 \times [\text{CHL}]^{\eta}; \qquad k_0 = 0.407; \qquad \eta = 0.795$$

and its spectral variation is taken to be (Morel et al., 2002a)

$$k_{\text{pig}}(\lambda) = k_{\text{pig}}(660) \times (\lambda/660)^{\nu} \qquad (\text{T.38})$$

where λ is given in nm, and

$$\nu = \begin{cases} 0.5 \times [\log_{10} \text{CHL} - 0.3] & 0.02 < \text{CHL} < 2.0 \\ 0 & \text{CHL} > 2.0. \end{cases}$$

The spectral variation of the scattering coefficient for *pigmented particles* follows from

$$\sigma_{\text{pig}}(\lambda) = k_{\text{pig}}(\lambda) - \alpha_{\text{pig}}(\lambda). \qquad (\text{T.39})$$

The absorption coefficient due to CDOM is given by (Babin et al., 2003b):

$$\alpha_{\text{CDOM}}(\lambda) = \alpha_{\text{CDOM}}(443) \times \exp[-S(\lambda - 443)] \qquad (\text{T.40})$$

where a slope parameter of $S = 0.0176$ represents an average value for different types of water. The total *absorption* and *scattering coefficients* due to water *impurities* for the CCRR bio-optical model are given by

$$\alpha_{\text{tot}}(\lambda) = \alpha_{\text{MIN}}(\lambda) + \alpha_{\text{pig}}(\lambda) + \alpha_{\text{CDOM}}(\lambda) \qquad (\text{T.41})$$

$$\sigma_{\text{tot}}(\lambda) = \sigma_{\text{MIN}}(\lambda) + \sigma_{\text{pig}}(\lambda). \qquad (\text{T.42})$$

Scattering Phase Function

For pure water, we use the *Rayleigh scattering phase function* [see Eq. 3.27 and Fig. 6.4] with *depolarization ratio* $\rho = 0.09$, and thus $f = (1 - \rho)/(1 + \rho) = 0.835$. For mineral particles the average *Petzold scattering phase function* (§6.5.4) with a *backscattering ratio* of 0.019 is used to describe the *scattering phase function*. For *pigmented (phytoplankton) particles* we may use the FF *scattering phase function* [see Eq. 6.46 and Fig. 6.4] with a *backscattering ratio* (see Eq. 6.47) equal to $b_{\text{FF}} = 0.006$ (Mobley et al., 2002; Morel

et al., 2002a). Mobley et al. (2002) showed that with proper choices of the real part of the *refractive index* m_r and the PSD slope ξ, the FF scattering phase function is an excellent proxy for the well-known Petzold (1972) measurements. In one particular study, Li et al. (2008) used $m_r = 1.069$ and $\xi = 3.38$, which correspond to a *backscattering ratio* of $b_{FF} = 0.0067$. As noted by Mobley et al. (2002), this choice of $\{m_r, \xi\}$ values is consistent with a certain mixture of living microbes and resuspended sediments. We may use Eq. 6.22 or Eq. 6.29 to compute Legendre *expansion coefficients* (or *moments* χ_ℓ) of the *scattering phase function*. For strongly forward-peaked scattering typical of the Petzold and FF scattering phase functions the moment-fitting methods of Wiscombe (1977b) and Hu et al. (2000) are very useful for computing $\chi_{\ell,PETZ}$ and $\chi_{\ell,FF}$. Thus, in the CCRR bio-optical model adopted in AccuRT the user must specify the three input parameters CHL, MIN, and $\alpha_{CDOM}(443)$ in addition to the vertical location of the impurities.

T.1.5 Spectral averaging of absorption coefficients

Since the scattering coefficient is a smooth function of wavelength, no spectral averaging is needed. In contrast, the absorption coefficient varies rapidly and erratically with wavelength making spectral averaging necessary.[5]

The Chandrasekhar Mean

The extraterrestrial (TOA) solar irradiance $F^s(\lambda)$ decreases rapidly with (decreasing) wavelength for $\lambda < 350$ nm, and the ozone absorption cross section increases rapidly between 350 nm and 250 nm. The steep gradients in the solar irradiance and ozone absorption cross section suggest that it may be useful to define a mean absorption cross section (called the Chandrasekhar Mean[6].) by weighting it with $F^s(\lambda)$ as follows:

$$\langle \alpha_n \rangle \equiv \frac{\int_{\lambda_1}^{\lambda_2} d\lambda\, \alpha_n(\lambda) F^s(\lambda)}{\int_{\lambda_1}^{\lambda_2} d\lambda\, F^s(\lambda)}. \tag{T.43}$$

Absorption by atmospheric gases

The TOA solar irradiance $F_0(\lambda) \equiv F^s(\lambda)$ will be attenuated due to absorption by gases in the atmosphere. The transmitted solar irradiance in the

---

[5] In the following we describe an approach in which the IOPs are averaged over a spectral bandwidth allowing for a single "quasi-monochromatic" computation. Note that a more accurate (but also more computationally demanding) way to average over a bandwidth is to compute radiances or irradiances at many monochromatic wavelengths, and then average the computed quantities.

[6] Two other definitions of the mean absorption cross section (the Planck and the Rosseland mean) were given in Chapter 8 (§8.4)

nadir direction at atmospheric depth level ℓ, with $\ell = 0$ at the TOA, can be expressed as:

$$F_\ell(\lambda) = F_0(\lambda) \, e^{-\tau_\ell(\lambda)}. \tag{T.44}$$

Hence, the atmospheric transmittance at level ℓ becomes

$$\mathcal{T}_\ell(\lambda) = \frac{F_\ell(\lambda)}{F_0(\lambda)} = e^{-\tau_\ell(\lambda)} \tag{T.45}$$

and the corresponding optical depth is

$$\tau_\ell(\lambda) = -\ln[\mathcal{T}_\ell(\lambda)]. \tag{T.46}$$

The irradiance measured by an instrument looking straight up at level ℓ with spectral response function $w(\lambda)$ and bandwidth $\Delta\lambda$ can be written

$$F_\ell^{\Delta\lambda} = \frac{\int_{\Delta\lambda} w(\lambda) F_\ell(\lambda) d\lambda}{\int_{\Delta\lambda} w(\lambda) d\lambda} = \frac{\int_{\Delta\lambda} w(\lambda) F_0(\lambda) \mathcal{T}_\ell(\lambda) d\lambda}{\int_{\Delta\lambda} w(\lambda) d\lambda} = \int_{\Delta\lambda} \tilde{w}(\lambda) F_0(\lambda) \mathcal{T}_\ell(\lambda) d\lambda \tag{T.47}$$

where $\tilde{w}(\lambda) = w(\lambda)/\int_{\Delta\lambda} w(\lambda) d\lambda$ is the "normalized" response function. Since $\mathcal{T}_0(\lambda) = 1$ (TOA), the band-weighted transmittance at level ℓ becomes:

$$\mathcal{T}_\ell^{\Delta\lambda} = \frac{F_\ell^{\Delta\lambda}}{F_0^{\Delta\lambda}} = \frac{\int_{\Delta\lambda} \tilde{w}(\lambda) F_0(\lambda) \mathcal{T}_\ell(\lambda) d\lambda}{\int_{\Delta\lambda} \tilde{w}(\lambda) F_0(\lambda) d\lambda}. \tag{T.48}$$

Hence, the band-weighted absorption optical depth at level ℓ becomes:

$$\tau_\ell^{\Delta\lambda} = -\ln[\mathcal{T}_\ell^{\Delta\lambda}]. \tag{T.49}$$

In AccuRT the band-weighted transmittance given by Eq. T.48 is evaluated numerically using a spectral resolution of 1 cm^{-1}.

Absorption by aerosol and cloud particles

Aerosol or cloud particles are assumed to consist of a polydispersion of homogeneous spheres with a specified wavelength-dependent refractive index. Since Mie computations are computing-intensive, Mie-computed absorption coefficients are tabulated at user-specified center wavelengths, and linear interpolation is used to obtain the absorption coefficient within the user-specified bandwidth.

Absorption by pure ice, impurities, inclusions, and snow grains

For pure ice, tabulated values of the imaginary part of the refractive index m_i (Warren and Brandt, 2008) are used to compute the absorption coefficient ($\alpha = 4\pi \, m_i/\lambda$), and linear interpolation is used to obtain the average

absorption coefficient within the user-specified bandwidth. Impurities (e.g. algae and soot) are assumed to be uniformly distributed within the ice and the absorption is given in terms of a user-specified imaginary part of the refractive index. Brine pockets and air bubbles embedded in the ice as well as snow grains are assumed to be spherical particles. For direct Mie calculations, computed absorption coefficients are tabulated at user-specified center wavelengths, and linear interpolation is used to obtain the average absorption coefficient within the user-specified bandwidth. For the parameterized option, we use the absorption coefficient of snow/ice particles given by Eq. T.28, which depends on the refractive index of ice. We use tabulated data for the real and the imaginary part of the refractive index of ice as a function of wavelength (Warren and Brandt, 2008) and linear interpolation to obtain values between wavelength grid points.

Absorption by liquid water

We use tabulated data for the absorption coefficient of pure water as a function of wavelength (Pope and Fry, 1997; Kou et al., 1993) and linear interpolation to obtain values between tabulated wavelength grid points. The absorption coefficient is obtained at 100 evenly spaced wavelengths within the user-specified wavelength bandwidth using liner interpolation between tabulated values, and then the average is computed. The absorption coefficient due to impurities in water is computed from a bio-optical model (see Eq. T.41) at user-specified center wavelengths, and linear interpolation is used to obtain the average absorption coefficient within the user-specified bandwidth.

Spectral solar irradiance

The solar irradiance is also averaged over 100 evenly spaced wavelengths within each user-specified wavelength bandwidth.

Appendix U

Model Atmospheres

Reference atmospheric models have long been used for a variety of purposes: validation of theoretical atmospheric models, intercomparison of radiation codes, and design and mission planning for aerospace systems, to mention a few applications. Standard atmospheres typically provide numerical values for the thermodynamic variables (pressure, temperature, density, etc.) and concentrations of minor species.

Atmospheric models may be considered to be the result of an ingestion of the best available data sets available at the time – consequently the older models (such as the 1976 U. S. Standard Atmosphere) do not represent the current state-of-the-art knowledge. For our purposes they are most useful for comparing the output of radiation codes, see for example Ellingson and Fouquart (1991).

In Tables C.1 to C.6 we present six model atmospheres which contain, among other variables, the temperature, and constituent concentrations for H_2O, CO_2, O_3 and NO_2. With the exception of CH_4 (not listed) these five species are the most important infrared-active gases in Earth's atmosphere. It should be mentioned that the tabulated values of H_2O and NO_2 in the upper stratosphere and mesosphere are not to be trusted as representative of the Earth's upper regions, since these models were created more than 40 years ago[1]. Modern remote sensing measurements of these constituents provide much more accurate values of H_2O, O_3, and NO_2,[2] as well as other species, such as NO and O.

---

[1] McClatchey, R. A., R. W. Fenn, J. E. A. Selby, F. E. Volz, and J. S. Garing, *Optical properties of the atmosphere*, Rep. AFCRL-71-0279, 85pp, Air Force Cambridge Res. Lab., Bedford, Mass, 1973.

[2] COSPAR International Reference Atmosphere: 1986, Part II: Middle Atmosphere Models, Adv. Space Res., 10, No. 12, 1990.

Table C.1. *AFGL Atmospheric Constituent Profiles, U.S. Standard Atmosphere 1976 (AFGL-TR-86-0110).*

z(km)	p(mb)	T(K)	air(cm^{-3})	O_3(cm^{-3})	O_2(cm^{-3})	H_2O(cm^{-3})	CO_2(cm^{-3})	NO_2(cm^{-3})
100.000	0.00032	195.100	1.187967E+13	4.756001E+06	1.902400E+12	4.756001E+06	2.318550E+09	2.021300E+03
95.000	0.00076	188.400	2.921760E+13	2.046800E+07	5.263200E+12	1.578960E+07	7.894800E+09	5.146240E+03
90.000	0.00184	186.900	7.130506E+13	4.995200E+07	1.355840E+13	6.065600E+07	2.212160E+10	1.305888E+04
85.000	0.00446	188.900	1.710073E+14	8.555000E+07	3.422000E+13	2.275630E+08	5.475200E+10	3.285120E+04
80.000	0.01050	198.600	3.829322E+14	1.149600E+08	8.008879E+13	7.855600E+08	1.256896E+11	7.740640E+04
75.000	0.02400	208.400	8.341139E+14	2.086750E+08	1.744523E+14	2.358028E+09	2.754510E+11	1.794605E+05
70.000	0.05220	219.600	1.721670E+15	5.169000E+08	3.601070E+14	6.030500E+09	5.685899E+11	3.980130E+05
65.000	0.10900	233.300	3.383947E+15	2.370200E+09	7.076740E+14	1.422120E+10	1.117380E+12	8.566580E+05
60.000	0.21900	247.000	6.421832E+15	7.068600E+09	1.343034E+15	3.052350E+10	2.120580E+12	1.831410E+06
55.000	0.42500	260.800	1.180302E+16	2.125800E+10	2.468290E+15	6.023100E+10	3.897300E+12	4.003590E+06
50.000	0.79780	270.700	2.134605E+16	6.621600E+10	4.464240E+15	1.116060E+11	7.048799E+12	9.462480E+06
47.500	1.09000	270.600	2.917498E+16	1.197200E+11	6.102800E+15	1.533000E+11	9.636000E+12	1.944720E+07
45.000	1.49100	264.200	4.087489E+16	2.147250E+11	8.548099E+15	2.137025E+11	1.349700E+13	4.703500E+07
42.500	2.06000	257.300	5.798815E+16	3.597860E+11	1.212827E+16	2.988545E+11	1.914990E+13	1.259251E+08
40.000	2.87100	250.400	8.304447E+16	6.066300E+11	1.736790E+16	4.175775E+11	2.742300E+13	3.348930E+08
37.500	4.15000	242.900	1.237464E+17	9.656401E+11	2.587420E+16	6.128100E+11	4.085400E+13	7.749880E+08
35.000	5.74600	236.500	1.759731E+17	1.380096E+12	3.680490E+16	8.628900E+11	5.811300E+13	1.282008E+09
32.500	8.01000	230.000	2.522415E+17	1.860945E+12	5.275160E+16	1.217830E+12	8.329200E+13	1.819804E+09
30.000	11.97000	226.500	3.827699E+17	2.509799E+12	8.004700E+16	1.809675E+12	1.263900E+14	2.359280E+09
27.500	17.43000	224.000	5.635873E+17	3.272892E+12	1.178760E+17	2.580300E+12	1.861200E+14	2.712840E+09
25.000	25.49000	221.600	8.331283E+17	4.266877E+12	1.742433E+17	3.689123E+12	2.751210E+14	3.118038E+09
24.000	29.72000	220.600	9.757872E+17	4.518265E+12	2.040885E+17	4.198950E+12	3.222450E+14	2.988090E+09
23.000	34.67000	219.600	1.143492E+18	4.768192E+12	2.390960E+17	4.804800E+12	3.775200E+14	2.951520E+09
22.000	40.47000	218.600	1.340895E+18	4.894274E+12	2.804780E+17	5.455230E+12	4.428600E+14	2.898720E+09
21.000	47.29000	217.600	1.574064E+18	4.769100E+12	3.291750E+17	6.260625E+12	5.197500E+14	2.772000E+09
20.000	55.29000	216.700	1.847990E+18	4.768571E+12	3.864410E+17	7.211100E+12	6.101700E+14	2.570110E+09
19.000	64.67000	216.700	2.161503E+18	4.390890E+12	4.520670E+17	8.327550E+12	7.137900E+14	2.292780E+09
18.000	75.65000	216.700	2.528494E+18	4.015110E+12	5.287700E+17	9.677249E+12	8.349000E+14	1.950630E+09
17.000	88.50000	216.700	2.957987E+18	3.513520E+12	6.186399E+17	1.139600E+13	9.768000E+14	1.536240E+09
16.000	103.50000	216.700	3.459340E+18	3.012286E+12	7.235580E+17	1.367490E+13	1.142460E+15	1.104378E+09
15.000	121.10000	216.700	4.047595E+18	2.634525E+12	8.464500E+17	2.025000E+13	1.336500E+15	6.925500E+08
14.000	141.70000	216.700	4.736121E+18	2.383717E+12	9.904510E+17	2.808805E+13	1.563870E+15	3.544772E+08
13.000	165.80000	216.700	5.541629E+18	2.132992E+12	1.159114E+18	6.017410E+13	1.830180E+15	2.467970E+08
12.000	194.00000	216.700	6.484174E+18	2.008345E+12	1.356201E+18	1.236803E+14	2.141370E+15	2.044035E+08
11.000	227.00000	216.800	7.583652E+18	1.630876E+12	1.586101E+18	2.741906E+14	2.504370E+15	1.988318E+08
10.000	265.00000	223.300	8.595457E+18	1.129443E+12	1.797818E+18	6.017959E+14	2.838660E+15	2.047276E+08
9.000	308.00000	229.700	9.711841E+18	8.910379E+11	2.031271E+18	1.538518E+15	3.207270E+15	2.254808E+08
8.000	356.50000	236.200	1.093179E+19	6.526804E+11	2.286460E+18	4.011698E+15	3.610200E+15	2.516200E+08
7.000	411.10001	242.700	1.226845E+19	6.151052E+11	2.566520E+18	7.024160E+15	4.052400E+15	2.824400E+08
6.000	472.20001	249.200	1.372429E+19	5.645776E+11	2.869570E+18	1.270574E+16	4.530900E+15	3.157900E+08
5.000	540.50000	255.700	1.531006E+19	5.772576E+11	3.201880E+18	2.140204E+16	5.055600E+15	3.523600E+08
4.000	616.59998	262.200	1.703267E+19	5.771448E+11	3.561360E+18	3.677232E+16	5.623200E+15	3.919200E+08
3.000	701.20001	268.700	1.890105E+19	6.274337E+11	3.952190E+18	6.017162E+16	6.240300E+15	4.349300E+08
2.000	795.00000	275.200	2.092331E+19	6.778279E+11	4.376460E+18	9.697315E+16	6.910200E+15	4.816201E+08
1.000	898.79999	281.700	2.310936E+19	6.779402E+11	4.834170E+18	1.404222E+17	7.632900E+15	5.319900E+08
0.000	1013.00000	288.200	2.545818E+19	6.777680E+11	5.325320E+18	1.973426E+17	8.408400E+15	5.860400E+08

Table C.2. *AFGL Atmospheric Constituent Profiles, Tropical (AFGL-TR-86-0110).*

z(km)	p(mb)	T(K)	air(cm^{-3})	O_3(cm^{-3})	O_2(cm^{-3})	H_2O(cm^{-3})	CO_2(cm^{-3})	NO_2(cm^{-3})
100.000	0.00029	190.700	1.097638E+13	4.392000E+06	1.756800E+12	4.392000E+06	2.141100E+09	1.866600E+03
95.000	0.00069	184.300	2.703802E+13	1.353000E+07	4.870800E+12	1.461240E+07	7.306201E+09	4.762560E+03
90.000	0.00172	177.000	7.038287E+13	3.662360E+07	1.338170E+13	5.986550E+07	2.183330E+10	1.288869E+04
85.000	0.00440	177.100	1.799476E+14	9.005000E+07	3.602000E+13	2.341300E+08	5.763200E+10	3.457920E+04
80.000	0.01100	184.800	4.311244E+14	1.423620E+08	9.016260E+13	9.059399E+08	1.414992E+11	8.714280E+04
75.000	0.02600	201.800	9.331769E+14	1.680840E+08	1.951642E+14	3.081540E+09	3.081540E+11	2.007670E+05
70.000	0.05800	218.900	1.919084E+15	5.760000E+08	4.012800E+14	8.640000E+09	6.336000E+11	4.435200E+05
65.000	0.12100	236.000	3.713515E+15	2.415400E+09	7.766440E+14	2.006640E+10	1.226280E+12	9.401481E+05
60.000	0.23900	253.100	6.839393E+15	7.528400E+09	1.430396E+15	4.106400E+10	2.258520E+12	1.950540E+06
55.000	0.45600	263.400	1.253894E+16	2.259000E+10	2.622950E+15	7.530000E+10	4.141500E+12	4.254450E+06
50.000	0.85400	270.200	2.289203E+16	6.414800E+10	4.788190E+15	1.374600E+11	7.560300E+12	1.014913E+07
47.500	1.16000	269.600	3.116377E+16	1.076055E+11	6.518710E+15	1.840210E+11	1.029270E+13	2.077254E+07
45.000	1.59000	264.800	4.349160E+16	1.958400E+11	9.095680E+15	2.480640E+11	1.436160E+13	5.004800E+07
42.500	2.20000	259.400	6.142774E+16	3.626730E+11	1.284723E+16	3.380850E+11	2.028510E+13	1.333899E+08
40.000	3.05000	254.000	8.697170E+16	6.527249E+11	1.818927E+16	4.525560E+11	2.871990E+13	3.507309E+08
37.500	4.26000	248.500	1.241638E+17	1.093840E+12	2.597870E+16	6.090700E+11	4.101900E+13	7.781180E+08
35.000	6.00000	243.100	1.787632E+17	1.735330E+12	3.739010E+16	8.229400E+11	5.903700E+13	1.302392E+09
32.500	8.52000	237.700	2.596105E+17	2.559030E+12	5.429820E+16	1.117140E+12	8.573400E+13	1.873158E+09
30.000	12.20000	232.300	3.803842E+17	3.540510E+12	7.956630E+16	1.522800E+12	1.256310E+14	2.345112E+09
27.500	17.63000	227.000	5.625204E+17	4.390620E+12	1.176461E+17	2.026440E+12	1.857570E+14	2.707549E+09
25.000	25.70000	221.400	8.407510E+17	4.543020E+12	1.758317E+17	2.734225E+12	2.776290E+14	3.146462E+09
24.000	30.00000	219.200	9.912712E+17	4.265600E+12	2.073280E+17	3.174400E+12	3.273600E+14	3.035520E+09
23.000	35.00000	217.000	1.168208E+18	3.974600E+12	2.443210E+17	3.390100E+12	3.857700E+14	3.016020E+09
22.000	40.90000	214.600	1.380402E+18	3.314400E+12	2.886290E+17	3.866800E+12	4.557300E+14	2.982960E+09
21.000	48.00000	210.700	1.650017E+18	2.971800E+12	3.450590E+17	4.375150E+12	5.448300E+14	2.905760E+09
20.000	56.50000	206.700	1.979793E+18	2.773400E+12	4.140290E+17	5.150600E+12	6.537300E+14	2.753590E+09
19.000	66.60000	202.700	2.379755E+18	2.261950E+12	4.976290E+17	6.190600E+12	7.857300E+14	2.523860E+09
18.000	78.90000	198.800	2.874567E+18	1.438500E+12	6.012930E+17	7.911750E+12	9.494100E+14	2.218167E+09
17.000	93.70000	194.800	3.483874E+18	8.715000E+11	7.285740E+17	1.010940E+13	1.150380E+15	1.809234E+09
16.000	111.00000	197.000	4.081019E+18	5.897296E+11	8.535560E+17	1.225200E+13	1.347720E+15	1.302796E+09
15.000	132.00000	203.700	4.693478E+18	5.899431E+11	9.816730E+17	1.878800E+13	1.550010E+15	8.031870E+08
14.000	156.00000	210.300	5.372756E+18	5.645850E+11	1.123793E+18	3.344494E+13	1.774410E+15	4.021996E+08
13.000	182.00000	217.000	6.074680E+18	5.646784E+11	1.270511E+18	6.018210E+13	2.006070E+15	2.705155E+08
12.000	213.00000	223.600	6.899532E+18	5.395476E+11	1.442936E+18	2.005612E+14	2.278320E+15	2.174760E+08
11.000	247.00000	230.100	7.774853E+18	5.144914E+11	1.626020E+18	5.684068E+14	2.567400E+15	2.038360E+08
10.000	286.00000	237.000	8.740364E+18	4.893947E+11	1.828123E+18	1.672426E+15	2.886510E+15	2.081786E+08
9.000	329.00000	243.600	9.782062E+18	4.894500E+11	2.045901E+18	4.011532E+15	3.230370E+15	2.271048E+08
8.000	378.00000	250.300	1.093812E+19	4.895745E+11	2.288550E+18	8.362515E+15	3.613500E+15	2.518500E+08
7.000	432.00000	257.000	1.217482E+19	5.143614E+11	2.545620E+18	1.570002E+16	4.019400E+15	2.801400E+08
6.000	492.00000	263.600	1.351859E+19	5.397117E+11	2.827770E+18	2.842653E+16	4.464900E+15	3.111900E+08
5.000	559.00000	270.300	1.497882E+19	5.646733E+11	3.132910E+18	5.015654E+16	4.946700E+15	3.447700E+08
4.000	633.00000	277.000	1.655144E+19	5.897016E+11	3.461040E+18	7.354296E+16	5.464800E+15	3.808800E+08
3.000	715.00000	283.700	1.825402E+19	6.401807E+11	3.818430E+18	1.571220E+17	6.029100E+15	4.202100E+08
2.000	805.00000	287.700	2.026599E+19	6.777576E+11	4.238520E+18	3.110952E+17	6.692400E+15	4.664400E+08
1.000	904.00000	293.700	2.229340E+19	7.027649E+11	4.662790E+18	4.348219E+17	7.362299E+15	5.131300E+08
0.000	1013.00000	299.700	2.448130E+19	7.029050E+11	5.120500E+18	6.352850E+17	8.085000E+15	5.635000E+08

Table C.3. *AFGL Atmospheric Constituent Profiles, Midlatitude Summer (AFGL-TR-86-0110).*

z(km)	p(mb)	T(K)	air(cm^{-3})	O$_3$(cm^{-3})	O$_2$(cm^{-3})	H$_2$O(cm^{-3})	CO$_2$(cm^{-3})	NO$_2$(cm^{-3})
100.000	0.00026	190.500	9.809267E+12	3.926400E+06	1.570560E+12	3.926400E+06	1.914120E+09	1.668720E+03
95.000	0.00062	178.300	2.538870E+13	1.778700E+07	4.573800E+12	1.372140E+07	6.860700E+09	4.472160E+03
90.000	0.00164	165.000	7.198993E+13	5.403000E+07	1.368760E+13	6.123400E+07	2.233240E+10	1.318332E+04
85.000	0.00448	165.100	1.965363E+14	1.121190E+08	3.934000E+13	2.616110E+08	6.294400E+10	3.776640E+04
80.000	0.01200	174.100	4.992227E+14	9.992000E+07	1.044164E+14	1.049160E+09	1.638688E+11	1.009192E+05
75.000	0.03000	196.100	1.108040E+15	2.107100E+08	2.317810E+14	3.271550E+09	3.659700E+11	2.384350E+05
70.000	0.06700	218.100	2.225005E+15	8.908001E+08	4.654430E+14	8.239900E+09	7.349100E+11	5.144370E+05
65.000	0.13900	240.100	4.193093E+15	3.356800E+09	8.769640E+14	1.846240E+10	1.384680E+12	1.061588E+06
60.000	0.27200	257.100	7.662644E+15	9.968400E+09	1.602612E+15	3.834000E+10	2.530440E+12	2.185380E+06
55.000	0.51500	269.300	1.385105E+16	2.494800E+10	2.896740E+15	7.415099E+10	4.573800E+12	4.698540E+06
50.000	0.95100	275.700	2.498363E+16	7.000000E+10	5.225000E+15	1.375000E+11	8.250000E+12	1.107500E+07
47.500	1.29000	275.200	3.395104E+16	1.189300E+11	7.101820E+15	1.868900E+11	1.121340E+13	2.263068E+07
45.000	1.76000	269.900	4.723040E+16	2.126700E+11	9.877339E+15	2.575670E+11	1.559580E+13	5.434900E+07
42.500	2.41000	263.700	6.619401E+16	3.908160E+11	1.384416E+16	3.510720E+11	2.185920E+13	1.437408E+08
40.000	3.33000	257.500	9.366532E+16	7.076615E+11	1.958957E+16	4.780230E+11	3.093090E+13	3.777319E+08
37.500	4.64000	251.300	1.337326E+17	1.164060E+12	2.796420E+16	6.690000E+11	4.415400E+13	8.375880E+08
35.000	6.52000	245.200	1.925923E+17	1.715030E+12	4.027430E+16	9.538649E+11	6.359100E+13	1.402856E+09
32.500	9.30000	239.000	2.818363E+17	2.284200E+12	5.893800E+16	1.367700E+12	9.306000E+13	2.033220E+09
30.000	13.20000	233.700	4.090977E+17	2.865800E+12	8.556460E+16	1.924180E+12	1.351020E+14	2.521904E+09
27.500	19.07000	228.450	6.046045E+17	3.630000E+12	1.264450E+17	2.692250E+12	1.996500E+14	2.910050E+09
25.000	27.70000	225.100	8.912839E+17	4.281120E+12	1.864071E+17	3.745980E+12	2.943270E+14	3.335706E+09
24.000	32.20000	223.900	1.041630E+18	4.168000E+12	2.177780E+17	4.168000E+12	3.438600E+14	3.188520E+09
23.000	37.60000	222.800	1.222319E+18	4.158200E+12	2.556070E+17	4.708550E+12	4.035900E+14	3.155340E+09
22.000	43.70000	221.600	1.428313E+18	4.144100E+12	2.986610E+17	5.144399E+12	4.715700E+14	3.086640E+09
21.000	51.00000	220.400	1.675986E+18	4.024800E+12	3.504930E+17	5.785650E+12	5.534100E+14	2.951520E+09
20.000	59.50000	219.200	1.966021E+18	3.934000E+12	4.111030E+17	6.491100E+12	6.491100E+14	2.734130E+09
19.000	69.50000	217.900	2.310146E+18	3.468000E+12	4.832080E+17	7.398400E+12	7.629600E+14	2.450720E+09
18.000	81.20000	216.800	2.712742E+18	2.715000E+12	5.674350E+17	8.552250E+12	8.959500E+14	2.093265E+09
17.000	95.00000	215.700	3.189961E+18	2.234400E+12	6.671280E+17	1.021440E+13	1.053360E+15	1.656648E+09
16.000	111.00000	215.700	3.727217E+18	2.238000E+12	7.795700E+17	1.230900E+13	1.230900E+15	1.189870E+09
15.000	130.00000	215.700	4.365209E+18	2.184000E+12	9.129120E+17	1.485120E+13	1.441440E+15	7.469280E+08
14.000	153.00000	215.700	5.137515E+18	2.262040E+12	1.074469E+18	2.570500E+13	1.696530E+15	3.845468E+08
13.000	179.00000	215.800	6.007772E+18	1.803600E+12	1.256508E+18	4.809600E+13	1.983960E+15	2.675340E+08
12.000	209.00000	222.300	6.809554E+18	1.519522E+12	1.424126E+18	2.006042E+14	2.248620E+15	2.146410E+08
11.000	243.00000	228.800	7.692404E+18	1.380251E+12	1.608882E+18	7.356209E+14	2.540340E+15	2.016876E+08
10.000	281.00000	235.300	8.649604E+18	1.128742E+12	1.809104E+18	2.139763E+15	2.856480E+15	2.060128E+08
9.000	324.00000	241.700	9.709126E+18	1.079448E+12	2.030644E+18	4.011736E+15	3.206280E+15	2.254112E+08
8.000	372.00000	248.200	1.085558E+19	9.910836E+11	2.269740E+18	7.019904E+15	3.583800E+15	2.497800E+08
7.000	426.00000	254.700	1.211414E+19	9.409968E+11	2.533080E+18	1.236240E+16	3.999600E+15	2.787600E+08
6.000	487.00000	261.200	1.350416E+19	8.657207E+11	2.823590E+18	2.040010E+16	4.458300E+15	3.107300E+08
5.000	554.00000	267.200	1.501707E+19	8.284536E+11	3.141270E+18	3.344175E+16	4.959900E+15	3.456900E+08
4.000	628.00000	273.200	1.664910E+19	8.031786E+11	3.481940E+18	6.352458E+16	5.497800E+15	3.831800E+08
3.000	710.00000	279.200	1.841852E+19	7.781146E+11	3.851870E+18	1.102851E+17	6.081900E+15	4.238900E+08
2.000	802.00000	285.200	2.036745E+19	7.528372E+11	4.259420E+18	1.972784E+17	6.725400E+15	4.687400E+08
1.000	902.00000	289.700	2.255121E+19	7.531609E+11	4.717130E+18	3.110146E+17	7.448100E+15	5.191100E+08
0.000	1013.00000	294.200	2.493898E+19	7.530432E+11	5.216640E+18	4.682496E+17	8.236800E+15	5.740800E+08

Tabel C.4. *AFGL Atmospheric Constituent Profiles, Midlatitude Winter (AFGL-TR-86-0110).*

z(km)	p(mb)	T(K)	air(cm^{-3})	O$_3$(cm^{-3})	O$_2$(cm^{-3})	H$_2$O(cm^{-3})	CO$_2$(cm^{-3})	NO$_2$(cm^{-3})
100.000	0.00041	218.600	1.349841E+13	5.404000E+06	2.161600E+12	5.404000E+06	2.634450E+09	2.296700E+03
95.000	0.00088	208.300	3.049454E+13	2.441600E+07	5.493600E+12	1.648080E+07	8.240400E+09	5.371520E+03
90.000	0.00198	199.500	7.188431E+13	5.755200E+07	1.366860E+13	6.114900E+07	2.230140E+10	1.316502E+04
85.000	0.00456	199.800	1.653032E+14	9.097000E+07	3.308000E+13	2.199820E+08	5.292800E+10	3.175680E+04
80.000	0.01030	210.100	3.550774E+14	8.171900E+07	7.425770E+13	7.106000E+08	1.165384E+11	7.177059E+04
75.000	0.02220	220.400	7.295469E+14	1.825250E+08	1.525909E+14	1.971270E+09	2.409330E+11	1.569715E+05
70.000	0.04700	230.700	1.475577E+15	4.726400E+08	3.086930E+14	4.874100E+09	4.874100E+11	3.411870E+05
65.000	0.09500	240.900	2.856266E+15	1.571900E+09	5.973220E+14	1.143200E+10	9.431400E+11	7.230740E+05
60.000	0.18800	250.800	5.429278E+15	5.433000E+09	1.135497E+15	2.444850E+10	1.792890E+12	1.548405E+06
55.000	0.36200	260.600	1.006111E+16	1.711900E+10	2.104630E+15	4.883950E+10	3.323100E+12	3.413730E+06
50.000	0.68300	265.700	1.861834E+16	5.123250E+10	3.893670E+15	9.221850E+10	6.147900E+12	8.253090E+06
47.500	0.94000	265.100	2.568206E+16	9.509000E+10	5.371300E+15	1.285000E+11	8.481000E+12	1.711620E+07
45.000	1.29000	258.500	3.614440E+16	1.663820E+11	7.559530E+15	1.808500E+11	1.193610E+13	4.159550E+07
42.500	1.80000	250.800	5.198245E+16	3.069180E+11	1.087218E+16	2.601080E+11	1.716660E+13	1.128834E+08
40.000	2.53000	243.200	7.534749E+16	5.202600E+11	1.575860E+16	3.732300E+11	2.488200E+13	3.038620E+08
37.500	3.60000	235.500	1.107193E+17	7.977600E+11	2.315720E+16	5.429200E+11	3.656400E+13	6.936080E+08
35.000	5.18000	227.900	1.646256E+17	1.169370E+12	3.442230E+16	7.987950E+11	5.435100E+13	1.199016E+09
32.500	7.56000	220.400	2.484403E+17	1.690480E+12	5.195740E+16	1.193280E+12	8.203800E+13	1.792406E+09
30.000	11.10000	217.400	3.698071E+17	2.257610E+12	7.735090E+16	1.757975E+12	1.221330E+14	2.279816E+09
27.500	16.46000	215.500	5.532155E+17	3.100160E+12	1.157024E+17	2.601920E+12	1.826880E+14	2.662816E+09
25.000	24.40000	215.200	8.212197E+17	4.191180E+12	1.717562E+17	3.821370E+12	2.711940E+14	3.073532E+09
24.000	28.60000	215.200	9.625772E+17	4.527510E+12	2.013297E+17	4.431180E+12	3.178890E+14	2.947698E+09
23.000	33.40000	215.200	1.124129E+18	4.837501E+12	2.351250E+17	5.118751E+12	3.712500E+14	2.902500E+09
22.000	39.10000	215.200	1.315971E+18	5.136300E+12	2.752530E+17	5.966010E+12	4.346100E+14	2.844720E+09
21.000	45.80000	215.200	1.541470E+18	5.400500E+12	3.224870E+17	6.943500E+12	5.091900E+14	2.715680E+09
20.000	53.70000	215.200	1.807356E+18	5.246100E+12	3.780810E+17	8.140500E+12	5.969700E+14	2.514510E+09
19.000	62.80000	215.200	2.113631E+18	4.864500E+12	4.420350E+17	9.517500E+12	6.979500E+14	2.241900E+09
18.000	73.60000	215.700	2.471380E+18	4.451400E+12	5.168570E+17	1.112850E+13	8.160900E+14	1.906683E+09
17.000	86.10000	216.200	2.884426E+18	4.040400E+12	6.031740E+17	1.298700E+13	9.523800E+14	1.497834E+09
16.000	100.70000	216.700	3.365754E+18	3.704800E+12	7.039120E+17	1.549280E+13	1.111440E+15	1.074392E+09
15.000	117.80000	217.200	3.928234E+18	3.537900E+12	8.215790E+17	1.847570E+13	1.297230E+15	6.722010E+08
14.000	137.80000	217.700	4.584612E+18	3.670400E+12	9.588920E+17	2.202240E+13	1.514040E+15	3.431824E+08
13.000	161.10001	218.200	5.347523E+18	3.764963E+12	1.118359E+18	2.675500E+13	1.765830E+15	2.381195E+08
12.000	188.20000	218.700	6.232793E+18	3.263198E+12	1.303533E+18	3.742200E+13	2.058210E+15	1.964655E+08
11.000	219.89999	219.200	7.266018E+18	2.635010E+12	1.519639E+18	7.271000E+13	2.399430E+15	1.905002E+08
10.000	256.79999	219.700	8.465970E+18	2.007864E+12	1.770648E+18	2.507712E+14	2.795760E+15	2.016336E+08
9.000	299.29999	225.700	9.604770E+18	1.506200E+12	2.008908E+18	5.350039E+14	3.171960E+15	2.229984E+08
8.000	347.29999	231.700	1.085652E+19	1.128354E+12	2.269740E+18	1.169622E+15	3.583800E+15	2.497800E+08
7.000	401.60001	237.700	1.223704E+19	9.666475E+11	2.560250E+18	2.843225E+15	4.042500E+15	2.817500E+08
6.000	462.70001	243.700	1.375168E+19	8.031712E+11	2.875840E+18	7.021728E+15	4.540800E+15	3.164800E+08
5.000	531.29999	249.700	1.541108E+19	7.278240E+11	3.222780E+18	1.270762E+16	5.088600E+15	3.546600E+08
4.000	608.09998	255.700	1.722488E+19	6.149508E+11	3.603160E+18	2.206720E+16	5.689200E+15	3.965200E+08
3.000	693.79999	261.700	1.920182E+19	6.150400E+11	4.016980E+18	4.013136E+16	6.342600E+15	4.420600E+08
2.000	789.70001	265.200	2.156753E+19	6.148142E+11	4.510220E+18	6.016504E+16	7.121400E+15	4.963400E+08
1.000	897.29999	268.700	2.418699E+19	6.776000E+11	5.057800E+18	8.358680E+16	7.986000E+15	5.566000E+08
0.000	1018.00000	272.200	2.708766E+19	7.531159E+11	5.665990E+18	1.170068E+17	8.946300E+15	6.235300E+08

Table C.5. *AFGL Atmospheric Constituent Profiles, Subarctic Summer (AFGL-TR-86-0110).*

z(km)	p(mb)	T(K)	air(cm^{-3})	O_3(cm^{-3})	O_2(cm^{-3})	H_2O(cm^{-3})	CO_2(cm^{-3})	NO_2(cm^{-3})
100.000	0.00025	190.400	9.434015E+12	3.776400E+06	1.510560E+12	3.776400E+06	1.840995E+09	1.604970E+03
95.000	0.00061	176.800	2.482574E+13	1.987200E+07	4.471200E+12	1.341360E+07	6.706800E+09	4.371840E+03
90.000	0.00161	161.600	7.215997E+13	6.498900E+07	1.371990E+13	6.137850E+07	2.238510E+10	1.321443E+04
85.000	0.00451	161.700	2.020125E+14	1.314300E+08	4.044000E+13	2.689260E+08	6.470400E+10	3.882240E+04
80.000	0.01250	170.600	5.306923E+14	9.559800E+07	1.109999E+14	1.062200E+09	1.742008E+11	1.072822E+05
75.000	0.03200	193.600	1.197172E+15	2.396000E+08	2.503820E+14	3.234600E+09	3.953400E+11	2.575700E+05
70.000	0.07100	216.600	2.374169E+15	9.504000E+08	4.965840E+14	7.840800E+09	7.840800E+11	5.488560E+05
65.000	0.14700	239.700	4.441822E+15	3.556000E+09	9.290050E+14	1.778000E+10	1.466850E+12	1.124585E+06
60.000	0.28800	262.700	7.940434E+15	9.535200E+09	1.660714E+15	3.575700E+10	2.622180E+12	2.264610E+06
55.000	0.53700	274.000	1.419501E+16	2.415700E+10	2.969890E+15	6.891850E+10	4.689300E+12	4.817190E+06
50.000	0.98700	277.200	2.578907E+16	6.452500E+10	5.394290E+15	1.277595E+11	8.517300E+12	1.143383E+07
47.500	1.34000	276.200	3.513929E+16	1.125120E+11	7.348440E+15	1.758000E+11	1.160280E+13	2.341656E+07
45.000	1.82000	273.600	4.818004E+16	2.024820E+11	1.007589E+16	2.410500E+11	1.590930E+13	5.544150E+07
42.500	2.48000	269.500	6.665071E+16	3.601800E+11	1.394030E+16	3.335000E+11	2.201100E+13	1.447390E+08
40.000	3.40000	262.100	9.395583E+16	6.581400E+11	1.965018E+16	4.701000E+11	3.102660E+13	3.789006E+08
37.500	4.72000	254.600	1.342751E+17	1.048320E+12	2.808960E+16	6.720000E+11	4.435200E+13	8.413440E+08
35.000	6.61000	247.200	1.936711E+17	1.492260E+12	4.050420E+16	9.690000E+11	6.395400E+13	1.410864E+09
32.500	9.40000	240.000	2.836798E+17	1.958910E+12	5.933510E+16	1.419500E+12	9.368700E+13	2.046919E+09
30.000	13.40000	235.100	4.128230E+17	2.354670E+12	8.633790E+16	2.065500E+12	1.363230E+14	2.544696E+09
27.500	19.23000	231.000	6.029470E+17	3.198020E+12	1.261106E+17	2.986830E+12	1.991220E+14	2.902354E+09
25.000	27.80000	228.100	8.827370E+17	3.975300E+12	1.846306E+17	4.328660E+12	2.915220E+14	3.303916E+09
24.000	32.28000	226.600	1.031776E+18	4.338600E+12	2.158970E+17	5.010049E+12	3.408900E+14	3.160980E+09
23.000	37.50000	225.200	1.206076E+18	4.465900E+12	2.522630E+17	5.829810E+12	3.983100E+14	3.114060E+09
22.000	43.60000	225.200	1.402264E+18	4.629900E+12	2.932270E+17	6.734400E+12	4.629900E+14	3.030480E+09
21.000	50.70000	225.200	1.630615E+18	4.406400E+12	3.410880E+17	7.670400E+12	5.385600E+14	2.872320E+09
20.000	59.00000	225.200	1.897560E+18	3.987900E+12	3.968910E+17	8.735400E+12	6.266700E+14	2.639610E+09
19.000	68.60000	225.200	2.206315E+18	3.753600E+12	4.614720E+17	9.936000E+12	7.286400E+14	2.340480E+09
18.000	79.80000	225.200	2.566530E+18	3.338400E+12	5.367120E+17	1.104240E+13	8.474400E+14	1.979928E+09
17.000	92.80000	225.200	2.984637E+18	2.987000E+12	6.242830E+17	1.209735E+13	9.857100E+14	1.550253E+09
16.000	108.00000	225.200	3.473499E+18	2.954600E+12	7.264840E+17	1.390400E+13	1.147080E+15	1.108844E+09
15.000	126.00000	225.200	4.052416E+18	2.838500E+12	8.474950E+17	1.622000E+13	1.338150E+15	6.934050E+08
14.000	146.00000	225.200	4.695657E+18	2.819400E+12	9.820909E+17	1.879600E+13	1.550670E+15	3.514852E+08
13.000	170.00000	225.200	5.467545E+18	2.735500E+12	1.143439E+18	2.434595E+13	1.805430E+15	2.434595E+08
12.000	197.70000	225.200	6.358433E+18	2.608830E+12	1.329867E+18	3.817800E+13	2.099790E+15	2.004345E+08
11.000	230.00000	225.200	7.397267E+18	2.257610E+12	1.547018E+18	9.844661E+13	2.442660E+15	1.939324E+08
10.000	267.70001	225.200	8.609776E+18	1.628424E+12	1.800744E+18	3.653184E+14	2.843280E+15	2.050608E+08
9.000	310.79999	232.200	9.694616E+18	1.377542E+12	2.027509E+18	1.261130E+15	3.201330E+15	2.250632E+08
8.000	359.00000	239.200	1.087039E+19	9.916032E+11	2.273920E+18	4.347648E+15	3.590400E+15	2.502400E+08
7.000	413.00000	246.100	1.215487E+19	9.409409E+11	2.541440E+18	9.692736E+15	4.012800E+15	2.796800E+08
6.000	474.00000	253.100	1.356432E+19	8.907348E+11	2.836130E+18	1.804810E+16	4.478100E+15	3.121100E+08
5.000	541.00000	260.100	1.506498E+19	8.034624E+11	3.151720E+18	3.344744E+16	4.976400E+15	3.468400E+08
4.000	616.00000	265.500	1.680459E+19	7.531996E+11	3.515380E+18	5.685160E+16	5.550600E+15	3.868600E+08
3.000	700.00000	270.900	1.871548E+19	7.280351E+11	3.914570E+18	9.027860E+16	6.180900E+15	4.307900E+08
2.000	792.90002	276.300	2.078497E+19	7.028321E+11	4.347200E+18	1.404000E+17	6.864000E+15	4.784000E+08
1.000	896.00000	281.700	2.303737E+19	6.776700E+11	4.817450E+18	2.005581E+17	7.606500E+15	5.301500E+08
0.000	1010.00000	287.200	2.547116E+19	6.148188E+11	5.327410E+18	3.043506E+17	8.411700E+15	5.862700E+08

Table C.6. *AFGL Atmospheric Constituent Profiles, Subarctic Winter (AFGL-TR-86-0110).*

z(km)	p(mb)	T(K)	air(cm^{-3})	O_3(cm^{-3})	O_2(cm^{-3})	H_2O(cm^{-3})	CO_2(cm^{-3})	NO_2(cm^{-3})
z(km)	p(mb)	T(K)	air(cm-3)	o3(cm-3)	o2(cm-3)	h2o(cm-3)	co2(cm-3)	no2(cm-3)
100.000	0.00042	218.500	1.402170E+13	5.612000E+06	2.244800E+12	5.612000E+06	2.735850E+09	2.385100E+03
95.000	0.00091	211.000	3.113413E+13	2.492800E+07	5.608800E+12	1.682640E+07	8.413200E+09	5.484160E+03
90.000	0.00202	202.300	7.239309E+13	5.795200E+07	1.376360E+13	6.157400E+07	2.245640E+10	1.325652E+04
85.000	0.00450	213.100	1.529470E+14	1.148250E+08	3.062000E+13	2.036230E+08	4.899200E+10	2.939520E+04
80.000	0.00966	223.900	3.124891E+14	4.065100E+07	6.535430E+13	6.254000E+08	1.025656E+11	6.316540E+04
75.000	0.02000	234.700	6.172040E+14	2.038080E+08	1.290784E+14	1.667520E+09	2.038080E+11	1.327840E+05
70.000	0.04000	245.400	1.180585E+15	5.905000E+08	2.468290E+14	3.897300E+09	3.897300E+11	2.728110E+05
65.000	0.07900	248.400	2.303495E+15	1.498250E+09	4.817450E+14	9.220000E+09	7.606500E+11	5.831650E+05
60.000	0.15500	250.900	4.474483E+15	4.254100E+09	9.359020E+14	2.015100E+10	1.477740E+12	1.276230E+06
55.000	0.29900	259.100	8.358255E+15	1.338240E+10	1.748076E+15	4.056540E+10	2.760120E+12	2.835396E+06
50.000	0.57190	259.300	1.597458E+16	4.157400E+10	3.341910E+15	7.915050E+10	5.276700E+12	7.083570E+06
47.500	0.79000	253.200	2.259827E+16	6.783000E+10	4.725491E+15	1.130500E+11	7.461300E+12	1.505826E+07
45.000	1.11300	247.000	3.263698E+16	1.339060E+11	6.825940E+15	1.633000E+11	1.077780E+13	3.755900E+07
42.500	1.57000	240.800	4.722316E+16	2.410260E+11	9.877339E+15	2.363000E+11	1.559580E+13	1.025542E+08
40.000	2.24300	234.700	6.921943E+16	4.086930E+11	1.447743E+16	3.463500E+11	2.285910E+13	2.791581E+08
37.500	3.23000	228.500	1.023831E+17	6.406250E+11	2.142250E+16	5.125000E+11	3.382500E+13	6.416500E+08
35.000	4.70100	222.300	1.531661E+17	9.504599E+11	3.203970E+16	7.664999E+11	5.058900E+13	1.116024E+09
32.500	6.91000	218.500	2.290543E+17	1.352280E+12	4.790280E+16	1.146000E+12	7.563600E+13	1.652532E+09
30.000	10.20000	216.000	3.420253E+17	1.848420E+12	7.154070E+16	1.711500E+12	1.129590E+14	2.469454E+09
27.500	15.13000	213.600	5.130379E+17	2.515660E+12	1.073006E+17	2.567000E+12	1.694220E+14	2.469454E+09
25.000	22.56000	211.200	7.736723E+17	3.638740E+12	1.618078E+17	3.871000E+12	2.554860E+14	2.895508E+09
24.000	26.49000	211.800	9.058741E+17	4.169900E+12	1.894585E+17	4.532500E+12	2.991450E+14	2.773890E+09
23.000	31.09000	212.400	1.060176E+18	4.774500E+12	2.217490E+17	5.251950E+12	3.501300E+14	2.737380E+09
22.000	36.47000	213.000	1.240132E+18	5.212200E+12	2.593690E+17	6.080900E+12	4.095300E+14	2.680560E+09
21.000	42.77000	213.600	1.450273E+18	5.804000E+12	3.032590E+17	7.037350E+12	4.788300E+14	2.553760E+09
20.000	50.14000	214.200	1.695418E+18	6.278900E+12	3.546730E+17	8.145601E+12	5.600100E+14	2.358830E+09
19.000	58.75000	214.800	1.981004E+18	6.144200E+12	4.142380E+17	9.414500E+12	6.540600E+14	2.100920E+09
18.000	68.82000	215.400	2.314093E+18	5.674200E+12	4.840440E+17	1.088520E+13	7.642800E+14	1.785636E+09
17.000	80.58000	216.000	2.702000E+18	5.137600E+12	5.651360E+17	1.257360E+13	8.923200E+14	1.403376E+09
16.000	94.31000	216.600	3.153632E+18	4.734000E+12	6.596040E+17	1.451760E+13	1.041480E+15	1.006764E+09
15.000	110.30000	217.200	3.678134E+18	4.417200E+12	7.693290E+17	1.674855E+13	1.214730E+15	6.294510E+08
14.000	129.10001	217.200	4.305051E+18	3.877200E+12	9.003720E+17	1.938600E+13	1.421640E+15	3.222384E+08
13.000	151.00000	217.200	5.035342E+18	3.275350E+12	1.053151E+18	2.242355E+13	1.662870E+15	2.242355E+08
12.000	176.60001	217.200	5.889016E+18	2.357200E+12	1.231637E+18	3.535800E+13	1.944690E+15	1.856295E+08
11.000	206.70000	217.200	6.892749E+18	2.414300E+12	1.441682E+18	6.898000E+13	2.276340E+15	1.807276E+08
10.000	241.80000	217.200	8.063216E+18	2.420700E+12	1.686421E+18	1.613800E+14	2.662770E+15	1.920422E+08
9.000	282.89999	217.200	9.433762E+18	1.982400E+12	1.972960E+18	2.809344E+14	3.115200E+15	2.190080E+08
8.000	330.79999	220.600	1.086105E+19	1.130480E+12	2.271830E+18	3.678408E+14	3.587100E+15	2.500100E+08
7.000	385.29999	227.300	1.227754E+19	8.912709E+11	2.568610E+18	1.806630E+15	4.055700E+15	2.826700E+08
6.000	446.70001	234.100	1.382058E+19	6.148818E+11	2.890470E+18	3.276327E+15	4.563900E+15	3.180900E+08
5.000	515.79999	240.900	1.550802E+19	5.899152E+11	3.243680E+18	6.687568E+15	5.121600E+15	3.569600E+08
4.000	593.20001	247.700	1.734551E+19	5.647208E+11	3.628240E+18	1.371093E+16	5.728800E+15	3.992800E+08
3.000	679.79999	252.700	1.948443E+19	5.395650E+11	4.075500E+18	2.273700E+16	6.435000E+15	4.485000E+08
2.000	777.50000	255.900	2.200604E+19	5.143872E+11	4.602180E+18	3.142254E+16	7.266600E+15	5.064600E+08
1.000	887.79999	259.100	2.481759E+19	5.146847E+11	5.191560E+18	4.011660E+16	8.197200E+15	5.713200E+08
0.000	1013.00000	257.200	2.852662E+19	5.144710E+11	5.966950E+18	4.011275E+16	9.421500E+15	6.566500E+08